Abyssal ocean circulation driven by geothermal fluxes

Jowan M. Barnes

School of Natural and Environmental Sciences

Thesis submitted for Doctor of Philosophy qualification

June 2019

Abstract

Geothermal heating is increasingly recognised as an important factor affecting ocean circulation, with modelling studies suggesting that this heat source could lead to first-order changes in the formation rate of Antarctic Bottom Water, as well as a significant warming effect in the abyssal ocean. Where it has been represented in numerical models, however, the geothermal heat flux into the ocean is generally treated as an entirely conductive flux, despite an estimated one third of the global geothermal flux being introduced to the ocean via hydrothermal sources.

In this project I use analytical and computational modelling methods to explore how the geothermal heat flux affects the deep ocean in both its forms, conductive and hydrothermal. There is a focus on the Panama Basin in the eastern equatorial Pacific, as the bathymetry and prevalence of geothermal heating in the region make it an appropriate area to study.

The main difference between the two geothermal mechanisms is the addition of a volume flux through the seabed for the hydrothermal heating. The circulations caused by such a volume flux through the seabed - initially ignoring the attending heat fluxes - are the focus of the first section of this thesis. It can be seen that these flows have the potential to drive abyssal circulations significantly different from those resulting from heating the bottom water.

The second section of the project takes a close look at how the partitioning of a heat flux between conductive and hydrothermal sources affects the circulation and hydrography in an idealised domain. In the first study of its kind, a hydrothermal input is added to the bottom boundary of a primitive equation model and simulations are completed to look at how the circulation changes as the proportion of the heat flux entering the ocean in this way increases. It is found that vertical transport of heat from the abyss is increased when hydrothermal fluxes are present.

In the final section, a 3-dimensional regional model of the Panama Basin is used to simulate the effects of geothermal heating on circulation in a semi-enclosed ocean basin. Of particular interest is the change to the flow through the deepest channels which connect the basin to the greater Pacific Ocean, where the heat transport is doubled. The simulations indicate that geothermal heating of the basin is a significant driver of its overturning circulation.

Acknowledgements

This project was undertaken at the National Oceanography Centre in Liverpool starting in September 2014, and at Newcastle University from September 2015 onwards. It was conceived as part of a major interdisciplinary NERC-funded collaboration entitled "Oceanographic and Seismic Characterisation of heat dissipation and alteration by hydrothermal fluids at an Axial Ridge" (OSCAR), led by Richard Hobbs of Durham University. I was supported financially by a NERC studentship (NE/JS00227/1) via the National Oceanography Centre and Durham University, and by the OSCAR project (NE/I022868/1).

Firstly, thanks to my supervisor, Miguel Morales Maqueda, for his regular support and advice throughout the project, and for sharing in my frustration when encountering technical problems beyond my control. I received additional support from co-supervisors Jeff Polton and Alex Megann at the National Oceanography Centre, for which I am also very grateful.

Additional thanks go to all the researchers of OSCAR for interesting discussions and feedback at project meetings during the course of the project, and to Catherine Landers, John Barnes and Anna Tobenhouse for their proofreading efforts as I approached the end.

I am grateful to my examiners David Stevens, who travelled up from the University of East Anglia, and Rob Upstill-Goddard of Newcastle University, for taking the time to read my thesis and then ensuring that the viva ran smoothly, engaging in interesting discussion and feedback.

Finally, thanks to my family for making the journey from Bournemouth to help me move around the North not just once, but three times during the course of the PhD. I shall try not to relocate quite so often in the future.

Contents

List of Figures

Chapter 1

Introduction

1.1 Heat loss of the Earth

Heat is continuously being released from the centre of the Earth. It is a global phenomenon, occurring across the entire surface of the planet and influencing natural systems within the ground, oceans and atmosphere. The majority of this heat enters the oceans, where the geothermal heat flux can be classified into two distinct processes. The first, conductive heat flux through the lithosphere (a term which encompasses the crust and upper mantle), occurs all over the ocean. It is distributed unevenly, with more heat escaping through areas where the Earth's crust is thinner and where there is less sedimentation on the seabed. The second process is that of hydrothermal circulation, in which sea water permeates the crust and takes heat with it back up into the ocean. This mainly takes place in relatively young oceanic crust, near the spreading centres of ocean ridges where the crust is thinner and has not existed long enough for large amounts of sediment to build up (Harris and Chapman, 2004). Surveys in the East Pacific suggest that hydrothermal circulation in the region occurs on a large scale, with heat flow observations implying hydrothermal activity up to 1000km from the crest of the East Pacific Rise (Anderson and Hobart, 1976).

Over the years there have been several studies which attempt to estimate the magnitude of the Earth's heat loss. These are summarised in Table 1.1 An early example is Lee and Uyeda (1965), a review of about 2000 heat flow measurements available at the time. A value of 26×10^{12} W was arrived at for the global heat flow, but this was calculated before knowledge of plate tectonics and the importance of hydrothermal flow (Sclater et al., 1980). A later estimate of 42.7×10^{12} W (Williams and Von Herzen, 1974) took into account the effects of sea floor spreading. Sclater et al. (1980) combined observations with thermal models, based on relationships between heat loss and crustal age, to calculate a global heat loss of 42×10^{12} W, with 29×10^{12} W escaping through oceanic crust. They estimated that 10.1×10^{12} W of this heat loss was due to hydrothermal circulation.

Publication	Global heat flow estimate	Ocean heat flux
Lee and Uyeda, 1965	26×10^{12} W	-
Williams and Von Herzen, 1974	42.7×10^{12} W	-
Sclater et al., 1980	42×10^{12} W	-
Pollack et al., 1993	44.2×10^{12} W	$0.101\,\mathrm{Wm^{-2}}$
Davies and Davies, 2010	47×10^{12} W	$0.1054\,\mathrm{Wm^{-2}}$

Table 1.1: A summary of estimations of the total global heat loss, and mean oceanic heat fluxes calculated from them.

Later, Pollack et al. (1993) compiled 24,774 observations into a dataset which covered 62 % of the Earth's surface on a $5° \times 5°$ grid. Their calculations yielded a global heat loss of 44.2×10^{12} W and a mean heat flow of $0.101\,\mathrm{Wm^{-2}}$ into the oceans. Most recently, Davies and Davies (2010) presented a new analysis of an even larger dataset consisting of 38,347 observations, reaching an estimate of 47×10^{12} W for the global heat loss with 31.9×10^{12} W of that in the oceans, giving a mean oceanic heat flow of $0.1054\,\mathrm{Wm^{-2}}$.

The thermal evolution of the oceanic lithosphere can be modelled using knowledge of the crustal age. A resource which is used in the more recent of the above studies is the heat flow model of Stein and Stein (1992), which relates heat flow to lithospheric age with an equation derived from heat flow observations. It is generally regarded as the best model of its kind.

1.2 The ocean's response to geothermal heat fluxes

Geothermal processes have an effect on the abyssal circulation, which is the area of interest for this PhD project. There is fairly extensive literature on localised effects of geothermal sources. In response to the discovery by Lupton and Craig (1981) of a westward-moving helium-3 (^{3}He) plume in the Pacific, Stommel (1982) presented a theory that the plume was dynamically active, driven by the high heat flux at the East Pacific Rise. Based on observations, Joyce et al. (1986) argued that geothermal heating was a likely cause for temperature variations in the deep North Pacific not accompanied by the salinity changes which would be consistent with normal mixing processes. In Joyce and Speer (1987), this line of thought led to a modelling study which continued the ideas of Stommel (1982) and showed that circulation driven by geothermal heating could have a significant upstream influence even in the presence of some background flow.

While known to contribute to mixing (eg. Thomson et al., 1995; Huang, 1999), geothermal heating is often neglected in global circulation models due to its low heat fluxes compared to surface sources. However, this comparison does not take into account some important considerations. Surface fluxes can be positive or negative, whereas the con-

ductive component of the geothermal heat flux is always directed upwards. So while the magnitude of surface fluxes is higher, when direction is taken into account this can lead to some fluxes cancelling each other out on a global scale, decreasing the net global flux. Additionally, the deep water masses affected by geothermal fluxes are rarely in contact with the surface of the ocean. The surface area of outcropping Antarctic Bottom Water, for example, is about one thousand times less than the area of contact with the seabed. Thus the integrals of heat fluxes from above and below into the deep ocean are of the same order for this water mass (eg. Emile-Geay and Madec, 2009).

When heating from below has been included in global circulation models, it has been found to cause much larger changes in the circulation than its magnitude alone would suggest. The first study of the influence of geothermal heating on a global scale model was undertaken by Adcroft et al. (2001) and Scott et al. (2001). These companion papers compared a model without geothermal heating to one with a uniform geothermal heat flux of $0.05\,\mathrm{Wm}^{-2}$, the average flux away from ridges. The addition of geothermal heating to the model resulted in an average temperature change of $0.3\,^{\circ}\mathrm{C}$, and a $25\,\%$ increase in Pacific overturning. These findings inspired further investigations into geothermal heating as a driving force of abyssal circulation. Hofmann and Morales Maqueda (2009) used the data of Pollack et al. (1993) to construct a more accurate geographically varying geothermal flux, as well as using a uniform flux equal to the global average of $0.101\,\mathrm{Wm}^{-2}$. Comparing these models to the same one with no geothermal flux provided similar results to those of Adcroft et al. (2001) in the Pacific ocean. Emile-Geay and Madec (2009) followed a different method, using the formula of Stein and Stein (1992) relating heat flow to crustal age and the high-resolution dataset of crustal age from Müller et al. (1997), to produce similar results.

More recently, there has been an increasing interest in the effects of heat input at the seabed on ocean circulation, with Mashayek et al. (2013) investigating the global role of these heat fluxes and Park et al. (2013) studying the East/Japan Sea in particular. In another modelling study Piecuch et al. (2015) found that inclusion of geothermal heating raised the global mean sea level trend, showing that its effects can be seen throughout the entire water column.

1.3 Hydrothermal heat flow

Hydrothermal systems exist at the interface between the ocean and the solid Earth. Cold, dense water seeps down through cracks and fissures in the seabed, percolating deep into the Earth's crust. Here it is heated until it is forced upwards, entering the ocean again at a higher temperature. The process is most prevalent at mid-ocean ridges where new

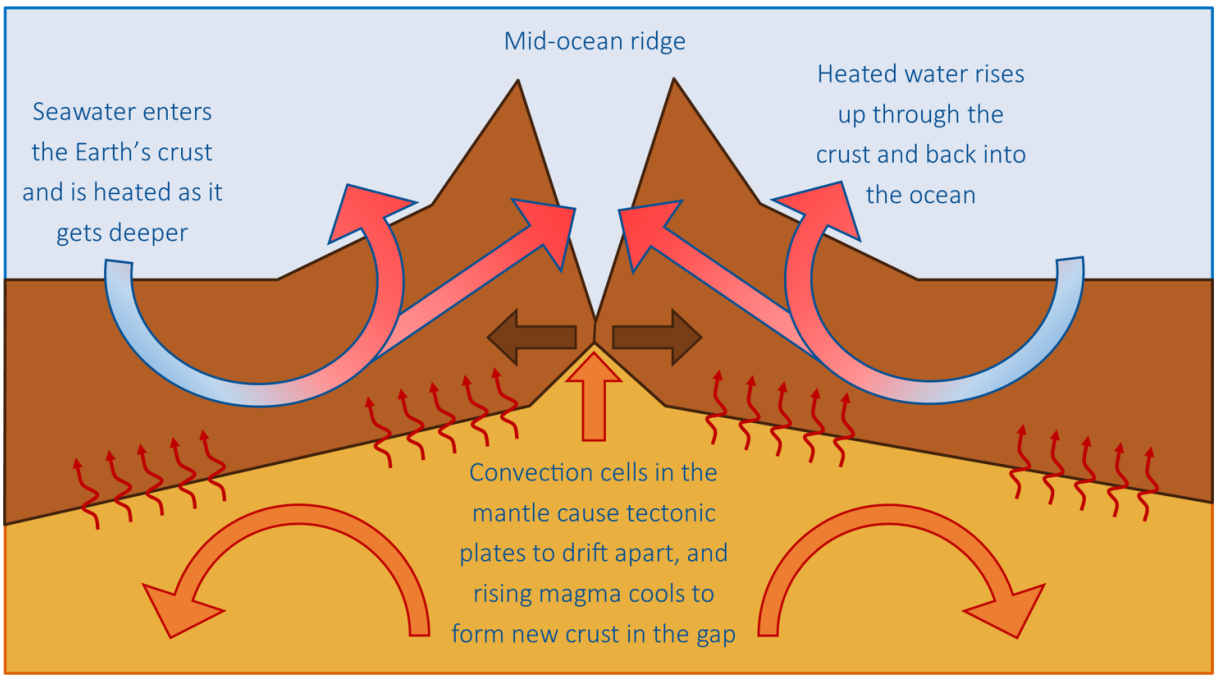

Figure 1.1: A sketch of the process of hydrothermal circulation at a mid-ocean ridge.

crust is being formed by rising magma, bringing heat closer to the seabed. This is shown in Figure 1.1, a sketch of the process.

Many scientific disciplines have an interest in hydrothermal venting. Vent fields, which are areas of hydrothermal activity up to around 800 square metres surrounded by normal seabed, provide a unique habitat and house the only biological communities whose immediate source of energy is not the sun (Hessler and Kaharl, 1995). Creatures here rely instead on the heat in hydrothermal fluids, which have been recorded as being up to 464 °C for brief periods of time, with stable temperatures over 400 °C (Koschinsky et al., 2008). In addition, chemicals from the Earth's crust are carried up into the ocean by hydrothermal circulation. Some of these precipitate as the heated water meets the cold ocean, creating massive sulphide deposits containing copper, zinc and lead. There is much debate over the possibility of mining these large mineral deposits (Hannington et al., 2011). Other chemicals remain dissolved in the water and are distributed around the ocean, providing an important source of elements such as iron and manganese to the ecosystem (Saito et al., 2013). Van Dover (2000) gives a detailed overview of the ecology of hydrothermal vents.

In addition to the chemicals mentioned above, hydrothermal fluids are enriched with helium-3 (^{3}He). Most atmospheric helium is the heavier helium-4 (^{4}He) isotope, which means that ratios of ^{3}He/^{4}He have been found to be higher in the deep ocean than the atmosphere (Clarke et al., 1969). In the helium flux over the East Pacific Rise, the ratio was found to be about 11 times that of the atmosphere (Craig et al., 1975). This injection of ^{3}He causes the average helium ratio of deep Pacific water to be 20-30% higher than

that of the atmosphere (Lupton et al., 1977). Studying helium ratios can therefore be used to trace water masses originating in hydrothermal systems, and potentially to locate the major hydrothermal sources for regions of the ocean.

Hydrothermal systems are also an important contributer of heat to the abyssal ocean. Towards the young crust on the flanks of mid-ocean ridges there is a discrepancy between predicted and observed geothermal heating (Anderson and Hobart, 1976), known as the heat flow anomaly. As the observational methods measure conductive heat, this discrepancy can be explained by the co-existence of conductive heating and heat flow from hydrothermal sources, the latter being dominant in areas where the crust is highly permeable and pathways exist which allow water to flow in and out of the ocean through the seafloor (eg. Harris and Chapman, 2004). Stein and Stein (1994) compared the heat flow model of Stein and Stein (1992) to observations and, by studying the heat flow anomaly, concluded that more than half of the geothermal heat flux through 10 million year old crust is advective in nature (i.e. hydrothermal) and that the proportion increases as the crust becomes younger. They estimated that 34 % of global heat flow is hydrothermal, which is in agreement with the earlier estimate of Sclater et al. (1980) that one third of the total heat entering the ocean from below does so hydrothermally.

The hydrothermal component of the geothermal heat flux has not been included in modelling studies such as those mentioned in the previous section. The heat fluxes have always been prescribed as purely conductive, but this may be an oversight. The global flow of hydrothermal fluids is estimated (Elderfield and Schultz, 1996) to be up to 0.35 Sverdrups, which is one third of the global river runoff (Jacobson et al., 2000) and therefore not an insignificant flux.

A variety of flow velocities from hydrothermal systems have been observed, from slow seeps of only $0.04\,\mathrm{ms}^{-1}$ to chimneys emitting water at several metres per second. Ramondenc et al. (2006) and Sarrazin et al. (2009) contain summaries of such measurements. Turbine flowmeters have recorded hot vents and chimneys on the East Pacific Rise emitting water at velocities from $0.7 - 2.4\,\mathrm{ms}^{-1}$ (Converse et al., 1984), and chimneys on the Juan de Fuca Ridge emitting at up to $6.2\,\mathrm{ms}^{-1}$ (Ginster et al., 1994). At a very localised level flows such as these from vent fields will likely have a significant impact on circulation, but these are point values and may not have any wider-reaching effects.

Methods have been developed for inferring fluid flow through the crust from measurements of heat flow at the seabed. Fisher and Harris (2010) provides a review of this topic, along with a more general overview of advances in the studies of heat flow. One important feature which can help to identify potential locations of hydrothermal activity is outcrops,

where peaks in the bedrock rise above the surrounding sediment layer. These allow for unimpeded exchange of water between the ocean and the crust. Heat flow measurements have been used to learn more about the hydrothermal circulation which occurs between such outcrops (eg. Fisher et al., 2003; Hutnak et al., 2006), finding that the regional heat flow can be suppressed due to sufficiently vigorous circulation transporting heat through the crust towards a concentrated release of heat at an outcrop.

1.4 Area of interest: The Panama Basin

The Panama Basin is located at the equator in the eastern Pacific. It is entirely enclosed below about 2000m except at two specific locations. The saddle of the Carnegie Ridge on the southern edge extends to a depth of 2300 m, and the Ecuador Trench allows abyssal water to be exchanged with the southern Pacific along a narrow 2900 m deep channel at the edge of the South American continental shelf (see Figure 1.2).

The enclosed nature of the basin causes a thick mixed layer below the level of the ridge crests which is subject to geothermal fluxes from below, making it an ideal location to study the effects of these fluxes on circulation. The basin also contains the spreading tectonic boundary between the Cocos and Nazca plates, along which there is much hydrothermal activity. A large amount of heat enters the basin via the Galapagos Rift, Ecuador Rift and Costa Rica Rift, which all lie on the plate boundary. Observations

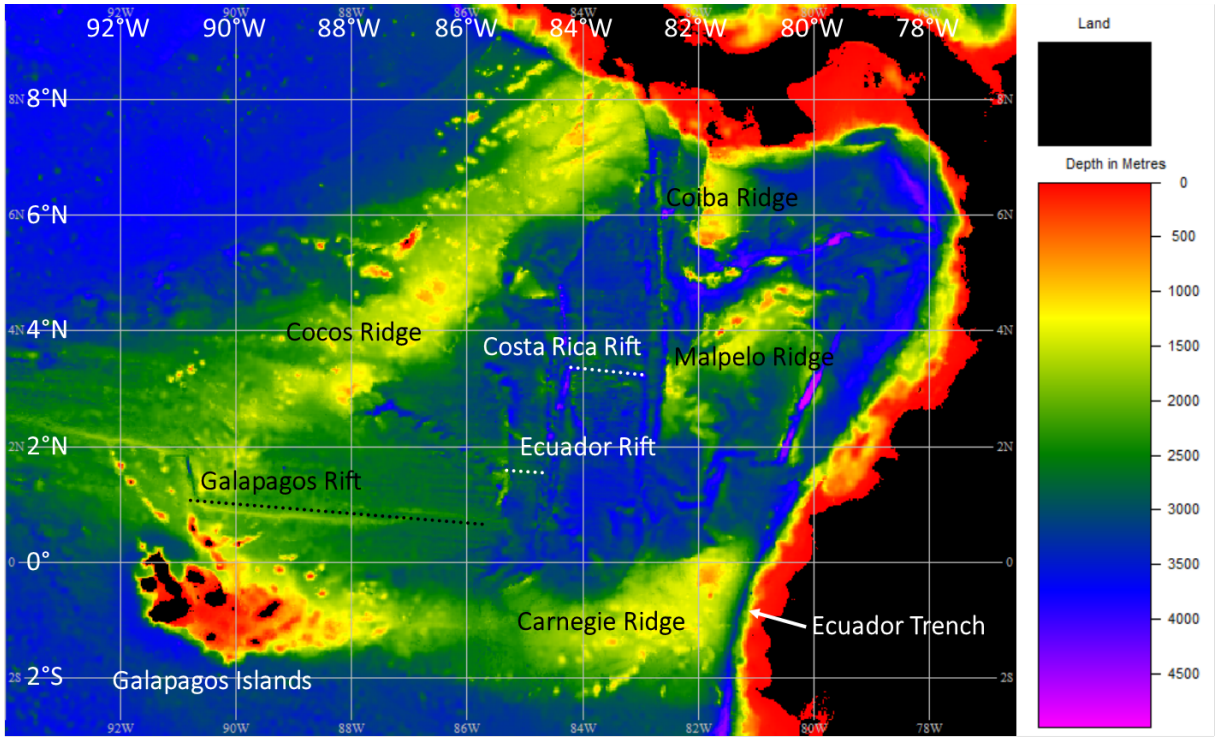

Figure 1.2: A map showing the bathymetry of the Panama Basin, using data from GEBCO (BODC, 2015), with major geological features labelled.

collected in the World Ocean Atlas (Locarnini et al., 2018) are displayed in Figure 1.3 for a depth of 2700 m, where the only connection to the rest of the Pacific is through the bottom of the Ecuador Trench. Temperatures at this depth are about 0.2°C warmer inside the basin than outside of it (Figure 1.3a), showing that the Panama Basin's abyssal hydrography and circulation are independent of the external Pacific ocean.

Until 1970, there were not many observations of the deep waters in the Panama Basin. Using what little data existed, Laird (1969) noted the existence of horizontal temperature gradients in the bottom water. He theorised that this was due either to geothermal heating of the water or uncharted topographical features. In the following year, the NOAA ship *Oceanographer* was dispatched to the Panama Basin to take observational measurements of the deep water properties and start to build an improved dataset. Laird (1971) looked at these new data and presented a description of the deep water circulation and properties. He split the basin into 6 'sub-basins', due to the basin interior being interrupted by features such as the Malpelo Ridge and the Coiba Ridge. In each of these sub-basins the bottom salinity was almost constant. In fact, the salinity measurements across the whole Panama Basin only varied by 0.005 parts per thousand. Within these sub-basins, though, there were potential temperature gradients. Since these were not accompanied by changes in salinity, it was suggested that there was very little vertical mixing and that these temperature changes were probably caused by geothermal heating. By looking at the hydrography data, he concluded that the deep water in the basin had all entered through the Ecuador Trench. Using the assumption that geothermal heating was driving any renewal of water within the Panama Basin, and by looking at the oxygen data, Laird calculated that the renewal period for the Panama Basin is 175-220 years.

A couple of years later, a detailed survey of the Galapagos spreading centre was carried out (Sclater and Klitgord, 1973). One of the subjects of this survey was heat flow, and it was discovered that variations in heat flow correlated closely with variations in potential temperature over the spreading centre, explained as the effect of water circulating through fissures in the unsedimented seabed. A set of companion papers were published presenting results from this survey, with one (Detrick et al., 1974) focusing on the importance of geothermal heating and using a higher, more accurate heat flux to predict a residence time of less than 100 years for the bottom water in the Panama Basin, about half of what Laird (1971) calculated.

Lonsdale (1977) calculated an even shorter residence time of 42.3 years, based on measurements of inflow through the Ecuador Trench. The data were collected on a Scripps expedition, *Cocotow*; along with a detailed survey of the trench, which revealed a far more complex bathymetry than had been previously assumed.

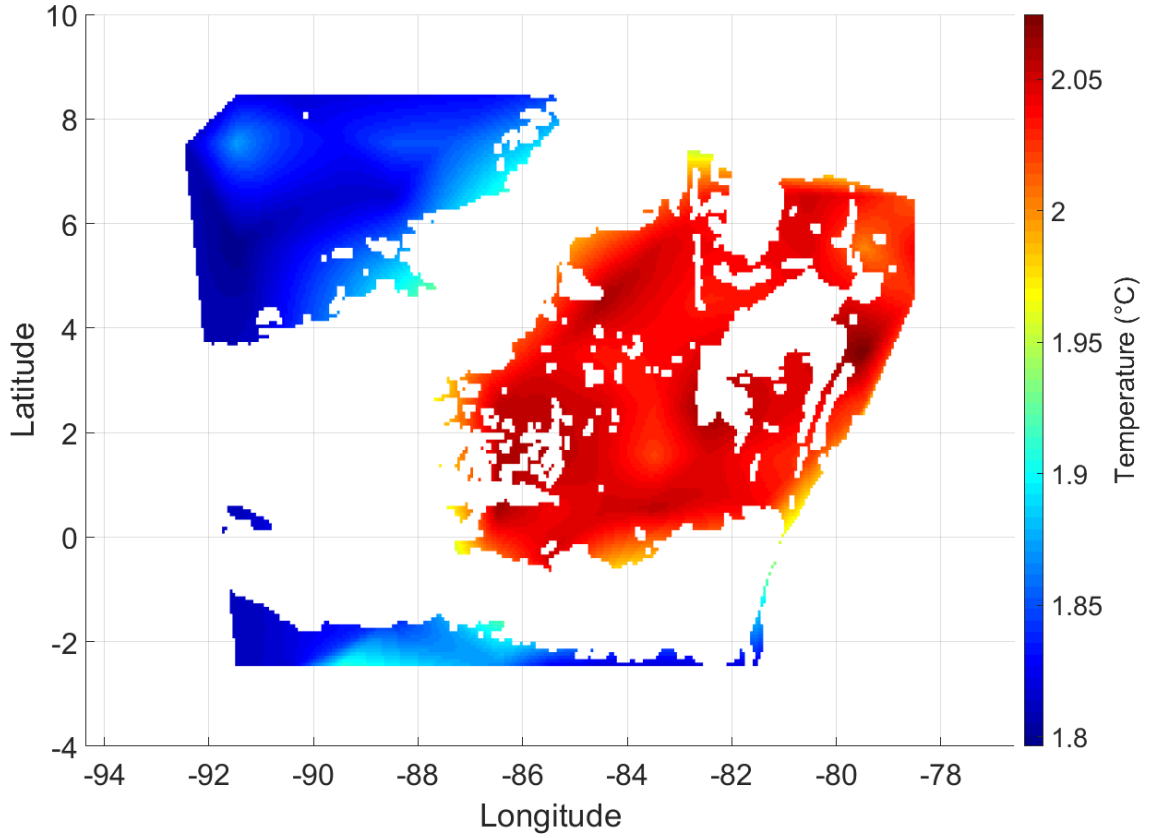

(a) Temperature (Locarnini et al., 2018).

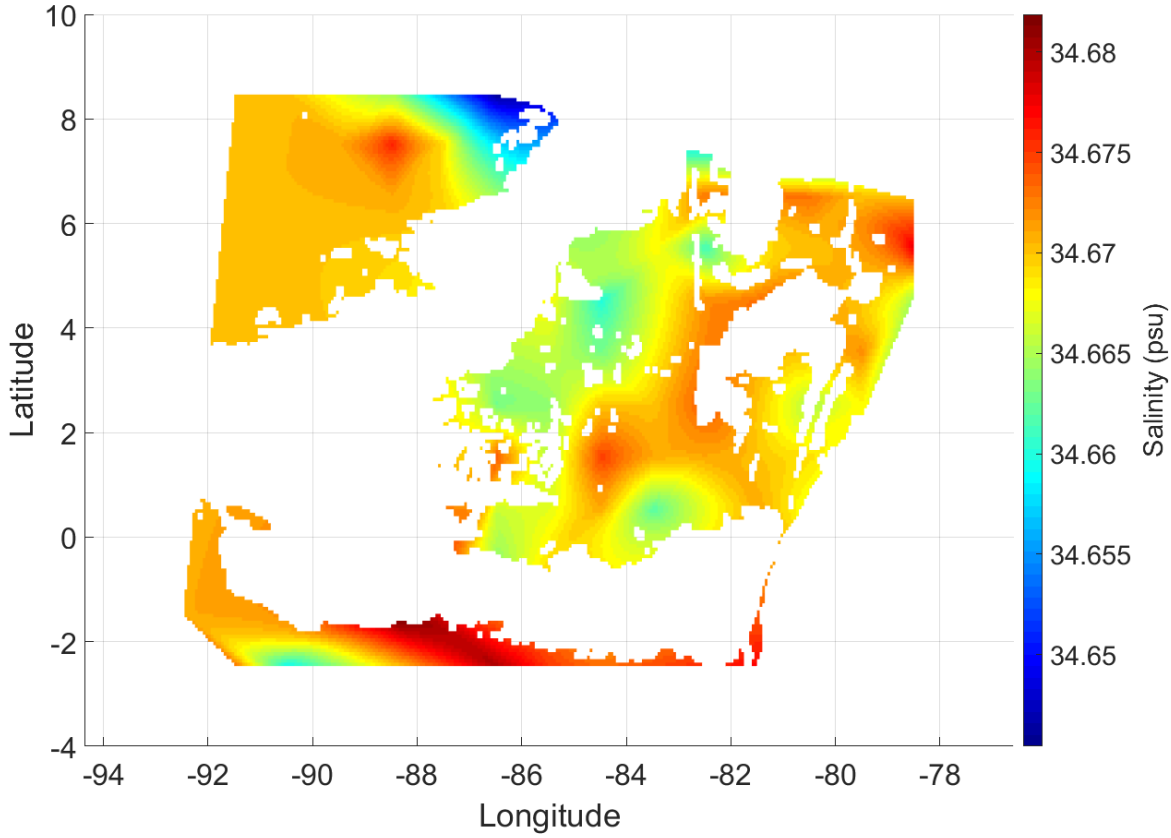

(b) Salinity (Zweng et al., 2018).

Figure 1.3: Observed temperature and salinity at 2700 m depth in and around the Panama Basin, interpolated from World Ocean Atlas data at 1° resolution.

Since then, very little attention appears to have been given to the oceanography of the Panama Basin. However, the structure of the crust beneath the basin and hydrothermal circulation within it have been subject to much investigation, centered around boreholes drilled as part of the Deep Sea Drilling Project (DSDP) and Ocean Drilling Program (ODP). DSDP Hole 504B on the Costa Rica Rift is of particular interest, being the first reference section extending more than 1 km into the crust (Anderson et al., 1982). Research around the area has looked at the process of hydrothermal alteration within the crust, along with the attendant mineralogy and chemistry (eg. Alt et al., 1986).

Recently a series of three cruises took place between November 2014 and March 2015 as part of the OSCAR project (Oceanographic and Seismic Characterisation of heat dissipation and alteration by hydrothermal fluids at an Axial Ridge). The project, which supported some of the work presented in this thesis, was an interdisciplinary collaboration between oceanographers and earth scientists, investigating intereactions between the solid earth and abyssal oceans via hydrothermal systems. The Panama Basin was chosen as a survey area due to the prevalence of hydrothermal activity and its isolation at depth from the rest of the ocean.

A recent publication from the OSCAR project (Banyte et al., 2018) looked in more detail at the abyssal hydrography of the Panama Basin. In it, an estimate of 0.29 Sv was made for the inflow through the Ecuador Trench. The effects of geothermal heating in the basin were found to reach as high as 2200 m depth.

1.5 About this project

This PhD project aims to discover more about the effects which geothermal fluxes, both conductive and hydrothermal, have upon circulation in the abyssal ocean. I use analytical and computational modelling to investigate circulations produced by conductive and hydrothermal heat fluxes through the seabed. There is a particular focus on the Panama basin, features of which are represented in the modelling experiments.

The main difference between the two geothermal heating mechanisms is the addition of a volume flux through the seabed for the hydrothermal flow. Such fluxes, without the accompanying heat, are the focus of Chapter 2, in which I use simple analytical models to investigate the circulations caused by vertical flow through the seabed. As a first look at the process of introducing water from the bottom of a basin, this is an important study. It will be seen that the volume fluxes have the potential to drive abyssal circulations and have effects reaching far into the water column.

After this, Chapter 3 takes a close look at how the partitioning of a heat flux between conductive and hydrothermal sources affects the circulation and hydrography in an idealised domain. In the first study of its kind, a hydrothermal input is added to the bottom boundary of a primitive equation model (NEMO - Madec (2008)) and simulations completed to investigate how the circulation changes as the proportion of the heat flux entering the ocean in this way increases. It will be seen that, among other differences, vertical transport of heat from the abyss is increased when hydrothermal fluxes are dominant over conductive fluxes.

In the final chapter, a three-dimensional regional model of the Panama Basin is used to simulate the effects of geothermal heating on circulation in a semi-enclosed ocean basin. Of particular interest is the change to the flow through the Ecuador Trench which connects the basin to the greater Pacific Ocean at depth. The simulations show that the geothermal heating of the basin has a large effect on the strength of flow through the Ecuador trench, and on circulation within the basin itself.

Chapter 2

Modelling of circulation driven by velocity through the seabed

2.1 Introduction and the primitive equations

This project seeks to gain greater understanding of how hydrothermal and geothermal activity affects the movement of water in the oceans. While some models have included heating at the ocean floor as a boundary condition, the effects of flow through the seabed on large-scale circulation have not previously been investigated in detail. The first major aim of this project is to identify the impacts of fluid flow through the seabed. I start by creating simple two-dimensional analytical models with fluid flow as the only driving force for circulation.

The first case utilises the simplest of conditions, a single area of mass injection at the centre of the seabed in a rectangular basin. From there I move on to calculating solutions for a larger variety of inputs, and add bathymetry to the domain in place of the flat bottom of the rectangle. An alternate approach to the problem, adding a thin boundary layer in which friction increases near the seabed, is investigated, and I also explore the problem in a cylindrical coordinate sytem.

I initially work on the problems analytically in order to explore the underlying mathematics of the physical system, and then I use MATLAB in order to calculate solutions quickly and efficiently, and to visualise the results utilising its range of plotting tools.

As a starting point for setting up problems, the primitive equations of geophysical fluid dynamics are used, as stated in Cushman-Roisin and Beckers (2011):

$$\frac{\partial u}{\partial t} + u\frac{\partial u}{\partial x} + v\frac{\partial u}{\partial y} + w\frac{\partial u}{\partial z} - fv = -\frac{1}{\rho_0}\frac{\partial p}{\partial x} + \frac{\partial}{\partial x}\left(\mathcal{A}\frac{\partial u}{\partial x}\right) + \frac{\partial}{\partial y}\left(\mathcal{A}\frac{\partial u}{\partial y}\right) + \frac{\partial}{\partial z}\left(\nu_E\frac{\partial u}{\partial z}\right) \tag{2.1a}$$

$$\frac{\partial v}{\partial t} + u\frac{\partial v}{\partial x} + v\frac{\partial v}{\partial y} + w\frac{\partial v}{\partial z} + fu = -\frac{1}{\rho_0}\frac{\partial p}{\partial y} + \frac{\partial}{\partial x}\left(\mathcal{A}\frac{\partial v}{\partial x}\right) + \frac{\partial}{\partial y}\left(\mathcal{A}\frac{\partial v}{\partial y}\right) + \frac{\partial}{\partial z}\left(\nu_E\frac{\partial v}{\partial z}\right) \tag{2.1b}$$

$$0 = -\frac{\partial p}{\partial z} - \rho g \tag{2.1c}$$

$$\frac{\partial \rho}{\partial t} + u\frac{\partial \rho}{\partial x} + v\frac{\partial \rho}{\partial y} + w\frac{\partial \rho}{\partial z} = \frac{\partial}{\partial x}\left(\mathcal{B}\frac{\partial \rho}{\partial x}\right) + \frac{\partial}{\partial y}\left(\mathcal{B}\frac{\partial \rho}{\partial y}\right) + \frac{\partial}{\partial z}\left(\kappa_E\frac{\partial \rho}{\partial z}\right) \tag{2.1d}$$

$$\frac{\partial u}{\partial x} + \frac{\partial v}{\partial y} + \frac{\partial w}{\partial z} = 0, \tag{2.1e}$$

in which

- $u(x, y, z, t)$, $v(x, y, z, t)$ and $w(x, y, z, t)$ are velocities in the x-, y- and z-directions
- f is the Coriolis parameter, taken as a constant here
- ρ_0 is a constant reference density
- $\rho(x, y, z, t)$ is the density perturbation from ρ_0
- $p(x, y, z, t)$ is the pressure perturbation from the reference pressure $p_0(z) = P_0 - \rho_0 g z$, where P_0 is a constant
- $\mathcal{A}$ and ν_E are the horizontal and vertical eddy viscosities which can be taken as constants or as functions of the flow variables
- g is the gravitational acceleration, a constant coefficient. The value of g can be chosen to represent the reduced gravity in the bottom layer of an ocean
- $\mathcal{B}$ and κ_E are the horizontal and vertical eddy diffusivities, which can be taken as constants or as functions of the flow variables. Cushman-Roisin and Beckers (2011) uses $\mathcal{B} = \mathcal{A}$. This is an adequate assumption, since large turbulent motions in the horizontal disperse momentum and heat with the same efficiency.

Equations (2.1a), (2.1b) and (2.1c) are the x-, y- and z-momentum equations respectively, (2.1d) is the energy equation and (2.1e) is the continuity equation.

The z-momentum equation (2.1c) employs the hydrostatic approximation, that the pressure of the ocean at any point is dependent only on the weight of the water above it.

This relies on the horizontal scale being large relative to the vertical scale, and is valid when vertical acceleration of a fluid is small compared to the gravitational acceleration. I will need to keep this in mind when looking at my results, as the application of a vertical velocity boundary condition at the seabed could potentially lead to the hydrostatic approximation becoming invalid.

2.2 A Rayleigh friction model with a flat seabed

2.2.1 Simplifying the equations

Investigation will begin with a simple case, in order to isolate the process of vertical velocity through the seabed without signals from other processes interfering with the flow. The solutions being sought are steady state flows over a flat seabed ($z = 0$) in an otherwise static homogeneous ocean layer, in which the flow has no y-dependence. The free surface elevation is $\eta(x) = h(x) - H$, where $h(x)$ is the total water depth and H is a constant reference height above the seabed. Figure 2.1 is a sketch of these definitions within the two-dimensional model domain.

The equations (2.1) can be simplified to be solved more easily. Firstly, gradients with respect to t and y are discarded because this is a steady state flow with no y-dependence. Since the ocean is homogeneous, density gradients will also vanish so (2.1d) can be ignored entirely.

The perturbation density ρ in the hydrostatic equation (2.1c) is zero, which implies that the pressure is independent of z. Horizontal pressure gradients can only be produced by

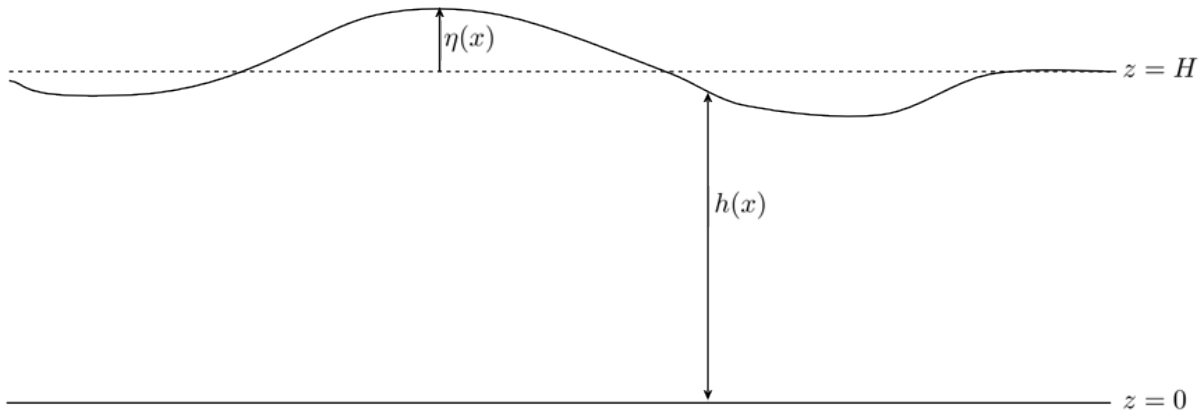

Figure 2.1: A sketch showing the definitions of functions in the Rayleigh friction model with a flat seabed.

the shape of the sea surface, so $p(x) = \rho_0 g(H + \eta(x))$. Using this definition,

$$\frac{1}{\rho_0}\frac{\partial p}{\partial x} = g\frac{\partial(H+\eta)}{\partial x} = g\frac{\partial \eta}{\partial x}.$$

With a flat seabed $\frac{\partial \eta}{\partial x} = \frac{\partial h}{\partial x}$, which shall be used for simplicity.

For simplicity, the eddy viscosity terms in (2.1a) and (2.1b) will be replaced by a "Rayleigh friction" acting against the direction of motion, which approximately mimics the behaviour of viscosity by allowing for losses of energy. This method is often used to simplify problems (see, for example, Gill (1982), Satoh (2013)). It was in use as far back as Airy (1845), in which it is explained that the choice is based on experimental observations where the resistance to objects moving through fluids at small velocities was found to be nearly proportional to velocity of motion. The constant R used from here on is the Rayleigh friction rate.

The simplifications described above leave the much reduced system of equations

$$-fv = -Ru - g\frac{\partial h}{\partial x} \tag{2.2a}$$

$$fu = -Rv \tag{2.2b}$$

$$\frac{\partial u}{\partial x} + \frac{\partial w}{\partial z} = 0, \tag{2.2c}$$

where the variables depend only on x and z. These simplified equations describe a slow, steady flow of a barotropic fluid and as such the Taylor-Proudman theorem takes effect, meaning that u and v are uniform in the vertical and do not depend upon z. This can be shown by taking vertical derivatives of (2.2a) and (2.2b):

$$-f\frac{\partial v}{\partial z} = -R\frac{\partial u}{\partial z} - g\frac{\partial}{\partial z}\left(\frac{\partial h}{\partial x}\right) \tag{2.3a}$$

$$f\frac{\partial u}{\partial z} = -R\frac{\partial v}{\partial z}. \tag{2.3b}$$

Rearranging (2.3b) produces $\frac{\partial u}{\partial z} = -\frac{R}{f}\frac{\partial v}{\partial z}$, which is then substituted into (2.3a) to give

$$\begin{aligned}
-f\frac{\partial v}{\partial z} &= \frac{R^2}{f}\frac{\partial v}{\partial z} - g\frac{\partial}{\partial z}\left(\frac{\partial h}{\partial x}\right) \\
\implies -f\frac{\partial v}{\partial z} &= \frac{R^2}{f}\frac{\partial v}{\partial z} - g\frac{\partial}{\partial x}\left(\frac{\partial h}{\partial z}\right) \\
\implies -f\frac{\partial v}{\partial z} &= \frac{R^2}{f}\frac{\partial v}{\partial z} \\
\implies -\frac{f^2}{R^2}\frac{\partial v}{\partial z} &= \frac{\partial v}{\partial z}.
\end{aligned}$$

Since f and R are real numbers, $\frac{f^2}{R^2}$ cannot equal -1, and therefore $\frac{\partial v}{\partial z}$ must be zero. A similar result occurs by substituting for $\frac{\partial v}{\partial z}$ in (2.3a), thus neither horizontal velocity is dependent on z.

2.2.2 Boundary conditions

The system (2.2) contains three equations, but there are four unknown variables to be found; $h(x)$, $u(x)$, $v(x)$ and $w(x,z)$. To form a solvable system, the boundary conditions of the problem must be known.

At the free surface, water must flow along the gradient of the surface and not pass through the boundary. Mathematically, this condition is described by

$$w(x,h(x)) = u\frac{\partial h}{\partial x}. \tag{2.4}$$

Next, the boundary at the seabed is considered. Since the problem is being constructed to investigate fluid flows similar to those from a hydrothermal vent, incorporating a volume flux through the bottom of the domain is essential. This flux is described with a vertical velocity function $w_b(x)$ which can be defined as desired for individual problems, so the boundary condition is

$$w(x,0) = w_b(x). \tag{2.5}$$

The function $w_b(x)$ can be set such that it is centred around $x = 0$ and is only non-zero in a finite region. Noting that the ocean is static beyond the influence of the flow being set up, this leads to imposing $\eta = 0$ (or equivalently $h = H$, since the seabed under consideration is flat) as $x \to -\infty$, and the boundary condition

$$u \to 0 \text{ as } x \to -\infty. \tag{2.6}$$

Using (2.4) and (2.5), a vertical integral of (2.2c) is performed over the depth of the ocean, resulting in

$$\begin{aligned} & \frac{\partial u}{\partial x}\int_0^h \mathrm{d}z + \left[w\right]_0^h = 0 \\ \implies & h\frac{\partial u}{\partial x} + u\frac{\partial h}{\partial x} - w_b = 0 \\ \implies & \frac{\partial (hu)}{\partial x} = w_b. \end{aligned} \tag{2.7}$$

This is the fourth equation which, together with (2.2), completes the full system which needs to be solved.

Through an integration of (2.7), the relationship obtained is

$$\begin{aligned} hu - h_0u_0 &= \int_{x_0}^{x} w_b(\xi)\,\mathrm{d}\xi \\ \implies \qquad u &= \frac{1}{h}\left(h_0u_0 + \int_{x_0}^{x} w_b(\xi)\,\mathrm{d}\xi\right), \end{aligned} \tag{2.8}$$

where h_0 and u_0 are the values of h and u at some point x_0, and ξ is a dummy variable of integration which is useful to avoid confusion in later examples when the mathematics becomes more complicated. For a solution valid over all x, $x_0 = -\infty$ can be used, for which $u_0 = 0$. It can however be useful to keep the above formulation in mind when solving problems in different intervals of x.

Rearranging (2.2b), a solution for v in terms of u can be obtained, which can be immediately substituted into (2.2a). At this point, the system of equations needed to solve the problem can be restated as

$$v(x) = -\frac{f}{R}u(x) \tag{2.9a}$$

$$u(x) = \frac{1}{h(x)}\int_{-\infty}^{x} w_b(\xi)\,\mathrm{d}\xi \tag{2.9b}$$

$$\frac{\partial h}{\partial x} = -\frac{(f^2+R^2)u(x)}{Rg} \tag{2.9c}$$

$$\frac{\partial w}{\partial z} = -\frac{\partial u}{\partial x}, \tag{2.9d}$$

which can be solved for a variety of flux functions w_b, as shall be explored in the following sections.

2.3 Initial case study: A single, uniform injection of water

The first problem I will look at is the fairly simple case of a uniform upward flux, symmetrical around $x = 0$ up to some distance ℓ away from the origin, and a uniform downward flux either side of this up to some distance L. This can be thought to represent a uniform 'jet' of water being injected into the ocean via a hydrothermal system, with water being drawn back into the Earth's crust at a uniform rate for an equal distance on either side of it. The flux is described by

$$w_b(x) = \begin{cases} w_u & \text{for } -\ell \le x \le \ell \\ w_d & \text{for } -L < x < -\ell \quad \text{or} \quad \ell < x < L \\ 0 & \text{otherwise,} \end{cases} \tag{2.10}$$

where w_u and w_d are constants. In the following, the upward velocity w_u may be referred to as a discharge or inflow, while the downward velocity w_d may be referred to as recharge or outflow.

Conservation of volume in the system is important since the problem is set up to calculate steady state solutions with no time variability, so evolution in the amount of water in the ocean would not be consistent with the basic framework. The following condition is applied to ensure that equal volumes of water enter and leave the system through the seabed:

$$w_d = -\frac{\ell}{L-\ell} w_u. \tag{2.11}$$

2.3.1 Solving the equations

Solving for u and v

The first step is to find expressions for u in terms of h. This is most easily achieved by splitting the problem into different regions due to the changes in w_b.

For $x \in (-\infty, -L]$, (2.9b) can be used to arrive at

$$\begin{aligned} u &= \frac{1}{h} \int_{-\infty}^{x} 0 \, \mathrm{d}\xi \\ &= 0, \end{aligned}$$

since $u(-\infty) = 0$ from (2.6). In other regions of the problem, (2.8) is used with different integral bounds to match the intervals of values for x. This yields the following results.

For $x \in (-L, -\ell]$,

$$\begin{aligned} u &= \frac{1}{h} \left(h(-L)u(-L) - \int_{-L}^{x} \frac{w_u \ell}{(L-\ell)} \, \mathrm{d}\xi \right) \\ &= -\frac{w_u \ell (x+L)}{h(L-\ell)}. \end{aligned}$$

For $x \in (-\ell, \ell]$,

$$\begin{aligned} u &= \frac{1}{h} \left(h(-\ell)u(-\ell) + \int_{-\ell}^{x} w_u \, \mathrm{d}\xi \right) \\ &= \frac{1}{h} \left(w_u(x+\ell) - \frac{w_u \ell (L-\ell)}{(L-\ell)} \right) \\ &= \frac{w_u x}{h}. \end{aligned}$$

For $x \in (\ell, L]$,

$$\begin{aligned} u &= \frac{1}{h}\left(h(\ell)u(\ell) + \int_{\ell}^{x}\left(-\frac{w_u \ell}{(L-\ell)}\right)\,\mathrm{d}\xi\right) \\ &= \frac{1}{h}\left(w_u\ell - \frac{w_u\ell(x-\ell)}{(L-\ell)}\right) \\ &= -\frac{w_u\ell(x-L)}{h(L-\ell)}. \end{aligned}$$

Finally, for $x \in (L, \infty)$,

$$\begin{aligned} u &= \frac{1}{h}\left(h(L)u(L) + \int_{L}^{x} 0\,\mathrm{d}\xi\right) \\ &= 0. \end{aligned}$$

Bringing these results together, the full solution of u in terms of h can be written

$$u(x) = \begin{cases} -\frac{w_u\ell(x+L)}{(L-\ell)h(x)} & \text{for } -L < x \leq -\ell \\ \frac{w_u x}{h(x)} & \text{for } -\ell < x \leq \ell \\ -\frac{w_u\ell(x-L)}{(L-\ell)h(x)} & \text{for } \ell < x \leq L \\ 0 & \text{otherwise.} \end{cases} \tag{2.12}$$

The solution for v (in terms of h) easily follows by substituting these values for u into (2.9a):

$$v(x) = \begin{cases} \frac{fw_u\ell(x+L)}{R(L-\ell)h(x)} & \text{for } -L < x \leq -\ell \\ -\frac{fw_u x}{Rh(x)} & \text{for } -\ell < x \leq \ell \\ \frac{fw_u\ell(x-L)}{R(L-\ell)h(x)} & \text{for } \ell < x \leq L \\ 0 & \text{otherwise.} \end{cases} \tag{2.13}$$

Solving for h

Utilising the previous result, solutions for h can now be found. Using (2.9c) and the solution above, it is easy to see that h must be constant for $x \leq -L$ and $x \geq L$ where $u(x) = 0$, thus equal to H for $x < -L$. In the other regions expressions for u from (2.12) are substituted into the equations.

For $x \in (-L, -\ell]$,

$$\frac{\partial h}{\partial x} = \left(\frac{f^2}{R} + R\right)\frac{w_u\ell(x+L)}{hg(L-\ell)}$$

$$
\begin{aligned}
\implies \qquad h\frac{\partial h}{\partial x} &= \left(\frac{f^2}{R}+R\right)\frac{w_u\ell(x+L)}{g(L-\ell)} \\
\implies \qquad \frac{1}{2}\frac{\partial h^2}{\partial x} &= \left(\frac{f^2}{R}+R\right)\frac{w_u\ell(x+L)}{g(L-\ell)} \\
\implies \int_{-L}^{x}\frac{\partial(h(\xi))^2}{\partial\xi}\,\mathrm{d}\xi &= \int_{-L}^{x}2\frac{(f^2+R^2)w_u\ell(\xi+L)}{Rg(L-\ell)}\,\mathrm{d}\xi \\
\implies \quad h^2-(h(-L))^2 &= 2\frac{(f^2+R^2)w_u\ell}{Rg(L-\ell)}\left[\frac{1}{2}\xi^2+L\xi\right]_{\xi=-L}^{\xi=x} \\
\implies \qquad h^2-H^2 &= \frac{(f^2+R^2)w_u\ell}{Rg(L-\ell)}\left(x^2+2Lx+L^2\right) \\
\implies \qquad h^2 &= H^2+\frac{(f^2+R^2)w_u\ell}{Rg(L-\ell)}(x+L)^2.
\end{aligned}
$$

Following a similar process for $x \in (-\ell, \ell]$,

$$
\begin{aligned}
\frac{\partial h}{\partial x} &= -\left(\frac{f^2}{R}+R\right)\frac{w_u x}{hg} \\
\implies \qquad h\frac{\partial h}{\partial x} &= -\left(\frac{f^2}{R}+R\right)\frac{w_u x}{g} \\
\implies \qquad \frac{1}{2}\frac{\partial h^2}{\partial x} &= -\left(\frac{f^2}{R}+R\right)\frac{w_u x}{g} \\
\implies \qquad \int_{-\ell}^{x}\frac{\partial(h(\xi))^2}{\partial\xi}\,\mathrm{d}\xi &= -\int_{-\ell}^{x}2\frac{(f^2+R^2)w_u x}{Rg}\,\mathrm{d}\xi \\
\implies \qquad h^2-(h(-\ell))^2 &= -2\frac{(f^2+R^2)w_u}{Rg}\left[\frac{1}{2}\xi^2\right]_{\xi=-\ell}^{\xi=x} \\
\implies h^2-\left(H^2+\frac{(f^2+R^2)w_u\ell}{Rg(L-\ell)}(-\ell+L)^2\right) &= -\frac{(f^2+R^2)w_u}{Rg}\left(x^2-\ell^2\right) \\
\implies \qquad h^2 &= H^2+\frac{f^2+R^2}{Rg}w_u(\ell L-x^2).
\end{aligned}
$$

For $x \in (\ell, L]$,

$$
\begin{aligned}
\frac{\partial h}{\partial x} &= \left(\frac{f^2}{R}+R\right)\frac{w_u\ell(x-L)}{hg(L-\ell)} \\
\implies \qquad h\frac{\partial h}{\partial x} &= \left(\frac{f^2}{R}+R\right)\frac{w_u\ell(x-L)}{g(L-\ell)} \\
\implies \qquad \frac{1}{2}\frac{\partial h^2}{\partial x} &= \left(\frac{f^2}{R}+R\right)\frac{w_u\ell(x-L)}{g(L-\ell)} \\
\implies \qquad \int_{\ell}^{x}\frac{\partial(h(\xi))^2}{\partial\xi}\,\mathrm{d}\xi &= \int_{\ell}^{x}2\frac{(f^2+R^2)w_u\ell(\xi-L)}{Rg(L-\ell)}\,\mathrm{d}\xi \\
\implies \qquad h^2-(h(\ell))^2 &= 2\frac{(f^2+R^2)w_u\ell}{Rg(L-\ell)}\left[\frac{1}{2}\xi^2-L\xi\right]_{\xi=\ell}^{\xi=x} \\
\implies h^2-\left(H^2+\frac{f^2+R^2}{Rg}w_u(\ell L-\ell^2)\right) &= \frac{(f^2+R^2)w_u\ell}{Rg(L-\ell)}\left(x^2-2Lx+L^2\right)
\end{aligned}
$$

$$\implies \qquad h^2 = H^2 + \frac{(f^2+R^2)w_u\ell}{Rg(L-\ell)}(x-L)^2.$$

Finally, for $x \geq L$, h is already known to be a constant, so it must be equal to the value of h at $x = L$,

$$\begin{aligned} h(L) &= \sqrt{H^2 + \frac{(f^2+R^2)w_u\ell}{Rg(L-\ell)}(L-L)^2} \\ &= H. \end{aligned}$$

Thus the full solution for h can be written

$$h(x) = \begin{cases} \sqrt{H^2 + \frac{(f^2+R^2)w_u\ell}{Rg(L-\ell)}(x+L)^2} & \text{for } -L < x \leq -\ell \\ \sqrt{H^2 + \frac{(f^2+R^2)w_u}{Rg}(\ell L - x^2)} & \text{for } -\ell < x \leq \ell \\ \sqrt{H^2 + \frac{(f^2+R^2)w_u\ell}{Rg(L-\ell)}(x-L)^2} & \text{for } \ell < x \leq L \\ H & \text{otherwise.} \end{cases} \tag{2.14}$$

These solutions can then be substituted into (2.12) and (2.13) to obtain solutions for u and v which are no longer in terms of h.

Solving for w

To solve for w the solutions (2.14) are substituted into (2.12) and then (2.9d) is used. For $x \leq -L$ and $x \geq L$, $\frac{\partial w}{\partial z} = 0$. This means that w does not vary with z and due to the boundary conditions in these regions, $w = 0$. The solutions in the other regions are a little more complicated.

For $x \in (-L, -\ell]$,

$$\begin{aligned} \frac{\partial w}{\partial z} &= -\frac{\partial}{\partial x}\left(-\frac{w_u\ell(x+L)}{(L-\ell)\sqrt{H^2 + \frac{(f^2+R^2)w_u\ell}{Rg(L-\ell)}(x+L)^2}} \right) \\ &= \frac{w_u\ell}{L-\ell}\left(\frac{\sqrt{H^2 + \frac{(f^2+R^2)w_u\ell}{Rg(L-\ell)}(x+L)^2}}{H^2 + \frac{(f^2+R^2)w_u\ell}{Rg(L-\ell)}(x+L)^2} - \frac{\left(\frac{(x+L)^2(f^2+R^2)w_u\ell}{Rg(L-\ell)\sqrt{H^2 + \frac{(f^2+R^2)w_u\ell}{Rg(L-\ell)}(x+L)^2}} \right)}{H^2 + \frac{(f^2+R^2)w_u\ell}{Rg(L-\ell)}(x+L)^2} \right). \end{aligned} \tag{2.15}$$

After using (2.11) and (2.14) to shorten the equation by substituting w_d and h back into it,

$$\begin{aligned}\frac{\partial w}{\partial z} &= -\frac{w_d}{h}\left(1+\frac{(x+L)^2(f^2+R^2)w_d}{Rgh^2}\right)\\ &= -\frac{1}{h}\left(w_d+\frac{(f^2+R^2)u^2}{Rg}\right),\end{aligned}$$

which, after integrating, yields

$$w(x,z) = w_d - \frac{z}{h(x)}\left(w_d+\frac{(f^2+R^2)(u(x))^2}{Rg}\right).$$

The same process is followed for the remaining intervals. For $x \in (-\ell, \ell]$,

$$\begin{aligned}\frac{\partial w}{\partial z} &= -\frac{\partial}{\partial x}\left(\frac{w_u x}{\sqrt{H^2+\frac{(f^2+R^2)w_u}{Rg}(\ell L - x^2)}}\right)\\ &= -w_u\left(\frac{\sqrt{H^2+\frac{(f^2+R^2)w_u}{Rg}(\ell L-x^2)}}{H^2+\frac{(f^2+R^2)w_u}{Rg}(\ell L-x^2)} + \frac{\left(\frac{x^2(f^2+R^2)w_u}{Rg\sqrt{H^2+\frac{(f^2+R^2)w_u}{Rg}(\ell L-x^2)}}\right)}{H^2+\frac{(f^2+R^2)w_u}{Rg}(\ell L-x^2)}\right)\\ &= -\frac{w_u}{h}\left(1+\frac{x^2(f^2+R^2)w_u}{Rgh^2}\right)\\ &= -\frac{1}{h}\left(w_u+\frac{(f^2+R^2)u^2}{Rg}\right),\end{aligned}$$

which, after integrating, yields

$$w(x,z) = w_u - \frac{z}{h(x)}\left(w_u+\frac{(f^2+R^2)(u(x))^2}{Rg}\right).$$

Finally, for $x \in (\ell, L]$,

$$\begin{aligned}\frac{\partial w}{\partial z} &= -\frac{\partial}{\partial x}\left(-\frac{w_u\ell(x-L)}{(L-\ell)\sqrt{H^2+\frac{(f^2+R^2)w_u\ell}{Rg(L-\ell)}(x+L)^2}}\right)\\ &= \frac{w_u\ell}{L-\ell}\left(\frac{\sqrt{H^2+\frac{(f^2+R^2)w_u\ell}{Rg(L-\ell)}(x-L)^2}}{H^2+\frac{(f^2+R^2)w_u\ell}{Rg(L-\ell)}(x-L)^2} - \frac{\left(\frac{(x-L)^2(f^2+R^2)w_u\ell}{Rg(L-\ell)\sqrt{H^2+\frac{(f^2+R^2)w_u\ell}{Rg(L-\ell)}(x-L)^2}}\right)}{H^2+\frac{(f^2+R^2)w_u\ell}{Rg(L-\ell)}(x-L)^2}\right)\\ &= -\frac{w_d}{h}\left(1+\frac{(x-L)^2(f^2+R^2)w_d}{Rgh^2}\right)\\ &= -\frac{1}{h}\left(w_d+\frac{(f^2+R^2)u^2}{Rg}\right),\end{aligned}$$

which, after integrating, yields

$$w(x,z) = w_d - \frac{z}{h(x)}\left(w_d + \frac{(f^2+R^2)(u(x))^2}{Rg}\right).$$

Noting that in each region the only difference in the final solution for w is the the inclusion of either w_u or w_d, the solution for all x can be written simply as

$$w(x,z) = w_b(x) - \frac{z}{h(x)}\left(w_b(x) + \frac{(f^2+R^2)(u(x))^2}{Rg}\right). \tag{2.16}$$

Since solutions for h and u have already been found, the necessary substitutions can easily be made.

2.3.2 Visualising the solutions in MATLAB

A script can be written in MATLAB to plot the solutions of this analytical problem. Many of the variables will have to be given values, and these are chosen based on some realistic values from the ocean, particularly considering the Panama Basin region which is of interest to later stages of this project. In the example shown here, the velocity of the discharge w_u is chosen to be $10^{-7}\,\mathrm{ms}^{-1}$. Velocity values to use must be guessed based on observed velocities and the distribution of hydrothermal activity on the seabed. Velocities of hydrothermal vents have been recorded as high as $6.2\,\mathrm{ms}^{-1}$ (Sarrazin et al., 2009), but those point values are rare and for modelling purposes an average discharge over a large area must be considered. Hydrothermal emissions at the seabed are scattered rather than continuous, so much lower values are used. $10^{-7}\,\mathrm{ms}^{-1}$ represents a reasonable guess at an average vertical velocity over a large area of seabed, but there is very little real data available to base a more reliable estimate upon. The distances from the centre of the discharge ℓ and L are chosen to be 10 km and 100 km, not unreasonable distances for a mid-ocean ridge system around which a majority of hydrothermal activity takes place. Additionally, $H = 1000\,\mathrm{m}$, the approximate depth of the bottom mixed layer below the ridge crests of the Panama Basin, $f = 7.63 \times 10^{-6}\,\mathrm{s}^{-1}$, the value of the Coriolis force in the middle of the Panama Basin at 3° North, and $g = 0.029\,\mathrm{ms}^{-2}$, representing a reduced gravity in the bottom layer of an ocean. The Rayleigh friction rate is given the value $R = 1\,\mathrm{s}^{-1}$ for the first experiment, but shall be looked at in more detail in the next section.

Running the model using these parameters produces a fountain-shaped overturning flow, shown in Figure 2.2a, with an upward displacement of the layer surface above the inflow area. The streamlines in the plot show the path which would be followed by a particle released in the water. The water discharged from the centre of the seabed flows vertically through the entire unstratified layer, and then moves to either side of the middle, falling towards the area of outflow at the seabed. The colours display the speed of the circulation,

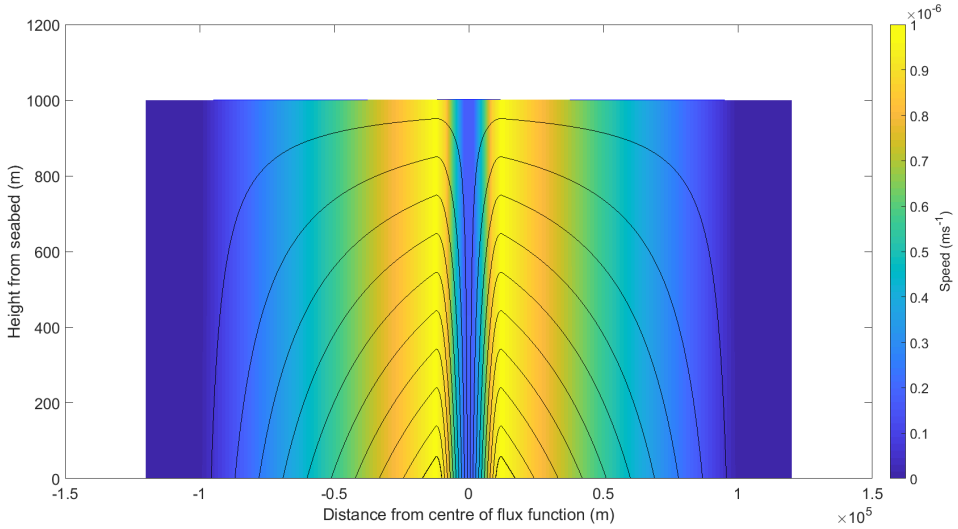

(a) Streamlines plotted over speed.

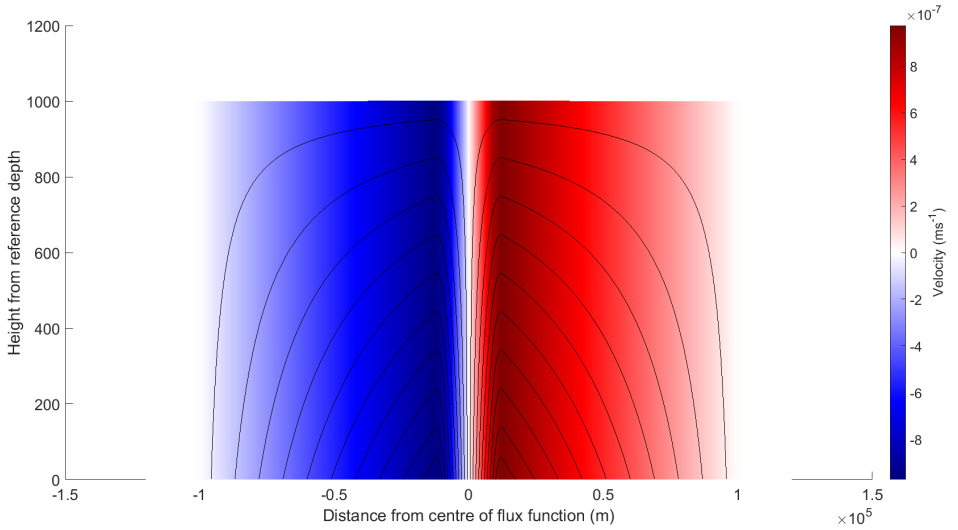

(b) Streamlines plotted over horizontal velocity (u).

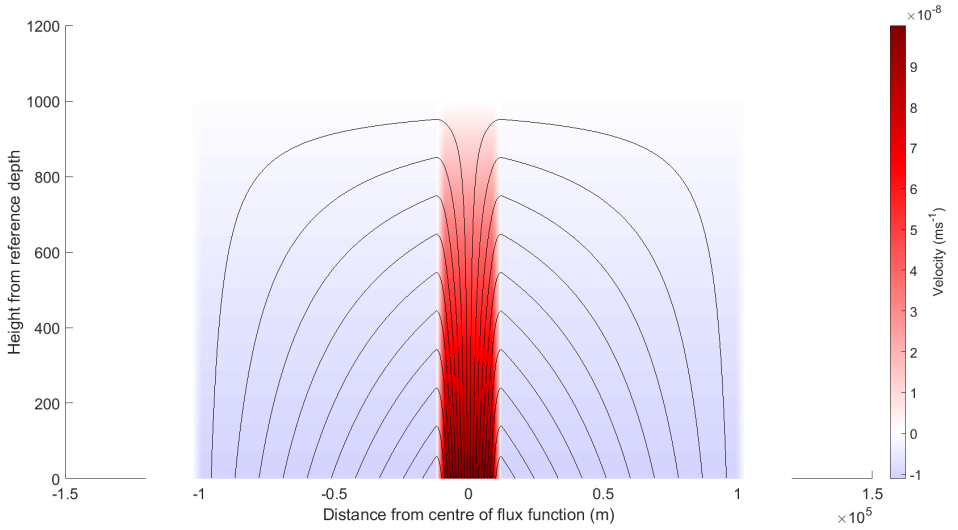

(c) Streamlines plotted over vertical velocity (w).

Figure 2.2: The speed and velocities of the circulation induced by a single uniform inflow of water through the seabed, with wider regions of uniform outflow to either side.

which is fastest as it transitions out of the column of predominantly vertical flow above the region of inflow. This is where the velocity at the seabed is greatest, which affects the entire height of the water column above. The circulation then slows down again further away from the centre.

By splitting the flow into its velocity components in the x- and z-directions (Figure 2.2), it can be seen that the speed of the flow is dominated by u. The velocity in this direction is heavily influenced by the forcing flow function, with fast motion away from the centre out towards the middle of the recharge region. Further from the centre, as more of the water starts to flow downwards and back through the seabed, there is less rapid horizontal movement. The vertical velocity, meanwhile, is about ten times slower at its fastest point directly above the inflow, on the order of $10^{-7}\,\mathrm{ms}^{-1}$ compared to the horizontal velocities approaching $10^{-6}\,\mathrm{ms}^{-1}$. As water moves up it becomes slower, and is slowest near the surface. It then picks up a little more speed again as it approaches the seabed to either side, but the maximum downward speed is an order of magnitude less than of the maximum upward speed, at around $10^{-8}\,\mathrm{ms}^{-1}$. This difference in speed is accounted for by the difference in distance between ℓ and L, and the use of (2.11) to conserve volume in the system. With the chosen values for L and ℓ, the magnitude of the inflow velocity w_u is in fact nine times that of the outflow w_d.

Figure 2.3 shows a system in which the regions of inflow and outflow are equal in distance, with all variables given the same values as before except for $\ell = 50\,\mathrm{km}$. In this case, the vertical velocity of the flow is the same coming up from the discharge area as it is moving

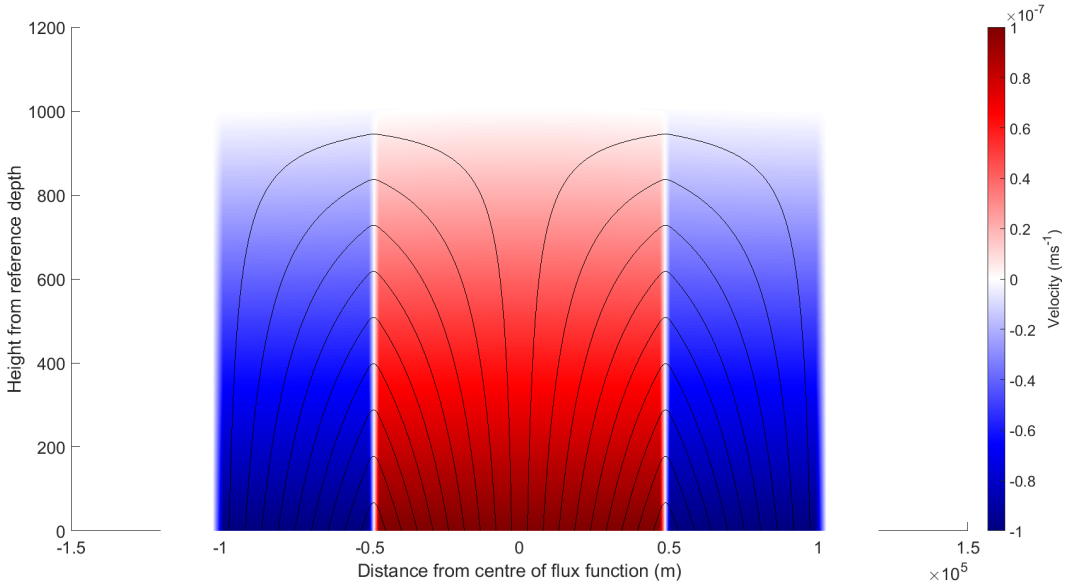

Figure 2.3: The circulation induced by a single uniform inflow of water through the seabed, with an equal amount of outflow distributed uniformly in regions to either side. Streamlines plotted over vertical velocity.

back downwards to the recharge area. This shows a great dependence of the shape and properties of the circulation on the function defining the inflow and outflow which drives it.

When solutions using other prescribed values are investigated, it is found that the choice of L is an important factor affecting the speed of the circulation. Figure 2.4 shows the circulation produced by inflow with all the same values as previously, except that L=100 m and ℓ=10 m, rather than being kilometers. In this case, the order of magnitude of the vertical velocity is unchanged, while the u-velocity becomes slower as the length of L is decreased. In (2.14), it can be seen that the value of h will increase as the length L increases. Then, in (2.12) it is clear that u will become smaller with a larger h. This means in turn that the v-velocity is also dependent on the length scale. The result of these differences is that the vertical velocity dominates the speed of the flow where the u-velocity used to be the larger of the two, but the shape of the circulation remains the same once scaled to fit the new horizontal domain.

Here it is worth returning to the subject of the hydrostatic approximation. For the results presented in Figure 2.2, the approximation holds up. The horizontal length scale and velocities are larger than those in the vertical. While acceleration is not one of the variables given by the steady state equations, the magnitude of the vertical velocities is lower than that of the gravitational acceleration by several orders of magnitude, suggesting that the vertical acceleration would be similarly small in comparison. The results presented in Figure 2.4, however, have a larger length scale and larger velocities in the vertical. This means that the hydrostatic approximation may not be valid in this case, although

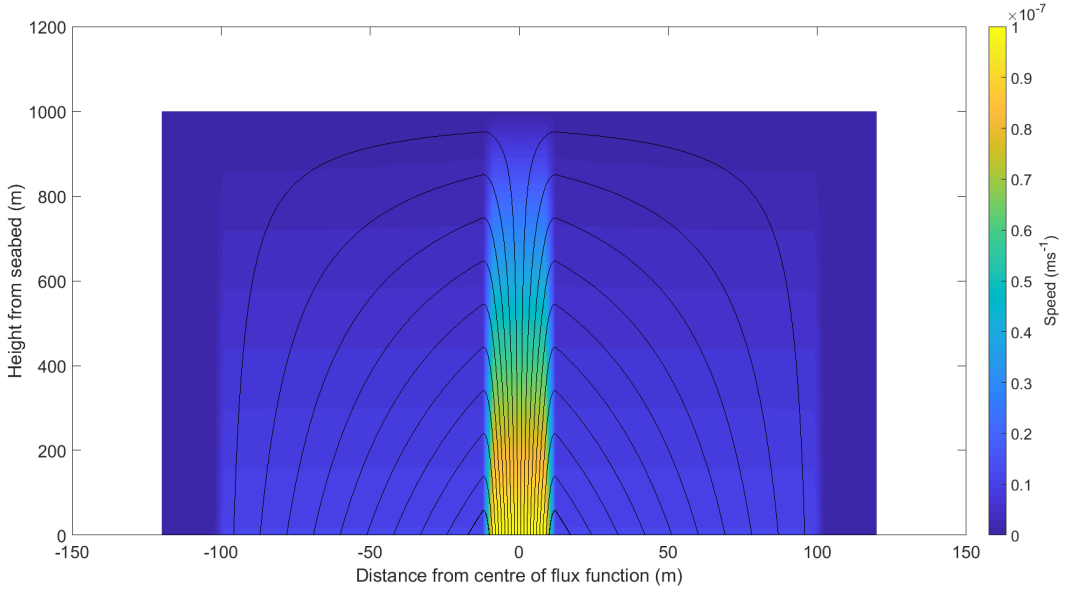

Figure 2.4: The circulation induced by a uniform inflow with uniform outflow to either side, in a domain with small horizontal lengths. Streamlines plotted over speed.

the vertical acceleration has not changed, and the result may not be representative of a realistic circulation for the given dimensions. Since the horizontal velocity is directly related to the length of L, keeping the length scale large is important in ensuring that the approximation remains valid. All further experiments will use the larger L.

2.3.3 Effects of varying the Rayleigh friction

It has already been demonstrated that the parameters prescribed before plotting solutions can have an important impact on the circulation. While most of the variables in the equations that produce plots can be chosen to represent realistic values, the Rayleigh friction rate is a more abstract variable standing in for the more complex and realistic viscosity terms. It is difficult to pick a value for it which is grounded in real world data. The effects of varying the Rayleigh friction are quite small when looking at the circulation on the scale of the full domain, but noticeable when focusing on the change to the free surface elevation. Changing the value of R also causes a corresponding change to the value of v, as is obvious from (2.13). Using the original example above ($L = 100\,\text{km}$, $\ell = 10\,\text{km}$) as a basis for investigation, the shape of the free surface always remains the same when plotted, but the displacement from the reference height H varies as R changes.

Figure 2.5 shows the maximum displacement of the free surface for a range of values for R. The axes are logarithmic, because for large parts of the range of values the relationship between the value of R and the displacement it causes is logarithmic. Interestingly, the direction of this relationship switches at around $R = 10^{-5}$, which is roughly where $R = f$.

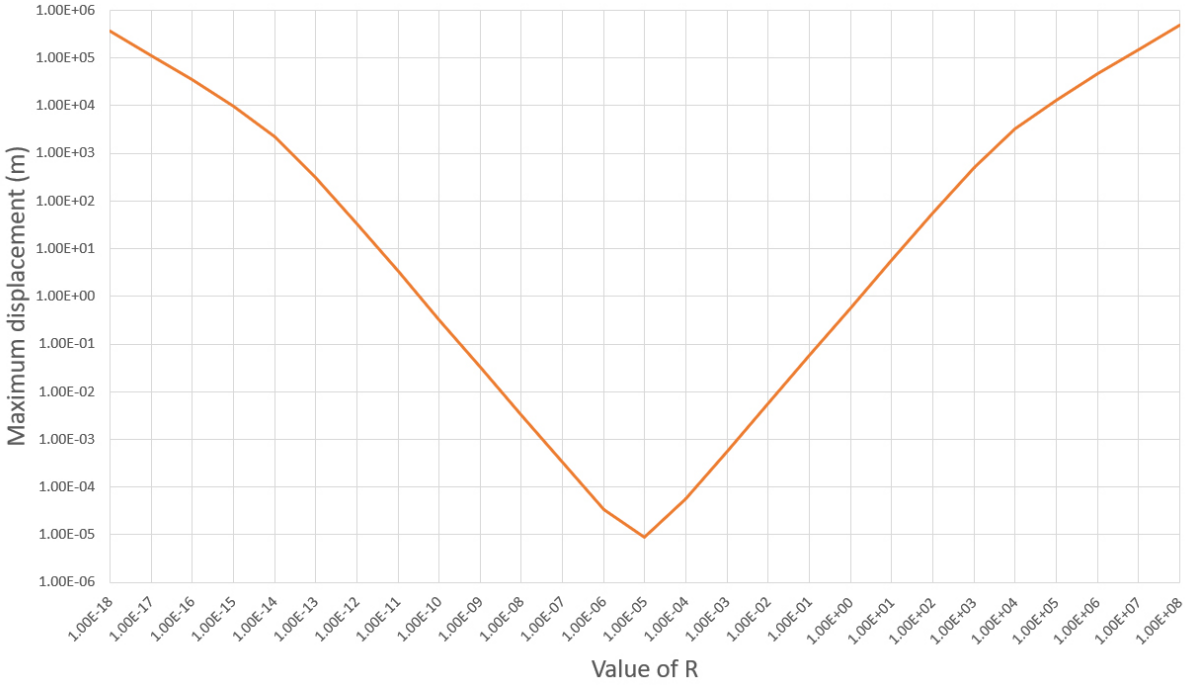

Figure 2.5: The effects on free surface elevation of varying the value of R.

This is no coincidence, as further investigation shows the maximum displacement curve to always be centred on a minimum at which $R = f$, for different choices of f.

Perturbations to the free surface of an ocean layer might be expected to be on the order of centimetres or metres. By choosing $R = 1$ in the previous examples, the maximum displacement to the free surface was about 1 m, which is of the same order as values that might be expected. Thus the value of $R = 1$ will continue to be used in further experiments.

2.4 Second case study: A cosine flux function

In this example, $w_b = \cos(\frac{\pi}{L}x)$ in the region $-L < x < L$, and is zero elsewhere. This formulation of w_b has been constructed so that the flux is exactly one period of the cosine function, centred about 0. As before, there will be no flow in the regions $x \leq -L$ and $x \geq L$. The same steps are followed as in the previous section to find the solution for $-L < x < L$. Using (2.8) with $x_0 = -L$, it is found that

$$\begin{aligned} u &= \frac{1}{h}\left(\int_{-L}^{x} \cos\left(\frac{\pi}{L}\xi\right)\,\mathrm{d}\xi\right) \\ &= \frac{1}{h}\left[\frac{L}{\pi}\sin\left(\frac{\pi}{L}\xi\right)\right]_{\xi=-L}^{\xi=x} \\ \implies u(x) &= \frac{L\sin\left(\frac{\pi}{L}x\right)}{\pi h(x)}. \end{aligned} \tag{2.17}$$

This value is now substituted into (2.9c) to work out the solution for h:

$$\begin{aligned} \frac{\partial h}{\partial x} &= -\left(\frac{f^2}{R} + R\right)\frac{L\sin(\frac{\pi}{L}x)}{hg\pi} \\ \implies \quad \frac{1}{2}\frac{\partial h^2}{\partial x} &= -\frac{(f^2+R^2)L\sin(\frac{\pi}{L}x)}{Rg\pi} \\ \implies \quad \frac{\partial h^2}{\partial x} &= -2\frac{(f^2+R^2)L\sin(\frac{\pi}{L}x)}{Rg\pi} \\ \implies h^2 - h_{-L}^2 &= 2\frac{(f^2+R^2)L^2}{Rg\pi^2}\left[\cos\left(\frac{\pi}{L}\xi\right)\right]_{\xi=-L}^{\xi=x} \\ \implies \quad h^2 &= H^2 + 2\frac{(f^2+R^2)L^2}{Rg\pi^2}\left(\cos\left(\frac{\pi}{L}x\right)+1\right) \\ \implies \quad h(x) &= \sqrt{H^2 + 2\frac{(f^2+R^2)L^2}{Rg\pi^2}\left(\cos\left(\frac{\pi}{L}x\right)+1\right)}. \end{aligned} \tag{2.18}$$

Finally, the solution for w is found by using (2.9d):

$$\begin{aligned}
\frac{\partial w}{\partial z} &= -\frac{\partial}{\partial x}\left(\frac{L\sin\left(\frac{\pi}{L}x\right)}{\pi\sqrt{H^2+2\frac{(f^2+R^2)L^2}{Rg\pi^2}\left(\cos\left(\frac{\pi}{L}x\right)+1\right)}}\right) \\
&= -\frac{\cos(\frac{\pi}{L})\sqrt{H^2+2\frac{(f^2+R^2)L^2}{Rg\pi^2}\left(\cos\left(\frac{\pi}{L}x\right)+1\right)}}{H^2+2\frac{(f^2+R^2)L^2}{Rg\pi^2}\left(\cos\left(\frac{\pi}{L}x\right)+1\right)} - \frac{\left(\frac{(f^2+R^2)L^2\sin^2(\frac{\pi}{L}x)}{Rg\pi^2\sqrt{H^2+2\frac{(f^2+R^2)L^2}{Rg\pi^2}\left(\cos\left(\frac{\pi}{L}x\right)+1\right)}}\right)}{H^2+2\frac{(f^2+R^2)L^2}{Rg\pi^2}\left(\cos\left(\frac{\pi}{L}x\right)+1\right)} \\
&= -\frac{\cos(\frac{\pi}{L}x)}{h} - \frac{(f^2+R^2)L^2\sin^2(\frac{\pi}{L}x)}{Rg\pi^2h^3} \\
&= -\frac{1}{h}\left(\cos\left(\frac{\pi}{L}x\right)+\frac{(f^2+R^2)u^2}{Rg}\right)
\end{aligned}$$

which, after integrating, yields the solution

$$w(x,z) = \cos\left(\frac{\pi}{L}x\right) - \frac{z}{h(x)}\left(\cos\left(\frac{\pi}{L}x\right)+\frac{(f^2+R^2)(u(x))^2}{Rg}\right). \tag{2.19}$$

The flow represented by these solutions (Figure 2.6) is similar in shape to that produced by the uniform inflow, but is heavily influenced by the function w_b which drives it. Instead of the horizontally uniform vertical gradients of vertical velocity seen above the discharge and recharge areas of Figure 2.3, the cosine flow function produces a gradient in the horizontal to match the inflow, such that the higher speeds occur above the peaks and troughs of the trigonometric curve. The streamlines also follow a smoother curve when transitioning from upwards to downwards motion, in line with the less abrupt changes to

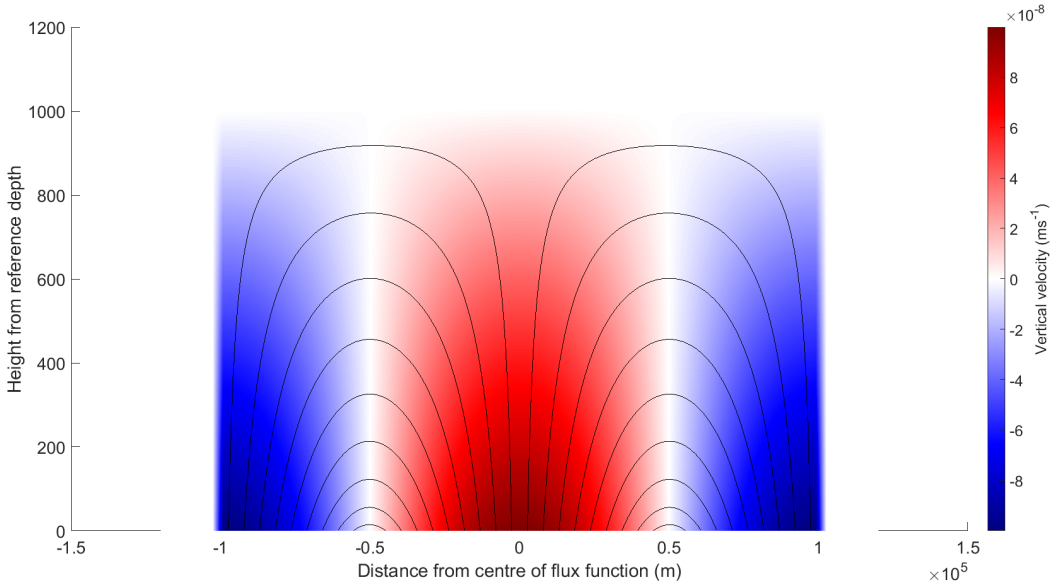

Figure 2.6: The circulation induced by a single inflow of water through the seabed, with outflow to either side, defined by a cosine function. Streamlines plotted over vertical velocity.

the seabed flow function at $x = \ell$ and $x = -\ell$.

2.5 A general solution and further examples

2.5.1 Calculating the general solution

In the previous examples, there are similarities in the solutions to the equations. The only difference between them is the flow through the seabed defined by the function w_b. It will be very useful to reach a more general solution, for any flux function $w_b(x)$ which conserves the water volume of the system and is of finite length. This way the full set of equations will not have to be solved for each change to the bottom boundary condition. To ensure that the entire domain is covered by this general solution, the value $x_0 = -\infty$ is specified in (2.8) to give

$$u(x) = \frac{\int_{-\infty}^{x} w_b(\xi)\,\mathrm{d}\xi}{h(x)}. \tag{2.20}$$

Next, from (2.9c), it follows that

$$\begin{aligned}
&\frac{\partial h}{\partial x} = -\frac{(f^2+R^2)u(x)}{Rg} \\
\implies &\frac{1}{2}\frac{\partial h^2}{\partial x} = -\frac{(f^2+R^2)}{Rg}\int_{-\infty}^{x} w_b(\xi)\,\mathrm{d}\xi \\
\implies &h^2 - (h(-\infty))^2 = -\frac{2(f^2+R^2)}{Rg}\int_{-\infty}^{x}\left(\int_{-\infty}^{\zeta} w_b(\xi)\,\mathrm{d}\xi\right)\mathrm{d}\zeta \\
\implies &h(x) = \sqrt{H^2 - \frac{2(f^2+R^2)}{Rg}\int_{-\infty}^{x}\left(\int_{-\infty}^{\zeta} w_b(\xi)\,\mathrm{d}\xi\right)\mathrm{d}\zeta}.
\end{aligned} \tag{2.21}$$

The above solution for $h(x)$ can be substituted into (2.20) and the solution for $u(x)$ in turn substituted into (2.9a). So now all that remains is to find a solution for $w(x,z)$. For this, (2.9d) is used to obtain

$$\begin{aligned}
\frac{\partial w}{\partial z} &= -\frac{\partial u}{\partial x} \\
&= -\frac{w_b(x)h(x) - \left(\int_{-\infty}^{x} w_b(\xi)\,\mathrm{d}\xi\right)h'(x)}{(h(x))^2} \\
&= -\frac{w_b(x)}{h(x)} + \frac{u(x)h'(x)}{h(x)} \\
&= -\frac{w_b(x)}{h(x)} - \frac{(f^2+R^2)(u(x))^2}{Rgh(x)}.
\end{aligned}$$

Integrating with respect to z produces

$$w(x,z) = -\frac{w_b(x)z}{h(x)} - \frac{(f^2+R^2)(u(x))^2 z}{Rgh(x)} + c(x),$$

in which, by application of either of the boundary conditions (2.4) and (2.5) it can be easily seen that

$$c(x) = w_b(x).$$

So,

$$w(x,z) = w_b(x) - \frac{w_b(x)z}{h(x)} - \frac{(f^2+R^2)(u(x))^2 z}{Rgh(x)}. \tag{2.22}$$

Thus the entire solution of the problem, for all four unknown quantities, can be stated as

$$h(x) = \sqrt{H^2 - \frac{2(f^2+R^2)}{Rg}\int_{-L}^{x}\left(\int_{-L}^{\zeta} w_b(\xi)\,\mathrm{d}\xi\right)\,\mathrm{d}\zeta} \tag{2.23a}$$

$$u(x) = \frac{\int_{-L}^{x} w_b(\xi)\,\mathrm{d}\xi}{h(x)} \tag{2.23b}$$

$$v(x) = -\frac{f}{R}u(x) \tag{2.23c}$$

$$w(x,z) = w_b(x) - \left(w_b(x) + \frac{(f^2+R^2)u(x)^2}{Rg}\right)\frac{z}{h(x)}. \tag{2.23d}$$

These solutions show that in all cases the flow velocity u, in the x-direction, results from the horizontal divergence caused by the discharge and recharge of water through the seabed (2.23b), while the cross flow, v, is a balance between the Rayleigh friction rate and the Coriolis force (2.23c). The horizontal flow is vertically uniform (from the Taylor-Proudman theorem) and the vertical velocity varies linearly from its value at the seabed w_b to that at the top of the layer, which is generally non-zero to ensure that there is no flow across the interface. The shape of the interface itself is determined by the shape of the velocity function w_b.

I have written a Matlab script (Appendix A.1) which can calculate these solutions and produce figures for any seabed flow function, which must be manually entered near the start of the script. The prescribed variables can also be given different values at the beginning of the script. It is assumed that the flow functions are finite, being non-zero within the region $-L \leq x \leq L$. The definitions for flow functions can make use of the prescribed values for L and ℓ when setting distances and locations for regions of inflow and outflow.

2.5.2 Comparison of uniform and cosine flow functions

Having a general solution for any flow function w_b allows the investigation of many possible formulations of the flow through the seabed. The first example here is an adapted cosine

flow function, with discharge and recharge areas of widths ℓ and L as is the case in the the uniform flow function in Section 2.3. The flow through the seabed is described by

$$w_b = \begin{cases} w_0 \frac{\ell}{L-\ell} \sin\left(\frac{\pi(x+\ell)}{L-\ell}\right) & \text{if } -L \leq x < -\ell \\ w_0 \cos\left(\frac{\pi x}{2\ell}\right) & \text{if } -\ell \leq x \leq \ell \\ -w_0 \frac{\ell}{L-\ell} \sin\left(\frac{\pi(x-\ell)}{L-\ell}\right) & \text{if } \ell < x \leq L \\ 0 & \text{otherwise,} \end{cases} \tag{2.24}$$

where w_0 is the maximum velocity of the flow, at the peak of the cosine curve at $x = 0$. The segments of this piecewise function have been calculated to ensure that volume is conserved, as needs to be done for all such functions w_b used in the general solution.

Choosing the same values for the prescribed variables as before, the flow produced by this forcing function is shown in Figure 2.7d. A direct comparison of this solution with the case of a uniform flow function is useful, as it shows the differences that a change to the flux function can make when discharge and recharge occur over the same regions, but with different formulations. The differences between the cosine and uniform flows are highlighted by showing both flows side by side in Figure 2.7. In this figure, the uniform flow has been given a value of $\frac{2}{\pi}w_0$ so that the total volume of water entering and leaving the basin due to the flow is exactly the same as that in the case using the cosine function. The solutions clearly show a difference in the distribution of the speeds. There is a horizontal gradient in the vertical velocity above each region of discharge or recharge caused by using a cosine flow function to drive the circulation, due to the faster flow at the peaks and troughs of the cosine functions. The speeds, dominated by the larger u-velocities, shows a corresponsing difference. The flow remains at fast speeds further away from the region of inflow, as more of the water is travelling towards the centre of the outflow region. The transition from fast to slow horizontal flow is more sudden with the cosine forcing function, at the halfway point of the outflow region, whereas with a uniform outflow the gradient across the area of recharge is constant.

The difference in the circulation's transition from a region of inflow to a region of outflow is shown more clearly by displaying the streamlines together on the same plot (Figure 2.8). The uniform flow functions cause a sharper change in direction of the flow, as the flow function at the seabed jumps abruptly from positive to negative. In the case of cosine functions, however, the transition is much smoother as the inflow function gradually reaches zero at the boundary with the region of outflow, and then gradually becomes more negative. The continuous flow function at the seabed, while generating a slightly calmer circulation compared to the step function of uniform flows, also causes differences to the distance from the centre reached by the streamlines. Due to the majority of the outflow being focused towards the centre of the recharge region, the widest reaching line

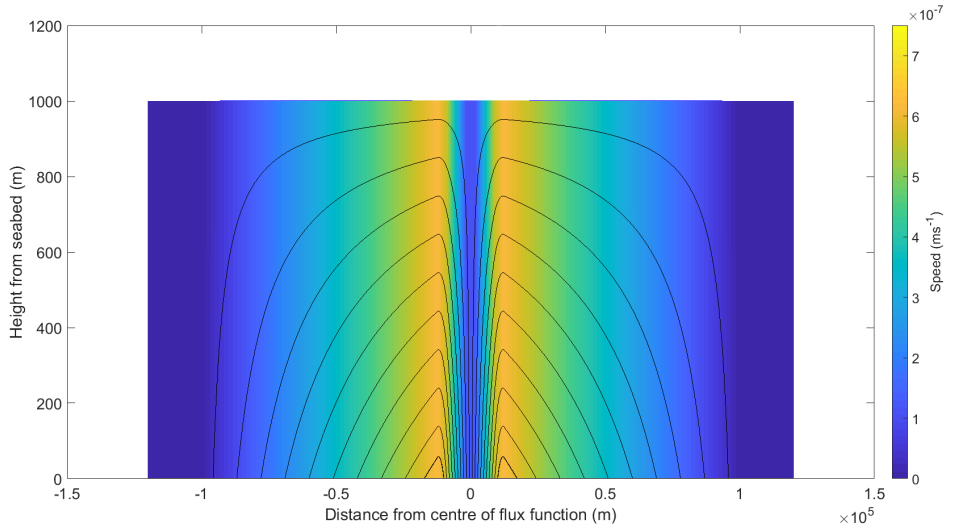

(a) Streamlines plotted over speed.

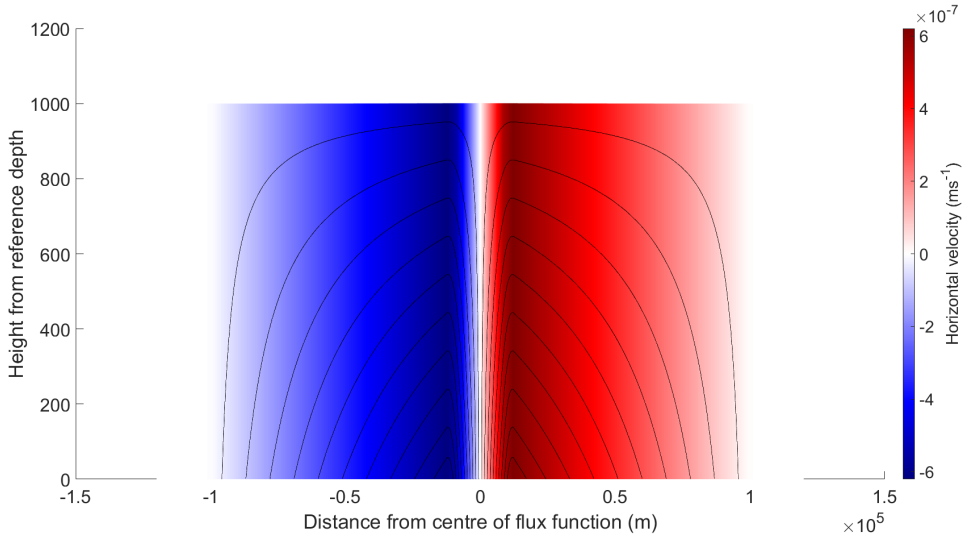

(b) Streamlines plotted over horizontal velocity (u).

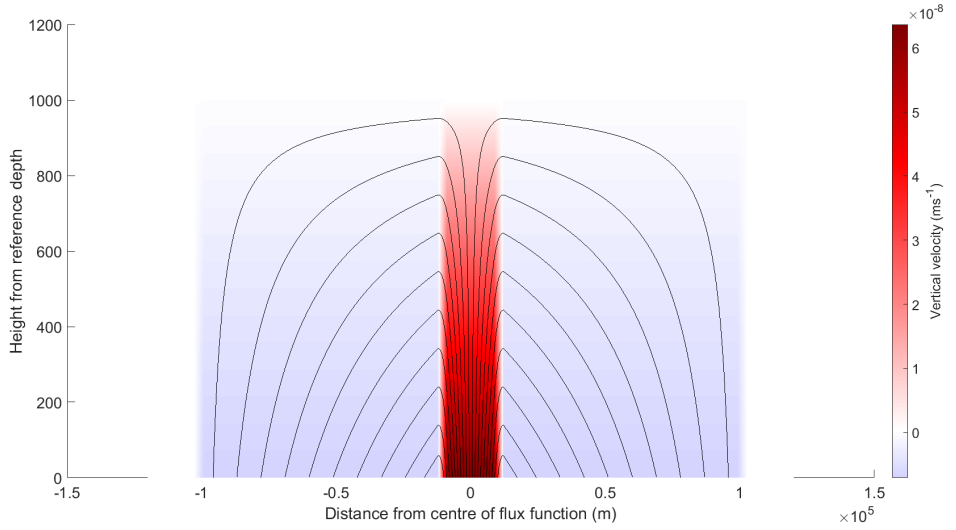

(c) Streamlines plotted over vertical velocity (w).

Figure 2.7: A comparison of circulations induced by different formulations of the flow function w_b. This page shows results from using a step function with uniform regions of inflow and outflow.

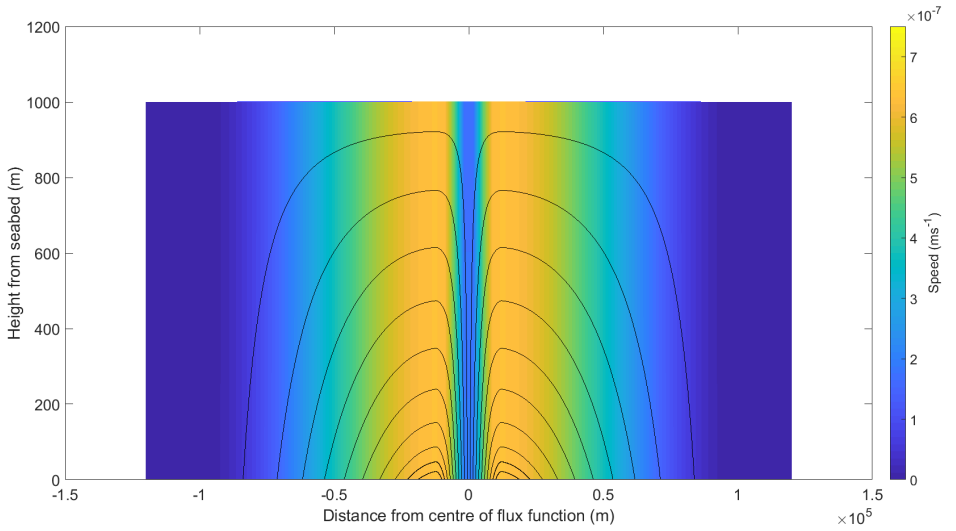

(d) Streamlines plotted over speed.

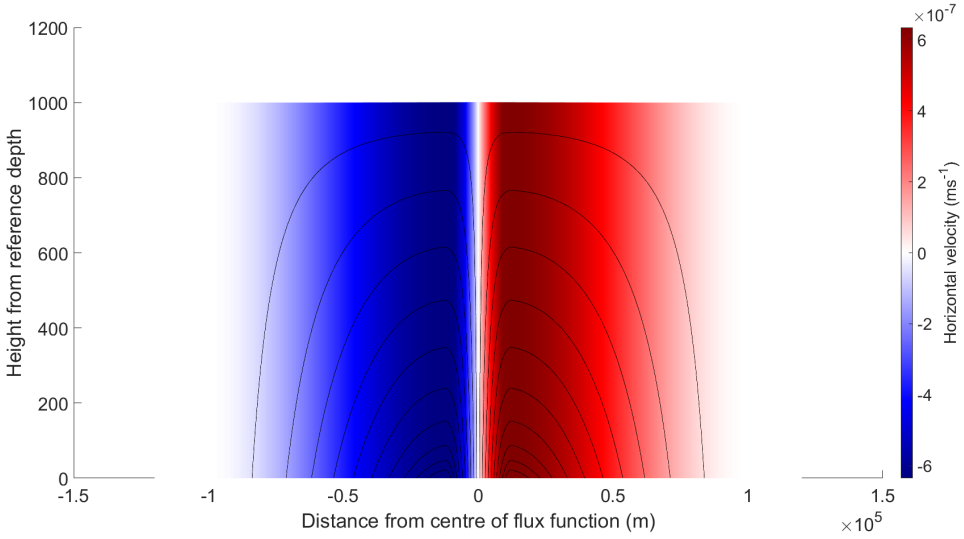

(e) Streamlines plotted over horizontal velocity (u).

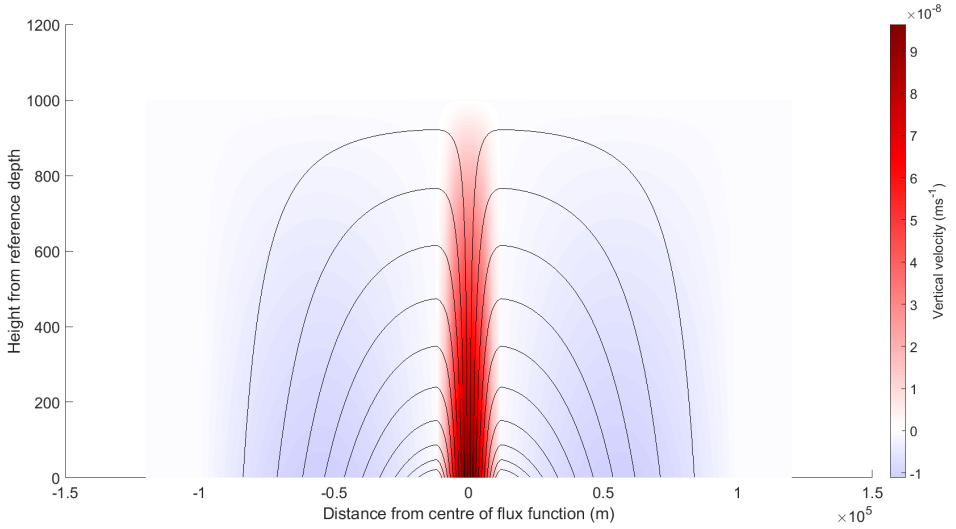

(f) Streamlines plotted over vertical velocity (w).

Figure 2.7: Continued from opposite page. This page shows results from using a step function with cosine formulations of inflow and outflow.

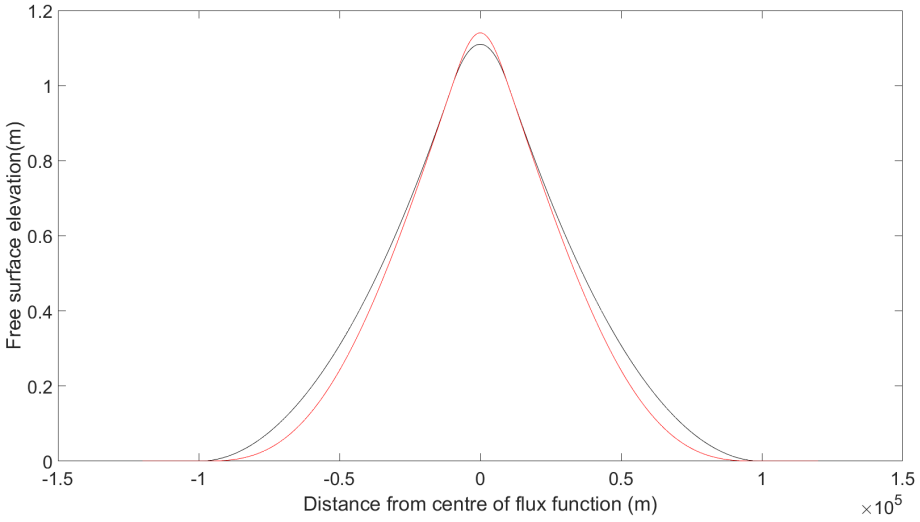

(a) Free surface elevations resulting from both flow functions.

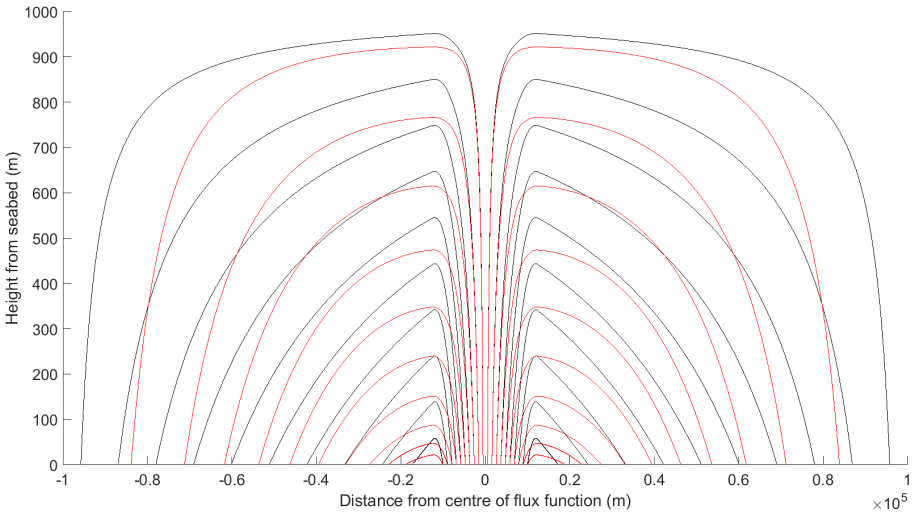

(b) Streamlines resulting from both flow functions.

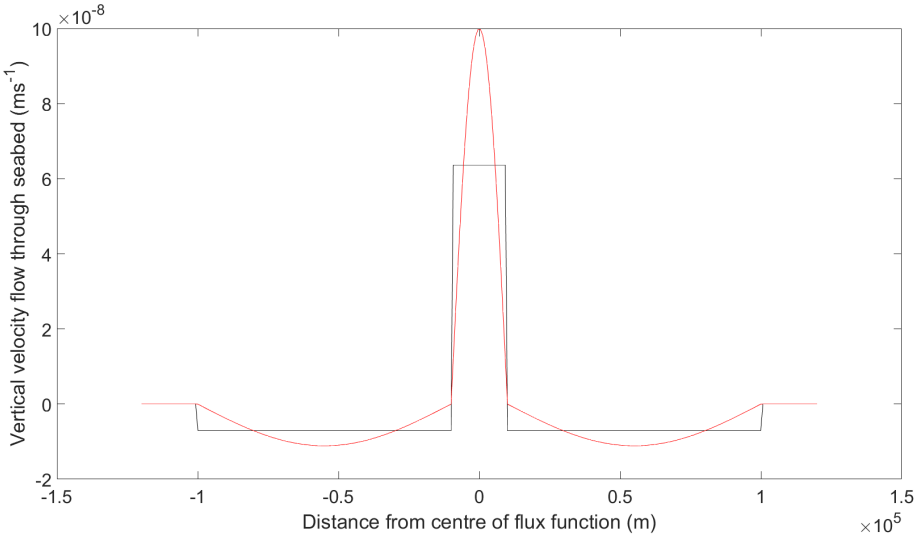

(c) The flow functions (w_b).

Figure 2.8: A comparison of circulations induced by different formulations of the flow function w_b. Here the plots are displayed on the same image, with results from the uniform flow in black and from the cosine flow function in red.

of flow does not extend as far as the equivalent streamline from the uniform flow function. The streamlines originating towards the edge of the discharge region, meanwhile, do not reach the same heights as those from the uniform inflow since their velocities are much lower at those points of entry to the basin, due to the shape of the flow function. The maximum free surface heights do not differ much between the two cases, but a wider peak can be seen with the uniform inflow to match the wider-reaching circulation below it.

2.5.3 Further examples

Since there are very few data available on the exact distributions of hydrothermal discharge and recharge in the oceans, I will now use the general solution obtained previously to look at several different possible arrangements of inflow and outflow. There are some hydrothermal systems known to consist of linked areas of discharge and recharge separated by about 50 km (Fisher et al., 2003), so the scale of the flows investigated here is not unreasonable.

The first case here is one in which there is only a single region of outflow. The discharge and recharge are set to be equal in magnitude, over equal distances either side of $x = 0$, with a gap between the two in which there is no flow through the seabed. This is the first asymmetrical flow function to be tried, which reveals a new effect of changing the flow function. Figure 2.9a shows that the free surface is at different heights either side of the circulation induced by the flow through the seabed. The value $h(x) = H$ is prescribed at $x = -\infty$, but the is no such prescription at the other side of the domain. Until now, with symmetrical flow functions, the water level has been the same on both sides, but this does not necessarily have to be the case. It's important to note that H is a reference height above the seabed, and not the initial height of the free surface in an undisturbed domain, as these problems have no time dimension. As such, much of the domain being below this reference height does not mean that volume is leaving the system as it may first appear.

Now that a few circulations driven by a single inflow have been investigated, the general solution can be put to use, in order to look at circulations driven by multiple inflows. Multiple regions of discharge could cause interesting interactions between the inflowing water masses and cause different behaviour in the circulation than that seen already. The first example does not show anything particularly different. Figure 2.10 shows the circulation induced by three periods of a cosine function for flow through the seabed. The effect of this is simply a repetition of the same pattern of circulation previously seen for a cosine forcing function (Section 2.4). However, in this case, the regions of discharge and recharge are all of the same magnitude, and distributed such that inflow and outflow alternate across the domain. There is potential for far more irregular flow, which is where

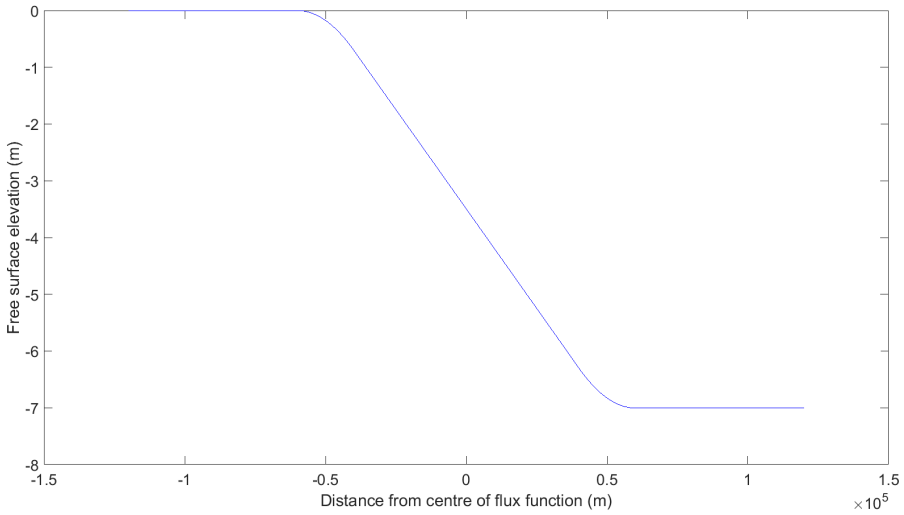

(a) Free surface elevation (h).

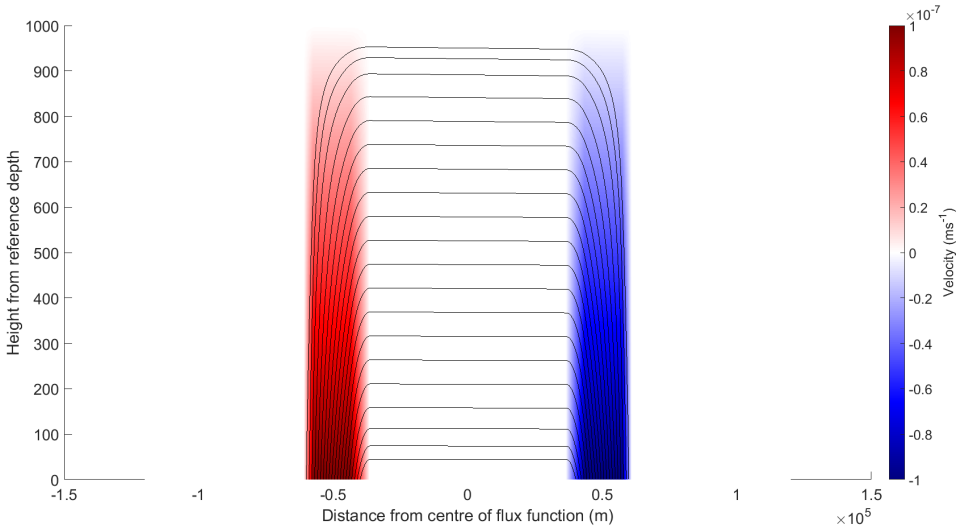

(b) Streamlines plotted over vertical velocity (w).

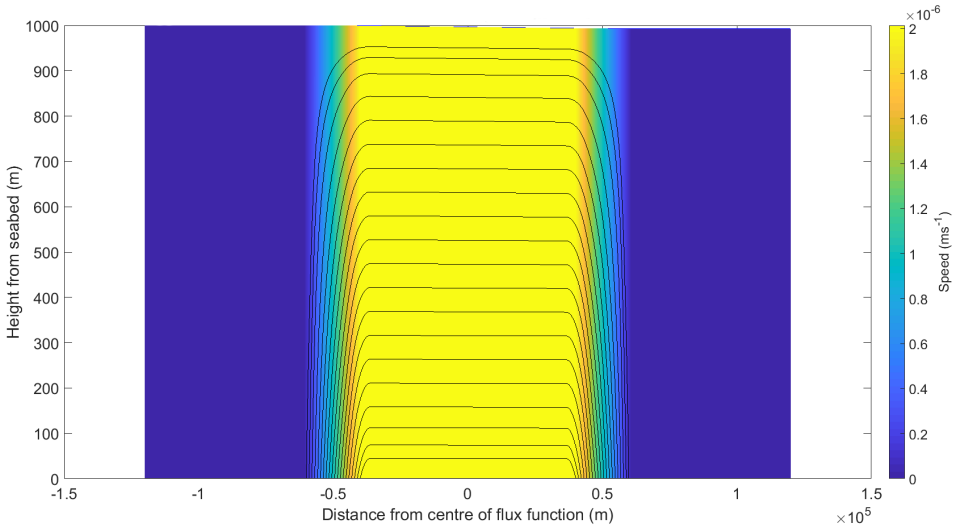

(c) Streamlines plotted over speed.

Figure 2.9: The circulation induced by a uniform inflow through the seabed with a single uniform recharge region to the right.

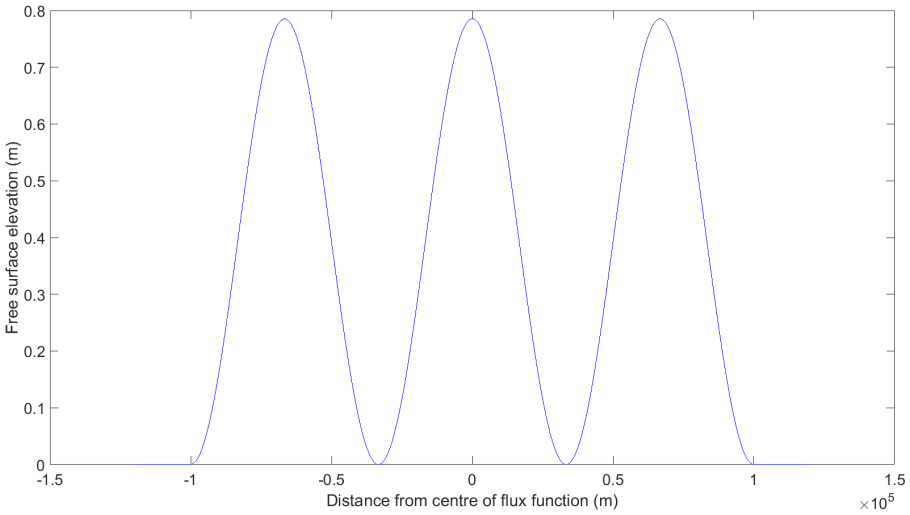

(a) Free surface elevation (h).

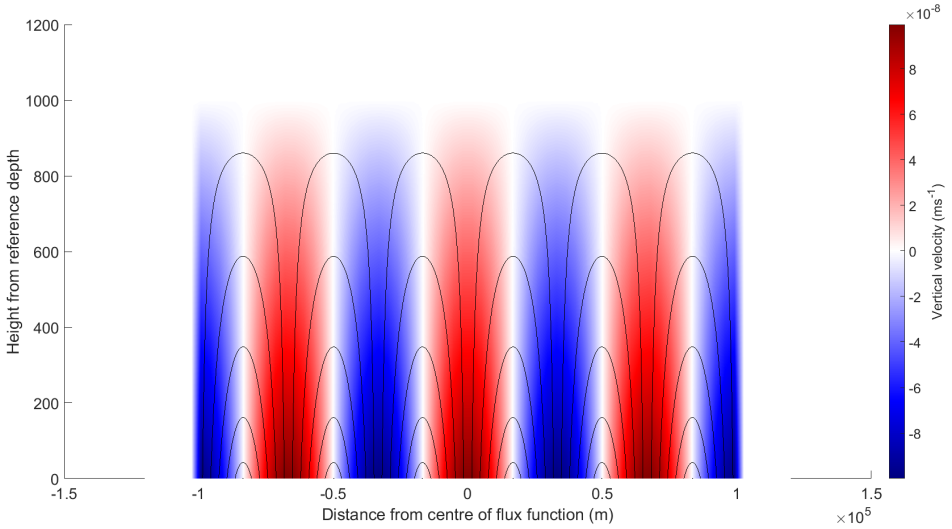

(b) Streamlines plotted over vertical velocity (w).

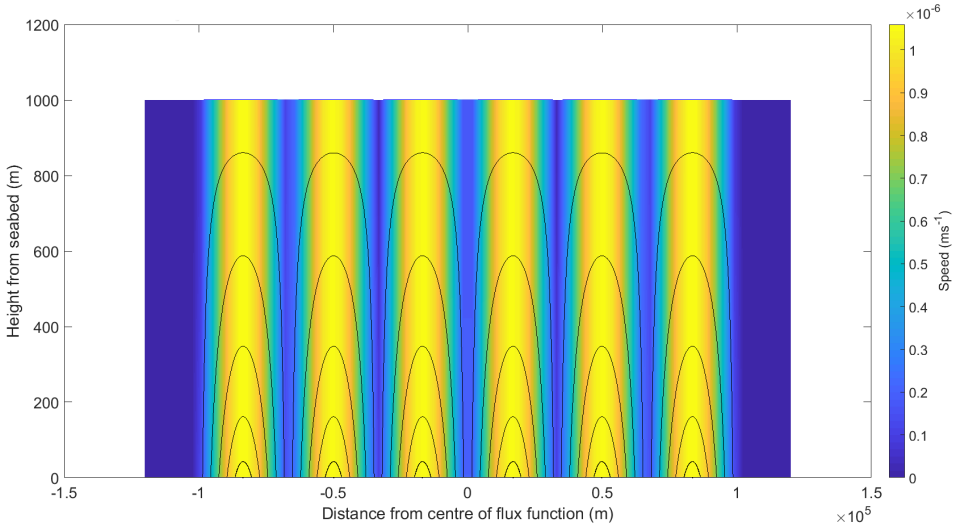

(c) Streamlines plotted over speed.

Figure 2.10: The circulation induced by a flow through the seabed described by three periods of a cosine function.

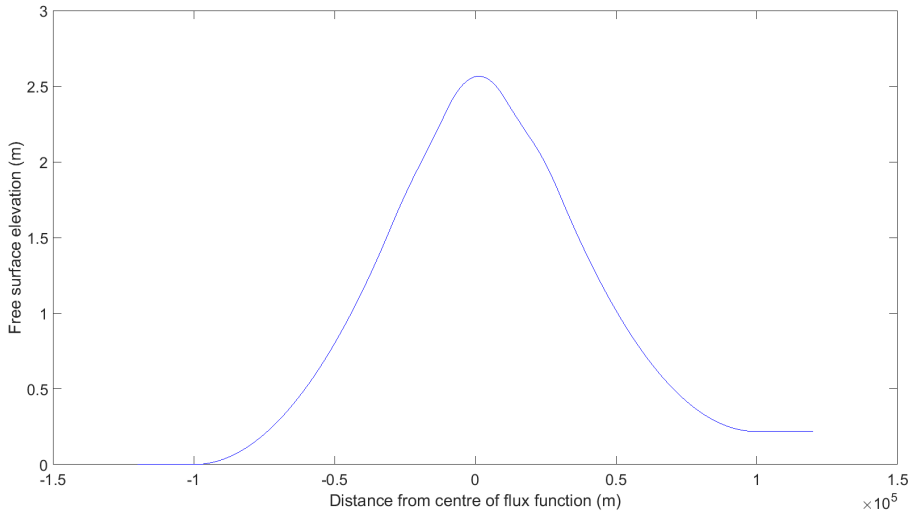

(a) Free surface elevation (h).

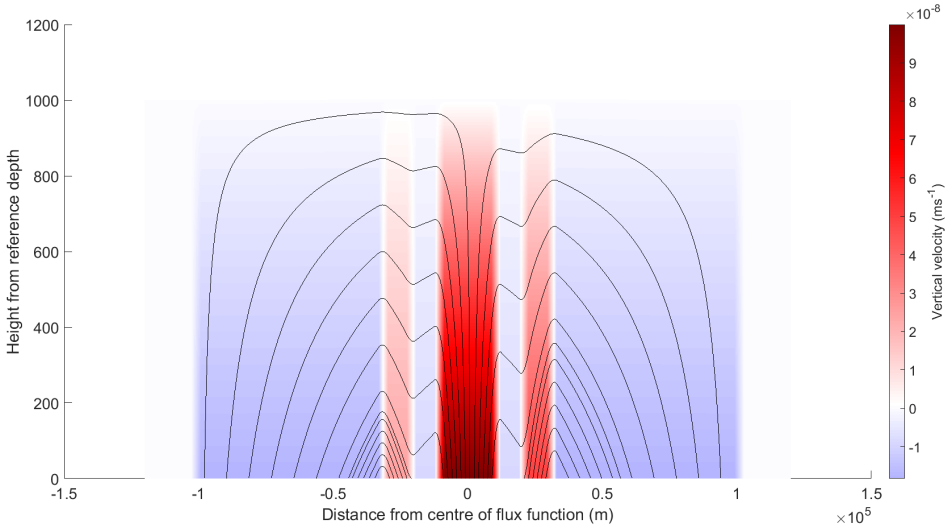

(b) Streamlines plotted over vertical velocity (w).

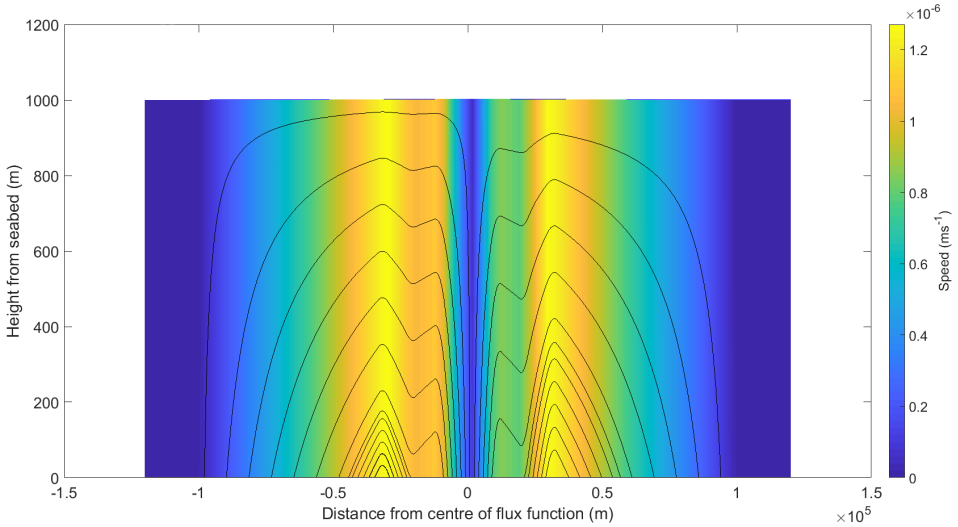

(c) Streamlines plotted over speed.

Figure 2.11: The circulation induced by a flow through the seabed consisting of three regions of inflow with different velocities, and outflow to either side.

more interesting behaviour may be seen.

In the final example, the flow through the seabed is described by a step function, with a central discharge region flanked by two of differing lower velocities. The inflow to the right is half the velocity of the central discharge, and the inflow to the left one quarter of the velocity. In Figure 2.11, it is once again seen that the asymmetry in the seabed flow function produces an asymmetric free surface, with differing elevations at either side. The weaker inflows to either side of the centre are contained close to the seabed by the circulation above originating from the main central discharge. The inflow on the right, being twice the velocity of that on the left, penetrates roughly twice as far into the water column before being turned back towards the seabed by the water emanating from the centre.

2.6 A Rayleigh friction model with seabed bathymetry

2.6.1 Solving the equations with added bathymetry

Since hydrothermal activity occurs along plate boundaries where the seabed is composed of mid-ocean ridges and axial valleys, it makes sense to add bathymetry into the problems. Taking away the assumption of a flat seabed means that $\eta(x)$ can no longer be equated with $h(x) - H$. In fact now $\eta(x) = h(x) + b(x) - H$, where $h(x)$ is the total water depth and $b(x)$ is a function which describes the bathymetry (see Figure 2.12 for a sketch of these function definitions). The boundary condition at the seabed changes to

$$w(x, b(x)) = u\frac{\partial b}{\partial x} + w_b. \tag{2.25}$$

Going through all the same steps as in Section 2.2.1, the equations (2.9) do not actually change much:

$$v(x) = -\frac{f}{R}u(x) \tag{2.26a}$$

$$u(x) = \frac{1}{h(x)}\int_{-\infty}^{x} w_b(\xi)\,\mathrm{d}\xi \tag{2.26b}$$

$$\frac{\partial \eta}{\partial x} = -\frac{(f^2 + R^2)u(x)}{Rg} \tag{2.26c}$$

$$\frac{\partial w}{\partial z} = -\frac{\partial u}{\partial x}. \tag{2.26d}$$

However, the added bathymetry brings up a problem during the process of analytical solution. The issue is demonstrated by going through the general solution for an arbitrary bathymetry function $b(x)$. The process starts exactly as in Section 2.5, with the solution

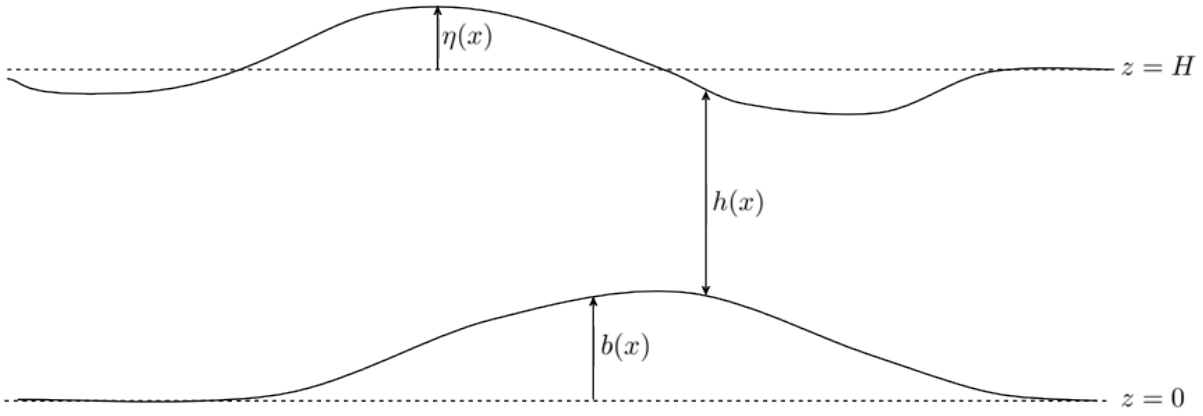

Figure 2.12: A sketch showing the definitions of functions in the Rayleigh friction model with bathymetry.

for u being unaffected by the bathymetry:

$$u(x) = \frac{\int_{-\infty}^{x} w_b(\xi)\,\mathrm{d}\xi}{h(x)}. \tag{2.27}$$

The problem in analytical solution is encountered when trying to find an expression for h. For $x \leq -L$, $h = H$ as before. But for $x > -L$, (2.26c) produces

$$\begin{aligned} \frac{\partial \eta}{\partial x} &= -\frac{(f^2 + R^2)}{Rg} \frac{\int_{-\infty}^{x} w_b(\xi)\,\mathrm{d}\xi}{h(x)} \\ \implies h\frac{\partial (h + b - H)}{\partial x} &= -\frac{(f^2 + R^2)}{Rg} \int_{-\infty}^{x} w_b(\xi)\,\mathrm{d}\xi \\ \implies \quad \frac{1}{2}\frac{\partial h^2}{\partial x} + h\frac{\partial b}{\partial x} &= -\frac{(f^2 + R^2)}{Rg} \int_{-\infty}^{x} w_b(\xi)\,\mathrm{d}\xi. \end{aligned}$$

Since $\frac{\partial \eta}{\partial x}$ is no longer equivalent to $\frac{\partial h}{\partial x}$, an extra term enters the equation which makes a straight-forward analytical solution impossible. To get around this the approximation $h(x) \approx H - b(x)$ is used in front of the $\frac{\partial b}{\partial x}$ term, which allows analytical work to be continued. This means that η is being omitted from the definition of h. This will result in the solution for h being slightly less accurate but, since η is generally at least three orders of magnitude smaller than H due to the choice of R, there will not be a negative impact to the overall length scale of the problem. Additionally, when $b(x)$ is non-zero, it will be given maxima on the order of hundreds of metres, at least two orders of magnitude larger than η. Making this approximation is a reasonable way of ensuring that solutions can be reached with very little change to the accuracy of results.

Continuing after making this approximation,

$$\begin{aligned}
\frac{1}{2}\frac{\partial h^2}{\partial x} &= -\frac{(f^2+R^2)}{Rg}\int_{-\infty}^{x} w_b(\xi)\,\mathrm{d}\xi - (H-b)\frac{\partial b}{\partial x} \\
\implies h^2 - H^2 &= -2\int_{-\infty}^{x}\left(\frac{(f^2+R^2)}{Rg}\int_{-\infty}^{\zeta} w_b(\xi)\,\mathrm{d}\xi + (H-b(\zeta))\frac{\partial b}{\partial \zeta}\right)\mathrm{d}\zeta \\
\implies \qquad h &= \sqrt{H^2 - 2\int_{-\infty}^{x}\left(\frac{(f^2+R^2)}{Rg}\int_{-\infty}^{\zeta} w_b(\xi)\,\mathrm{d}\xi + (H-b(\zeta))\frac{\partial b}{\partial \zeta}\right)\mathrm{d}\zeta}.
\end{aligned}$$

The solution for w follows from (2.26d) as before, with some of the mathematics being a little more complicated:

$$\begin{aligned}
\frac{\partial w}{\partial z} &= -\frac{\partial u}{\partial x} \\
&= -\frac{w_b(x)h(x) - \left(\int_{-\infty}^{x} w_b(\xi)\,\mathrm{d}\xi\right)h'(x)}{(h(x))^2} \\
&= -\frac{w_b}{h} - \frac{u}{h^2}\left(\frac{(f^2+R^2)}{Rg}\int_{-\infty}^{x} w_b(\xi)\,\mathrm{d}\xi + (H-b)\frac{\partial b}{\partial x}\right) \\
&= -\frac{w_b}{h} - \frac{(f^2+R^2)u^2}{Rgh} - \frac{(H-b)u}{h^2}\frac{\partial b}{\partial x}.
\end{aligned}$$

Integrating with respect to z, it is seen that

$$w(x,z) = -\frac{w_b z}{h} - \frac{(f^2+R^2)u^2 z}{Rgh} - \frac{(H-b)uz}{h^2}\frac{\partial b}{\partial x} + c(x),$$

where the boundary condition (2.25) can be used to calculate

$$c(x) = \left(\frac{(H-b)bu}{h^2} + u\right)\frac{\partial b}{\partial x} + \left(1+\frac{b}{h}\right)w_b + \frac{(f^2+R^2)u^2 b}{Rgh}.$$

So,

$$w(x,z) = \frac{1}{h}\left((h+b-z)w_b + \frac{(f^2+R^2)(b-z)u^2}{Rg}\right) + \left(\frac{(H-b)(b-z)}{h^2} + 1\right)u\frac{\partial b}{\partial x}.$$

Thus the full solution can be stated as

$$h(x) = \sqrt{H^2 - 2\int_{-\infty}^{x}\left(\frac{(f^2+R^2)}{Rg}\int_{-\infty}^{\zeta} w_b(\xi)\,\mathrm{d}\xi + (H-b(\zeta))\frac{\partial b}{\partial \zeta}\right)\mathrm{d}\zeta} \tag{2.28a}$$

$$u(x) = \frac{\int_{-\infty}^{x} w_b(\xi)\,\mathrm{d}\xi}{h(x)} \tag{2.28b}$$

$$v(x) = -\frac{f}{R}u(x) \tag{2.28c}$$

$$w(x,z) = \frac{1}{h(x)}\left((h(x)+b(x)-z)w_b(x) + \frac{(f^2+R^2)(b(x)-z)u(x)^2}{Rg}\right) + \left(\frac{(H-b(x))(b(x)-z)}{h(x)^2}+1\right)u(x)\frac{\partial b}{\partial x}. \tag{2.28d}$$

Looking at these equations, it can be seen that the bathymetry has a large impact on the free surface elevation, but that the divergence caused by the flux function through the seabed is still the main influencing factor for the horizontal velocities. The vertical velocity still varies linearly between its values at the seabed and at the surface, with the bathymetry now taken into account. As before, I produced a script in Matlab to plot results from these equations, which can be found in Appendix A.2.

2.6.2 Example: a simple cosine ridge

Since hydrothermal activity occurs predominantly over mid-ocean ridges, bathymetries are chosen to represent such systems. This first example makes use of a simple cosine function to define the ridge shape, and the previously used piecewise cosine flow through the seabed given in (2.24). A height of 400 m has been chosen for the ridge, similar in size to ridges upon which hydrothermal systems are known to appear, so it takes up a significant proportion of the 1000 m depth of the layer.

The results (Figure 2.13) show a similar flow to that created by the same flow function through a flat seabed. The shape of the flow follows the same fountain-like path, and the vertical velocity has the same signal, becoming weaker towards the surface. This would appear to suggest that the bathymetry does not have much influence over the flow. However, the effects of bathymetry on the free surface can be seen here, with an increase of around 65 % in the maximum height of elevation above the ridge. With a more complex bathymetry, more effects on the flow may be seen.

2.6.3 A mid-ocean ridge section

The bathymetry for this experiment was given a profile similar to that of a mid-ocean ridge, with sloping sides up to peaks of 500 m, and a deep axial valley in the centre which equals the depth of the flat seabed to either side. The dimensions were roughly based on bathymetry from the ridges in the Panama Basin. The equation describing the ridge is piecewise, and can be seen in the script in Appendix A.2.

With this more irregular bathymetry, effects can be seen in the shape of the flow itself in Figure 2.14. The inflow occurs within the axial valley, up to the peaks either side. The dramatic change in depth can be seen in the streamlines. Where a cosine inflow would usually be stronger at the centre, the horizontal gradient in vertical velocity at the top

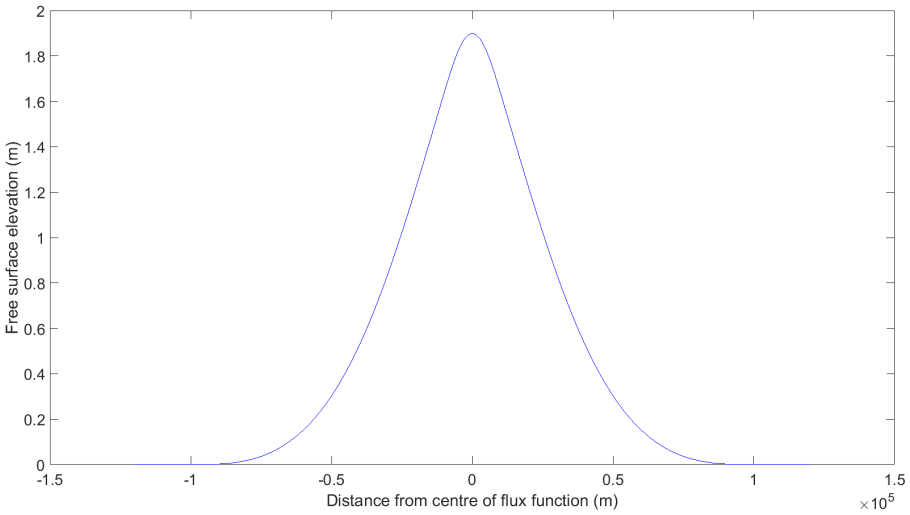

(a) Free surface elevation (h).

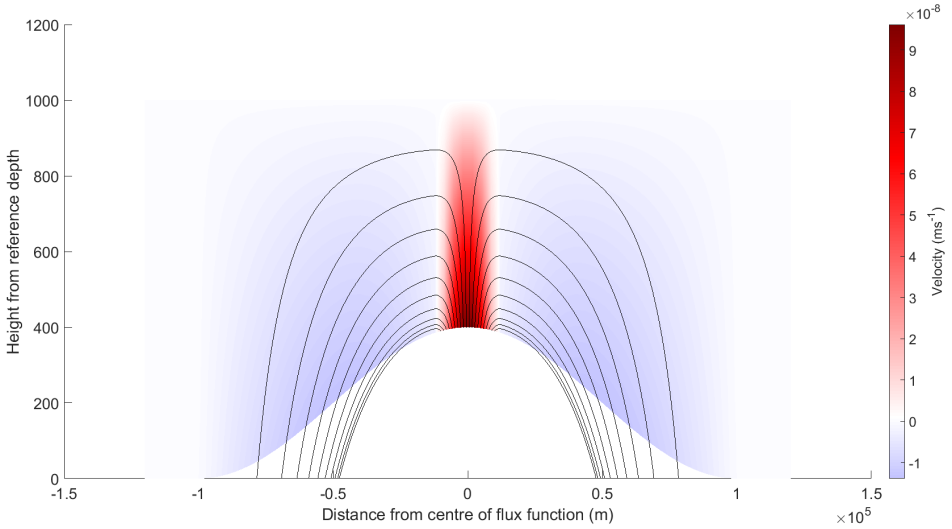

(b) Streamlines plotted over vertical velocity (w).

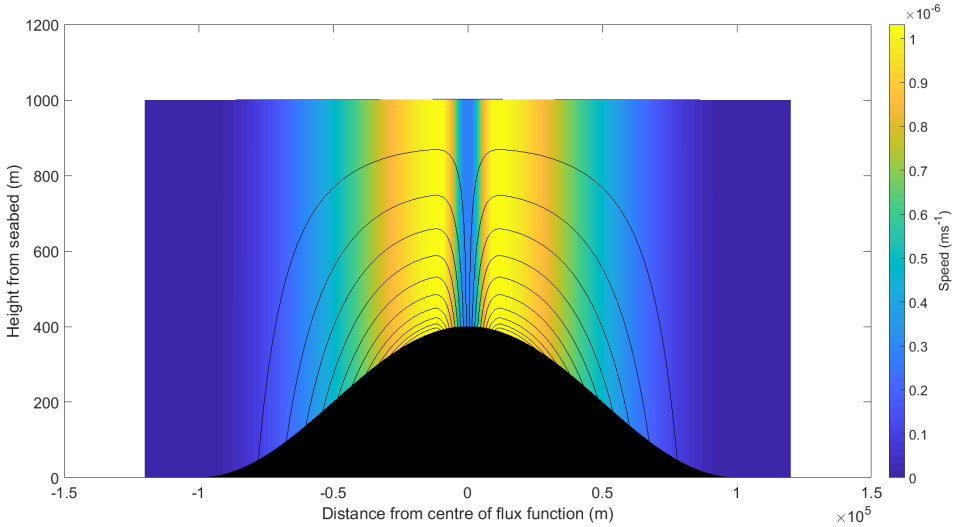

(c) Streamlines plotted over speed.

Figure 2.13: The circulation induced by a flow through the seabed with a cosine distribution, over a cosine bathymetry.

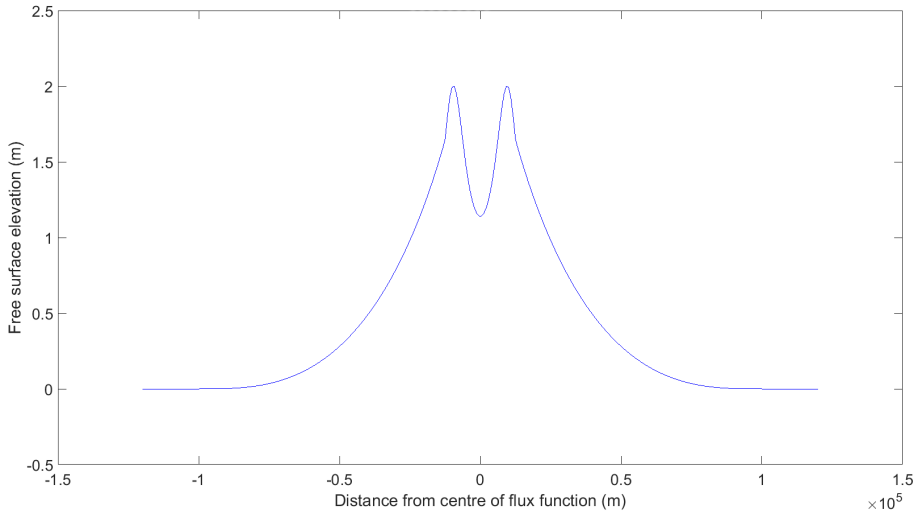

(a) Free surface elevation (h).

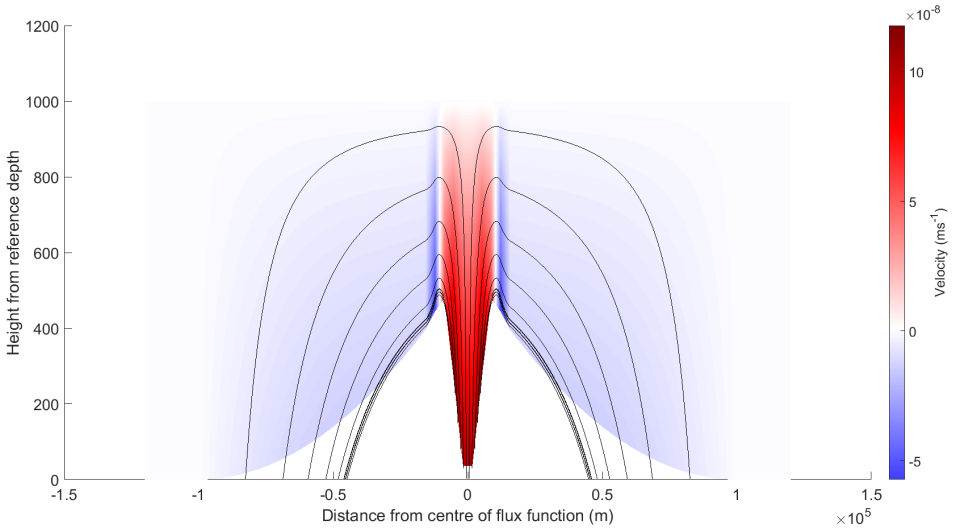

(b) Streamlines plotted over vertical velocity (w).

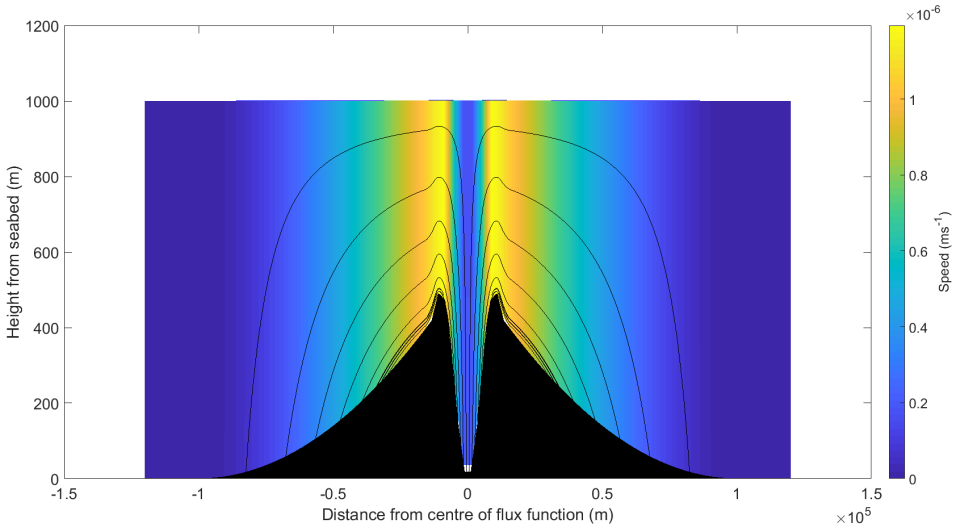

(c) Streamlines plotted over speed.

Figure 2.14: The circulation induced by a flow through the seabed with a cosine distribution, over a bathymetry resembling a mid-ocean ridge cross section.

of the ridge is very different. The water at the centre is already 500 m from its source and halfway through the linear decrease towards the surface value. To either side is water which has just been discharged, travelling almost at its full initial velocity. To move sideways towards the recharge region, water from the middle must pass over the stronger upward flow, which results in a bump in the streamlines, followed immediately by a rapid dip when clear of the influence of the rising water. This dip is seen in the vertical velocity field as a narrow column of strong downward velocity, before the flow starts to resume its more familiar behaviour.

The changes to the free surface elevation follow a similar theme. At the very centre, the elevation is about the same as in the experiment using the same seabed flow function through a flat seabed. But now, this is not the maximum elevation. To either side, above the peaks of the ridges, are two maxima in the free surface. They are about 70 % higher than the height at the centre. Together with the comparison of Figure 2.13a to earlier results, this shows that the shallower the water column, the larger the perturbation to the free surface will be when using the same inflow.

2.7 The Rayleigh friction models in cylindrical coordinates

2.7.1 The equations in cylindrical form

A three-dimensional domain can be explored in a limited way, without adding much complexity to the equations, by using cylindrical coordinates. In this coordinate system, shown in Figure 2.15, the equations take a very similar form. The primitive equations, taking into account the Rayleigh friction approximation, are

$$\frac{\partial \mathcal{U}}{\partial t} + \mathcal{U}\frac{\partial \mathcal{U}}{\partial r} + \frac{\mathcal{V}}{r}\frac{\partial \mathcal{U}}{\partial \theta} + w\frac{\partial \mathcal{U}}{\partial z} - \frac{\mathcal{V}^2}{r} - f\mathcal{V} = -\frac{1}{\rho_0}\frac{\partial p}{\partial r} - R\mathcal{U} \tag{2.29a}$$

$$\frac{\partial \mathcal{V}}{\partial t} + \mathcal{U}\frac{\partial \mathcal{V}}{\partial r} + \frac{\mathcal{V}}{r}\frac{\partial \mathcal{V}}{\partial \theta} + w\frac{\partial \mathcal{V}}{\partial z} + \frac{\mathcal{U}\mathcal{V}}{r} + f\mathcal{U} = -\frac{1}{r\rho_0}\frac{\partial p}{\partial \theta} - R\mathcal{V} \tag{2.29b}$$

$$0 = -\frac{\partial p}{\partial z} - \rho g \tag{2.29c}$$

$$\frac{1}{r}\frac{\partial (r\mathcal{U})}{\partial r} + \frac{1}{r}\frac{\partial \mathcal{V}}{\partial \theta} + \frac{\partial w}{\partial z} = 0, \tag{2.29d}$$

where $\mathcal{U}$ is the radial velocity in the r-direction and $\mathcal{V}$ is the azimuthal velocity in the θ-direction. The energy equation is unimportant due to the constant density.

These equations are simplified for problems with a flat seabed using the same methods as in Section 2.2.1, with no gradients in the θ-direction and assuming negligible acceleration.

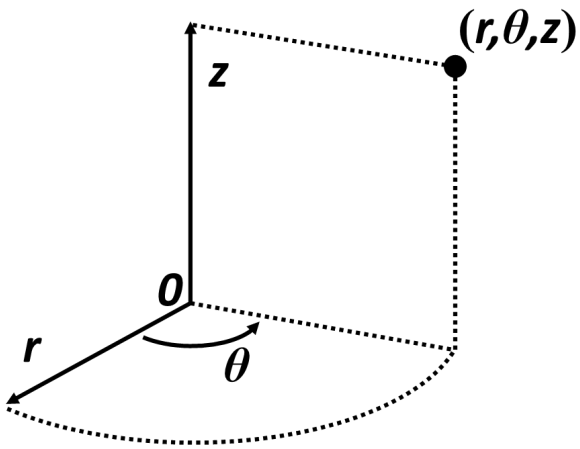

Figure 2.15: The notation used for the cylindrical coordinate system.

The resulting equations look very similar to (2.9). The integral starts at ∞ rather than $-\infty$ and works backwards, as boundary conditions for h and u at $r = 0$ are unknown, and r is never negative in cylindrical polar coordinates. The resulting system which needs to be solved is

$$\mathcal{V}(r) = -\frac{f}{R}\mathcal{U}(r) \tag{2.30a}$$

$$\mathcal{U}(r) = \frac{1}{rh(r)}\int_{\infty}^{r} \xi w_b(\xi)\,\mathrm{d}\xi \tag{2.30b}$$

$$\frac{\partial h}{\partial r} = -\frac{(f^2 + R^2)\mathcal{U}(r)}{Rg} \tag{2.30c}$$

$$\frac{\partial w}{\partial z} = -\frac{1}{r}\frac{\partial (r\mathcal{U})}{\partial r}. \tag{2.30d}$$

The boundary conditions are similar to the Cartesian case:

$$w(r, h(r)) = \mathcal{U}\frac{\partial h}{\partial r} \tag{2.31}$$

$$w(r, 0) = w_b(r) \tag{2.32}$$

$$\mathcal{U} \to 0 \text{ and } h \to H \text{ as } r \to \infty. \tag{2.33}$$

2.7.2 The initial case study revisited

The flux functions which can be evaluated by this cylindrical system are limited to those with rotational symmetry, since gradients in the θ-direction are not being allowed. A simple example of such flux would be a single circular inflow in the centre and a surrounding ring of outflow, the cylindrical equivalent of the initial case study in Section 2.3. If the discharge is of radius ℓ with a constant upward velocity of w_u, then a surrounding area of

uniform downward flux up to a radius L has velocity

$$w_d = -\frac{\ell^2 w_u}{L^2 - \ell^2}. \tag{2.34}$$

The full flux function is then defined by

$$w_b = \begin{cases} w_u & \text{for } 0 \le r < \ell \\ w_d & \text{for } \ell \le r < L \\ 0 & \text{otherwise.} \end{cases} \tag{2.35}$$

Following the same procedure as in Section 2.3, solution begins by splitting the problem into three regions and using (2.30b) to obtain

$$\mathcal{U} = \begin{cases} \frac{w_u r}{2h(r)} & \text{for } 0 \le r < \ell \\ -\frac{w_u \ell^2 (r^2 - L^2)}{2rh(r)(L^2 - \ell^2)} & \text{for } \ell \le r < L \\ 0 & \text{otherwise.} \end{cases} \tag{2.36}$$

Next, solutions for h must be found. The easiest case is when $\mathcal{U} = 0$, where $h = H$. Then, for $r \in [\ell, L)$, substituting the appropriate part of (2.36) into (2.30c) yields

$$\begin{aligned} \frac{\partial h^2}{\partial r} &= -\frac{(f^2 + R^2) w_u \ell^2 (r^2 - L^2)}{Rgr(L^2 - \ell^2)} \\ \implies h^2 - h(L)^2 &= -\frac{(f^2 + R^2) w_u \ell^2}{Rg(L^2 - \ell^2)} \left[\frac{\xi^2}{2} - L^2 \ln(\xi) \right]_{\xi = L}^{\xi = r} \\ \implies \quad h^2 - H^2 &= \frac{(f^2 + R^2) w_u \ell^2}{2Rg(L^2 - \ell^2)} \left(r^2 - L^2 - 2L^2 \ln\left(\frac{r}{L}\right) \right). \end{aligned}$$

Similiarly, for $r \in [0, \ell)$,

$$\begin{aligned} \frac{\partial h^2}{\partial r} &= -\frac{(f^2 + R^2) w_u r}{Rg} \\ \implies h^2 - h(\ell)^2 &= -\frac{(f^2 + R^2) w_u}{Rg} \left[\frac{\xi^2}{2} \right]_{\xi = \ell}^{\xi = r} \\ \implies \qquad h^2 &= H^2 + \frac{(f^2 + R^2) w_u \ell^2}{2Rg(L^2 - \ell^2)} \left(\ell^2 - L^2 - 2L^2 \ln\left(\frac{\ell}{L}\right) \right) - \frac{(f^2 + R^2) w_u (r^2 - \ell^2)}{2Rg} \\ &= H^2 + \frac{(f^2 + R^2) w_u}{2Rg(L^2 - \ell^2)} \left(\ell^2 \left(\ell^2 - L^2 - 2L^2 \ln\left(\frac{\ell}{L}\right) \right) - (L^2 - \ell^2)(r^2 - \ell^2) \right) \\ &= H^2 - \frac{(f^2 + R^2) w_u}{2Rg(L^2 - \ell^2)} \left(2\ell^2 L^2 \ln\left(\frac{\ell}{L}\right) + r^2 (L^2 - \ell^2) \right) \end{aligned}$$

So,

$$h = \begin{cases} \sqrt{H^2 - \frac{(f^2+R^2)w_u}{2Rg(L^2-\ell^2)}\left(2\ell^2L^2\ln\left(\frac{\ell}{L}\right) + r^2(L^2-\ell^2)\right)} & \text{for } 0 < r < \ell \\ \sqrt{H^2 + \frac{(f^2+R^2)w_u\ell^2}{2Rg(L^2-\ell^2)}\left(r^2 - L^2 - 2L^2\ln\left(\frac{r}{L}\right)\right)} & \text{for } \ell < r < L \\ 0 & \text{otherwise.} \end{cases} \tag{2.37}$$

Finally, solutions for w are calculated. Where $r \geq L$, $\mathcal{U} = 0$. This implies that w is constant with respect to z, therefore equal to w_b which is 0 in this region. For $r \in [\ell, L)$,

$$\begin{aligned} (2.30\text{d}) \implies \frac{\partial w}{\partial z} &= \frac{1}{r}\frac{\partial}{\partial r}\left(\frac{w_u(r^2-L^2)\ell^2}{2(L^2-\ell^2)h(r)}\right) \\ &= \frac{w_u\ell^2}{2(L^2-\ell^2)r}\left(\frac{2rh - (r^2-L^2)\frac{1}{2h}\left(\frac{(f^2+R^2)w_u\ell^2}{2Rg(L^2-\ell^2)}(2r - \frac{2L^2}{r})\right)}{h^2}\right) \\ &= \frac{w_u\ell^2}{2(L^2-\ell^2)rh}\left(2r - \frac{(f^2+R^2)w_u\ell^2(r^2-L^2)^2}{2Rg(L^2-\ell^2)rh^2}\right) \\ &= \frac{1}{h}\left(\frac{w_u\ell^2}{(L^2-\ell^2)} - \frac{(f^2+R^2)\mathcal{U}^2}{Rg}\right) \\ \implies \quad w &= \frac{z}{h}\left(\frac{w_u\ell^2}{(L^2-\ell^2)} - \frac{(f^2+R^2)\mathcal{U}^2}{Rg}\right) + c(r), \end{aligned} \tag{2.38}$$

where, using the boundary condition (2.32),

$$c(r) = w_d. \tag{2.39}$$

Similarly, for $r \in [0, \ell)$,

$$\begin{aligned} (2.30\text{d}) \implies \frac{\partial w}{\partial z} &= -\frac{1}{r}\frac{\partial}{\partial r}\left(\frac{w_u r^2}{2h(r)}\right) \\ &= -\frac{w_u}{2r}\left(\frac{2rh - r^2\frac{1}{2h}\left(-r\frac{(f^2+R^2)w_u}{Rg}\right)}{h^2}\right) \\ &= -\frac{w_u}{2rh}\left(2r + \frac{(f^2+R^2)w_u r^3}{2Rgh^2}\right) \\ &= -\frac{1}{h}\left(w_u + \frac{(f^2+R^2)\mathcal{U}^2}{Rg}\right) \end{aligned}$$

So it can be can seen that the solution for all r is

$$w(r,z) = -\frac{z}{h(r)}\left(w_b(r) + \frac{(f^2+R^2)(\mathcal{U}(r))^2}{Rg}\right) + w_b(r). \tag{2.40}$$

Plotting the results (Figure 2.16) shows one half of the flow seen in the previous rectangular domains. This solution is valid for all θ, thus rotationally symmetric about the

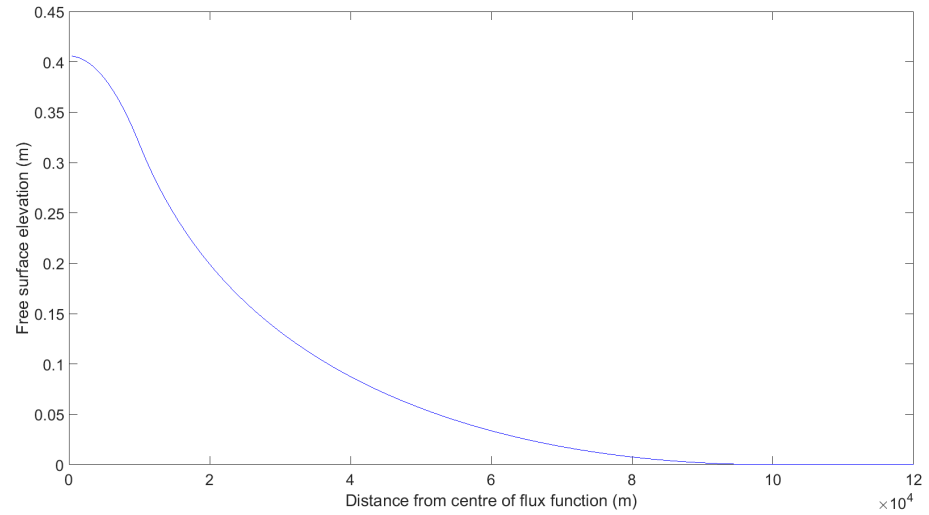

(a) Free surface elevation.

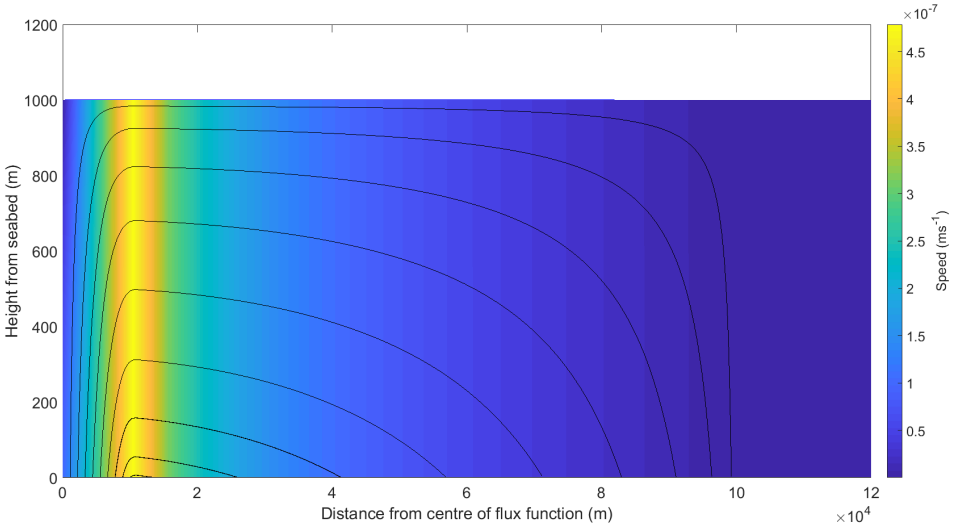

(b) Streamlines plotted over speed.

Figure 2.16: The circulation induced by a uniform inflow through the seabed with uniform outflow to either side, in a model using cylindrical coordinates.

z-axis. The shape of the flow is as before, showing that this is indeed just a shift in the coordinate system and not a dramatic change to the nature of the flows themselves.

2.7.3 The general solution with bathymetry in cylindrical coordinates

The bathymetry able to be investigated by this model is limited to that with rotational symmetry, as no variation is being allowed in the θ-direction. Similarly to the case of Cartesian coordinates, the seabed boundary condition changes to

$$w(r, b(r)) = \mathcal{U}\frac{\partial b}{\partial r} + w_b,$$

resulting in the slightly altered set of equations

$$\mathcal{V}(r) = -\frac{f}{R}\mathcal{U}(r) \tag{2.41a}$$

$$\mathcal{U}(r) = \frac{1}{rh(r)}\int_{\infty}^{r}\xi w_b(\xi)\,\mathrm{d}\xi \tag{2.41b}$$

$$\frac{\partial\eta}{\partial r} = -\frac{(f^2+R^2)\mathcal{U}(r)}{Rg} \tag{2.41c}$$

$$\frac{\partial w}{\partial z} = -\frac{1}{r}\frac{\partial(r\mathcal{U})}{\partial r}. \tag{2.41d}$$

Equations (2.41a) and (2.41b) are already in suitable forms, leaving only the general solutions of h and w to be found. As usual, the starting point is a substitution of (2.41b) into (2.41c):

$$\begin{aligned}
& h\frac{\partial(h+b)}{\partial r} = -\frac{(f^2+R^2)}{Rgr}\int_{\infty}^{r}\xi w_b(\xi)\,\mathrm{d}\xi \\
\implies \quad & \frac{1}{2}\frac{\partial h^2}{\partial r} = -\frac{(f^2+R^2)}{Rgr}\int_{\infty}^{r}\xi w_b(\xi)\,\mathrm{d}\xi - h\frac{\partial b}{\partial r} \\
\implies \quad & h^2 - H^2 = -2\int_{\infty}^{r}\left(\frac{(f^2+R^2)}{Rgr}\int_{\infty}^{\zeta}\xi w_b(\xi)\,\mathrm{d}\xi + (H-b(\zeta))\frac{\partial b}{\partial\zeta}\right)\mathrm{d}\zeta \\
\implies \quad & h(r) = \sqrt{H^2 - \frac{2(f^2+R^2)}{Rg}\int_{\infty}^{r}\frac{1}{\zeta}\left(\int_{\infty}^{\zeta}\xi w_b(\xi)\,\mathrm{d}\xi\right)\mathrm{d}\zeta - 2\left(Hb(r) - \frac{b(r)^2}{2}\right)},
\end{aligned} \tag{2.42}$$

where the approximation $h = (H - b)$ has been used on the right hand side to linearise the problem, as in Section 2.6.

Next, (2.41d) is used to work out a solution for w:

$$\begin{aligned}
\frac{\partial w}{\partial z} &= -\frac{1}{r}\frac{\partial}{\partial x}\left(\frac{1}{h}\int_{\infty}^{r}\xi w_b(\xi)\,\mathrm{d}\xi\right) \\
&= -\frac{1}{r}\left(\frac{rw_bh - \left(\int_{\infty}^{r}\xi w_b(\xi)\,\mathrm{d}\xi\right)\frac{1}{2h}\left(-2\left(\frac{(f^2+R^2)}{Rgr}\int_{\infty}^{r}\xi w_b(\xi)\,\mathrm{d}\xi + (H-b)\frac{\partial b}{\partial r}\right)\right)}{h^2}\right) \\
&= -\frac{1}{rh}\left(rw_b + \frac{(f^2+R^2)}{Rgrh^2}\left(\int_{\infty}^{r}\xi w_b(\xi)\,\mathrm{d}\xi\right)^2 + \frac{(H-b)\int_{\infty}^{r}\xi w_b(\xi)\,\mathrm{d}\xi}{h^2}\frac{\partial b}{\partial r}\right) \\
&= -\frac{1}{h}\left(w_b + \frac{(f^2+R^2)\mathcal{U}^2}{Rg} + \frac{(H-b)\mathcal{U}}{h}\frac{\partial b}{\partial r}\right).
\end{aligned}$$

Using this,

$$w - \left(\mathcal{U}\frac{\partial b}{\partial r} + w_b\right) = -\frac{(z-b)}{h}\left(w_b + \frac{(f^2+R^2)\mathcal{U}^2}{Rg} + \frac{(H-b)\mathcal{U}}{h}\frac{\partial b}{\partial r}\right)$$

$$\implies w(r,z) = w_b(r) + \mathcal{U}\frac{\partial b}{\partial r} - \frac{(z-b(r))}{h(r)}\left(w_b(r) + \frac{(f^2+R^2)(\mathcal{U}(r))^2}{Rg} + \frac{(H-b(r))\mathcal{U}(r)}{h(r)}\frac{\partial b}{\partial r}\right). \tag{2.43}$$

These general solutions have been written into a Matlab script (see Appendix A.3), and can be used to investigate any axisymmetric problems. This will be useful later in a comparison test with a numerical model using a cylindrical domain.

2.8 Alternate approach: an Ekman layer model

2.8.1 The Ekman layer equations

An alternative way of formulating problems with a flow through the seabed is to use a model with an Ekman layer. The Ekman layer lies directly above the seabed, and is a region in which frictional forces cause the horizontal velocities to approach zero near the bottom of the ocean. This approach is rather different than that previously taken. The ocean above the Ekman layer is considered to be homogeneous and infinitely deep, so there is no free surface. The equations include eddy viscosity terms, taken as constant for simplicity, since a Rayleigh friction approximation is not being used. The flow in the upper ocean, known as the interior flow, is vertically uniform and described by velocities $\bar{u}(x,y)$, $\bar{v}(x,y)$ and $\bar{w}(x,y)$. The flow in the Ekman layer will have boundary conditions relating to the interior flow.

The steady state flow is described by a reduced form of (2.1):

$$-fv = -\frac{1}{\rho_0}\frac{\partial p}{\partial x} + \nu_E\frac{\partial^2 u}{\partial z^2} \tag{2.44a}$$

$$fu = -\frac{1}{\rho_0}\frac{\partial p}{\partial y} + \nu_E\frac{\partial^2 v}{\partial z^2} \tag{2.44b}$$

$$0 = -\frac{1}{\rho_0}\frac{\partial p}{\partial z} \tag{2.44c}$$

$$\frac{\partial u}{\partial x} + \frac{\partial v}{\partial y} + \frac{\partial w}{\partial z} = 0. \tag{2.44d}$$

First, the horizonatal velocities are calculated. This procedure is standard and can be found in textbooks (eg. Cushman-Roisin and Beckers, 2011). The seabed under consideration is flat, for which the boundary conditions are

$$u(x,y,0) = 0, \qquad v(x,y,0) = 0. \tag{2.45a}$$

$$\text{as } z \to \infty, \qquad u \to \bar{u}, \qquad v \to \bar{v}. \tag{2.45b}$$

In the interior flow, the motion is described by the equations

$$-f\bar{v} = -\frac{1}{\rho_0}\frac{\partial p}{\partial x} \tag{2.46a}$$

$$f\bar{u} = -\frac{1}{\rho_0}\frac{\partial p}{\partial y}. \tag{2.46b}$$

Since (2.44c) tells us that the dynamic pressure $p(x, y)$ is independent of depth, a substitution of (2.46) allows (2.44a) and (2.44b) to be rewritten as

$$-f(v - \bar{v}) = \nu_E \frac{\partial^2 u}{\partial z^2} \tag{2.47a}$$

$$f(u - \bar{u}) = \nu_E \frac{\partial^2 v}{\partial z^2}, \tag{2.47b}$$

for which the solution satisfying the boundary conditions (2.45a) and (2.45b) is

$$u = \bar{u}\left(1 - e^{-z/d}\cos\left(\frac{z}{d}\right)\right) - \bar{v}e^{-z/d}\sin\left(\frac{z}{d}\right) \tag{2.48a}$$

$$v = \bar{u}e^{-z/d}\sin\left(\frac{z}{d}\right) + \bar{v}\left(1 - e^{-z/d}\cos\left(\frac{z}{d}\right)\right), \tag{2.48b}$$

where the Ekman depth d has the value $\sqrt{\frac{2\nu_E}{f}}$.

At this point, the model differs from standard Ekman layer problems. Rather than treating the seabed as a completely solid boundary, the model needs to include flow through the seabed and thus has non-zero vertical velocities. The boundary conditions on vertical velocity are

$$w \to \bar{w} \quad \text{as} \quad z \to \infty \tag{2.49a}$$

$$w(x, y, 0) = w_b(x, y). \tag{2.49b}$$

A solution for w is found using (2.44d).

$$\begin{aligned}
\frac{\partial w}{\partial z} &= -\left(\frac{\partial u}{\partial x} + \frac{\partial v}{\partial y}\right) \\
&= -\left(\left(\frac{\partial \bar{u}}{\partial x} + \frac{\partial \bar{v}}{\partial y}\right)\left(1 - e^{-z/d}\cos\left(\frac{z}{d}\right)\right) + \left(\frac{\partial \bar{u}}{\partial y} - \frac{\partial \bar{v}}{\partial x}\right)e^{-z/d}\sin\left(\frac{z}{d}\right)\right) \\
&= -\left(\frac{\partial \bar{u}}{\partial y} - \frac{\partial \bar{v}}{\partial x}\right)e^{-z/d}\sin\left(\frac{z}{d}\right),
\end{aligned} \tag{2.50}$$

since the interior flow is geostrophic with constant f, and therefore non-divergent. Integrating over depth between 0 and ∞ produces

$$\bar{w} - w_b = -\frac{d}{2}\left(\frac{\partial \bar{u}}{\partial y} - \frac{\partial \bar{v}}{\partial x}\right)$$

$$\implies \left(\frac{\partial \bar{u}}{\partial y} - \frac{\partial \bar{v}}{\partial x}\right) = -\frac{2(\bar{w} - w_b)}{d}. \tag{2.51}$$

Substituting this back into (2.50), an integration is then used to find an expression for w at any depth:

$$\begin{aligned}
\int_0^z \frac{\partial w(\xi)}{\partial \xi}\,\mathrm{d}\xi &= \int_0^z \frac{2}{d}(\bar{w}(x,y) - w_b(x,y))e^{-\xi/d}\sin\left(\frac{\xi}{d}\right)\,\mathrm{d}\xi \\
\implies \qquad w - w_b &= \frac{2}{d}(\bar{w} - w_b)\left(\frac{d}{2}\left(1 - e^{-z/d}\left(\sin\frac{z}{d} + \cos\frac{z}{d}\right)\right)\right) \\
\implies \qquad w &= (\bar{w} - w_b)\left(1 - e^{-z/d}\left(\sin\frac{z}{d} + \cos\frac{z}{d}\right)\right) + w_b. \qquad (2.52)
\end{aligned}$$

For the sake of simplicity and the ability to visualise in plots and compare with previous results, the functions w_b, $\bar{u}$, $\bar{v}$ and $\bar{w}$ will not vary in the y-direction, thus there will be no variablility in this direction in the solutions either. Taking this into account, and rearranged slightly, the full solutions for the Ekman layer flow are:

$$u(x,z) = \bar{u}(x) - e^{-z/d}\left(\bar{u}\cos\left(\frac{z}{d}\right) + \bar{v}(x)\sin\left(\frac{z}{d}\right)\right) \tag{2.53a}$$

$$v(x,z) = \bar{v}(x) + e^{-z/d}\left(\bar{u}\sin\left(\frac{z}{d}\right) - \bar{v}(x)\cos\left(\frac{z}{d}\right)\right) \tag{2.53b}$$

$$w(x,z) = \bar{w}(x) + e^{-z/d}(w_b(x) - \bar{w}(x))\left(\sin\left(\frac{z}{d}\right) + \cos\left(\frac{z}{d}\right)\right). \tag{2.53c}$$

I have written a script in Matlab which calculates results and produces figures for the Ekman layer flow described by these solutions, presented in Appendix A.4. Only two of the interior flow velocities are prescribed, and the third is calculated to ensure that (2.51) is true.

2.8.2 Results

The simplest case involves prescribing a static interior flow for the x-z plane, $\bar{u} = \bar{w} = 0$. This ensures that the interior flow will not cause changes in the plane being observed, and is the case most directly comparable to the Rayleigh friction model. Results from this experiment are shown in Figure 2.17.

The overall shape of the flow near the seabed is the same as before, with an overturning circulation moving water upwards from the centre, out to the sides and back down to the region of outflow. Without a free surface to restrict the height of the flow, it is instead determined by the tendancy of the solutions towards the prescribed interior flow away from the seabed. The Ekman depth d (or perhaps more accurately an Ekman height in this instance) is shown as a dotted line on Figure 2.17a. The circulation induced by the

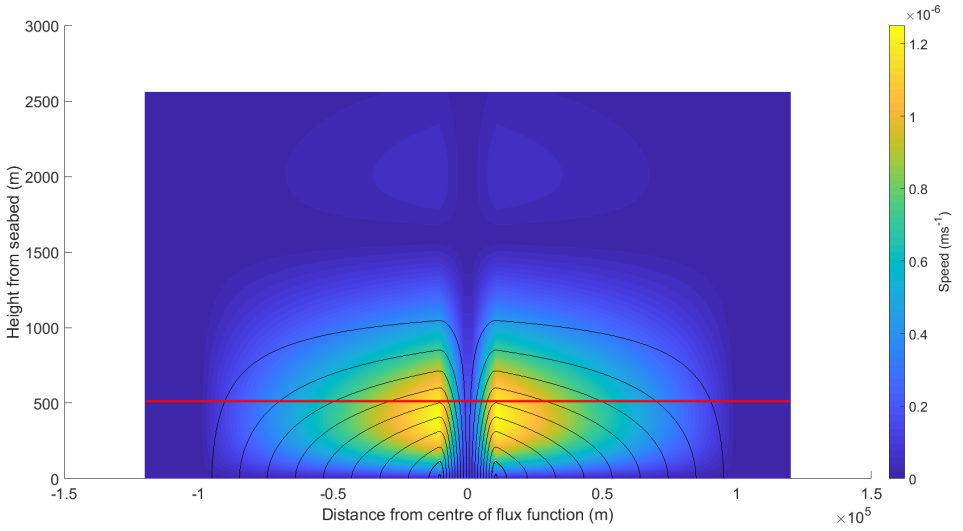

(a) Streamlines plotted over speed.

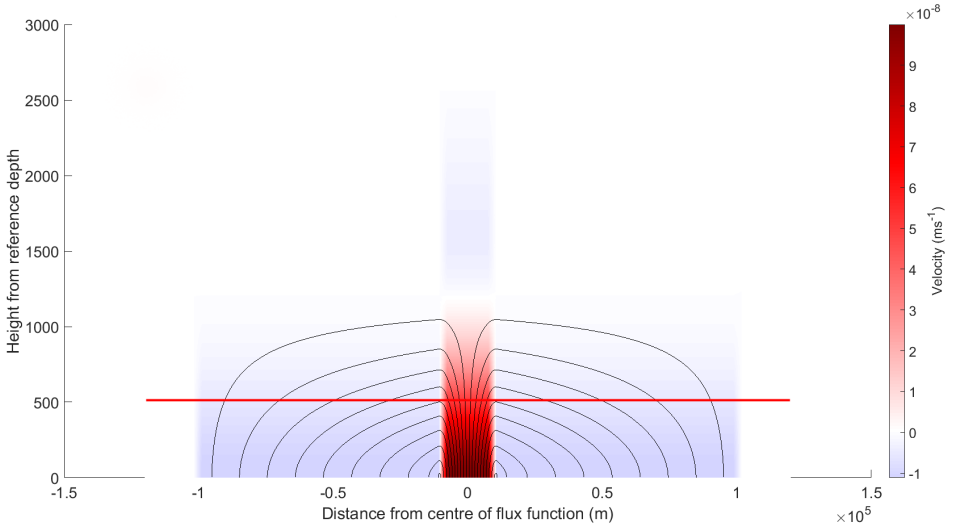

(b) Streamlines plotted over vertical velocity (w).

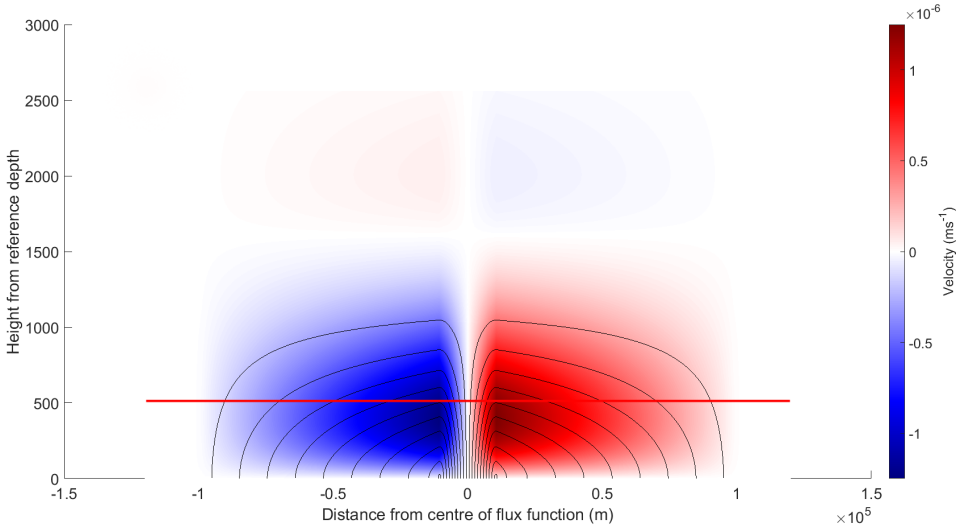

(c) Streamlines plotted over horizontal velocity (u).

Figure 2.17: The circulation induced by a uniform inflow through the seabed with uniform outflow to either side, in an Ekman layer model. The Ekman depth is marked with a red line.

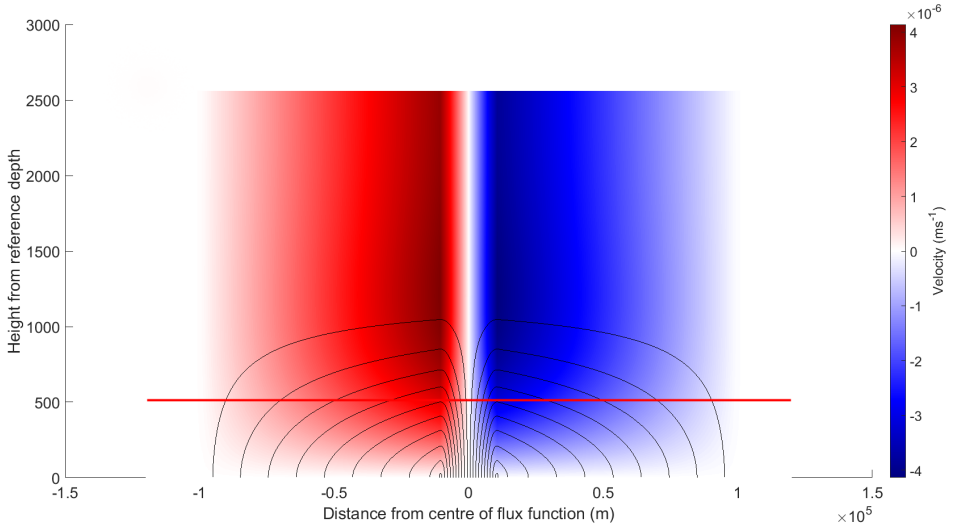

(d) Streamlines plotted over horizontal velocity (v).

Figure 2.17: Continued from opposite page.

flow through the seabed penetrates the water column to about twice this height.

Looking at the velocity fields, it can be seen that the horizontal velocities are no longer vertically uniform. The nature of the Ekman layer equations is to take away this effect seen previously. The u-velocity is at its highest just below the Ekman depth, carrying water outwards from the centre of the circulation. Above this, it starts to decay down to zero, as prescribed for the interior flow. It is much lower towards the seabed also, as friction takes effect. The v-velocity varies from zero at the seabed, to the value of the interior velocity $\bar{v}$ which was calculated by the script using the prescribed values of the other two components of the interior flow. Above the point at which it reaches this value, it does not vary in the vertical.

An interesting feature of these Ekman layer solutions is that the flow does not stop with the single familiar fountain shape. The presence of flow through the seabed causes a series of ever-weaker gyres above the main overturning circulation. They alternate in direction, so the signals of the first layer can be seen in Figure 2.17, acting in the opposite direction to the larger flow at the seabed. It is particularly evident in the vertical velocity, where a column of downward motion can be seen directly above the upward flow from the centre of the seabed. This alternating pattern, with decaying magnitudes in the velocities, makes sense when looking at the equations (2.53), which show the velocities being governed by an exponential decay multiplied by sinusoidal functions in the z-direction.

The effect on the ocean above the main circulation can be seen more clearly when a non-zero interior flow is prescribed. Figure 2.18a shows the streamlines for a circulation in which $\bar{u} = 10^{-7}\,\mathrm{ms}^{-1}$. The streamlines from the left hand side would be flat with no flow

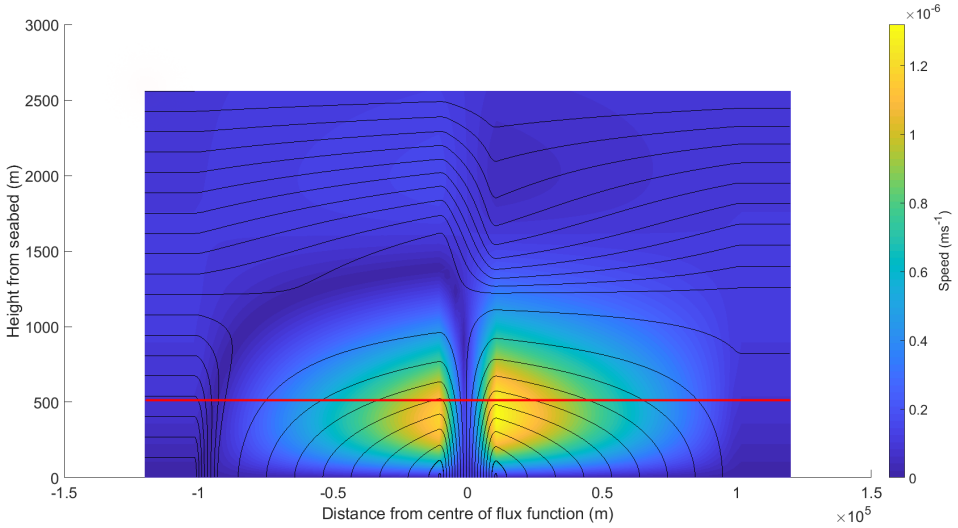

(a) $\bar{u} = 10^{-7}\,\mathrm{ms}^{-1}$.

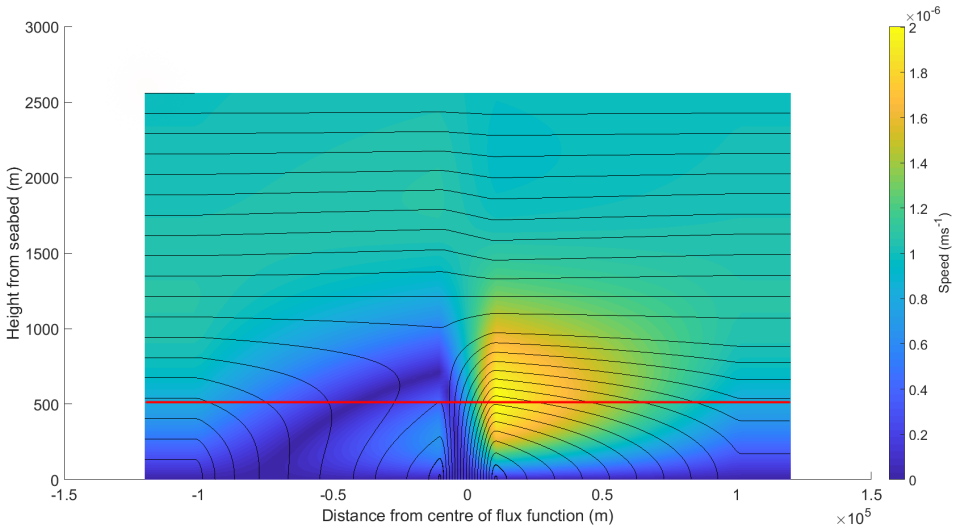

(b) $\bar{u} = 10^{-6}\,\mathrm{ms}^{-1}$.

Figure 2.18: The circulation induced by a uniform inflow through the seabed with uniform outflow to either side, in an Ekman layer model with non-zero $\bar{u}$. The Ekman depth is marked with a red line.

through the seabed. As expected, they curve downwards abruptly when they reach the area of outflow when at the same height as the fountain-shaped circulation. However, the lines above the main overturning circulation do not follow a straight path, but are distorted by upwards velocity above the recharge regions, and a stronger downwards velocity over the discharge region. This is the reverse of the flow function w_b. It can also be seen that the most central streamline reaches a higher point than the others and is caught up in the interior flow, resulting in some of the discharged water not flowing back into the seabed. Volume conservation is ensured, however, by the water flowing in from the left. The chosen velocity for the interior flow is equal to that of the inflow through the centre of the seabed. Choosing higher velocities will allow the interior flow to follow a flatter horizontal path and instead cause more distortion to the fountain flow, as in Figure 2.18b,

where $\bar{u}$ is an order of magnitude larger.

The results seen here, of a decaying pattern propagating through the water column, are reminiscent of processes seen in surface Ekman layers. In particular Ekman spirals, first theorised in Ekman et al. (1905), are structures driven by surface winds in which the velocity changes direction with depth, and becomes weaker as the spiral proagates further down from the surface. The structures seen in the results of this chapter are almost an inverted version of this, with the decaying u-velocity signal alternating between positive and negative as it gets further from the seabed.

2.9 Conclusions

The aim of this chapter was to take a first look at the inclusion of volume fluxes through the seabed in circulation models. Since this process has not been investigated previously in a modelling context, it was important to see how such fluxes might affect the circulation independently of other factors such as temperature. In all of the results contained within this chapter, a simple fact is seen. Namely, that volume fluxes through the seabed can drive a circulation which influences the entire water column. The specifics of that flow are determined by the nature of the flow through the seabed, specifically its magnitude and the distribution of velocities.

The circulations created are not small, or especially localised. While the circulations tend not to have influence in regions beyond where flows through the seabed are present, their vertical propagation is limited only by the top of the model layer. Where there is a free surface above, variations in the flow function or in the bathymetry can be identified by their signature on the surface. As I have only investigated single-layer models, it has not been seen whether evidence of influence from hydrothermal flows would be seen in the upper regions of a layered model. I believe this would be an interesting question to be tested by further analytical modelling. In the case of the Ekman layer with an infinite water column above, the effects of the seabed flow extend a long way beyond the top of the inital overturning circulation which feeds back to the sea floor. The signature of alternating gyres, decaying in magnitude, propagates far up into the model domain.

In the previous section I mentioned a similarity with the Ekman spiral. The Ekman layer solutions are not alone in evoking comparison to other physical processes in the ocean. The fountain-shaped circulations induced by vertical velocity through the seabed are similar in shape to an inverted version of turbulent convection as presented in a sketch in Zikanov et al. (2002), driven by heat and buoyancy fluxes at the surface.

This chapter has shown that volume fluxes through the seabed are not only a fascinating process on their own, but also cause circulations which could well make an important contribution within a more complex model. In the next chapter, coupled with heating, such fluxes will be used to represent hydrothermal flow in idealised modelling experiments.

Chapter 3

Investigating the differing effects of conductive and advective heat fluxes through the ocean floor

3.1 Introduction

Modelling the oceans is a large area of reasearch. There are several global circulation models used in the oceanographic community to investigate problems of many different kinds across the world, from the risks of flooding in the tropics to the effects of ice melting at the poles. In most applications geothermal heating is ignored, its impacts presumed to be negligible among other processes of greater magnitude. However, this is not necessarily a valid assumption, as has been demonstrated by previous modelling studies (outlined in Section 1.2). What the earlier studies did not look into was whether the nature of the heat flux matters. The addition of heat into the bottom of an ocean model by multiple methods (both conductive and hydrothermal) has not been previously investigated. Thus, the work presented in this chapter represents an original contribution to the field of ocean modelling.

In this chapter, I investigate the effects of adding heat into a simple system through both hydrothermal and conductive fluxes. These two physical systems of heat transfer will likely have differing effects on the abyssal ocean. Having examined the circulations which arise from volume fluxes alone, it is reasonable to assume that the flow of water into the bottom of the domain will cause noticeable differences to the circulation and hydrography of the deep ocean when compared to a conductive flux, while still supplying the same heat to the ocean since the temperature of hydrothermal discharges is typically higher than that of the surrounding abyssal water. Since temperature will now need to be added to the equations, they will no longer be linear or able to be solved using simple analytical

techniques. The calculations involved are more complex than those in the previous section, and therefore a numerical model is required.

Since this is the first study of its kind, I will investigate the geothermal processes in a highly idealised setting. This is done in order to isolate the effects of a change in the heat flux on the circulation, independent of other influencing factors, such as seasonal weather and tides, which would be present in a more realistic modelling scenario. The experiments carried out in this chapter are intended as a study of the processes themselves, not of their place in a full ocean model. It is a first look at the possibility of introducing hydrothermal flows into modelling and, importantly, an investigation of whether it is worth including as a process distinct from the conductive geothermal heating already employed in some models.

Some of the work featured in this chapter has been published in the journal *Ocean Modelling* (Barnes et al., 2018). The paper, entitled "Idealised modelling of ocean circulation driven by conductive and hydrothermal fluxes at the seabed", was published with open access and is freely available.

3.2 Model details and setup

3.2.1 NEMO: An ocean circulation model

For these experiments I make use of the global ocean circulation modelling framework NEMO (Nucleus for European Modelling of the Ocean). This is a widely-used model among the oceanographic community as it is extremely versatile, with module packages designed to model sea ice and biogeochemistry, and a nesting package allowing different regions to be modelled at different resolutions. For my purposes however, only the core ocean engine, known as OPA (Océan PArallélisé, French for "parallelised ocean"), is required.

The code which makes up NEMO is written in the Fortran programming language and has a modular structure, with different files controlling different aspects of ocean physics. When creating a configuration, the model can be instructed whether or not to read certain parts of the code by use of compiler flags. Each experiment within a compiled configuration also has its own control file, known as a namelist, which contains values for physical and technical properties of the model, options for switching between alternative model constraints and logical (true/false) variables which allow smaller sections of code within modules to be switched on or off.

The equations behind NEMO are similar to the primitive equations I started with previously (2.1), with the addition of temperature and salinity. Several common assumptions and approximations are applied:

- The Earth and all geopotential surfaces are assumed to be spherical, such that the gravity at any point is parallel to the line drawn from the centre of the Earth to that point. The average radius of the Earth is 6371 km, and the difference between the equatorial and polar radii is only 21 km. It is reasonable to use a constant radius and neglect the variation of less than one percent, in order to make the equations simpler and less computationally expensive.

- The depth of the ocean is neglected in comparison to the Earth's radius. This is known as the thin-shell approximation. Since the average ocean depth is around 3.7 km, with the deepest parts reaching 11 km, it is justifiable to neglect surface variation three orders of magnitude smaller than the radius when considering planetary-scale calculations.

- Turbulence fluxes, representing the effect that small-scale processes have on the larger scale, are expressed in terms of the large scale features. This means that the average effects of processes too small to be resolved properly in the model are seen. Closure is a common practice in modelling, as it avoids extra unknown variables entering the equations and rendering them unsolvable.

- The flow is assumed to be incompressible. This means that the volume of liquid does not change when the pressure changes. It is commonly used assumption when modelling incompressible fluids as it simplifies the calculations involved without losing much accuracy.

- Density differences are ignored except where they contribute to buoyancy (that is, where multiplied by g). This is called the Boussinesq approximation, and is another common method of improving modelling efficiency while introducing minimal error.

- The equation governing vertical momentum is reduced to a balance between buoyancy and the vertical pressure gradient. This removes convective processes, which are instead parameterised. This is the hydrostatic approximation introduced in Section 2.1.

A set of unit vectors $(\mathbf{i}, \mathbf{j}, \mathbf{k})$ is used in the x-,y- and z-directions with z being locally upward, parallel to the gravitational force. The vector velocity is $\mathbf{U} = \mathbf{U}_h + w\mathbf{k}$, with the subscript h denoting the horizontal vector on the (x, y) plane. As stated in the user

guide (Madec, 2008), the equations are

$$\frac{\partial \mathbf{U}_h}{\partial t} = -\left[(\nabla \times \mathbf{U}) \times \mathbf{U} + \frac{1}{2}\nabla(\mathbf{U}^2)\right]_h - f\mathbf{k} \times \mathbf{U}_h - \frac{1}{\rho_0}\nabla_h p + \mathbf{D}^{\mathbf{U}} + \mathbf{F}^{\mathbf{U}} \tag{3.1a}$$

$$\frac{\partial p}{\partial z} = -\rho g \tag{3.1b}$$

$$\nabla \cdot \mathbf{U} = 0 \tag{3.1c}$$

$$\frac{\partial T}{\partial t} = -\nabla \cdot (T\mathbf{U}) + D^T + F^T \tag{3.1d}$$

$$\frac{\partial S}{\partial t} = -\nabla \cdot (S\mathbf{U}) + D^S + F^S \tag{3.1e}$$

$$\rho = \rho(T, S, p), \tag{3.1f}$$

in which t is time, ρ is the density given by (3.1f), ρ_0 is a reference density, p is the pressure, f is the Coriolis acceleration, g is gravitational acceleration, T is the temperature and S is the salinity. $\mathbf{D}^{\mathbf{U}}$, D^T and D^S are paramaterisations of small-scale processes for momentum, temperature and salinity respectively, while $\mathbf{F}^{\mathbf{U}}$, F^T and F^S are surface forcing terms.

The numerical methods employed by the NEMO model are based on a centred second-order finite difference approximation. The spacial domain is split into a grid of three-dimensional cuboid cells, the dimensions of which are defined when setting up a configuration. The horizontal dimensions often relate to a geographic coordinate system, or a curvilinear grid, using lines of longitude and latitude to define the positions of cells in the x- and y-directions. At the centre of each grid cell are scalar points at which variables such as temperature, salinity, pressure and density are calculated. The vector points for u, v and w velocities are in the centre of each face of a grid cell. The Coriolis acceleration and vorticites are calculated on the centre of each edge. This structure is known as the Arakawa C-grid (Mesinger and Arakawa, 1976), and displayed in Figure 3.1.

3.2.2 Model configuration

The code used for my modelling work was built upon the existing "GYRE" configuration (Lévy et al., 2010), which is included when the model is installed as one of a few test cases to verify the consistency of code performance on a new system. This configuration consists of an angled rectangular domain designed to represent an idealised North Pacific or North Atlantic basin, but it is adaptable to new purposes when an idealised region is required.

In the case of my new configuration, modifications were made to allow the partitioning of

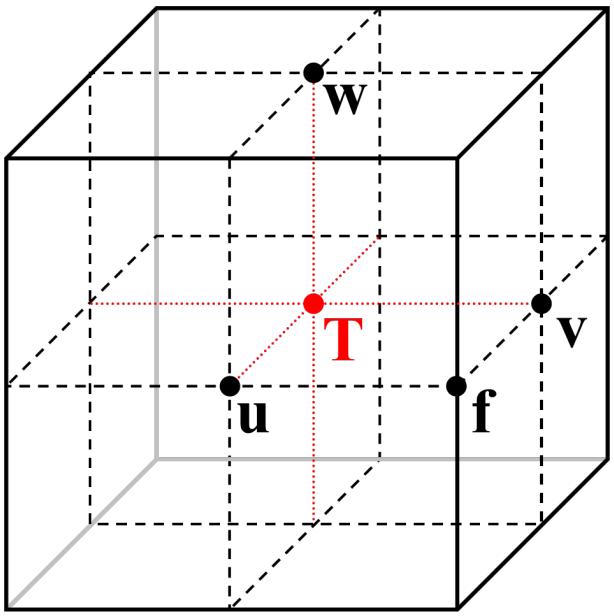

Figure 3.1: A grid cell with the variables located according to the Arakawa C-grid used in NEMO. The T point at the centre is where scalar variables such as temperature, salinity and density are calculated. The u, v and w points are for velocities, and the f point is for Coriolis acceleration and vorticities.

a geothermal heat flux between conductive and hydrothermal input at the seabed. Within the code a compiler flag, `key_geothermal`, was added and used to identify areas where modifications have been made. When this flag is activated, those sections of code will be read by the model compiler. Conversely, when the flag is removed and the configuration recompiled, any changes made using this flag will not be present. This is useful in order to isolate changes that have been made to the code so they can be found easily. It is also a good troubleshooting tool during development of a new configuration, and means that a full working version of the model can be reverted to in the case of problems arising.

The introduction of conductive fluxes through the seabed uses the existing paramaterisation of Emile-Geay and Madec (2009). This introduces a flux of heat in units of $\mathrm{W\,m^{-2}}$ to each grid cell at the seabed, and can be controlled by an input NetCDF file or by formulae written into the relevant module, `trabbc`, which controls the bottom boundary conditions. A namelist variable can be used to select the desired heat input condition.

Hydrothermal fluxes are formulated by prescribing a field of vertical velocities at the seabed, representing the net volume exchange per unit area between the oceanic crust and the abyssal ocean. These vertical velocities enter as a bottom boundary condition in the continuity equation, thus ensuring that volume is conserved, since NEMO uses the Boussinesq approximation. The advective flux of hydrothermal properties (e.g. temperature and salinity) across the ocean floor is calculated using an upstream transport approach. This means that waters flowing upwards from the crust into the ocean have

prescribed properties, while waters flowing downwards into the crust leave the ocean with the properties of the deepest oceanic model cell. The alterations required in the NEMO code to acheive this are detailed in Appendix B.2.

The configuration uses a TVD (Total Variance Dissipation) advection scheme that implements the method of Zalesak (1979). Lateral eddy diffusion and transport are parameterised through isopycnic Redi (Redi, 1982) and Gent-McWilliams (Gent and McWilliams, 1990) diffusion with uniform diffusivities of $30\,\mathrm{m^2\,s^{-1}}$ for both processes. In the vertical, this configuration uses a uniform diapycnal diffusivity of $1.2\times10^{-5}\,\mathrm{m^2\,s^{-1}}$ with the exception of areas where the water column becomes hydrostatically unstable, in which case the vertical diffusion is ramped up to $100\,\mathrm{m^2\,s^{-1}}$ in order to parameterise vertical convection. These options are all set in the namelist files for individual experiments, but were not altered between simulations.

3.3 Testing the volume flux

Since the addition of volume fluxes through the seabed did not previously exist in NEMO, the process had to be tested to ensure that the configuration was producing the correct physical responses to this new boundary condition. The first implementation of the new volume flux formulation was in a cylindrical basin, a simple pre-existing model domain to adapt for initial testing. An axisymmetric flow through a flat seabed was set up to be directly compared with results from analytical models. The basin is at a constant temperature, with the flow into the bottom at the same temperature to avoid thermal gradients, since the analytical models do not include any heat. The model was run for long enough to approach a steady state so as to resemble the analytical conditions as closely as possible. NEMO will never be able to exactly reproduce the analytical solutions as it uses a more complicated set of equations when computing results, but allowing the conditions to be as similar as possible helps to determine the robustness of the volume flux configuration.

The chosen flow through the seabed is an inflow with velocity $10^{-6}\,\mathrm{ms^{-1}}$ at the centre of the cylinder with a radius of 5 grid cells of the $\frac{1}{12}^\circ$ resolution grid. The outflow occurs in a ring between 25 and 30 grid cells radius, with a velocity calculated to ensure conservation of volume. The model has 62 vertical levels of equal thickness. Model parameters were chosen such that a comparison with the analytical model was both straight-forward and meaningful. The cylindrical basin in NEMO was given coordinates and dimensions roughly corresponding to the location and size of the Panama Basin, but for this simulation the Coriolis force was prescribed as a constant unaffected by latitude, calculated from 3°N as the reference latitide. The depth was set at 3500 m.

The prescribed parameters in the Matlab script were set up to match the NEMO simulation. With the full depth of 3500 m being unstratified and no further model layers above in the NEMO setup, full gravity at $9.81\,\mathrm{ms}^{-2}$ was used in the analytical model rather than the reduced gravity used in much of Chapter 2. During some initial test runs, the Rayleigh friction coefficient was tuned such that the sea surface height of the analytical model was equal to that of the NEMO experiment, as seen in Figure 3.2. The value decided upon for use in the comparison was $R = 3.9 \times 10^{-3}\,\mathrm{s}^{-1}$.

Results from NEMO experiments are in NetCDF format, but this can be imported into Matlab to produce comparable images as part of the data visualisation and analysis process. The model itself is not governed by equations in cylindrical coordinates, although the model domain created is a cylinder. So for the NEMO output, the radial velocity referred to in Figure 3.2 is in fact the u-velocity in a cross section at the x-coordinate of the centre of the cylindrical basin. In order to produce graphics which can be compared, the analytical results from Matlab were plotted along with their mirror images (or negative mirror image in the case of horizontal velocity).

Comparing the results of this NEMO simulation to the analytical model in cylindrical coordinates (Section 2.7) shows promising similarities. With the sea surface heights matched, the velocity fields show some consistency with the analytical results. The vertical velocity field has the same columns above the discharge and recharge areas, increasing in speed closer to the seabed with very similar velocities. The NEMO results show a downward flow directly to either side of the central inflow which does not appear in the analytical solution. This is linked to the radial velocity. The velocities themselves are similar, with a maximum of around 5×10^{-6} ms^{-1}, but the distribution is rather different. The NEMO model has a large amount of the horizontal movement from regions of inflow to outflow in the very bottom layer, along the seabed. This effect will likely be due to some of the smaller scale processes and extra complexities that the simplified equations of the analytical model do not account for, or due to the way the model layers interact. It could even be evidence of an Ekman layer forming within the model.

The sea surface elevation, although tuned in the analytical model to reach the same height, is not identical in both models. It has a slightly different structure in the NEMO results, with the perturbation at the centre being more confined to the area of vertical velocity input at the surface. The areas where outflow occurs at the seabed create a signal at the surface, where a dip in the elevation can be seen. The sea surface is generally less smooth in the NEMO output, presumably as a result of more complex processes which were not represented in the analytical model.

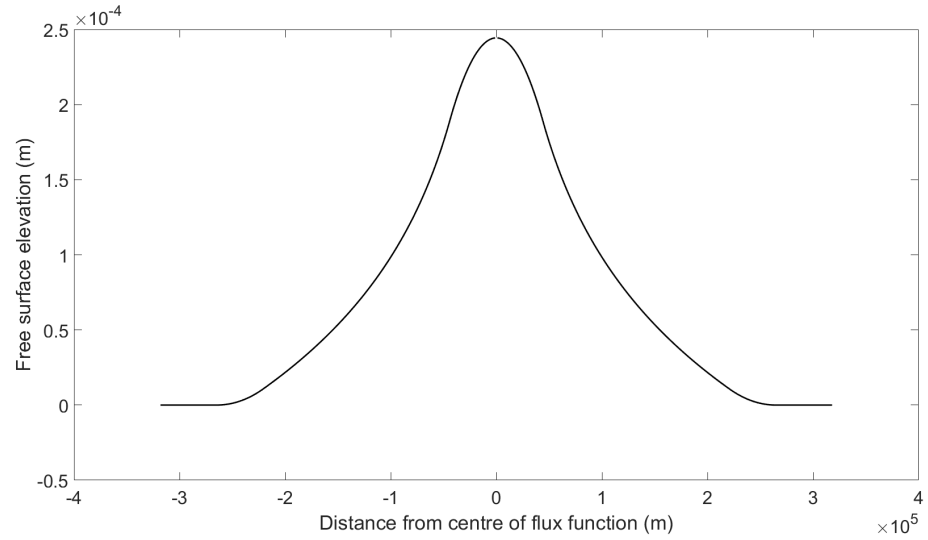

(a) Sea surface height (Matlab).

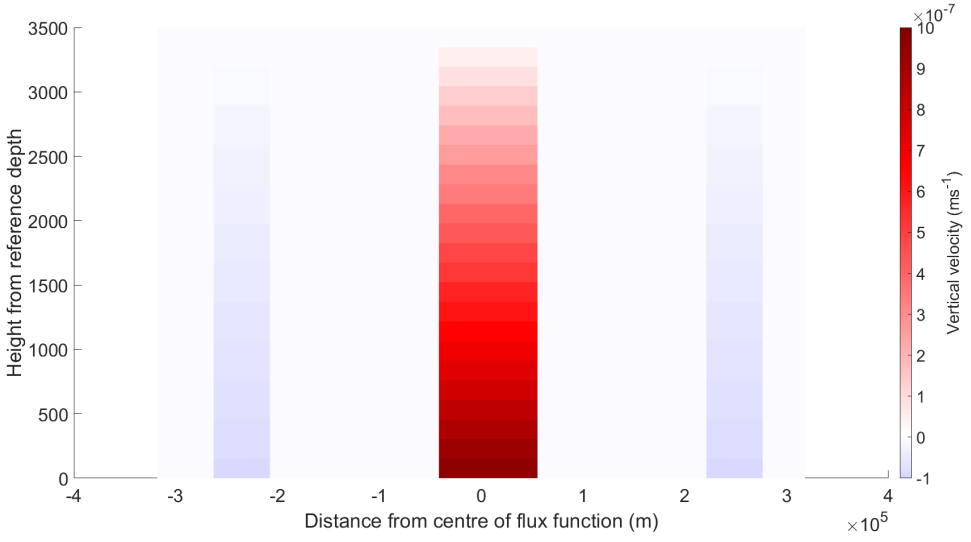

(b) Vertical velocity (Matlab).

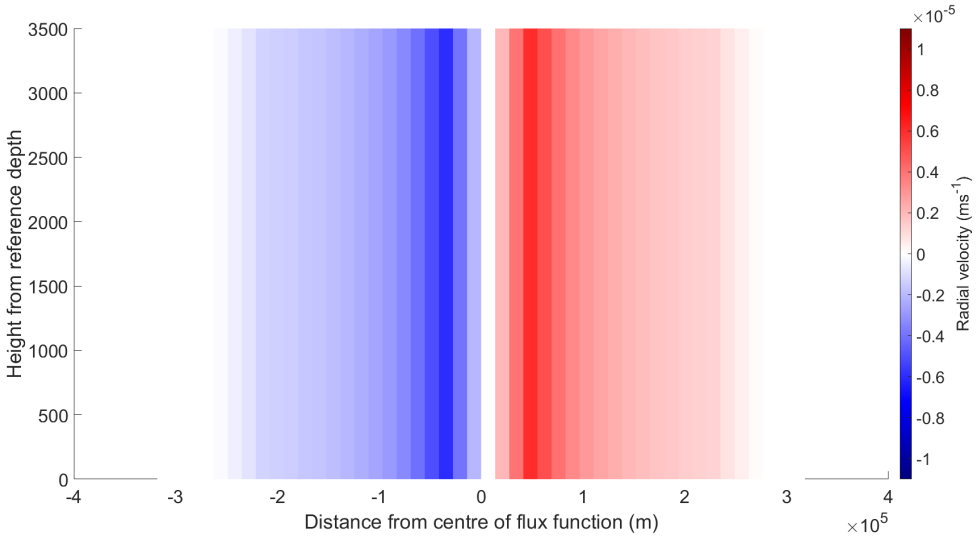

(c) Radial velocity (Matlab).

Figure 3.2: A comparison of circulations resulting from the analytical model in Matlab, and the configuration of NEMO with mass flux through the seabed.

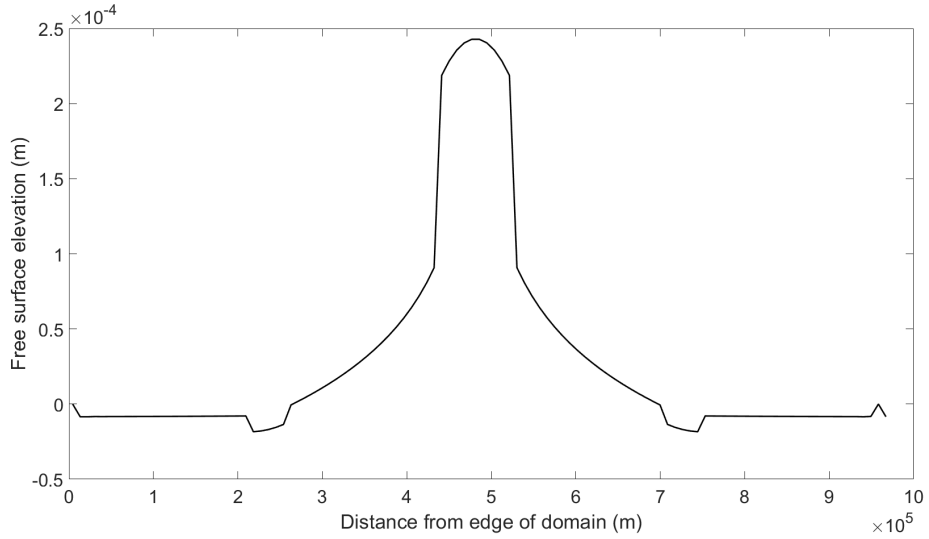

(d) Sea surface height (NEMO).

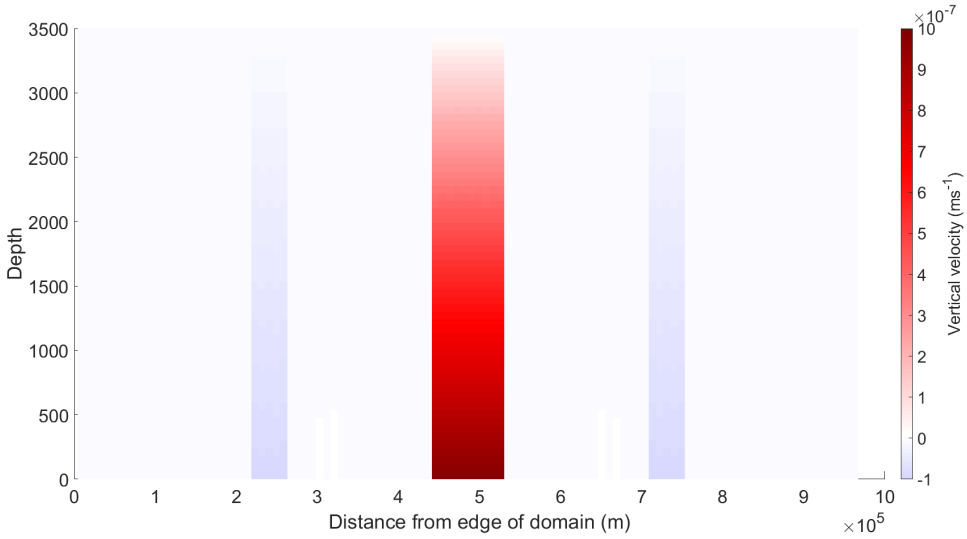

(e) Vertical velocity (NEMO).

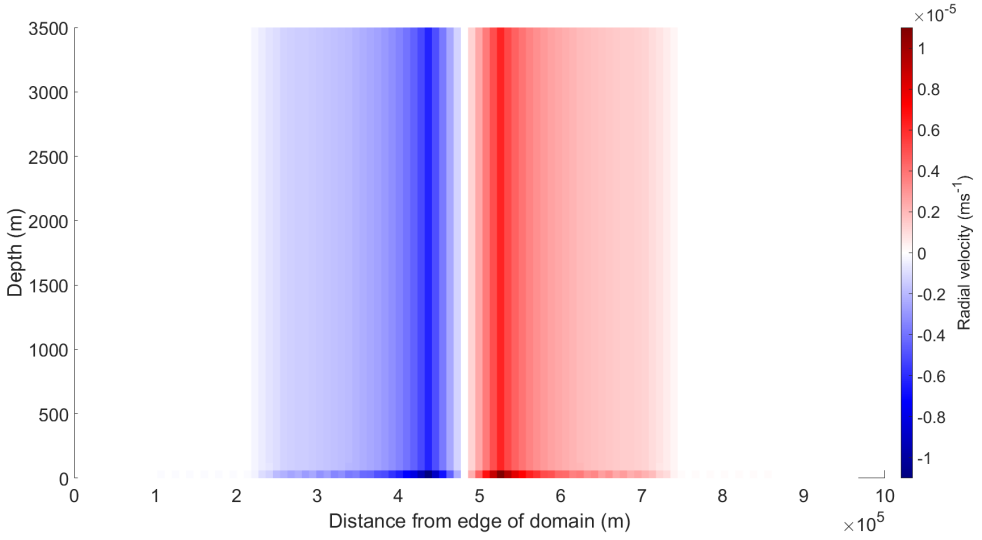

(f) Radial velocity (NEMO).

Figure 3.2: Continued from opposite page.

Evidently, NEMO produces results which, if not entirely identical, do share many features with those from the analytical model. It is reasonable to conclude that the volume flux configuration implemented in the numerical model operates correctly as indicated especially by the vertical velocity field, but that differences in the equations governing the systems cause disparities in the horizontal velocities.

3.4 The heat flux formulation

3.4.1 Mathematical formulation

A method of introducing heat fluxes must be designed to enable the two forms of geothermal heat input to be compared. The difficulty of hydrothermal heating is that there must be inflow and outflow, the distribution of which will dictate where water can flow through the seabed. In order to match the two heating methods as best as possible, it seems sensible to place the region of hydrothermal discharge in the same location as the conductive heat flux. Equal areas of recharge can be placed to either side of the discharge to preserve symmetry in the flux and avoid causing an imbalance in the system.

The model configuration will be set up so that heat is introduced into the ocean across an area of the seabed at the centre of the domain. The distribution of these heat fluxes will be controlled by analytical functions similar to those in Chapter 2. At either side are areas of hydrothermal recharge which allow water to flow out of the system at such a rate as to conserve the total volume, just as in the analytical models. An average total geothermal heat flux of G is applied over the length of the domain, L_G. This is partitioned into a conductive heat flux of C applied over a length ℓ_1, and a hydrothermal flux with a given temperature and discharge velocity. A hydrothermal discharge with temperature T_1 and average velocity v_1 is applied over ℓ_1. The recharge occurs over a length ℓ_2 (half at either side of the discharge) with temperature T_2 being equal to that of the bottom water as calculated by the model, averaged over the area of recharge, and with an average velocity $v_2 = -\frac{v_1 \ell_1}{\ell_2}$ in order to conserve volume. The heat fluxes H_1 and H_2 associated with the hydrothermal flows are $H_i = v_i T_i \rho c_p$, where ρ is a reference density and c_p is a specific heat capacity. The values used in this model configuration are $\rho = 1035\,\mathrm{kg\,m^{-3}}$ and $c_p = 4000\,\mathrm{J\,kg^{-1}K^{-1}}$. To continue the approximate portrayal of the Panama Basin, heating will take place over the width of a mid-ocean ridge. The length chosen is $\ell_1 = \frac{5}{4}^\circ$ (10 grid cells, approximately 139 km). A value of $\ell_2 = 5^\circ$ (40 grid cells, 555 km) is chosen, larger than ℓ_1 to ensure that the recharge velocity is less vigorous than the discharge.

In the following experiments the value of G is kept constant within each set of simulations. So the amount of heat entering the ocean is always the same, and thus the systems are

directly comparable. This heat input is partitioned between hydrothermal and conductive fluxes by use of the term $0 \leq \alpha_H \leq 1$, a measure of the proportion of the heat flux which is introduced hydrothermally. So when $\alpha_H = 0$, the heat flux is entirely conductive, and when $\alpha_H = 1$ it is entirely hydrothermal. Partitioning the heat flux in this way, and keeping α_H uniform for the entire length of the seabed, produces the relations

$$(1 - \alpha_H)GL_G = C\ell_1 \tag{3.2a}$$

$$\alpha_H GL_G = H_1\ell_1 + H_2\ell_2 \tag{3.2b}$$

for the conductive and hydrothermal heat fluxes respectively.

The hydrothermal heat flux is dependent on a product of the velocity and temperature of the water, which opens up options of how to specify it within the model. Inflowing fluxes must be prescribed in the model either by their temperature T_1 or their discharge velocity v_1 and then, to preserve the prescribed net heat flux, the unprescribed variable is calculated using either

$$v_1 = \frac{\alpha_H GL_G}{(T_1 - T_2)\ell_1 \rho c_p} \tag{3.3a}$$

$$\text{or} \quad T_1 = \frac{\alpha_H GL_G}{v_1 \ell_1 \rho c_p} + T_2. \tag{3.3b}$$

A sketch including these fluxes at the seabed of a model domain can be found in the next section (Figure 3.3).

3.4.2 Implementing the heat flux in NEMO

The heat flux formulation is introduced in two places within the model. Several formulations can been placed in the code to represent different flow functions w_b such as those seen in Chapter 2, and different distributions of conductive heating.

In the module `trabbc`, a new case is added to the options for the conductive geothermal heat flux of Emile-Geay and Madec (2009) which implements (3.2a) in the model analytically. Additionally, in the module `sbcana` which contains analytical surface boundary conditions, a new section is created to give options for hydrothermal fluxes, implementing (3.3a). In the existing model structure there is no module for advective bottom boundary conditions, since their inclusion has not been attempted previously, hence them being introduced in this module. The original segments of code written to achieve this can be found in Appendix B.3.

3.5 Initial experiments in a domain inspired by the Panama Basin

3.5.1 Setting up the model domain

Since the volume fluxes have now been tested and found to be operating correctly, the model can now be used to investigate the geothermal heat fluxes. Specifically, the differences to the circulation between using conductive and hydrothermal fluxes at the seabed. For the experiments in this section the model domain is a two-dimensional cross-section of a rectangular basin, achieved in a three-dimensional model by using cyclical boundary conditions to ensure no gradients in the x-direction. This means that anything exiting one end of the domain enters with the same value at the other end. There are only three cells in the x-direction, ensuring computational efficiency. Use of a two-dimensional domain prevents extra complexities in the model such as eddy formation, and allows simpler solutions in this first step towards understanding the effects of differing heat fluxes. The resolution is $\frac{1}{8}^\circ$ in the horizontal, with a constant grid cell width of 13.875 km, spanning the region from 1° S to 8° N in keeping with the location of the Panama Basin. A time step of 20 minutes is used.

The domain was designed to crudely represent some simple features of a North-South cross section through the Panama Basin. The initial stratification of these experiments is set according to temperature and salinity data from a hydrographic survey of the area taken from the World Ocean Atlas (Locarnini et al., 2013; Zweng et al., 2013), and data from the same source are used in a restoring condition. This means that in some areas the model is being constantly brought back towards a prescribed distribution of temperature and salinity. The restoring condition used is known as Newtonian damping, and involves an extra term in the temperature (3.1d) and salinity (3.1e) equations, such that

$$\frac{\partial T}{\partial t} = \cdots - \gamma(T - T_p) \tag{3.4a}$$

$$\frac{\partial S}{\partial t} = \cdots - \gamma(S - S_p), \tag{3.4b}$$

where T_p and S_p are the prescribed temperature and salinity fields, and γ is the damping coefficient, which is the inverse of a time scale. A larger value of γ represents a shorter time scale, meaning that with no other forcing the system would reach the prescribed field more quickly. At the south side of the domain the hydrography is restored with a time scale of one year to the World Ocean Atlas profile, over the three grid cells nearest to the edge of the domain with a linear progression from full strength at the edge to zero by the fourth grid cell in the domain. This damping represents the effects of the flow through the Ecuador Trench and over the saddle of the Carnegie Ridge from outside of the basin.

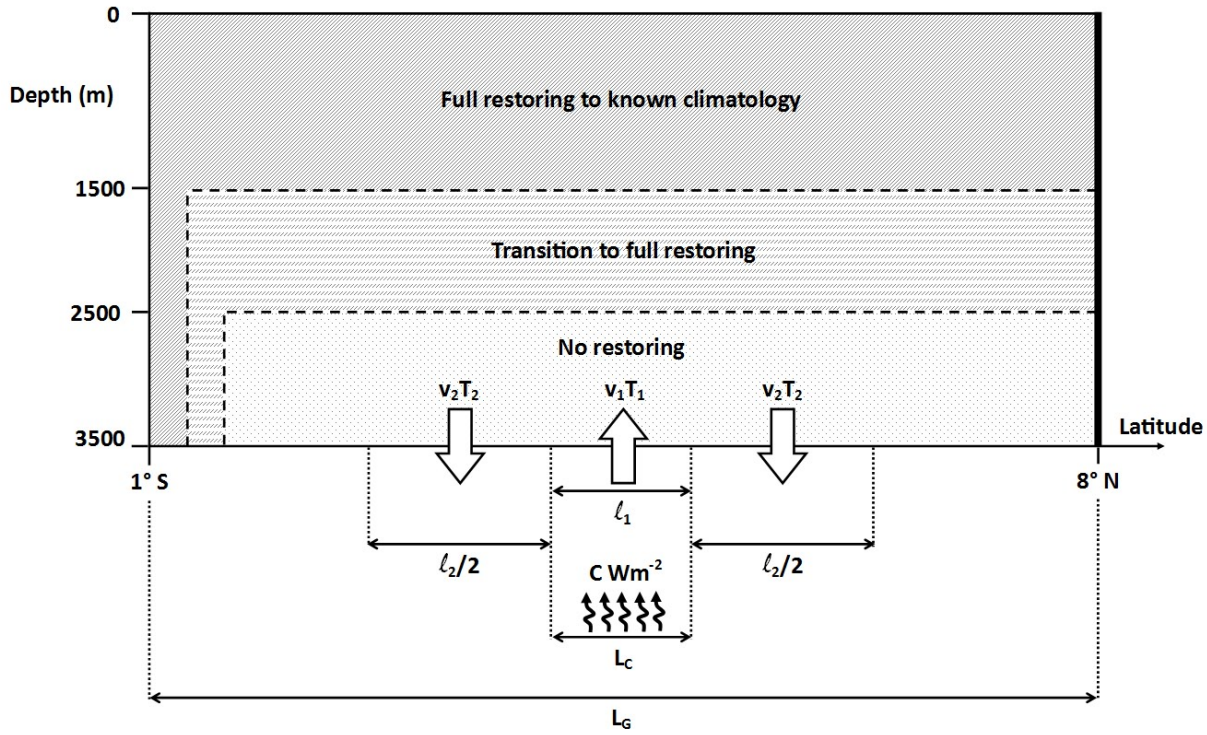

Figure 3.3: A sketch of the 2D model domain representing features of the Panama Basin, and the fluxes being applied through the seabed.

The north side of the model domain has a solid wall, representing the coastline of Central America.

Restoring is also used above 2500 m depth, with the strength of the restoration effect increasing linearly from zero to a time scale of one month at 2000 m, and remaining at that strength all the way to the surface. This represents the fact that the upper ocean is directly connected to the rest of the Pacific and thus affected by external processes. The deep ocean in the model domain is left unaffected by any restorative effects, so the changes in the abyss should be predominantly due to the prescribed geothermal fluxes. The original code segment written to control the restoring can be found in Appendix B.4. The restoring and heat fluxes affecting the model domain are shown in Figure 3.3.

3.5.2 Results

For this set of experiments, T_1 was chosen to be 2.3°C and G set at 0.101 Wm^{-2}, the global average geothermal heat flux according to Pollack et al. (1993). The heat was applied over a 5 grid cell distance either side of the centre of the domain, with the hydrothermal recharge area between 5 and 25 grid cells in each direction. The heat fluxes were applied uniformly over the regions of discharge and recharge. Five simulations were run for the values of $\alpha_H = 0$, 0.25, 0.5, 0.75, and 1, but the focus will be on results from the two extremes.

The stratification of the ocean is often looked at in terms of layers of density, which depend on temperature and salinity. In the case of these model results though, temperature is the variable focussed upon. In an incompressible fluid, as NEMO assumes, density is assumed to be linearly dependent on temperature and salinity according to the relationship, given in Cushman-Roisin and Beckers (2011),

$$\rho = \rho_0 \left((1 - \alpha(T - T_0) + \beta(S - S_0) \right), \tag{3.5}$$

where ρ_0, T_0 and S_0 are reference values of density, temperature and salinity, while α and β are known as the coefficients of thermal expansion and saline contraction. The values of α and β are typically of the same order. This means that the relative impact of temperature and salinity on the density stratification is largely down to the relative values of their differences. Using the initial temperature and salinity profiles used for restoring the model as the reference, the average value for $T - T_0$ is 0.536°C, while the average value for $S - S_0$ is -0.006 psu. This means that the effect of temperature on the density stratification is two orders of magnitude greater than that of salinity, which is why temperature is the variable being studied in the results.

The results show interesting differences between the experiments. The temperature fields shown in Figure 3.4 are similar in shape, but differ in important ways. At the north side of the domain the deep water has undergone more mixing, whereas a stronger stratification is maintained at the south side by the restoring. Both cases include a breakdown of stratification up to a depth of around 2400 m, above which the restoring takes effect and the initial stratification is not deviated from to any great extent. The effect of the restoring in the vertical is a very abrupt transition from near-vertical to horizontal thermoclines at about 2400 m depth. In the deep ocean, the circulation driven by hydrothermal fluxes is warmer on average, although there is a cone emanating from the centre in which the hydrothermal circulation is cooler than the conductively heated one. What this suggests is that the heated water is being moved away from the centre of the abyss more quickly in the hydrothermal case, either vertically into the upper ocean or sideways towards the areas of recharge. Much more heated water ends up near the seabed where the outflow is drawing water downwards.

Even with full strength restoring all the way up from 2000 m, the heat fluxes have different signatures at the sea surface. Figure 3.5 shows plots of the sea surface heights. The restoring down the side of the domain has an effect; both cases show a lower sea surface at the south side of the basin when compared to the north side. Above a conductive heat flux the surface follows a smooth curve, not dissimilar to those seen above some of the analytical flows in Chapter 2. In the hydrothermally driven circulation, there is a much higher

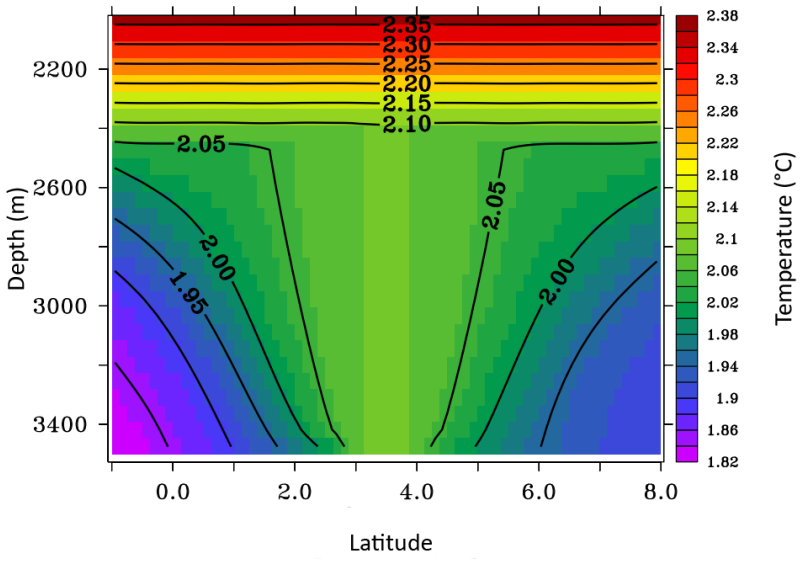

(a) Conductive

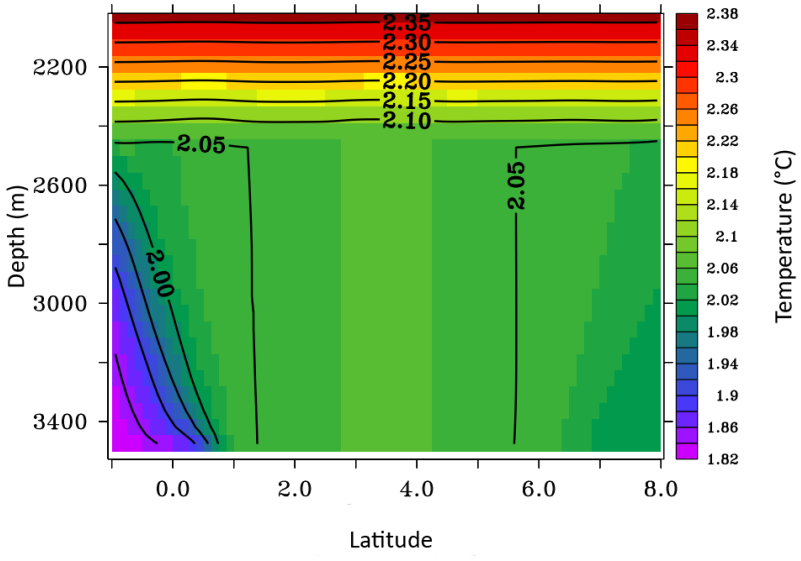

(b) Hydrothermal

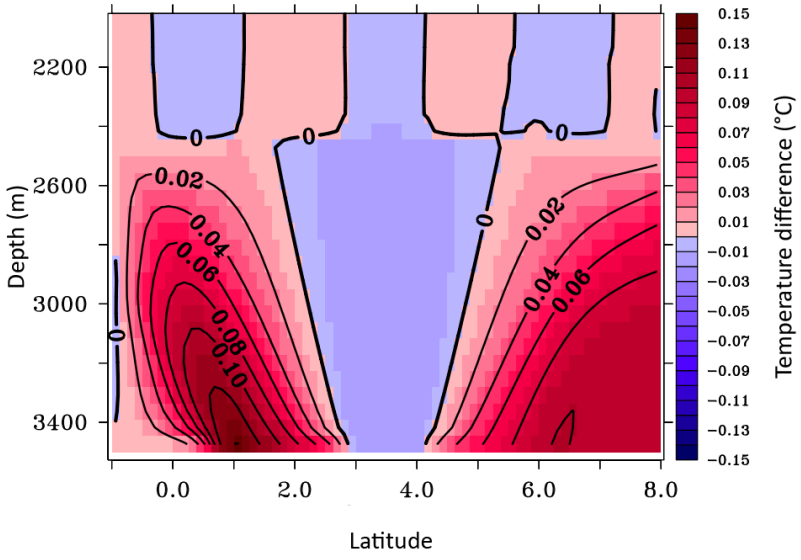

(c) Difference (hydrothermal - conductive)

Figure 3.4: A comparison of the temperature of the deep ocean below 2000 m, with fully conductive and fully hydrothermal fluxes.

perturbation above the region of inflow, indicating that the vertical advection caused by the discharge penetrates the entire height of the water column. To either side, the impact of the outflow is seen where the surface elevation changes suddenly. When looking at the difference between the two, it is clear that the hydrothermal boundary condition has a fairly significant impact at the surface. It causes a perturbation of 1.6 cm more than the conductive heating at the centre of the domain, a 98 % increase.

Varying α_H and ΔT allows a wide range of possibilities to be explored and produces some interesting observations in the average temperature of the deep ocean. Figure 3.6 shows the average abyssal temperatures for several experiments. Decreasing ΔT causes greater differences between the more hydrothermally-dominated systems (larger α_H) and the circulation driven by conduction (α_H=0). This is because a lower ΔT is balanced by a higher hydrothermal flow velocity. As the velocity of the inflow increases, the relationship between α_H and the temperature changes. The average abyssal temperature varies linearly with α_H at lower velocities, but as the inflow becomes faster the temperature difference between cases with higher values of α_H decreases. This suggests that there is an upper limit to the heating of the abyssal ocean in this configuration, and that the mechanisms removing heat from the abyss will act to prevent heating beyond this limit regardless of how the geothermal heat is introduced into the system.

Looking at the vertical velocities could have provided more insight into the distribution of heat. However, this is where a potential problem is encountered with this model configuration. The vertical velocities in both the conductive and hydrothermal cases have high magnitudes in very narrow strips above the edge of the inflow region. This must be connected to the boundary in the function introducing heat into the domain. Without heating in Section 3.3, the vertical velocity showed no such behaviour. This may be a result of hydrostatic instability created by the discontinuity in the step functions which describe the heat distribution. Plotting the velocities on a different scale to highlight slower motions (the bottom panels in Figure 3.7), the abrupt line between the abyss and the restored upper ocean is seen, as in the temperature field. A wider column of upwards velocity is seen in the hydrothermal case, and stronger velocities above the 2500 m depth. This is consistent with the idea that more of the heated water is being advected upwards from the centre of the abyssal ocean due to the advective boundary condition, and also that more warm water from above is downwelling to heat the abyssal ocean to either side. In the centre where the vertical velocity is largest, the water becomes hydrostatically unstable and the model employs enhanced vertical diffusivity and viscosity to parameterise vertical convection. This occurs across the entire central column between about 3°N and 4°N, spreading wider up until 2500 m where hydrostatic stability is restored by the Newtonian damping.

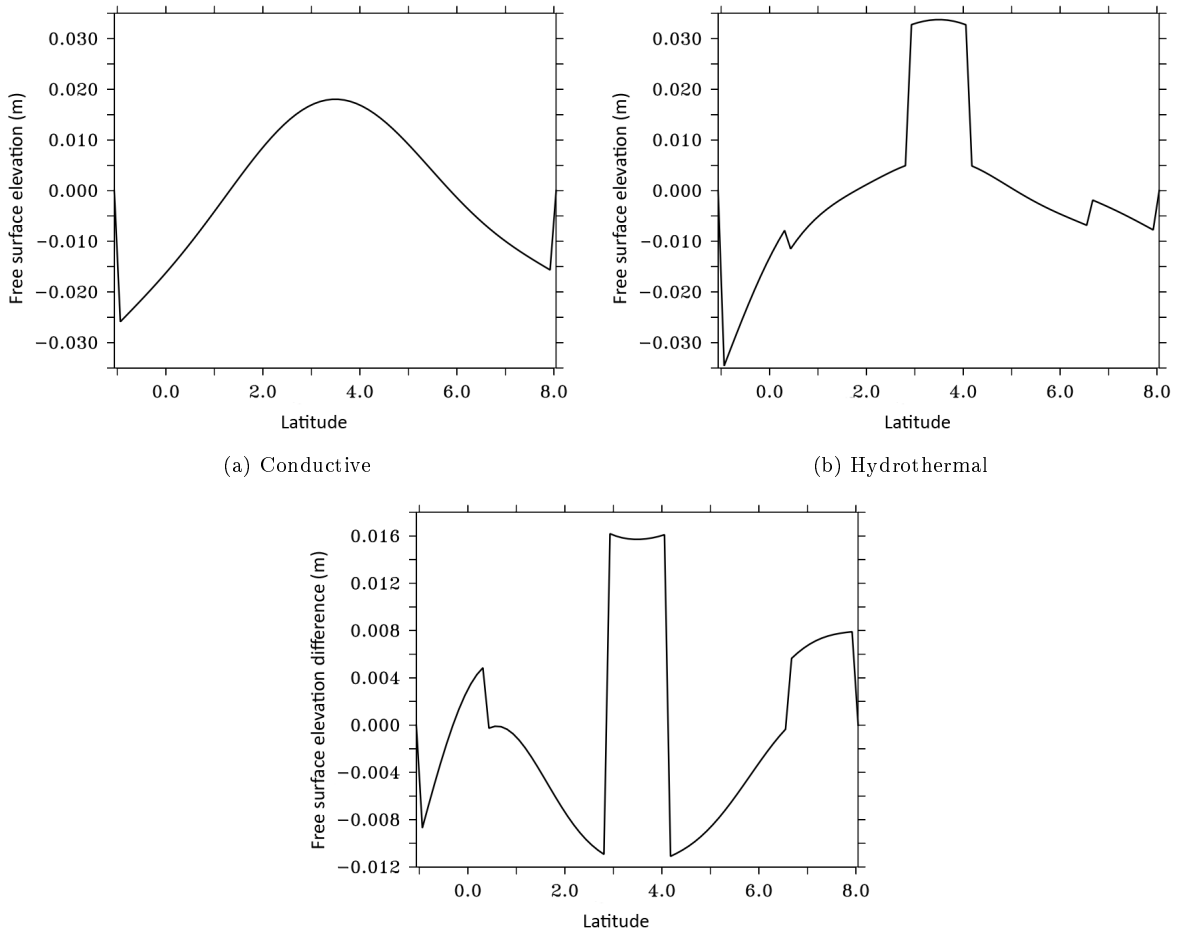

(a) Conductive

(b) Hydrothermal

(c) Difference (hydrothermal - conductive)

Figure 3.5: A comparison of the sea surface heights, with fully conductive and fully hydrothermal fluxes.

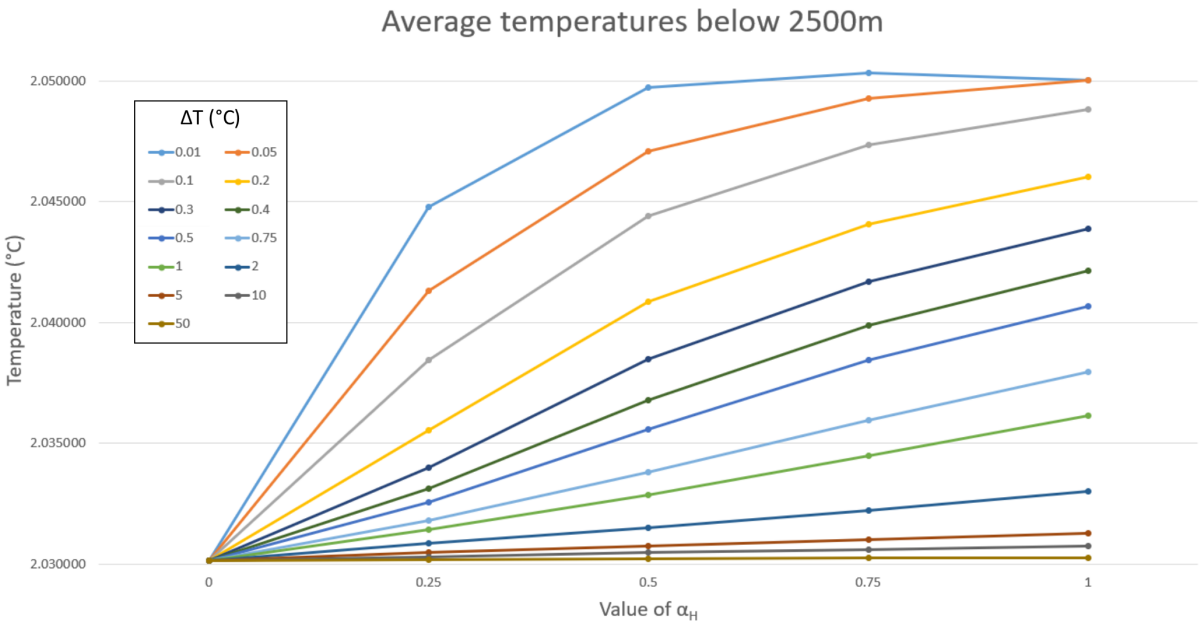

Figure 3.6: The average abyssal temperatures modelled for a range of geothermal fluxes with different values for α_H and ΔT.

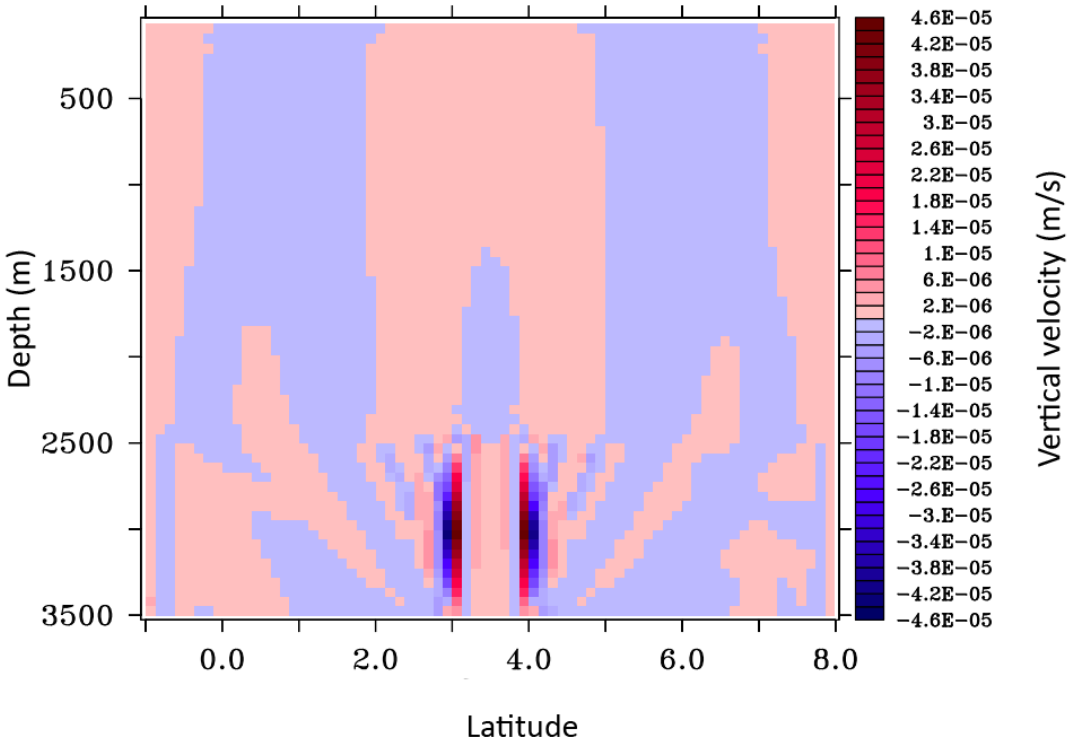

(a) Conductive

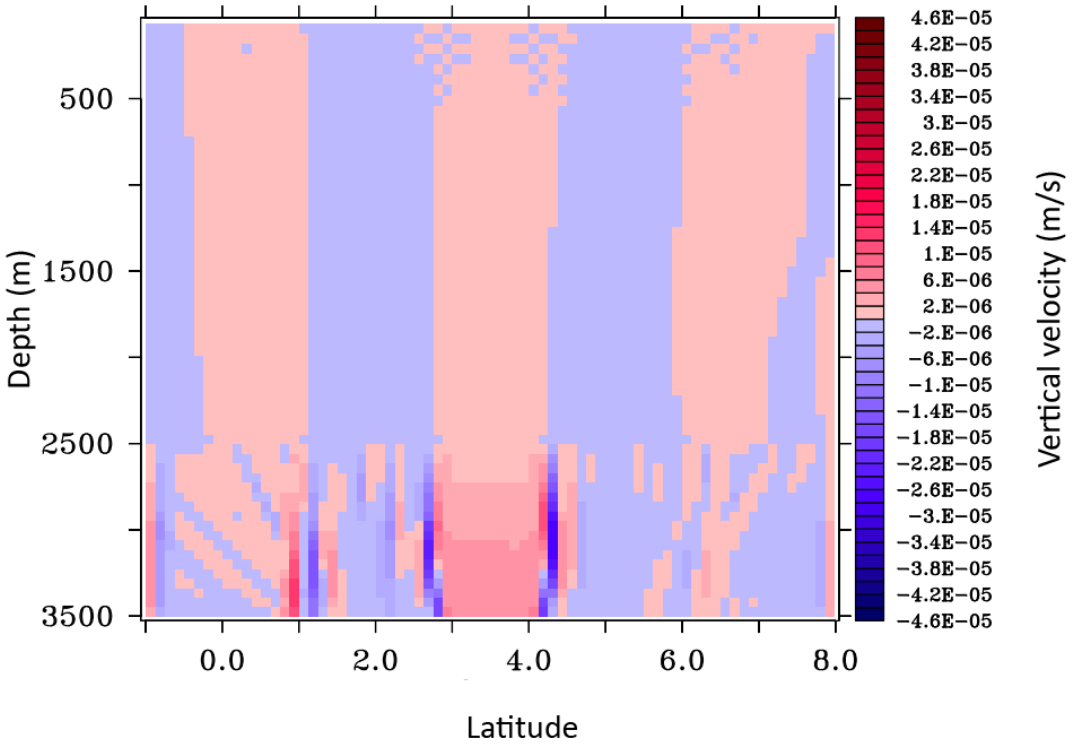

(b) Hydrothermal

Figure 3.7: The vertical velocities of the circulations, with fully conductive and fully hydrothermal fluxes.

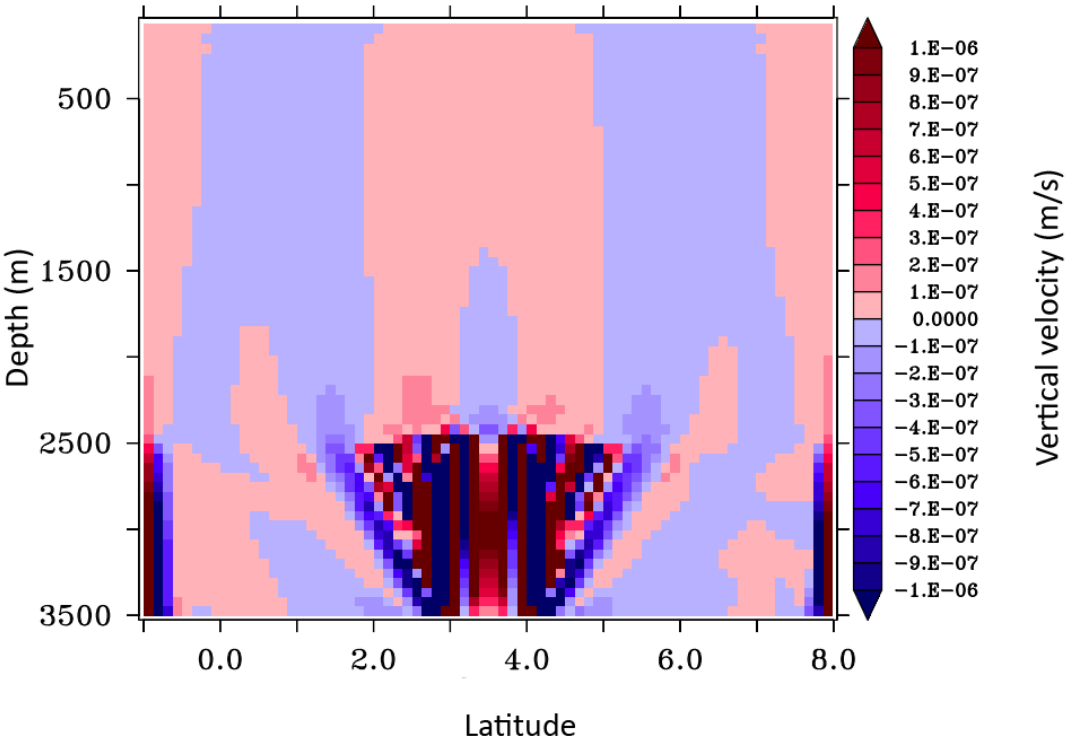

(c) Conductive, scaled to show slower velocities

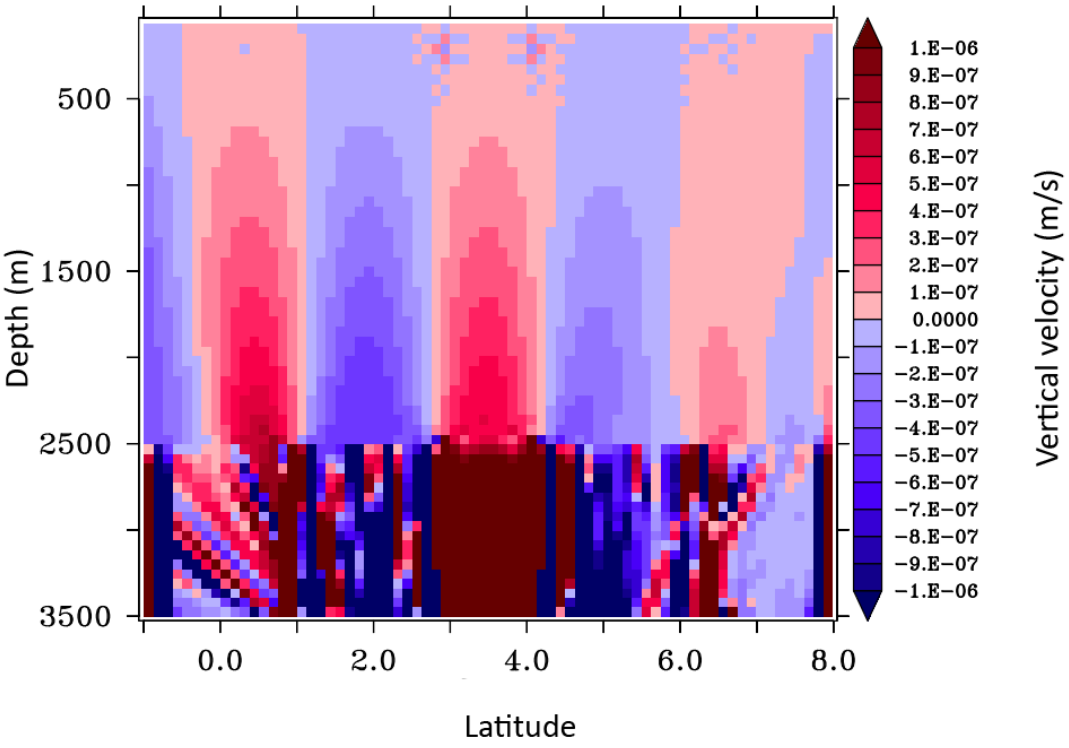

(d) Hydrothermal, scaled to show slower velocities

Figure 3.7: Continued from opposite page.

3.5.3 Conclusions

The results from this set of experiments show promise, in that the properties of the circulation and hydrography differ between flows driven by the different types of heat flux in ways which appear able to be physically explained. However, there are issues with this initial experimental setup. It serves as an illustration of some problems which, now having been encountered, must be resolved before starting any further experiments for deeper analysis.

The damping used by these simulations may be problematic. The strong effect of restoring in the upper ocean causes an abrupt barrier, or "ceiling", in the temperature and velocity. The circulation due to geothermal heating appears to almost entirely stop above 2500 m, as if there were a lid placed on the basin at that depth. The results seen here are not necessarily wrong; when looking at temperature and velocity fields, they do match the idea of the geothermal contributions to circulation being masked by water from the Pacific flowing into the basin above the ridges. However, the changes are very sudden and another approach may yield a more satisfactory transition between the abyss and upper ocean. A few variations of the restoring were tested, including a weaker damping coefficient and different heights for the distribution, but the abrupt boundary was still present.

A bigger issue is that the distribution of heat fluxes appears to be causing disruption to the vertical velocities, and that the hydrostatic approximation is breaking down over a wide area of the initial upward velocity. The problem is seen when trying to plot streamlines, with the majority of motion being around the narrow strips above the discontinuities of the heat flux functions, on the edge of the hydrostatically unstable column. The abrupt discontinuities in the step functions used to introduce heat into the domain could be causing instabilities to which the model reacts by significantly increasing vertical diffusion in the affected area. The next experimental design should distribute the heat fluxes along a continuous function to combat this problem.

3.6 An improved experimental design

3.6.1 The redesigned model domain

A new domain was created based upon that of Section 3.5, but with several important changes. In the vertical, the domain is now split into 61 levels. Instead of being uniform in nature as before, they are chosen to give greater resolution to the deepest parts of the ocean since that is where the differences between geothermal heating methods are expected to be more prevalent. The level thicknesses follow a polynomial distribution relating level number to depth, chosen to be cubic. This polynomial, and its derivative

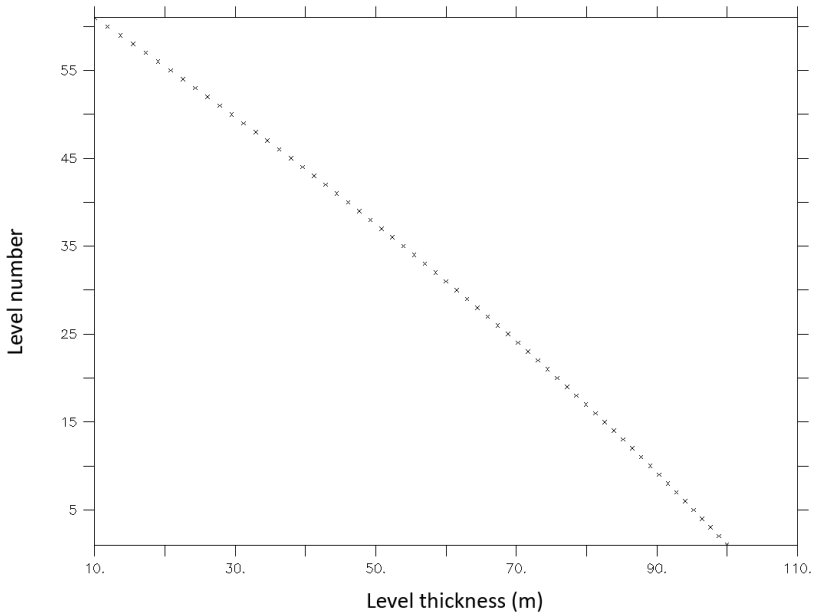

Figure 3.8: The level thicknesses in the improved model domain. Level 1 is at the top of the ocean, and level 61 at the bottom.

representing the level thicknesses, are defined to be of form

$$D = a(z-1)^3 + b(z-1)^2 + c(z-1) + d, \tag{3.6a}$$

$$D' = 3a(z-1)^2 + 2b(z-1) + c. \tag{3.6b}$$

By imposing $D(1) = 0$, $D(j) = D_M$, $D'(1) = K_S$ and $D'(j) = K_B$, where j is the deepest level number, D_M is the maximum depth, and K_S and K_B the prescribed thicknesses of the surface and bottom levels respectively, the coefficients of the polynomial become

$$a = \frac{(K_S + K_B)(j-1) - 2D_M}{(j-1)^3}, \tag{3.7a}$$

$$b = \frac{3D_M - (K_S + K_B)(j-1)}{(j-1)^2}, \tag{3.7b}$$

$$c = K_S, \tag{3.7c}$$

$$d = 0. \tag{3.7d}$$

The equations (3.6) with coefficients (3.7) are implemented in the NEMO module `domzgr`, with chosen values R_S=100 m and R_B=10 m. Figure 3.8 displays their arrangement.

The resolution is still $\frac{1}{8}^\circ$ (defined to be constant as 13.875 km) in the horizontal with a solid wall at the north side, but now spans the region from 2° S to 8° N. The extra space to the south side of the domain allows for a larger area over which to implement restoring

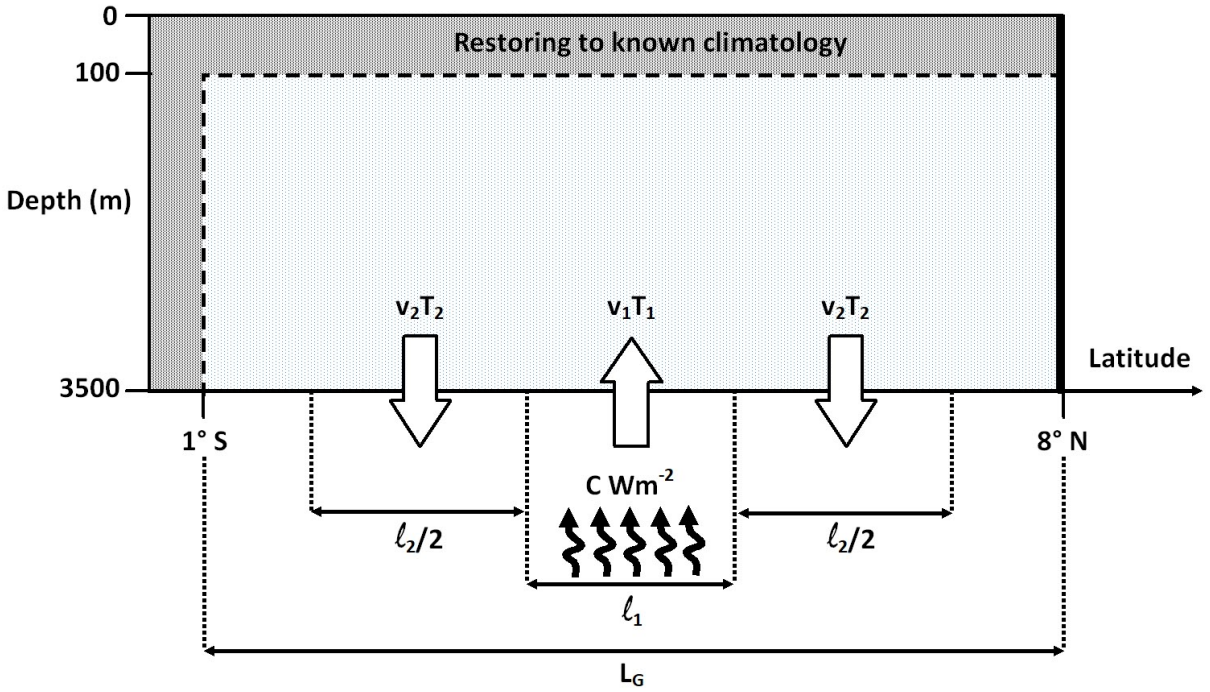

Figure 3.9: A sketch of the improved 2D model domain representing features of the Panama Basin, and the fluxes being applied through the seabed.

without it encroaching into the basin interior. The restoring will have its full strength at 2° S and decay linearly to zero by 1° S A wider region of restoring should allow a gentler relaxation towards the boundary conditions. On the other hand, the restoring in the vertical has been reduced significantly. To avoid the "ceiling" on the circulations that was seen in the previous simulations, vertical restoring has been limited to the surface level only, so will only take place in the top 100 m. This will allow the basin interior to evolve more naturally in response to the geothermal forcing, and should result in smoother flowing circulations. This restoring no longer represents effects from the outer Pacific ocean, but is still necessary in the top level as a proxy for surface heat and fresh water fluxes.

The distribution of heat fluxes will be according to cosine functions as in the analytical model. The formulation of these in NEMO is shown in the code segments in Section 3.4. The decision to change the flux distributions was made after seeing that the discontinuities in the step functions of uniform flows caused issues in the previous experiments. Using a cosine function not only provides a smooth transition from the region of heating, but also reflects the fact that more heat enters the abyssal ocean closer to the spreading centres of mid-ocean ridges such as those in the middle of the Panama Basin. While bathymetry is not being used in these experiments, the distribution of heat flux will be more representative of the Panama Basin this way. A sketch of the domain and fluxes is presented in Figure 3.9.

The value of the average total heat flux was updated to G=105.4 mW m^{-2}, based on the

Davies and Davies (2010) global average heat flow value, a more up to date study than that of Pollack et al. (1993). Another difference in this improved configuration is to prescribe T_1 as $T_1 = T_b + \Delta T$, where T_b is the average ocean bottom temperature over the discharge area and ΔT is a prescribed positive temperature anomaly. So the choice being made is how much warmer the discharged water is than the ambient temperature at the seabed. This is a better way of approaching the heat input, since in the previous configuration it would have been possible for the inflow to become cooler than the surrounding ocean, which is not a good representation of hydrothermal flux.

3.6.2 Initial testing: results in a symmetric domain

As a test of the new restoring field, two simulations were run in a domain with solid boundaries on both sides preventing any motion in or out. So the entire domain can be thought of as a two-dimensional cross-section of a rectangular tank. The choice of a symmetrical basin for this test was in order to more clearly see whether the streamlines of the circulation are following reasonable patterns. In a symmetrical basin, I have a good idea of what I expect to see. While the asymmetry will be an important part of the following set of experiments set in the Panama Basin domain, it could behave in more unusual ways. An initial test of whether the configuration is producing circulations with acceptable streamlines requires the more basic approach.

The hydrothermal discharge and conductive heating were applied between 2.875°N and 4.125°N at the centre of the symmetrical domain. Two experiments were run to near-steady state, one with a high-velocity purely hydrothermal flux ($\alpha_H = 1$, $\Delta T = 0.01$) and one with a purely conductive flux (α_H=0).

The outcome was a pair of circulations showing the sort of behaviour which was expected, and that can be physically interpreted. NEMO's enhanced vertical diffusivity and viscosity were employed in a very thin layer (one or two model levels) just above the vertical velocity input, but this was the only area in which hydrostatic instability had to be accounted for. The reduction in cell height near the seabed and smoothing of the flow function both contributed to this improvement. Overall, this new configuration of the model performed significantly better than the previous version.

The streamlines in Figure 3.10 show that the two types of heat flux cause rather different circulations. The flow induced by the conductive flux (Figure 3.10a) shows simple overturning cells where water that is heated and rises is replaced via a lateral flow. There is no way of exiting the domain, and so as water near the top of the circulation cools and sinks deeper, it is drawn inwards towards the centre to fill the gap left by that which is

rising. The water mass is then heated again and recirculates.

In the hydrothermal case (Figure 3.10b) there is a fountain shape reminiscent of that seen in the analytical solutions, although with extra complexities introduced by the hydrothermal source including heat in addition to just volume. While in the analytical study the horizontal flow is directed away from the discharge area at all depths, the numerical simulations show horizontal convergence towards the centre when approaching the seabed. This is most likely due to relatively cold water being advected towards the source area at depths below about 3000 m to replace the warmer water convecting upwards. This inward motion is reversed again as water approaches the central column, since it is still drawn towards leaving the domain through the recharge region rather than recirculating, and the rising water is replenished by the inflow. This behaviour suggests that the hydrothermal inflow is heating the surrounding abyssal water and causing a greater upwelling than can be balanced by the prescribed inflow alone, meaning that water needs to flow inwards from the sides up to a point to replace some of the bouyant rising water masses.

The upper extent of the main overturning circulations in each case is around 2600 m. This suggests that the upwelling water above the heat source reaches neutral buoyancy at the same depth in both cases, indicating little difference in the temperature of the water at that point. After reaching this maximum height, the flows spread outwards. The hydrothermal source induces a wider-reaching circulation, as the downward flow at the bottom boundary causes streamlines to terminate in the recharge zones on the seabed rather than circulating back around to the centre again. In reality the hydrothermal circulation continues under the surface of the oceanic crust, outside of the model domain. It is interesting to note that the widest streamline is very similar in shape to the upper half of the widest streamline of the convectively heated circulation, suggesting that perhaps the lower part of this streamline, within the Earth's crust, would follow a similar recirculating pattern if the domain were extended and the material were liquid enough to allow such flow.

The shape of these solutions is remarkably similar to convective circulations at the sea surface, as noted earlier for the analytical solutions. The shape of the circulation induced by conductive heating mirrors processes such as Langmuir circulations which are driven by winds at the sea surface, as presented in a sketch in Pollard (1977). Perhaps more relevant is the parallel with convection circulations caused by cooling at the sea surface (eg. Marshall and Schott, 1999), as they are also driven by heat fluxes.

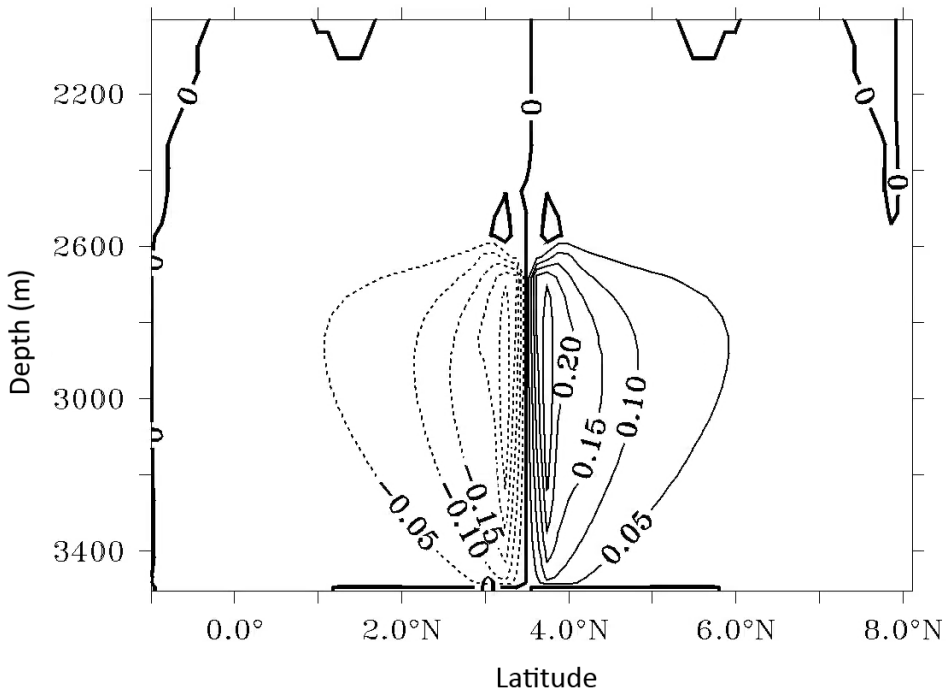

(a) Conductive

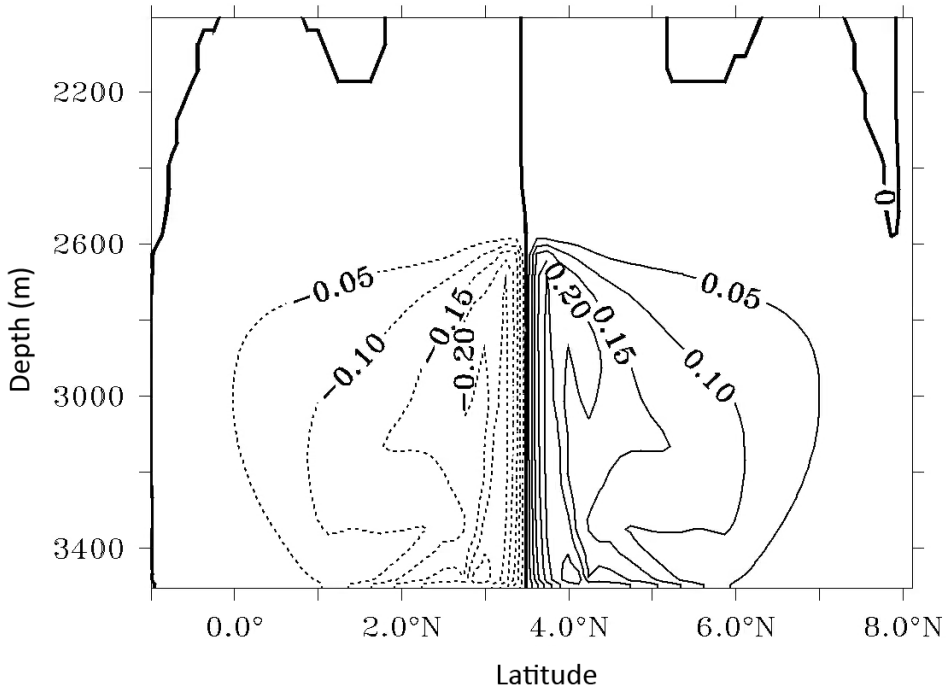

(b) Hydrothermal

Figure 3.10: The streamlines of the circulation induced in a symmetrical basin, in m^2s^{-1}, with (a) conductive ($\alpha_H = 0$) and (b) hydrothermal ($\alpha_H = 1$) fluxes. Positive values indicate a clockwise flow.

3.6.3 Results from the new Panama Basin domain

The only difference between the symmetrical experiments above and the improved Panama Basin domain described previously is the lateral restoring condition on the south side. However, this single difference is an important one. As a starting point, an experiment was run without any geothermal heating at all. The temperature field in Figure 3.11 for the deep ocean below 2000 m shows that the isotherm contours do not stay level. As a result of restoring occuring on one side only, the gradual warming of the deep ocean by vertical mixing takes effect on the north side, leading to temperature gradients across the width of the domain. The elevation of the sea surface is also asymmetric due to the restoring.

For each temperature difference ΔT that is chosen, a set of five simulations were run with $\alpha_H = 0$, 0.25, 0.5, 0.75 and 1. The model was integrated until it reached a near-steady state at which the maximum temperature change below 2500 m was smaller than 0.001°C over a decade. The results from these experiments with heating show several differences in circulation and temperature distribution between different ways of partitioning heat. The hydrothermal flux regime seems to be more effective at evacuating heat from the abyssal ocean than the conductive regime. As would be expected, this difference becomes more pronounced as the value of α_H increases and the heat flux becomes more dominated by its hydrothermal component. The evolution of the average temperature in the abyssal ocean varies fairly linearly with α_H, as is shown in Figure 3.12.

Due to the formulation of the fluxes as described in Section 3.4, a lower temperature difference between the hydrothermal discharge and bottom waters necessitates a larger mass flux. The choice of ΔT makes a big difference to the impacts of a hydrothermal heat flux. Where $\Delta T = 10$°C, the conductive and hydrothermal cases are almost indistinguishable in both heat distribution and circulation dynamics. As ΔT decreases and the velocity

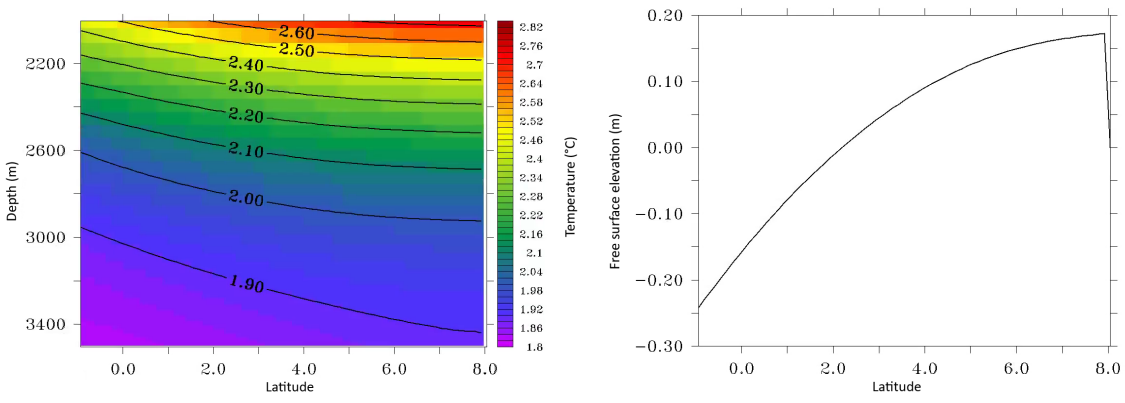

(a) The abyssal temperature.

(b) The sea surface elevation.

Figure 3.11: Properties of the circulation with no geothermal heating.

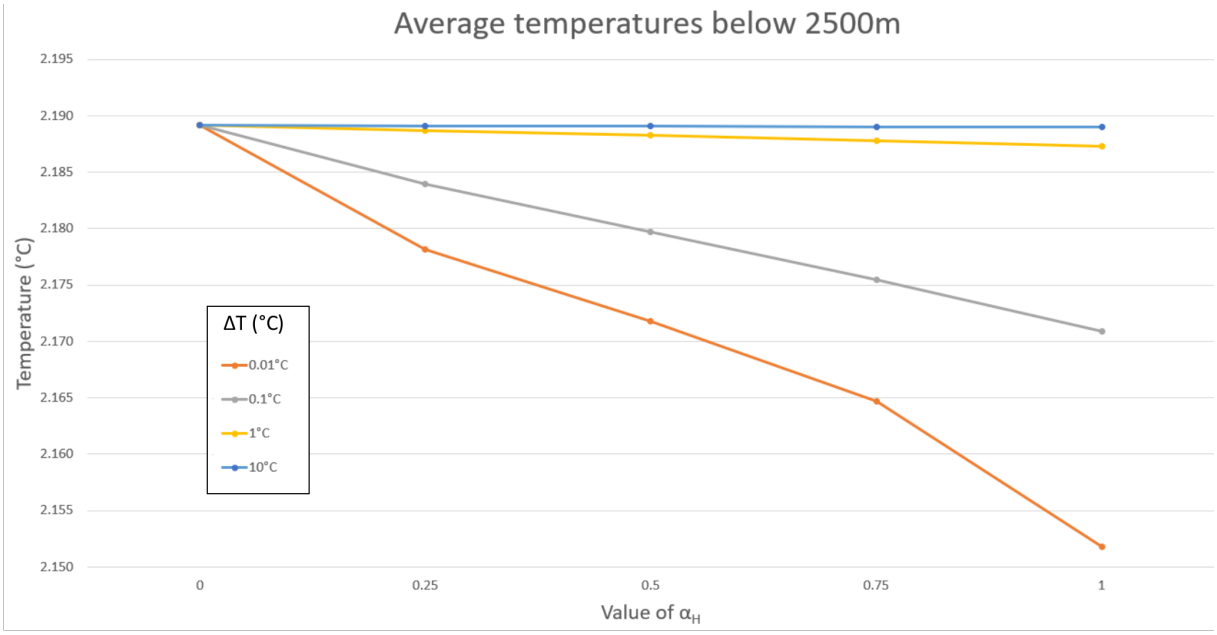

Figure 3.12: The average abyssal temperatures for hydrothermal flows with a range of different values of ΔT and α_H.

of the discharge increases, much larger differences are seen between the two cases. The changes in the circulation and heat distribution are intrinsically linked, so where larger differences in the average abyssal temperature are seen in Figure 3.12 larger differences in the circulation are also seen. The comparisons made throughout the rest of this section are between a purely conductive flux and a high velocity hydrothermal flux ($\Delta T = 0.01$°C), the two extreme cases among the range of experiments completed. The reality will lie somewhere between the two extremes, but this comparison allows clear investigation of the different effects these two types of heat flux have on the abyssal ocean, and how they differ as processes.

A consequence of applying a lateral restoring on the southern flank of the domain is the creation of an asymmetric circulation. On the north side of the basin where there is simply a wall, the abyssal ocean is well-mixed, but on the south side a strong stratification with slanted isotherms is maintained, as can be seen in Figure 3.13. The area south of 1° S in which lateral restoring is applied does not appear in any of the figures, as it is not intended to represent any part of the interior of the basin, only to mimic the effects of flow through the Ecuador Trench.

The addition of heating in either form makes a significant difference. The abyssal temperature is on average 0.168°C warmer with hydrothermal sources, and 0.211°C warmer with conductive heating, when compared to the simulation without heating. The largest differences are 0.341°C and 0.436°C respectively, with both maxima occuring at the seabed where the heat source is located. Looking at the abyssal temperature differences between the purely hydrothermal and the purely conductive cases (Figure 3.13e) it is found that,

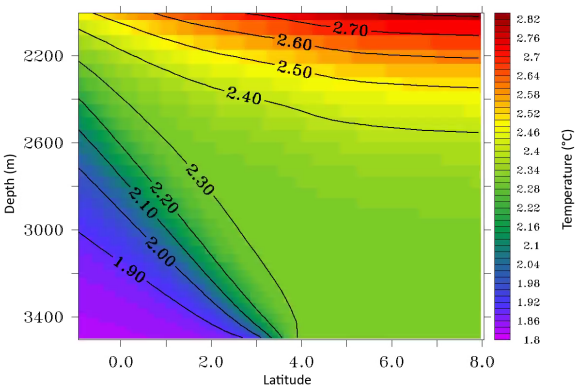

(a) Conductive, $\alpha_H = 0$, below 2000 m.

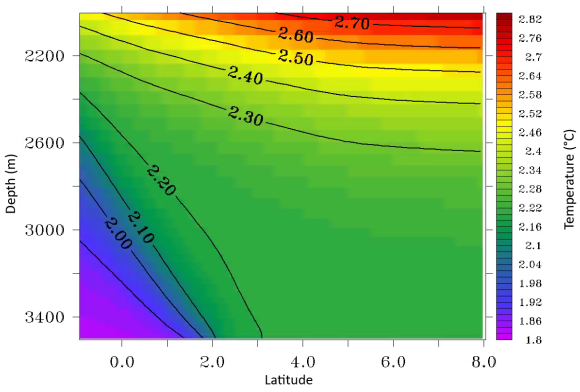

(b) Hydrothermal, $\alpha_H = 1$, $\Delta T = 0.01°C$ below 2000 m.

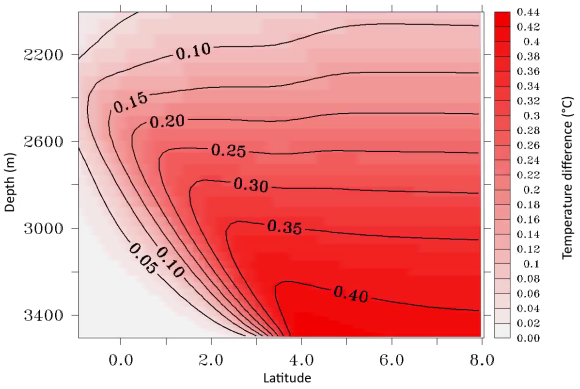

(c) Difference between conductive and no geothermal heating.

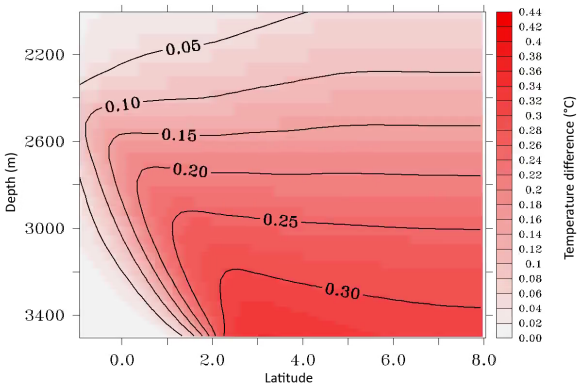

(d) Difference between hydrothermal and no geothermal heating.

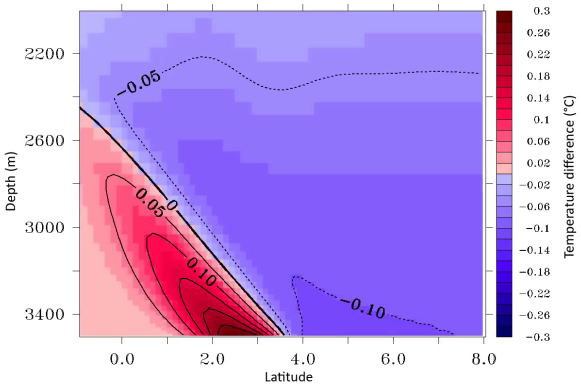

(e) Difference between hydrothermal and conductive heating.

Figure 3.13: (a)-(b) Temperature fields below 2000 m in the two extreme cases ($\alpha_H = 0$, and $\alpha_H = 1$ with $\Delta T = 0.01°C$). (c)-(e) Differences between simulations.

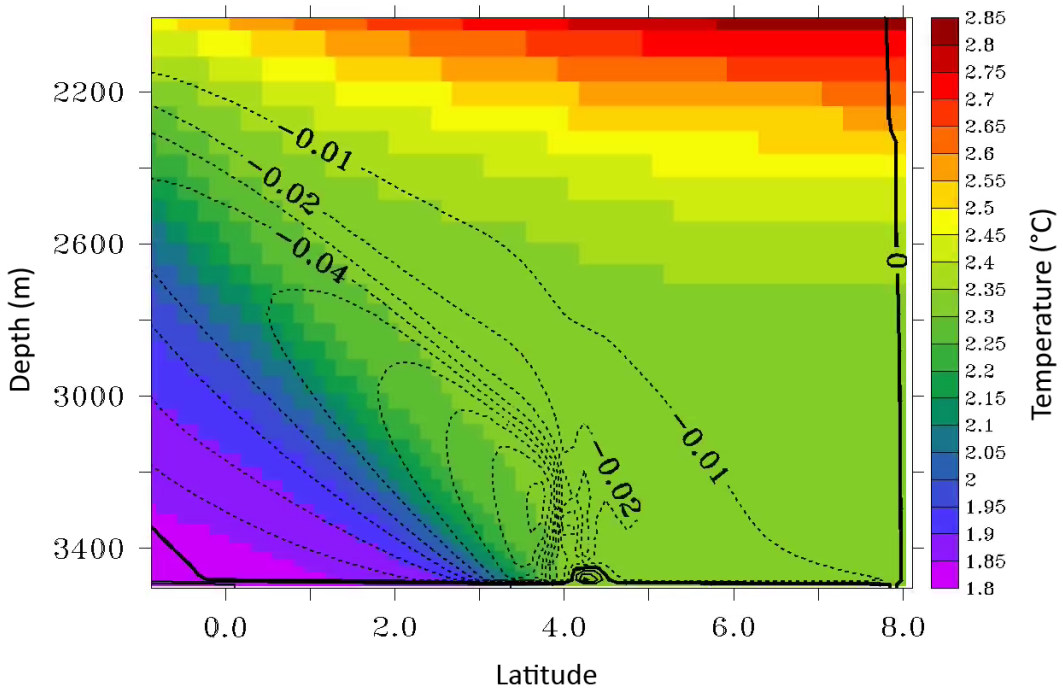

(a) Conductive, $\alpha_H = 0$.

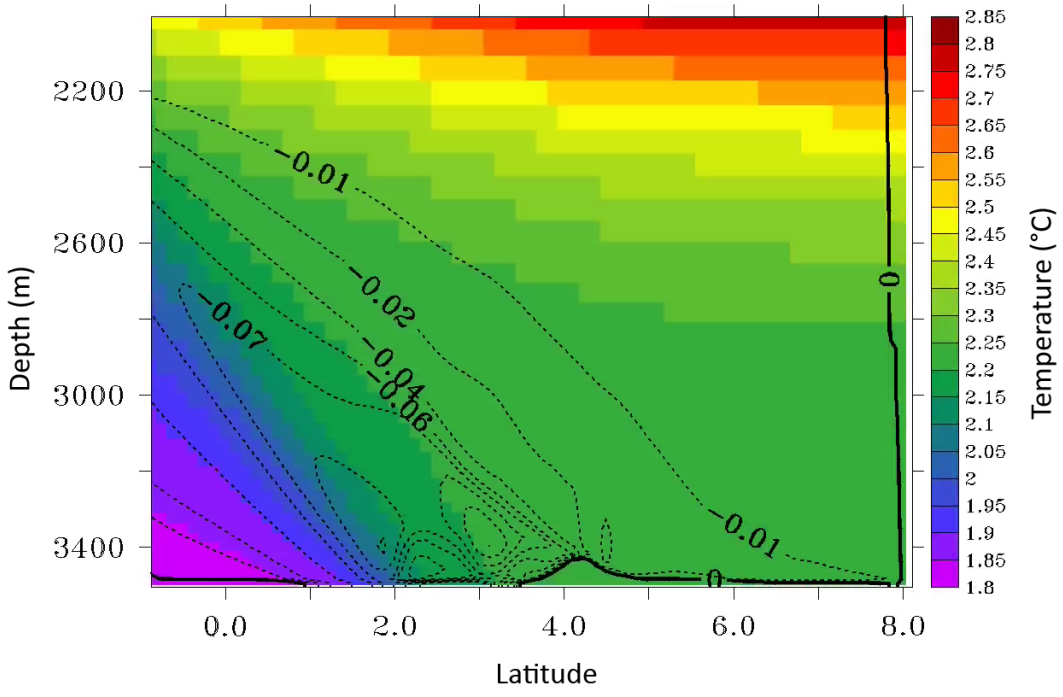

(b) Hydrothermal, $\alpha_H = 1$, $\Delta T = 0.01°\text{C}$.

Figure 3.14: Streamlines below 2000 m, in m^3s^{-1}, with conductive and hydrothermal fluxes, overlayed on the temperature fields. Positive values indicate a clockwise flow.

while the average temperature is lower in the former by 0.043°C, the temperature is higher at the southern side of the basin near the seabed. The maximum temperature difference of 0.293 °C occurs just above the southern recharge zone, at around 2.5°N.

Plotting the streamlines of the two different flows helps gain understanding about how differences in circulation are linked to the different temperature distributions (Figure 3.14). The effect of the lateral boundary restoring is seen again, with a strong circulation maintained throughout the southern half of the basin and comparatively little flow at the northern side. The hydrothermal fluxes also produce a relatively strong horizontal flow from the area of discharge to the area of recharge along the very bottom level of the ocean domain. The conductive case is in contrast, exhibiting a weak horizontal flow in the other direction, i.e. towards the centre of the basin, as water from the sides replaces the warmer water which rises due to buoyancy.

Looking more closely at the heat flux throughout the water column, some determination of further effects of the two different processes of geothermal heating can be attempted. By calculating different components of the heat flux, a more precise investigation of how the geothermal fluxes alter heat exchanges through the ocean can be carried out. Consider a section of the domain comprised between the seabed and a depth $z = d$, and between 1° S (y_{S}) and 8° N (y_{N}) where there is no restoring. The rate of change in the total heat content, Q, for this slab is due to the contributions of several heat transport processes, as illustrated in Figure 3.15. The main contributions are from geothermal heating (F_{geo}), lateral advection (F_{lat}), vertical advection (F_{adv}) and vertical diffusion (F_{dif}). The eddy parameterisation fluxes of the model are included when calculating the advection and diffusion. The residual is given the shorthand F_{res}, and includes all unaccounted for numerical contributions to $\partial Q/\partial t$ such as spurious dispersion from the model's TVD advection scheme which is not included in the method of calculating advection below. It also includes the effects of lateral diffusion, which were not of great importance to the analysis due to their comparitively small magnitudes. For the following heat flux calculations, fluxes into the slab are treated as positive and fluxes out of it as negative. Since the positive direction in the model is upwards, this means that components calculated from model results at the top of the slab must be multiplied by -1. Thus the heat content relationship is written mathematically as

$$\frac{\partial Q}{\partial t} = F_{\mathrm{geo}} + F_{\mathrm{lat}} - F_{\mathrm{adv}} - F_{\mathrm{dif}} + F_{\mathrm{res}}, \tag{3.8}$$

where

$$Q = \rho c_p \int_0^d \int_{y_{\mathrm{S}}}^{y_{\mathrm{N}}} T(y,z)\,\mathrm{d}y\,\mathrm{d}z \tag{3.9a}$$

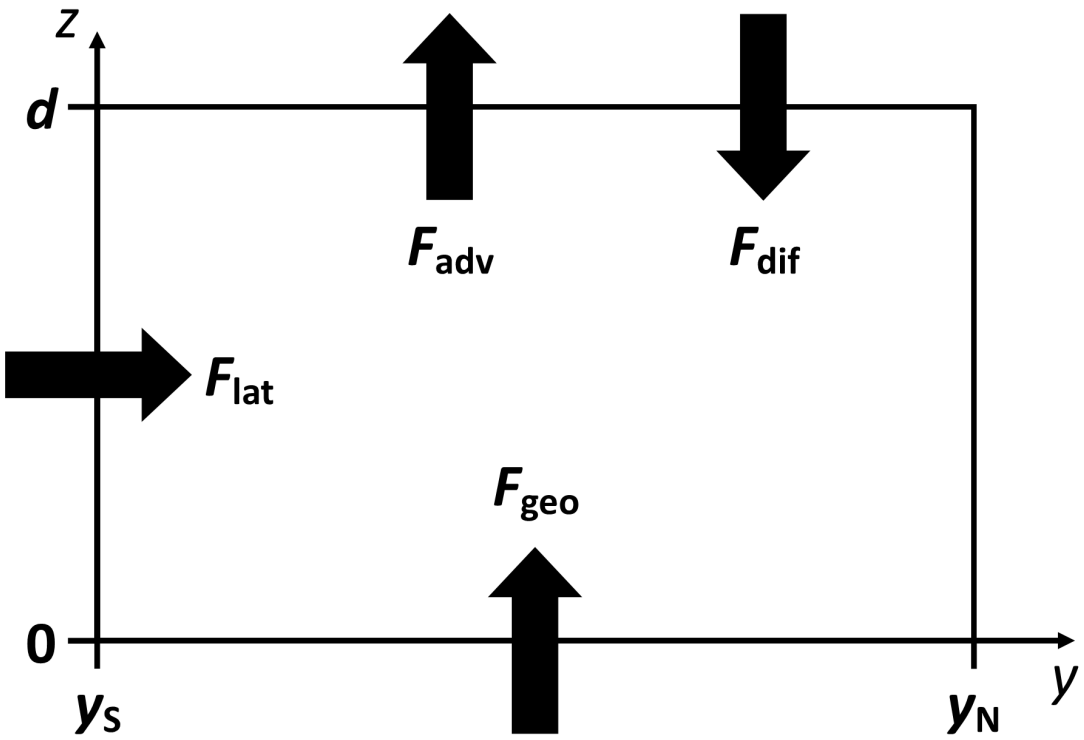

Figure 3.15: A sketch showing the main contributions to the heat content of a slab of the abyssal ocean, and the directions in which they act. F_{geo} is geothermal heating from below, F_{lat} is lateral advection, F_{adv} is vertical advection and F_{dif} is vertical diffusion.

$$F_{\text{geo}} = \int_{y_S}^{y_N} G(y)\,\mathrm{d}y \tag{3.9b}$$

$$F_{\text{lat}} = \rho c_p \int_0^d v(y_S, z)T(y_S, z)\,\mathrm{d}z \tag{3.9c}$$

$$F_{\text{adv}} = \rho c_p \int_{y_S}^{y_N} w(y, d)T(y, d)\,\mathrm{d}y \tag{3.9d}$$

$$F_{\text{dif}} = \rho c_p \int_{y_S}^{y_N} \kappa(y, d)\frac{\partial T(y, d)}{\partial z}\,\mathrm{d}y. \tag{3.9e}$$

In the expressions above, ρ is a reference density, c_p is heat capacity and G is average geothermal heat flux, with values $\rho = 1035\,\mathrm{kg\,m^{-3}}$, $c_p = 4000\,\mathrm{J\,kg^{-1}K^{-1}}$ and G=105.4 mW m^{-2}. Additionally, T is temperature, v and w are meridional and vertical velocity, and κ is vertical diffusivity.

These calculations are performed at each level interface by changing the value of d. In this way, information is obtained about the average heat fluxes of each type in slabs of increasing thickness. Figure 3.16 compiles the information into depth profiles of the heat fluxes from the seabed up to a given depth. Data from above 500 m depth are ignored as the surface restoring distorts the results. It can be seen that the changes caused by altering the heat flux at the seabed are confined to the deep ocean, and that above 1500 m depth there

is almost no difference between the hydrothermal and conductive cases. Importantly, the difference is also confined to the advective components of the heat flux, while changes in the vertical diffusive heat flux are negligible. This is also true of differences between the simulations with heating and the one without, showing that the diffusive flux is barely affected by geothermal heating.

Not unexpectedly, using a hydrothermal flux increases the strength of the advective components of the heat flux through the abyssal ocean. The vertical and lateral advective fluxes act to almost balance each other, irrespective of the value of α_H, with heat being evacuated from the abyss by the vertical advective flux and being replenished via lateral advection through the Ecuador Trench. In the hydrothermal case the magnitude of the vertical advective flux in the abyssal ocean increases by up to 35 % compared to the conductive case, being 21 % greater on average between 2500 m depth and the seabed. The lateral advection increases by an even greater amount, up to 45 % with an average change in the abyssal ocean of 28 %. The strong vertical advection reaches a little further up the water column with a conductive source, so that above about 2350 m the advective fluxes are actually smaller in the hydrothermal case.

It is interesting to observe that the one non-negligible change above 2000 m occurs due to the addition of geothermal heating. When compared to the simulation without heating, the other two cases have a weaker lateral advective flux higher up the water column. The magnitude by which it is weakened is similar to the magnitude of the flux added to the bottom of the ocean, resulting in these two fluxes balancing each other in the upper ocean. Comparing the simulations with and without heating also reveals how large the effect of a geothermal boundary condition is. The differences in the advective fluxes are far larger than the additional heat entering the system from below, indicating that geothermal processes can have a very active role in driving circulation, causing changes far beyond their input magnitude.

3.7 Discussion

From the experiments that have been run, it appears that introducing a portion of the geothermal heat flux hydrothermally makes an important contribution to circulation in the abyssal ocean. The analytical solutions of circulation driven by volume fluxes in Chapter 2 were the first indicators of the importance of these flows. Before even considering the effects of heating, the existence of a volume flux through the seabed contributes to the abyssal circulation in a way previously not implemented in ocean modelling. In the absence of other processes, the flow induced by these volume fluxes permeates the entire model layer and causes a vertical displacement of its top interface.

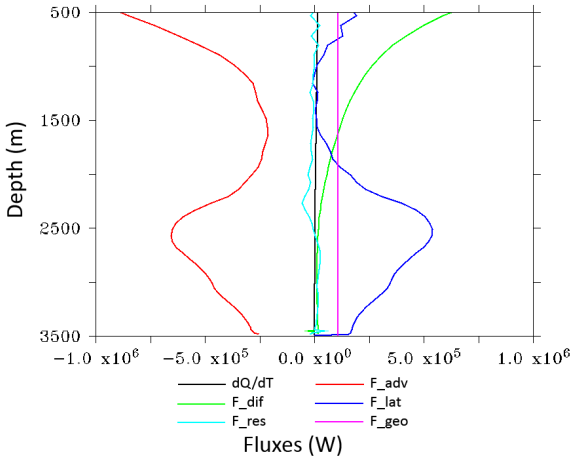

(a) Conductive, $\alpha_H = 0$.

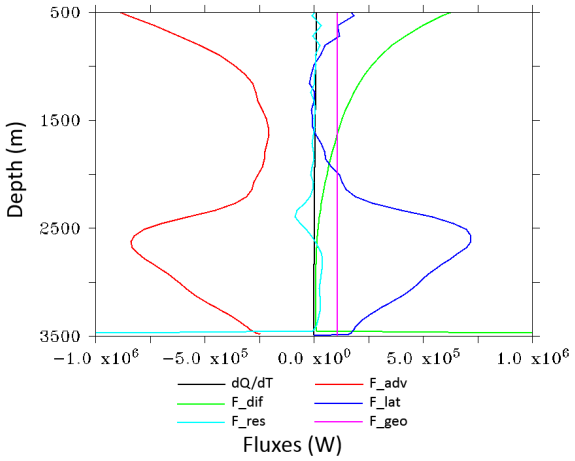

(b) Hydrothermal, $\alpha_H = 1$, $\Delta T = 0.01°\text{C}$.

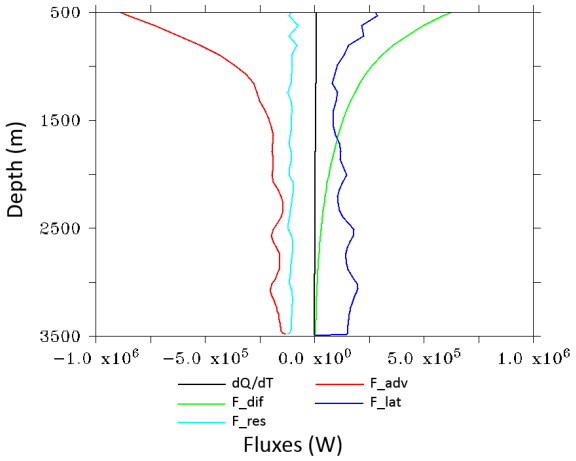

(c) No geothermal heating.

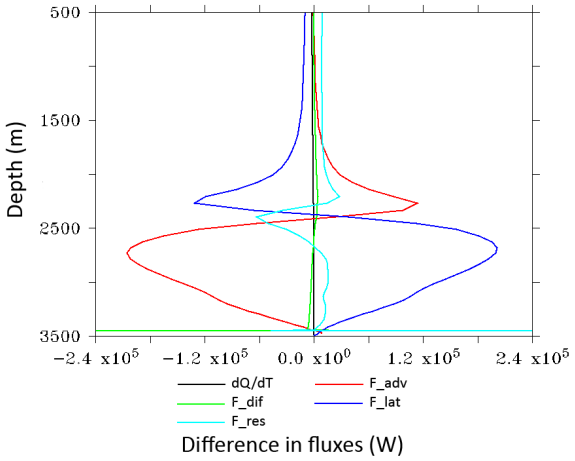

(d) Difference between hydrothermal and conductive.

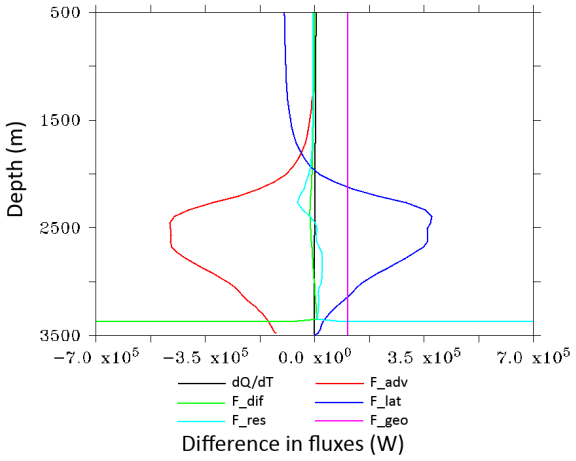

(e) Difference between conductive and no heating.

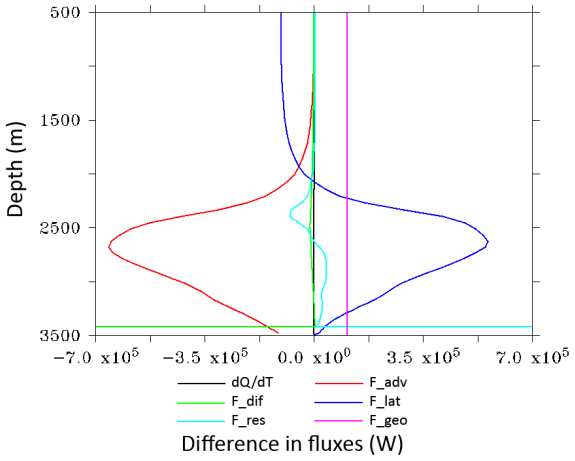

(f) Difference between hydrothermal and no heating.

Figure 3.16: (a)-(c) Depth profiles of various components of the heat flux, in Wm^{-2}, in simulations with conductive and hydrothermal fluxes, and with no geothermal heating. (d)-(f) The differences between simulations.

Two versions of the model domain have been presented in this chapter. It went through several iterations before arriving at the final improved domain of Section 3.6, implementing and testing changes gradually, version by version, as it evolved from the initial domain seen in Section 3.5. One particular aspect of the domain which causes significant differences to the resulting circulations is the extent of restoring. In the original domain, restoring in the vertical was implemented down to a depth of 2500 m to represent the external influence of the upper Pacific ocean. Under this regime, the abyssal ocean is warmer on average with hydrothermal heating than with conductive heating. With the restoring limited to the surface layer in the improved domain, the reverse is true. The flow is less restricted, and interacts far more with the lateral restoring representing the connection to the Pacific at the south side of the domain. Without this lateral restoring, the circulation is symmetrical as in Section 3.6.2. The deeper restoring allows this structure to remain in effect to some extent, with the restoring at the south side unable to affect the circulation on the north side, resulting in a slightly asymmetric circulation. Removing that restriction allows the influence of the lateral restoring to reach the entire basin, and results in one large overturning cell rather than two symmetric ones.

It is difficult to say which of the two versions of vertical restoring is more accurate in representing the Panama Basin. The earlier version was not necessarily wrong. There is certainly a thick mixed layer at the bottom of the Panama Basin which can be seen in observational data, but I was not satisfied by the abrupt changes in temperature and velocity fields seen in Section 3.5. Since the later version of the domain is a definite improvement in every other way, the results of Section 3.6 are the ones which shall be focused on. They certainly provide a lot of useful insights into the heating processes, whether or not they are the most accurate representation of the Panama Basin in particular. Later modelling work in a three-dimensional domain would be able to test the two vertical restoring regimes more thoroughly in relation to particular geographical areas.

Many differences are seen between the circulations, and in the distribution and transportation of heat, induced by hydrothermal and conductive heat fluxes. With a hydrothermal flux as opposed to a conductive one, the advective heat transport in the abyssal ocean is increased by up to 35 % in the vertical, and up to 45 % laterally through the side of the basin. Relating the lateral restoring condition to the Panama Basin, this represents an increased inflow though the Ecuador Trench. Meanwhile there is no appreciable change in the basin-averaged diffusive heat flux except at depths a few tens of metres above the seabed. So, in the purely hydrothermal simulation, the effect is the same as a conductive flux plus the additional advection caused by a velocity boundary condition. This was seen in the symmetrical domain (Section 3.6.2), which showed the streamlines of the hydrothermally-driven flow moving in towards the heat source just as those of the

conductive flow do, before turning back downwards to terminate in the seabed. In the Panama Basin setup, the increased vertical advection drives, through continuity, the increase in lateral advection through the side. It has previously been proposed, based on observational data, that flow through the Ecuador Trench is partly driven by upwelling in the basin interior caused by geothermal heating (Lonsdale, 1977). This theory agrees with the relationship seen between the vertical and lateral advective fluxes in the model.

When entering into this work one of the aims was to determine whether the use of hydrothermal, as opposed to purely conductive, fluxes in ocean models were a necessary addition to better represent the abyssal circulation, and under which circumstances it would be relevant if so. It has been found that the impacts on circulation and heat distribution of a high-velocity hydrothermal flux are significant at basin scales in the abyssal ocean. However, they are unlikely to make any noticeable difference in the upper ocean, so the usefulness of including these fluxes in ocean models very much depends on what one is interested in investigating. For future modelling of the abyssal circulation in the Panama Basin and other similar locations, it could be worth including hydrothermal boundary conditions in addition to conductive heat fluxes, if the distribution of hydrothermal flow were known to be in specific regions of inflow and outflow, rather than arranged more chaotically. The Panama Basin has an average heat flux of $256\,\mathrm{mW\,m^{-2}}$, calculated from the formula of Stein and Stein (1992) together with the crustal age data of Müller et al. (1997). This is about 2.5 times the global average used in our model, so could cause even more significant differences between the two extreme cases.

It was noted previously that the abyssal temperature and circulation in the model results are sensitive to the choice of ΔT, the difference in temperature between the hydrothermal flow and the bottom water. The extreme case focused on was $\Delta T = 0.01°\mathrm{C}$, but with larger values the difference when compared to a conductive geothermal flux are less pronounced. While fluids from individual vents have been recorded at stable temperatures above 400 °C (Koschinsky et al., 2008), these are extremely small points when put in the context of a basin scale model. Since the lateral grid resolution is $\frac{1}{8}^\circ$ the values used must represent the average ΔT over a large area. At this scale, taking into account the spacially sparce and scattered nature of hydrothermal venting and the fact that much of it occurs at much lower temperatures, a small fraction of one degree Celsius seems a reasonable value for the average ΔT in the ocean.

Features seen in the results of the experiments presented in this chapter show a great similarity to convection cells driven by surface processes. Not only do the overturning circulations resemble those caused by Langmuir circulations and surface cooling as previously noted, the stratification is also reminiscent of surface processes. Several cases presented in Marshall and Schott (1999) show a similar pattern of stratification breaking

down close to a heat flux, in this case a surface cooling. Further away from the heat flux stratification is normal, but in the shallower layers to either side of it the thermoclines reach the surface, causing deeper layers to outcrop. Directly beneath the heat sink is a deep mixed layer which can reach a depth of 1500 m (Jones and Marshall, 1997), just as a thick mixed bottom layer appears in the solutions with heating at the seabed.

Using a simple approach to this modelling was important in order to provide a clear first look at the processes, but it does come with some limitations. It is likely that areas of hydrothermal discharge and recharge are distributed in a far more disorderly manner than the symmetric boundary condition implemented for the majority of this modelling, creating more complex flow patterns than in our simulations as competing regions of upward and downward velocity interact. Such distributions could be modelled using the techniques of this chapter, and the scales of the resulting flows would likely be smaller in that case. Additionally, in a more realistic setting, the conductive portion of the heat flux will be present throughout the entire basin rather than only at the centre, although the distribution of heat will be more heavily weighted towards the mid-ocean ridges, which was the justification for the idealised boundary condition used here.

3.8 Conclusions

The results in this chapter reinforce the importance of geothermal heating to the deep ocean. Comparing the cases with and without heating reveals a large difference in heat content and distribution within the abyss. The advective transport increases by an amount far greater than the magnitude of heat being introduced to the basin, showing that the geothermal processes have an active role in changing the circulation and properties of deep water, rather than merely adding additional heat to be carried around as a passive tracer.

Idealised models have shown that the hydrothermal component of the global heat flux can affect the abyssal circulation in ways which a purely conductive heat flux cannot. Compared to the conductive case, the hydrothermal heat flux in the NEMO experiments increases vertical advection by up to 45 % in the abyssal ocean. While the water below 2500 m is only slightly cooler on average, the heat is distributed differently such that there are localised patches which see temperatures change by up to 0.293 °C. It remains to be seen, however, whether similar results will be present, and with what significance, in a more realistic model. There could be complications in taking this method forward to more realistic modelling experiments, as creating realistic boundary conditions will not necessarily be a simple task. At coarser resolutions, the models of Stein and Stein (1992) will suffice, but for more detailed regional models observational data would be preferable.

However, there are not many observations concerning the distribution of hydrothermal activity on the ocean floor, in particular how widespread or concentrated areas of discharge and recharge may be. Conducting a statistical study on the relative frequency of hydrothermal activity, Baker and German (2004) only had enough data to have a reasonable degree of confidence in their estimates for about 10 % of the global ocean ridges. Many known sites of hydrothermal discharge and recharge are extremely localised and too small to resolve in the horizontal grids of large-scale ocean models. Nevertheless, hydrothermal boundary conditions should be considered in future modelling studies, when technological advances make higher resolutions possible and more data are available.

For general usage, the importance of including a hydrothermal boundary condition will vary depending on the scales involved in the model, and the focus of the modelling project. For the upper ocean, no discernible difference is evident between using conductive or hydrothermal heat fluxes, so it would not be a worthwhile addition for projects with their focus here. Deeper down, more important differences are seen in the heat distribution, but some of these occur only over small areas and may lose significance in lower resolution models. The improved domain in particular, with its vertical levels designed to emphasise changes in the abyss, contains a much finer resolution in the abyssal ocean than standard ocean circulation models. Such significant differences between the two types of heat flux would not be expected when using standard vertical levels with resolutions often in the hundreds of metres in the abyss. The average abyssal temperature difference is 0.043 °C, but the high resolution brings out areas where the temperature changes by almost 0.3 °C between the two cases, which would not be seen otherwise. As such I would recommend a much higher vertical resolution than is usually present in this part of the ocean for any experiments involving geothermal heating. At the usual low resolutions, much of the detail of temperature distribution resulting from the introduction of hydrothermal boundary conditions will be lost.

The findings of this chapter have implications not only for the Panama Basin, but for other partially enclosed basins containing hydrothermal sources. Examples of such basins can be found across the globe, including the Scotia Sea, Cayman Trough, Red Sea, Sea of Japan and the Arctic Ocean. Simple models of the type I have have been using could be adapted to take on the features of these other ocean basins and produce representative values for the components of their heat fluxes, quite possibly revealing higher advective transport in the same way as my results have for the Panama Basin.

The question of whether or not to include hydrothermal fluxes in models would need to be addressed on a case-by-case basis taking into account the above considerations. For any work with a focus on the abyssal ocean at a reasonably high resolution, it could be a useful addition to the modelling process in the future.

Chapter 4

Investigating the effects of heat fluxes in a regional model of the Panama Basin

4.1 Introduction

In this chapter, I take a closer look at the effects of geothermal heat flux in the Panama Basin using a three-dimensional model domain in a configuration which makes use of observational data. Once again, the NEMO ocean model introduced in Section 3.2.1 is used. While still an idealised setup, ignoring wind forcing, tides and other external influences on the basin, the model domain used here is far more realistic than that of the previous chapter.

It was decided that the simulations in this chapter would ignore hydrothermal fluxes and concentrate on a conductive heat flux formulation. While the proportion of heat entering the basin hydrothermally (the value of α_H in the previous chapter) can be estimated based on the crustal age as in Stein and Stein (1994), the lack of observational data is still an issue. The distribution of hydrothermal inflow and outflow is currently unknown, and any attempt to create such a distribution for the Panama Basin would involve large amounts of conjecture without data to back it up. Since this distribution had already been observed to be critical to the resulting circulation, using hydrothermal fluxes was not feasible. Furthermore, the horizontal scales of known systems are generally too small to be properly resolved at the resolutions used here. In the future, however, with more observational data and a better understanding of the distribution of hydrothermal systems in the region, they could be an insightful addition to further modelling work with sufficient resolution.

Before going into these modelling experiments, I had an idea of what I would expect to see based on observations of the Panama Basin. It has been theorised that geothermal heating causes greater upwelling in the basin (Detrick et al., 1974), and in turn drives a stronger inflow through the bottom of the Ecuador Trench. This inflow has recently been estimated at 0.29 Sv (Banyte et al., 2018). By contrast, flow across the saddle of the Carnegie Ridge, the next deepest channel connecting the Panama Basin to the rest of the Pacific, has been measured in the past and found to be quite weak (Lonsdale, 1977).

4.2 Model details

The simulations in this chapter share similarities with those of the previous section, and the model domain is once more built upon the GYRE configuration of NEMO. The model domain covers the Panama Basin and some of the surrounding ocean to the south and west. The bathymetry used for this area is taken from the ETOPO 1 arc minute grid (Amante and Eakins, 2009) and is displayed in Figure 4.1a. The grid is a little more complex than in previous configurations. The zonal (west-east) resolution is $\frac{1}{20}^\circ$, and implements a curviliniar coordinate system such that the grid cell width changes with latitude, as shown in Figure 4.1b. The meridional resolution is $\frac{1}{15}^\circ$, defined as a uniform cell width of 7413 m. In the vertical there is a uniform resolution of 70 m, and a total of 72 levels. A time step of ten minutes is used.

Two simulations were run, one with a geothermal heat flux and one without. The heating used is conductive, and distributed according to the formula of Stein and Stein (1992) which relates heat flux to crustal age. For crust younger than 55 million years, this formula is $q(t) = 510t^{-\frac{1}{2}}$, where q is the heat flow in $\mathrm{mW\,m^{-2}}$ and t is age in millions of years. The crustal age used to calculate the heat flux was taken from the dataset of Müller et al. (1997), a 6 arc minute grid which interpolates the age of the crust between known

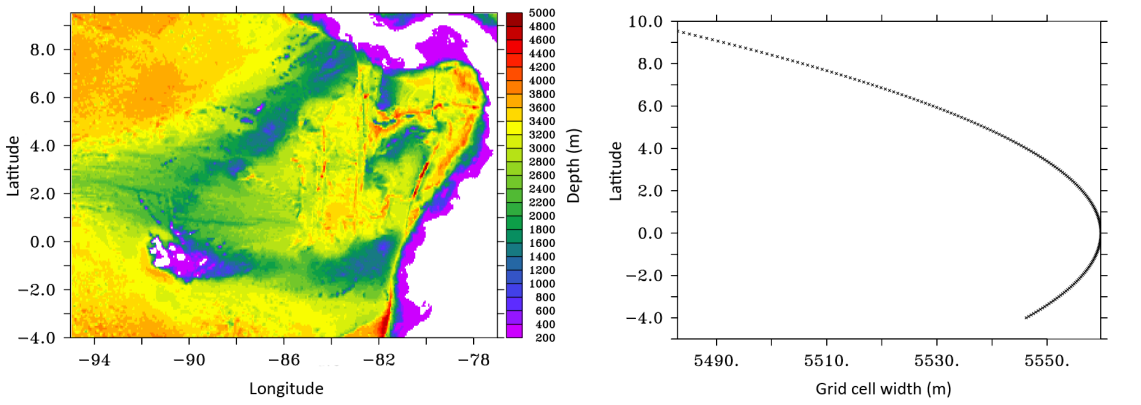

(a) The bathymetry.

(b) The change in grid cell widths with latitude.

Figure 4.1: Details of the three-dimensional model domain.

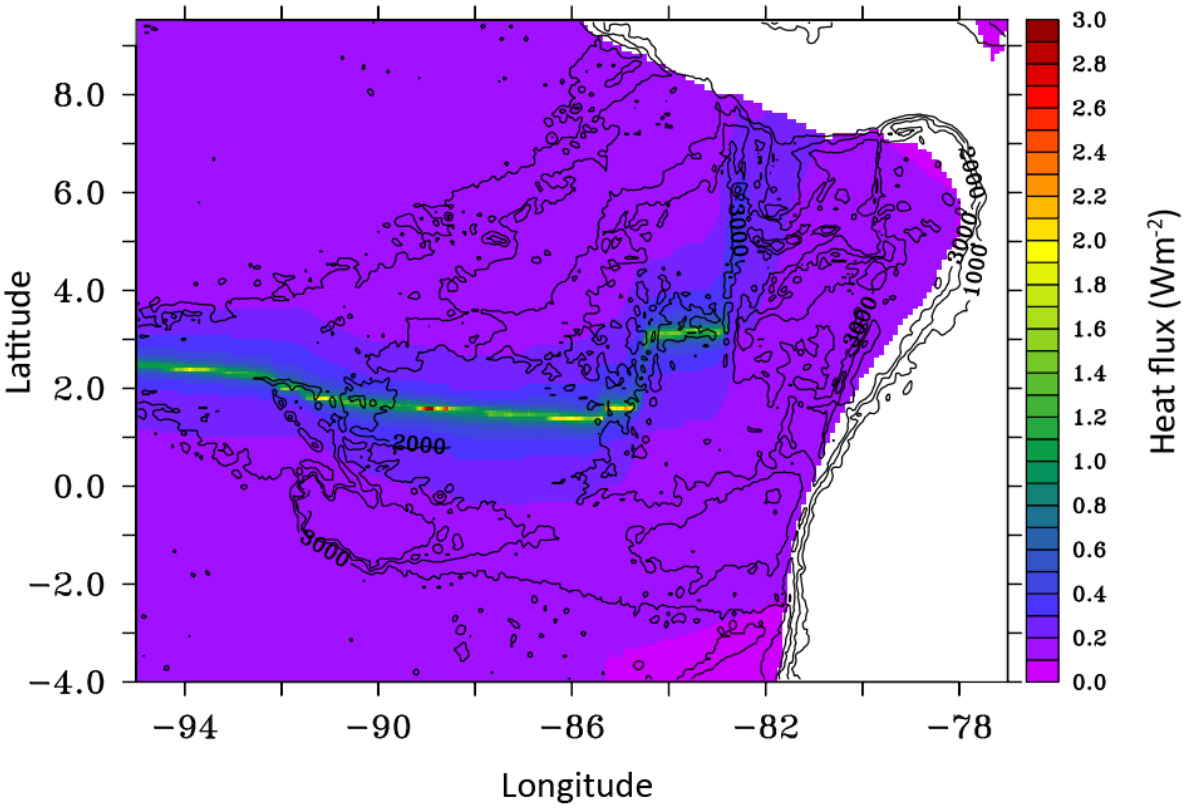

Figure 4.2: The geothermal flux used at the sea floor in the three-dimensional model, with bathymetry contours for every 1000 m depth.

observations. As a result, the geothermal boundary condition through the bottom of the model domain is the heat flux displayed in Figure 4.2. The lines of highest heat flux follow the plate boundaries, with the locations of the Costa Rica, Ecuador and Galapagos rifts being obvious sources of large amounts of heat. The average geothermal heat flux into the Panama Basin using this dataset is 0.256 Wm^{-2}, almost 2.5 times larger than the global average value of Davies and Davies (2010) used in the previous chapter.

The initial state of the domain is a uniform stratification taken from a profile of observational temperature and salinity measurements in the area from the World Ocean Atlas (Locarnini et al., 2013; Zweng et al., 2013). A boundary of two grid cells around the edges of the domain is restored to this stratification with a time scale of one year, as is the entire top level of the model. The rest of the domain is not affected by any damping terms.

4.3 Results

The simulations were run for 30 years each. This was not long enough for the system to reach a steady state but unfortunately, due to technical problems and subsequent time

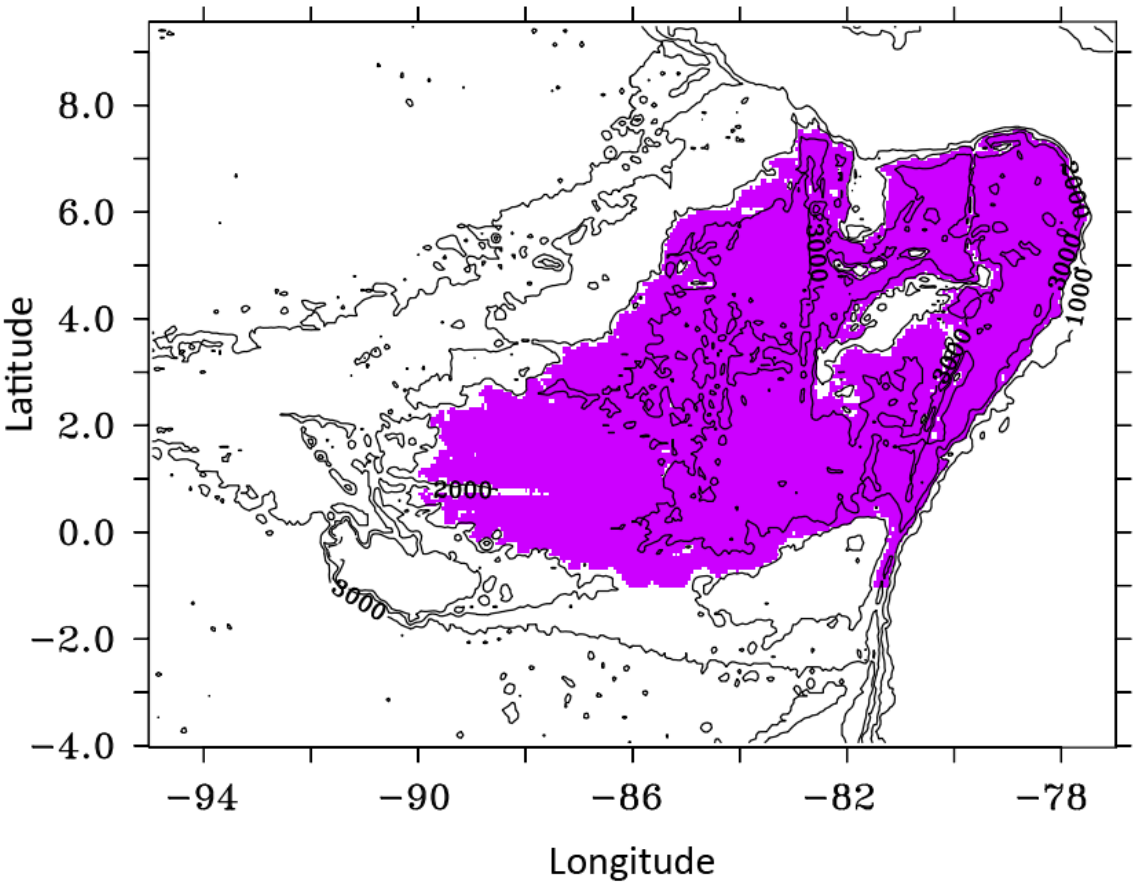

Figure 4.3: The area of the Panama Basin for which averages and integrals are obtained from the results of the three-dimensional model, after a mask has been applied. This is the masked area at 2205m, the top layer of the abyssal region used to calaculate results. The mask boundaries deeper down follow the bathymetry. The overlay shows bathymetry contours for every 1000 m depth.

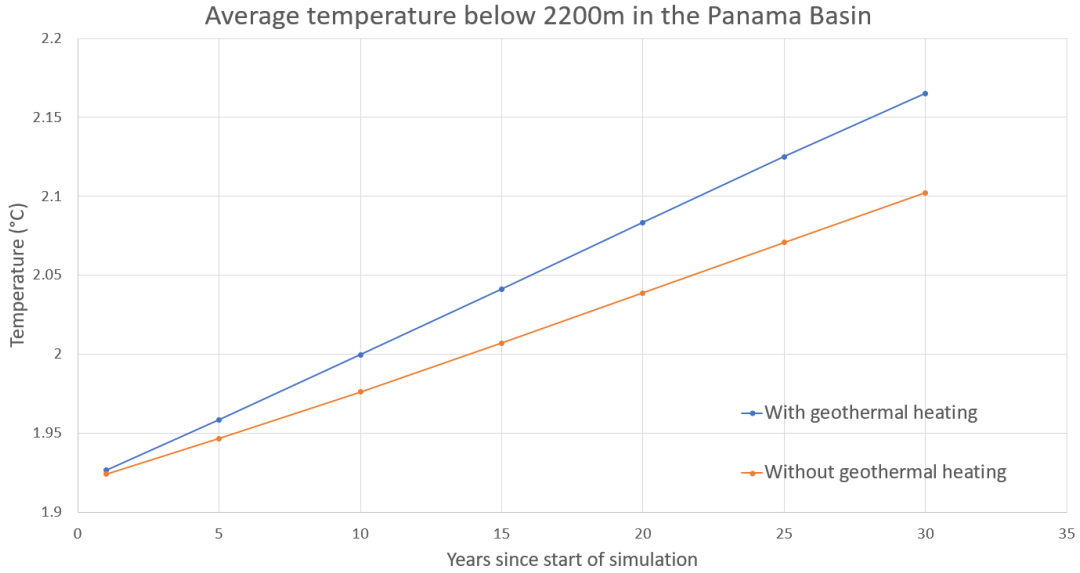

Figure 4.4: The average abyssal temperature trends of the Panama Basin in model simulations.

constraints on the available computer systems, it was not possible to complete longer simulations. However, the available results are indicative of the differences between the two systems, and comparing the way in which the simulations evolve over time reveals interesting details. To generate many of the results presented here, specifically averages and integrals, the interior of the basin was isolated by creating a mask to ignore the areas of the domain which lie outside of it. The area created by using this mask is displayed in Figure 4.3. Everything above 2200 m is ignored, as this region is above the ridges surrounding the deep basin and subject to more external forces. There is in fact not much difference between the two simulations at shallower depths, and no significant difference in the sea surface height.

In the unheated simulation, the interior of the Panama Basin still warms up, due to diapycnal mixing and diffusion. As could be expected, the rate at which the abyssal region of the basin warms up increases with the addition of geothermal heating. The heating trend is almost linear, as shown by the graph in Figure 4.4. With a warming of 0.00823°C per year, the deep water in the simulation with geothermal heating is warming at a rate 34 % greater than that without. This indicates that about 25 % of the overall heating is due to geothermal sources.

The deep water is warmer everywhere within the basin in the simulation using geothermal heating. The average temperature difference below 2200 m is 0.037°C after 30 years. Since the warming trend in both simulations is still linear at this point, extrapolation indicates that the difference will grow with time. The temperature fields at a depth of 2695 m are shown in Figure 4.5. Due to the presense of geothermal heating, the water is warmer at depth across the entire domain, but within the masked area the temperature difference is larger. The greatest difference between the two cases occurs at the western side of the basin, over the Galapagos Rift where the geothermal heat flux is at its highest.

Figure 4.6 shows the vertical and horizontal velocities at a depth of 2590 m, at which flow through the Ecuador Trench is possible in the model grid. In both simulations, a large anti-clockwise rotating gyre dominates the middle of the basin, with a smaller one to the north. In the northeast corner there are two smaller gyres, one fed by an eastward flow from the other side of the Malpelo ridge and the other by a northward current which follows the South American coastline. The large gyre in the middle of the basin appears stronger without geothermal heating.

There is complexity to the flow through the Ecuador Trench, as there is an outflow from the north as well as inflow from the south. The two opposing flows meet near the top of the trench, with the outflow of warmer water from the basin upwelling to pass over the

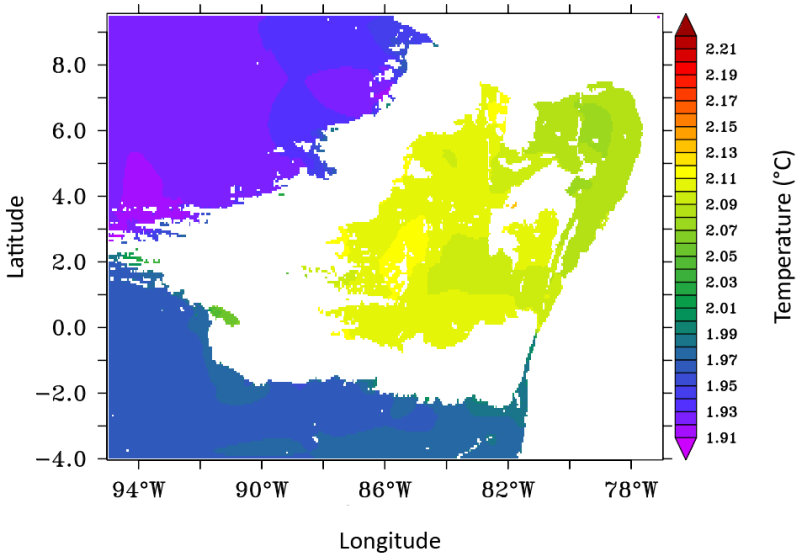

(a) Without geothermal heating.

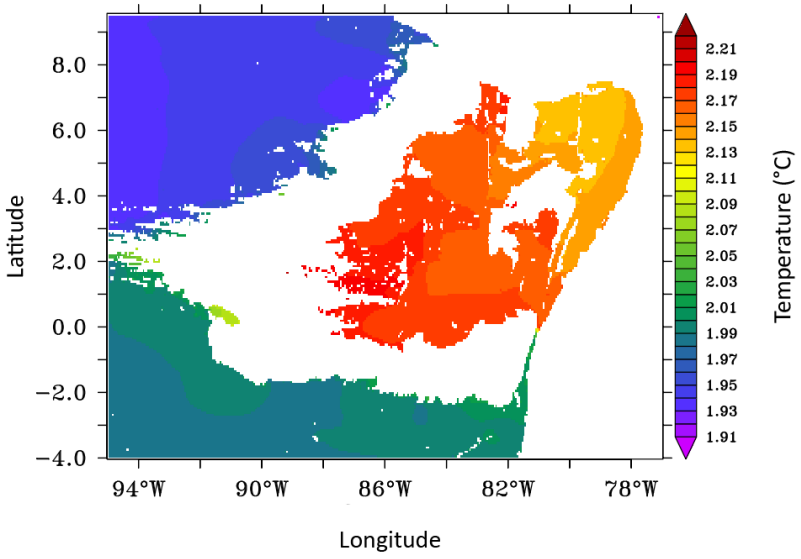

(b) With geothermal heating.

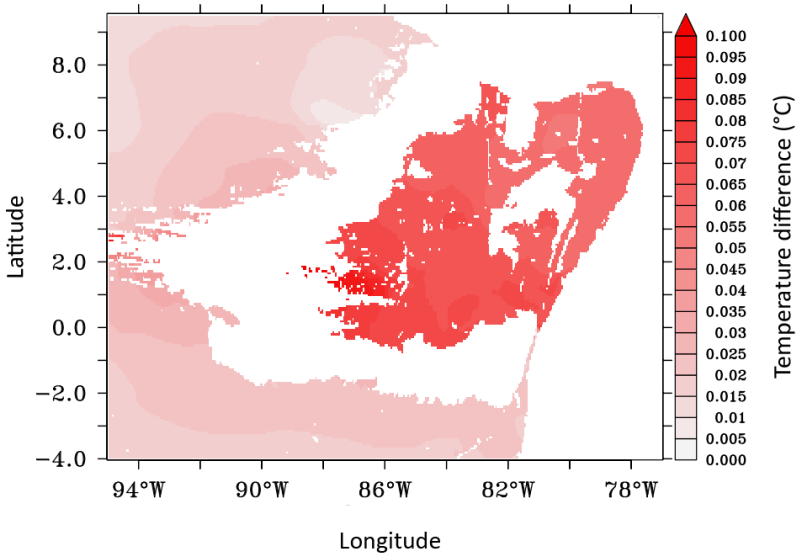

(c) Difference.

Figure 4.5: Temperatures at 2695 m with and without geothermal heating, and the difference between the two cases.

inflow, which sinks deeper into the basin as it travels northwards.The inflow through the bottom of the Ecuador Trench increases with the addition of geothermal heating to the model. The opposing southward flow is not enhanced in the same way, making the net effect of adding geothermal heating to the domain an increased inflow through the trench.

Upwelling occurs on many of the slopes of the ridges in the basin, but there are two places in particular which appear to provide major pathways for water leaving the abyss in both simulations. One is the south side of the Malpelo ridge, and the other is the southwest corner of the basin, south of the Galapagos Rift. Elsewhere in the basin, the addition of geothermal heating causes further changes to the abyssal circulation. There is an increased inflow of water downwelling over the Carnegie Ridge on the south side, and a very large outflow upwelling across the Galapagos Rift to the west which does not occur at all in the simulation without a geothermal boundary condition. On the other side of the basin, the northward flow along the South American coastline is weakened.

The effect of geothermal heating on vertical velocity varies from point to point, as can be seen by the patchy nature of the distribution of differences between the cases in Figure 4.6c. Some parts of the domain see more upwelling and some more downwelling, but looking at the entire basin, the net effect of heating is an increase in the upward vertical flow from the abyss. As is evident in Figure 4.7, the difference is confined to the region of the basin between about 3000 m and 2200 m, above which the difference quite abruptly diminishes.

The depth profiles of vertical flow show two regions of high activity. There is an upwelling region with a maximum flow of 0.080 Sv at 2380 m in the geothermal simulation, and an equivalent peak of 0.040 Sv at 2450 m in the unheated case. Above this is a downwelling region with its peak of 0.059 Sv in the unheated simulation, and 0.057 Sv in the geothermal case, at 2100 m. There is a sudden change from one direction to the other, which given the opposing directions of motion means that a large amount of water is flowing out of the basin where the two meet. The geothermal heating intensifies the upwelling, but not the downwelling, which implies that it casues a greater outflow at this depth. This matches with the hugely increased upwelling and outflow from the basin along the Galapagos Rift. The trend over the final ten years of simulation is fairly linear, with the maxima of the upwelling increasing. The rate of growth over the final five years is 2.5 times faster in the geothermal case, meaning that if the trend continues the difference between the two cases will increase further.

A meridional overturning circulation for the whole basin can be calculated from the northward velocity data, shown in Figure 4.8. The basic shape of the flow is the same in both

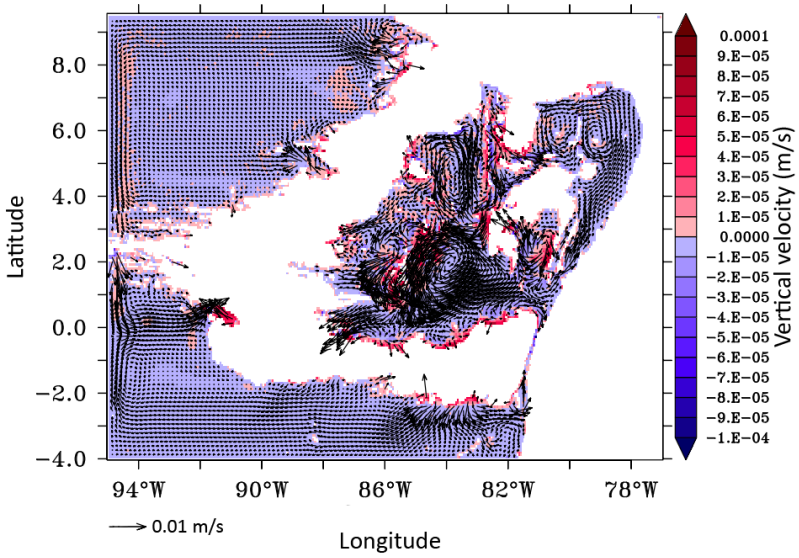

(a) Without geothermal heating.

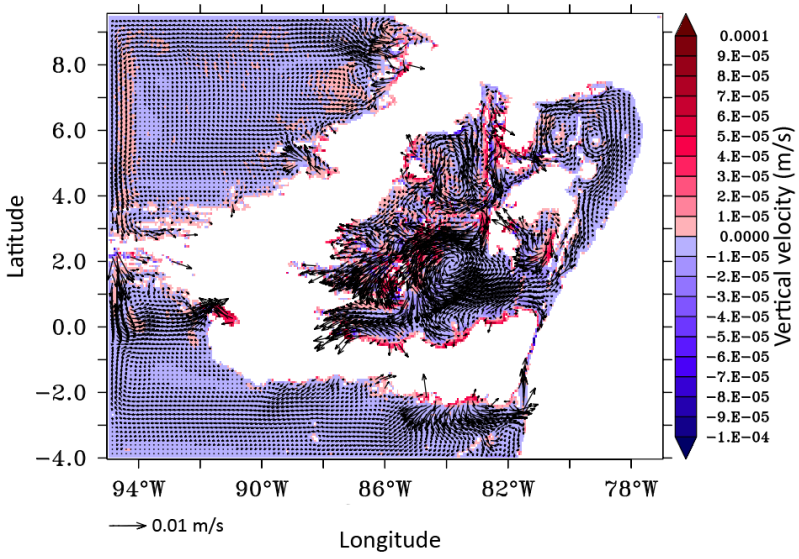

(b) With geothermal heating.

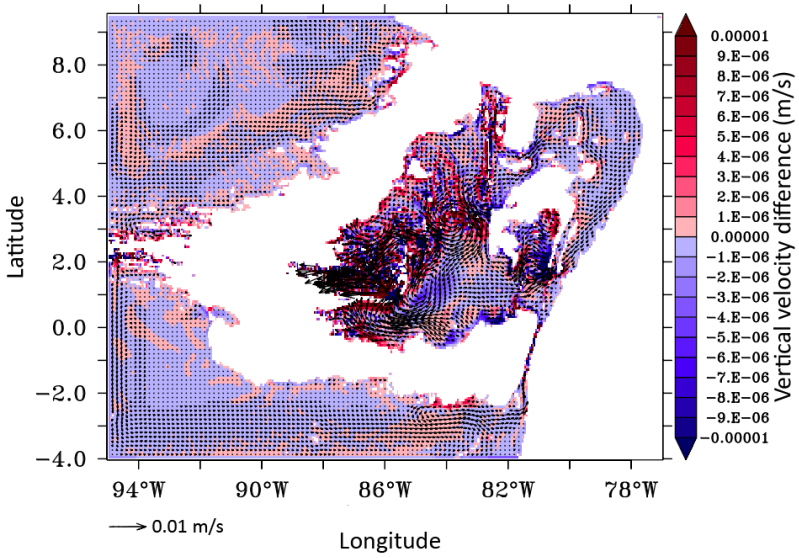

(c) Difference.

Figure 4.6: Vertical velocities at 2590 m with and without geothermal heating, and the difference between the two cases. Overlayed are the horizontal velocity vectors. The velocities shown are annual means for the last year of simulation.

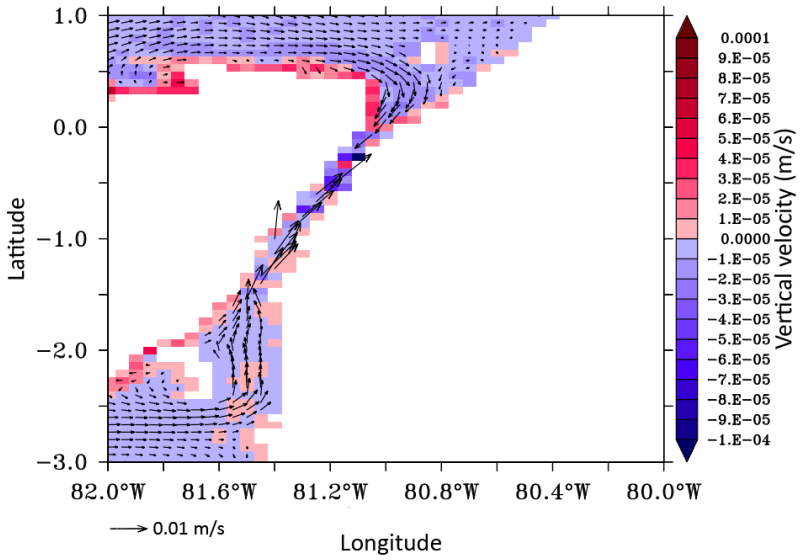

(d) Without geothermal heating (Ecuador Trench).

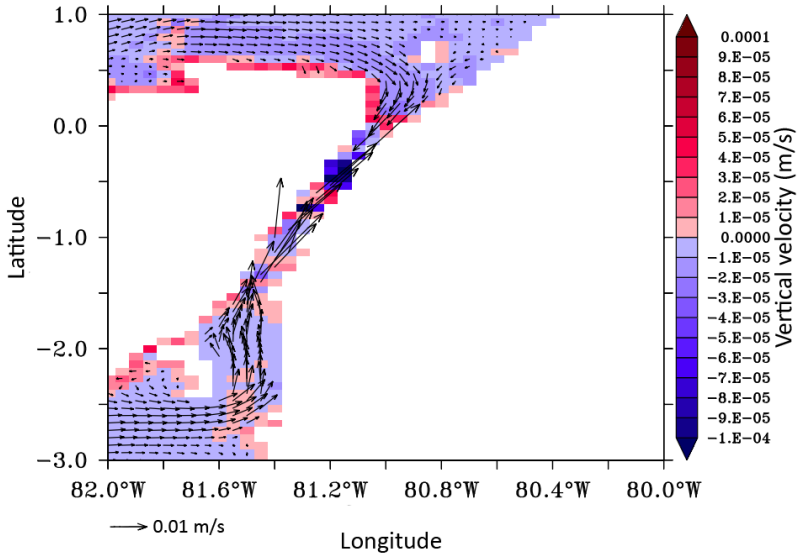

(e) With geothermal heating (Ecuador Trench).

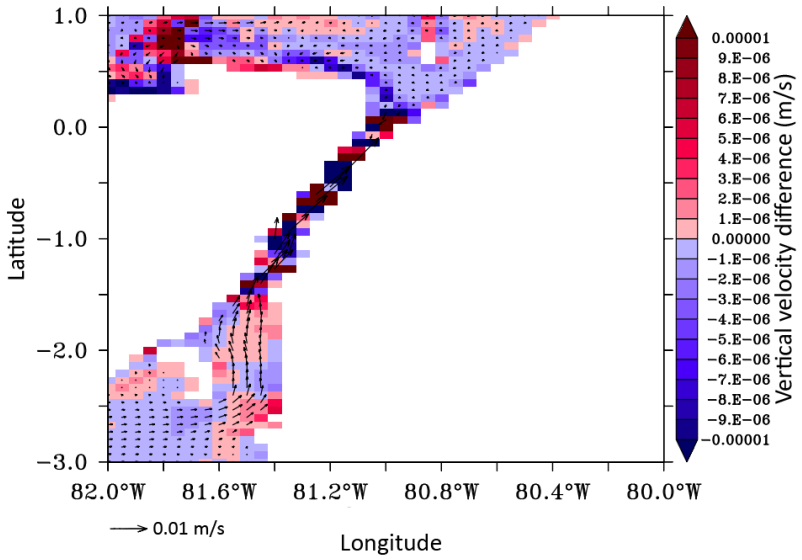

(f) Difference (Ecuador trench).

Figure 4.6: Continued from opposite page. The panels on this page are zoomed in to focus on the Ecuador Trench.

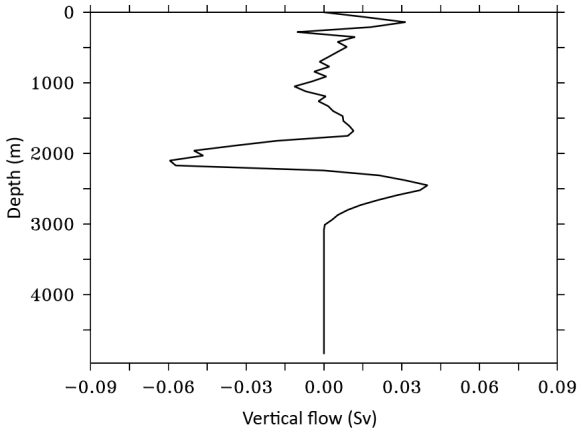

(a) Without geothermal heating.

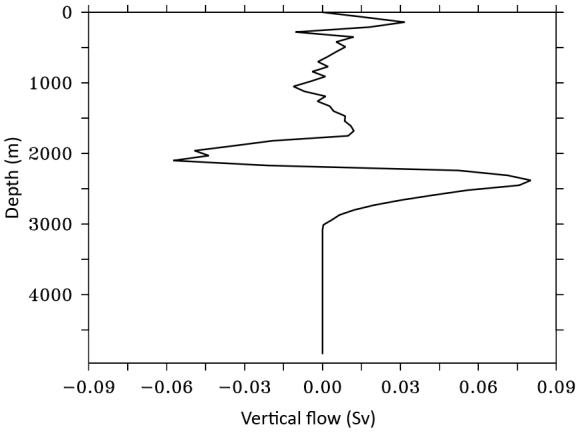

(b) With geothermal heating.

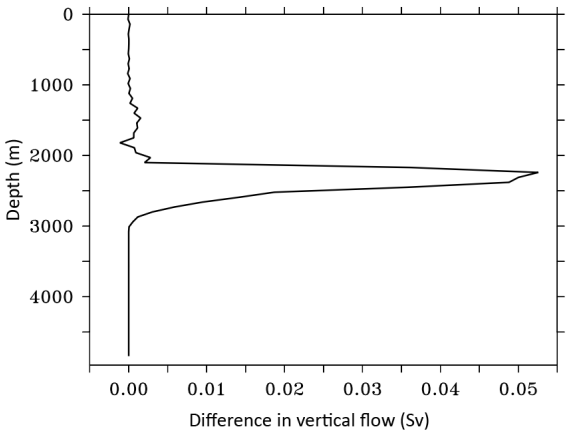

(c) Difference.

Figure 4.7: Depth profiles of the vertical flow for the entire masked Panama Basin area.

cases. The circulation is dominated by two overturning cells, rotating in opposite directions, in the middle of the basin. A smaller circulation occurs on the southern edge of the basin, with inflow at depths and outflow higher up the water column, which is the movement of water through the Ecuador Trench and over the Carnegie Ridge. In the case where geothermal heating is used, the overturning cells intensify, with values of the stream function 47.6 % larger on average below 2200 m. The majority of the intensification is at the southern end of the basin. South of 3.33°N, a latitude roughly between the two gyres, the stream function is on average 90.5 % greater with the addition of geothermal heating, whereas to the north it is only increased by 12.8 %.

At the 30 year point of these simulations, the southern boundary flow is separated from the large circulations at the middle of the basin, but there is a negative trend in the evolution of the stream function between the southern boundary and the anticlockwise overturning cell, suggesting that this may not continue to be the case as time goes on. This trend is more apparent in the simulation with geothermal heating.

An analysis of the components of heat transport to and from the abyssal Panama Basin is carried out, similarly to that in Section 3.6.3. The equations (3.9) are adapted to

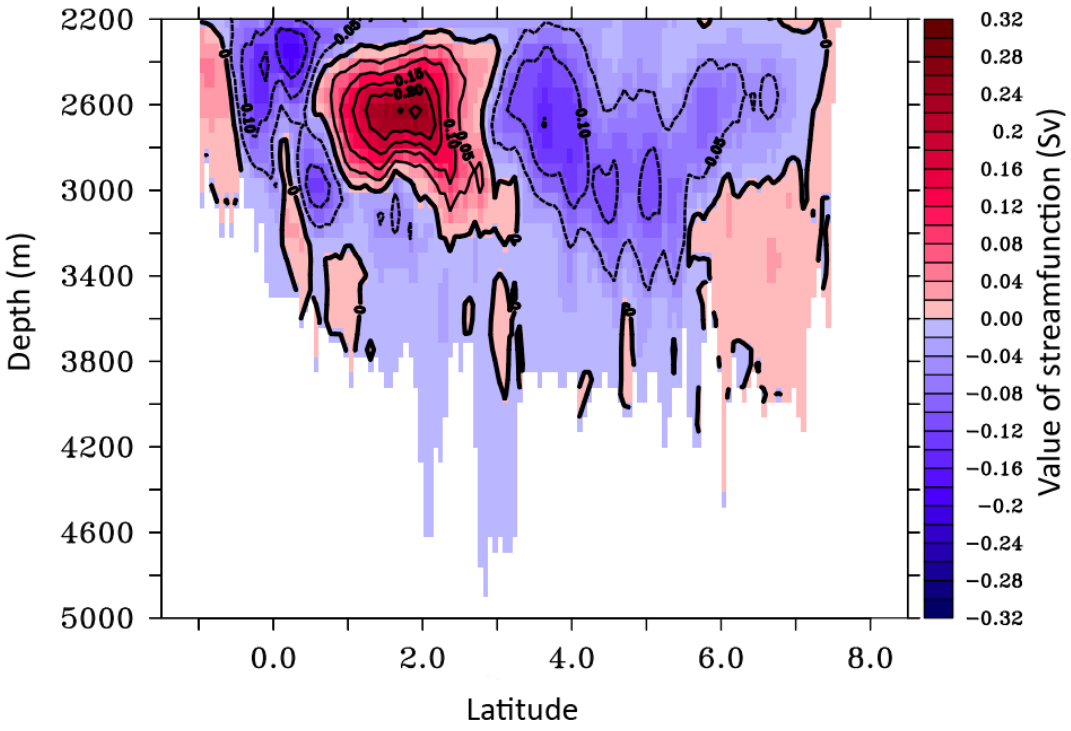

(a) Without geothermal heating.

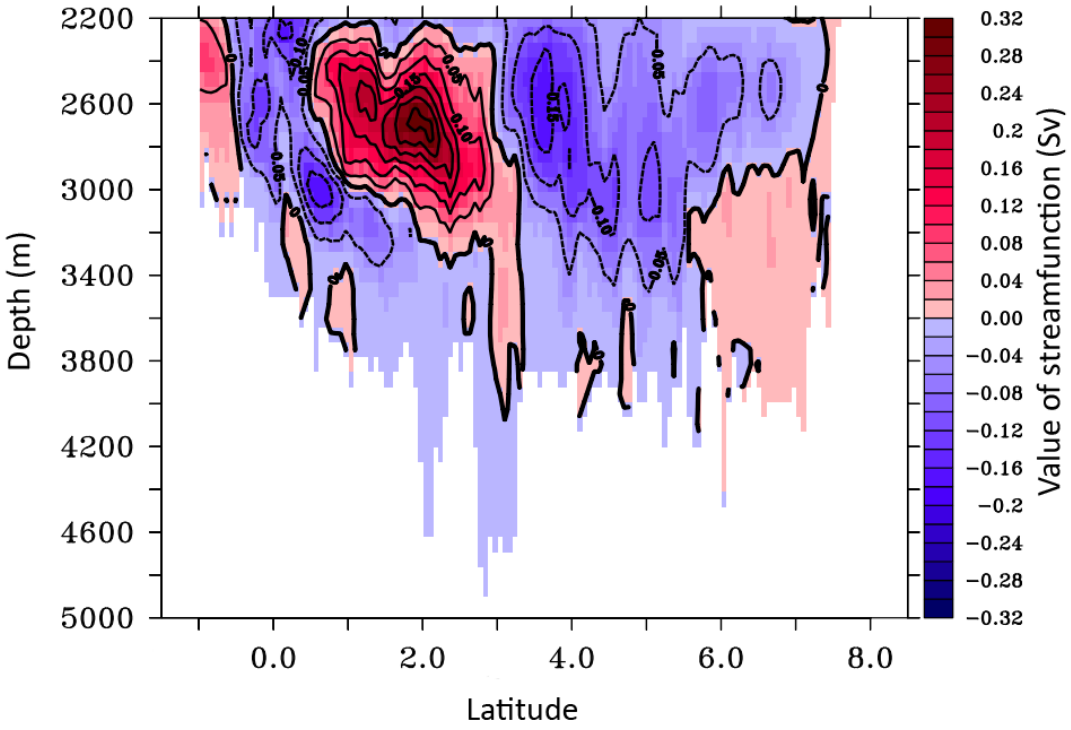

(b) With geothermal heating.

Figure 4.8: The overturning stream functions in units of Sverdrups with streamlines overlayed, where positive values indicate an anticlockwise flow direction.

account for the new domain and the extra dimension, with a direct integral added in the x-direction across the width of the masked region. Integrals are performed over PB, the masked Panama Basin region shown in Figure 4.3. The lateral advection term is treated in a very particular way. Rather than being a calculation across the entire domain, it concentrates on the inflow through the Ecuador Trench, the only horizontal flow of water in or out of the abyssal Panama Basin below the saddle of the Carnegie Ridge at about 2300 m. The latitude y_{ET} at which to calculate the lateral advection was carefully chosen, and the integration in the x-direction is only between two particular points either side of the trench, x_W and x_E. The values used are $y_{ET} = 0.33°\text{S}$, $x_W = 81.3°\text{W}$ and $x_E = 81.0°\text{W}$. For ease of comparison with the previous equations, I have chosen to keep $z = 0$ at the bottom of the deepest ocean level. Taking into account the changes, the heat content relationship is now given by

$$\frac{\partial Q}{\partial t} = F_{\text{geo}} + F_{\text{lat}} - F_{\text{adv}} - F_{\text{dif}} + F_{\text{res}}, \tag{4.1}$$

where

$$Q = \rho c_p \int_0^d \left(\iint_{PB} T(x, y, z)\, \mathrm{d}x\, \mathrm{d}y \right) \mathrm{d}z \tag{4.2a}$$

$$F_{\text{geo}} = \iint_{PB} G(x, y)\, \mathrm{d}x\, \mathrm{d}y \tag{4.2b}$$

$$F_{\text{lat}} = \rho c_p \int_0^d \int_{x_W}^{x_E} v(x, y_{ET}, z) T(x, y_{ET}, z)\, \mathrm{d}x\, \mathrm{d}z \tag{4.2c}$$

$$F_{\text{adv}} = \rho c_p \iint_{PB} w(x, y, d) T(x, y, d)\, \mathrm{d}x\, \mathrm{d}y \tag{4.2d}$$

$$F_{\text{dif}} = \rho c_p \iint_{PB} \kappa(x, y, d) \frac{\partial T(x, y, d)}{\partial z}\, \mathrm{d}x\, \mathrm{d}y. \tag{4.2e}$$

As before, depth profiles of the heat transport components are created, displayed in Figure 4.9. Only the deep waters of the basin below 2200 m are shown, as this is the area which is relevant to my investigation. In shallower waters the results become more noisy as the levels of external interference increase. It can be seen that the results of the two-dimensional simulations were good indicators for the three-dimensional case. A large increase in both vertical and lateral advections is caused by the addition of geothermal heating. As these models are still evolving it cannot be said what the steady state will look like, but at 30 years into the simulation the vertical heat transport out of the abyss is over twice as large with heating at the bottom boundary. The lateral transport through the Ecuador Trench is also at least doubled when geothermal activity is present and almost 2.5 times larger at some depths. By investigating previous years, it can be found that the trends show an increase in transport with time, at a similar rate to the vertical velocities, so it is likely to become an even more significant factor.

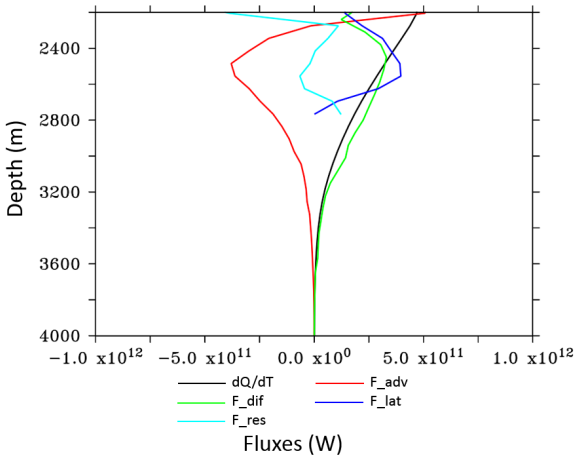

(a) Without geothermal heating.

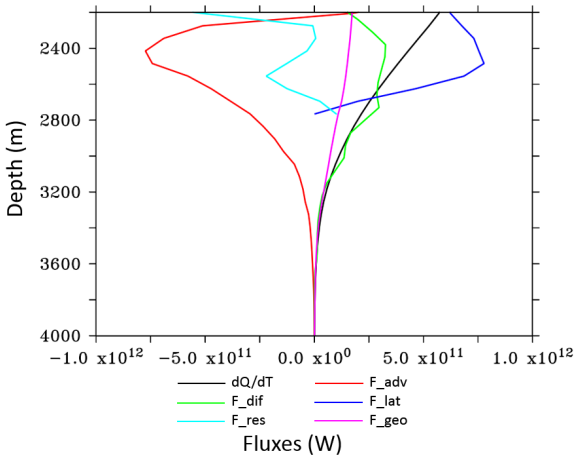

(b) With geothermal heating.

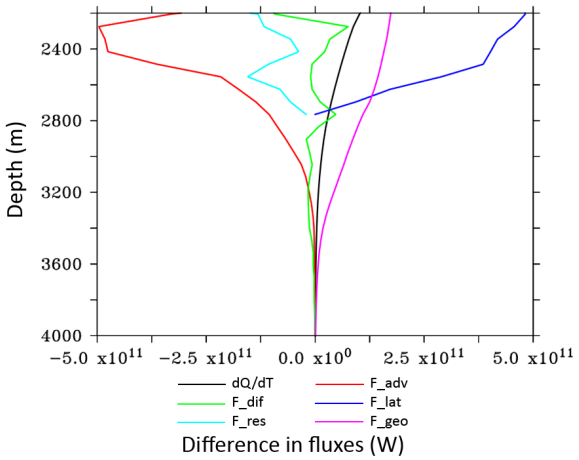

(c) Difference.

Figure 4.9: Profiles of various components of the heat flux, in Watts, with and without geothermal heating, and the difference between the two cases.

4.4 Discussion

The results in this chapter are from a model which is still evolving, and is not yet close to its steady state. The results must be considered in this context. The two-dimensional model in the previous chapter required hundreds of years to reach the near-steady state which was analysed, so it must be noted that conclusions drawn from the results presented here are not directly comparable. However, the trends in the evolution of variables suggest the direction in which the simulations are heading and give interesting insights into the effects of geothermal heating on a real ocean basin. The trends indicate that conclusions reached using the data from 30 years of simulation will continue to hold true, and that when steady states are reached the differences between the two simulations are likely to be more pronounced.

The results gathered from these simulations reinforce the importance of geothermal heating to ocean modelling, particularly at a regional scale. The additional boundary condition

causes many changes to the circulation, heat content and transport. The heating from below dramatically increases the lateral and vertical advective heat transport through the basin, doubling the heat flux in each direction. The increase in vertical advection is seen when looking at the vertical velocities, in which the maximum upwelling doubles in magnitude when driven by geothermal heating.

The circulation of water around the basin, while not entirely different in shape, has been altered significantly in certain places. It seems that where water was recirculating into the central rotating gyre system, the addition of heat causes enough buoyancy to allow the flow to upwell and follow the bathymetry of the Galapagos Rift out towards the Pacific instead. The weaker flow in the rotating gyre supports this theory, since it indicates that less water is retained by the gyre. It seems likely that a large proportion of the extra upwelling water in the geothermal simulation is due to the changes in this location.

The inflow through the bottom of the Ecuador Trench is increased by geothermal heating, as expected. This is due to a "suction" effect, as increased vertical upwelling necessitates a larger compensating flow, allowed for by a greater pressure gradient between the outer Pacific and the Panama Basin interior. The Ecuador Trench is the deepest connection between the two, and so water is channelled through it. The flow is in the region of 0.1 Sv after 30 years, but is increasing. Meanwhile, there is a comparatively weak flow of water upwelling across the saddle of the Carnegie Ridge, consistent with the observations of Lonsdale (1977).

It is interesting to note that the overturning circulation bears some similarity to the two-dimensional model of the previous chapter. The two overturning cells rotating in opposite directions are reminiscent of the circulation resulting from a conductive heat flux in a symmetrical domain (Section 3.6.2). The cells appear to be either side of 3°N, roughly the location of the Costa Rica Rift where a large amount of heat enters the basin in the geothermal boundary condition. However, since these overturning cells are present in the unheated simulation as well this location may be a coincidence, or linked to the bathymetry rather than the heat source. The intensification of this overturning by an average of 48 % with the addition of heat, however, could be enhanced by its positioning relative to the region of high heat flux. With the Ecuador Trench open, I would have expected to see the inflow/outflow system at the south end of the basin extend further into the interior, in line with previous estimations of the regional circulation. The nature of the results in their current form leads to some speculation, since the system is still moving towards an equilibrium state. Taking into account the negative trend in the stream function in the southern half of the basin, I think it can be expected that in time the southern boundary flow will link up with the central cell, resulting in a large overturning cell extending halfway through the basin fed by the Ecuador Trench inflow at depth.

In conclusion, despite the simulations having been run for a shorter time than originally planned due to the aforementioned technical problems, the results can reveal a lot about the abyssal circulation. Geothermal fluxes are shown to be important in the early stages of the system's evolution, and projections based on current trends indicate that their impact will become more significant by the time equilibrium states are achieved.

Chapter 5

Conclusion

5.1 Summary

In Chapter 1, I introduced the location and concepts relevant to this project, and discussed previous literature surrounding geothermal heating, particularly in a modelling context. The main points can be summarised as:

- Geothermal heating has been shown to have significant impacts on global ocean circulation in several modelling studies, despite often being ignored due to the comparitively small magnitude of the heat fluxes invloved.
- Hydrothermal activity accounts for an estimated 34 % of the global heat flux, yet the process has not been used in models.
- The Panama Basin is an ideal natural laboratory for experiments involving geothermal heating. This is due to its interior abyssal region being mostly isolated from the rest of the Pacific, and having a heat flux 2.5 times the global average.
- There has not been much investigation of the Panama Basin in relation to geothermal heating since the 1970s. The recent NERC-funded OSCAR project (through which my PhD was funded) sought to better understand the effects of heating in the area.

In Chapter 2 I took a first look at including volume fluxes though the seabed in circulation models. The scenarios presented were designed to examine the flows driven by such fluxes independent of other factors which would affect circulation in the ocean, such as temperature. The basic findings of this chapter were:

- Volume fluxes through the seabed are capable of driving a circulation which influences the entire water column.

- The magnitude and distribution of flow velocities play a large part in determining what shape the circulation will take.

- The circulations caused by volume fluxes could make an important contribution within a more complex system, and are certainly worth investigating further in the context of hydrothermal heat fluxes.

In Chapter 3, volume fluxes were added to the bottom boundary condition of an ocean circulation model for the first time. Global circulation models now often have the capacity to include geothermal heating by way of a conductive flux, but the hydrothermal contribution has not been represented at large scales. I used a simple configuration of NEMO to run simulations with different prescriptions of heat fluxes. The main results were

- Geothermal heating, regardless of the method of introduction into the ocean, plays an active role in driving abyssal circulation.

- The hydrothermal heat flux produces a vertical advective heat transport from the abyssal ocean which is up to 45 % larger than in the conductive case, and a lateral flow through the south side of the domain up to 35 % larger.

- The average abyssal temperature difference between simulations under the influence of hydrothermal and conductive heating is 0.043°C, with localised differences of up to 0.3 °C.

In Chapter 4, I use a realistic bathymetry and heat flux distribution to model the Panama Basin and compare the resulting circulations with and without a conductive heat flux. The simulations are not at a steady state and trends indicate that the differences will increase with time, but after 30 years of simulation the main results were:

- Geothermal heating doubles the advective transport of heat vertically upwards from the abyss, which is compensated by a similar increase in lateral transport through the Ecuador Trench.

- The basin below 2200 m is warming at a faster rate in the simualtion with geothermal heating. About 25 % of the total warming in this region can be attributed to geothermal heating.

- The net result of geothermal heating is an increase in upwelling from the abyss. This is highly localised, with the Galapagos Rift area seeing major differences.

- Meridional overturning is intensified by geothermal heating, by 47.6 % on average in the abyssal region.

While each chapter consists of a separate piece of work, they were designed to follow on from each other as parts of one process. Chapter 2 sets up the idea of including vertical velocity as a bottom boundary condition, a novel concept in ocean modelling. It shows the far-reaching impact of such mass fluxes on circulation within an ocean layer, including a signature of the inflow being present at the free surface. Chapter 3 extends the idea to look at the flux of heat as well as mass. It looks at the importance of how the flux is constructed, and the effects of the proportion of heat introduced within a mass flux rather than conductively. The speed and temperature at which hydrothermal flows enter the ocean also makes a difference to how the circulation is affected, with the faster flows causing the largest changes when compared to a conductive heat flux. The last chapter was originally intended to use the hydrothermal fluxes of Chapter 3 in a more realistic setting, before the problems in doing this were considered in full. Using conductive fluxes alone, it still manages to show the importance of geothermal heating when calculating heat transport in the basin.

5.2 Potential for further work, and the wider relevance of geothermal heating

There are several ways in which the work presented in this thesis could be continued or built upon in the future. Most simply, the methodology used for my idealised models of the Panama Basin could be adapted to other regions of the ocean. All that would need to be done is to change the bathymetry and boundary conditions which characterise the model domain. There are other partially enclosed basins around the globe which could be subject to similar effects of geothermal heating and hydrothermal fluxes. Examples include the Scotia Sea, Cayman Trough, Red Sea, Sea of Japan and the Arctic Ocean. Projects focusing on such areas could run experiments tailored to the particular region of interest.

A drawback to the final chapter of work presented in this thesis is that the available results are for systems which are still evolving. During my time working on them, I was unfortunate enough to be set back by technical issues beyond my control and a few false starts attempting to use an alternative density-layer circulation model. However, if the time were available it would be worthwhile to run the three-dimensional simulations for longer and reach steady state solutions. The residence time of water in the Panama Basin could be as low as the 42.3 year estimate of Lonsdale (1977), so given more accurate initial conditions a steady state could theoretically be reached fairly quickly. My experience with the two-dimensional models suggests otherwise, however, with even those simple idealised scenarios taking hundreds of years to approach an equilibrium. This is likely due to the influence of diffusive processes over the time taken for model simulations to

reach an equilibrium.

Based on the results of Chapter 3, I believe that using hydrothermal fluxes in a future version of my three-dimensional model would be a benefit to improving the accuracy of regional modelling. But there are barriers to using them more widely. The resolution of large-scale models is not fine enough to capture the scale of individual hydrothermal systems which can be only tens of metres across. Advances in computational processing technology are unlikely to make this achievable in the near future. Additionally, boundary conditions in realistic models would have to rely on more observational data than are currently available. Given how much variability is possible in prescribing a hydrothermal flux, simply guessing the distribution of fluxes would not be helpful in gaining a realistic picture of their contributions to the circulation. It could be beneficial, and would certainly be interesting, to construct several different distributions of fluxes based around the few observations which are available, and compare their effects with observations and hydrological data, but this would still be unlikely to yield a real distribution. I believe that more detailed surveys of the distribution of hydrothermal systems would be extremely useful in the future. In modelling, they would have the potential to improve our understanding of the impacts of different types of heat flux on the circulation.

In the future, with more observational data to use as a guide when setting up boundary conditions and higher resolution models, it would be interesting to see what effects hydrothermal fluxes might have on the global circulation. Conductive geothermal heating in global models can increase the meridional overturning by 25 % (Adcroft et al., 2001; Hofmann and Morales Maqueda, 2009), and my results in Chapter 3 show that that this could be boosted further by the use of hydrothermal fluxes.

From the perspective of understanding the physical processes affecting the ocean, there could be a lot more to learn from idealised or speculative modelling using geothermal fluxes of both varieties. As I have remarked upon several times, the results of my modelling experiments shared many similarities with surface processes. They were almost mirror images of convection circulations driven by surface cooling or winds, where the forces causing changes to the ocean are introduced from above rather than below. A review of convective processes, Marshall and Schott (1999), presents many results which are reminiscent of the circulations caused by geothermal heating in my models. In some cases (eg. Jones and Marshall, 1997) a very deep mixed column is produced by convection, extending down to around 1500 m before stratification is restored. This mirrors the 1000 m thick mixed layer above the geothermal heat flux in my experiments based on the Panama Basin.

The similarities to convective surface processes could hint at an as yet unknown importance of geothermal heating. Convection processes have been studied for decades, whereas geothermal heating is only starting to be used in modelling experiments. If similar convective processes could be occuring above the high heat fluxes of mid-ocean ridges, there could be much to discover about the local effects they have on hydrography and circulation.

In ocean modelling as a whole, the aim is to build the most accurate simulation of real life as possible with the available resources. As computing power imporves, more processes will be included in models. Geothermal heating, in both its forms, should be included in more modelling studies to gain a fuller understanding of how and where heat is transported and stored within the ocean. With 30% of ocean warming occuring below 700 m (Balmaseda et al., 2013), understanding the role of the deep ocean and processes affecting its circulation is crucial for future climate predictions. It is encouraging that of the ocean models used by the Intergovernmental Panel on Climate Change (IPCC) as mentioned in Flato et al. (2013), a couple now support geothermal heating as a boundary condition. Previous geothermal modelling studies have used NEMO (Emile-Geay and Madec, 2009) and COCO (Urakawa and Hasumi, 2009), which are both included in the IPCC list. In addition, several other ocean models have been adapted to include geothermal heating, which sets a good precident. I hope that models will continue to introduce these boundary conditions so that geothermal heating will be used far more often in the future.

Appendix A

MATLAB code

A.1 General solution for problems with a flat seabed

This example has the function w_b set as the uniform inflow from Section 2.3, with the option to select a cosine function instead. Further additions are simple, making use of the heaviside functions as shown here, and the script will successfully plot the results for the last uncommented 'w_bound' and 'startx' in the list of available fuctions.

Listing A.1: Matlab script for the analytical model with a flat seabed

```
% Give values to constants
lat = 3; %latitute
rho = 1027; %density of top layer
drho = 3; %change in density
res = 8; %resolution 1/res degrees of NEMO
l = 10000; %(111000/res)*5; % radius of upward flux
L = 100000; %(111000/res)*25; %radius of downward flux
R = 1; %friction
H = 1000; %water depth where b=0,eta=0
wr = 1e-7; %maximum vertical flux velocity
grid = 71; %grid spacing for plots

%Calculations from constants
f = 2*7.292115*10^(-5)*sin(lat*2*pi/360); %Coriolis force
g1 = 9.81;
g = g1*drho/rho; %reduced gravity

% Set bounds for plot
xl = -1.2*L;
xu = 1.2*L;
lims = [xl,xu,-100,1.2*H];
xvec = linspace(xl,xu,grid-1);

% Define symbolic variables
syms x z real;

%%%%%%%%%%%%%%%%%%%%%%%%%%%%%%%%%%%%%%%%%%%%%%%%%%%%%%%%%%%%%%%%%%%

% Symbolic seabed flux functions. Choose one (and corresponsing 'startx' value for
    plotting streamlines):

```

```
%Single inflow
wr = 2*wr/pi; %Use if matching input velocity to cos inflow
w_bound = (heaviside(x+L)-heaviside(x+l))*(-(wr*l)/(L-l)) ...
       + (heaviside(x+l)-heaviside(x-l))*wr ...
       + (heaviside(x-l)-heaviside(x-L))*(-(wr*l)/(L-l));
startx = linspace(-l,l,20);

%Cos inflow (to match single inflow)
%  w_bound = wr*(heaviside(x+L)-heaviside(x+l))*(l/(L-l))*sin((pi/(L-l))*(x+l)) ...
%          + wr*(heaviside(x+l)-heaviside(x-l))*cos((pi/(2*l))*x) ...
%          - wr*(heaviside(x-l)-heaviside(x-L))*(l/(L-l))*sin((pi/(L-l))*(x-l));
%  startx = linspace(-l,l,20);

%%%%%%%%%%%%%%%%%%%%%%%%%%%%%%%%%%%%%%%%%%%%%%%%%%%%%%%%%%%%

%Calculate h
dh2 = -2*(((f^2)+(R^2))*(int(w_bound,x,-L,x))/(R*g));
h = sqrt(H^2 + int(dh2,x,-L,x));

%Calculate u
u = int(w_bound,x,-L,x)/h;

%Calculate v
v = -f*u/R;

%Calculate w
w = (1 - z/h)*w_bound - (((f^2+R^2)*u*u*z)/(R*g*h));

%Set up empty vectors in preparation for loop
U=zeros(length(xvec));
W=zeros(length(xvec));
Z=zeros(length(xvec));
V=zeros(length(xvec));

%Vectors for x,u,z,w
X=repmat(xvec,length(xvec),1);
for i=1:length(xvec)
    U(:,i) = subs(u,x,xvec(i));
    Z(:,i) = linspace(subs(h,x,xvec(i)),subs(0,x,xvec(i)),length(xvec));
    V(:,i) = subs(v,x,xvec(i));
    for j=1:length(xvec)
        W(j,i) = subs(w,[x,z],[X(j,i),Z(j,i)]);
    end
end

%Speeds, for colorbar
speed = sqrt(U.^2 + W.^2);
maxspeed = max(speed(:));

%%%%%%%%%%%%%%%%%%%%%%%%%%%%%%%%%%%%%%%%%%%%%%%%%%%%%%%%%%%%

%Create plots

figure %Flow lines and speed
myplot(h,lims)
hold on
pcolor(X,Z,speed)
shading interp
ylabel('Height from seabed (m)')
xlabel('Distance from centre of flux function (m)')
col = colorbar;
col.Limits = [min(min(speed)),max(max(speed))];
```

```
col.Label.String = 'Speed (ms^{-1})';
startz = zeros(length(startx),1);
for i=1:length(startx)
    startz(i)= subs(0,x,startx(i));
end
sl = streamline(X,Z,U,W,startx,startz);
set(sl,'color','black','linewidth',1)
hTitle = title('Steady state flow in a homogeneous ocean layer with volume flux through
    the sea bed');
set(hTitle,'FontSize',28)
set(gca,'FontSize',20)
%
figure %Free surface elevation
myplot(h-H,lims)
ylabel('Free surface elevation (m)')
xlabel('Distance from centre of flux function (m)')
hTitle2 = title('Free surface of the flow');
set(hTitle2,'FontSize',28)
set(gca,'FontSize',20)
%
figure %Vertical velocity
hold on
pcolor(X,Z,W)
shading interp
ylabel('Height from reference depth')
xlabel('Distance from centre of flux function (m)')
hTitle3 = title('Vertical velocity (w)');
colormap(darkb2r(min(min(W)),max(max(W))))
col = colorbar;
col.Limits = [min(min(W)),max(max(W))];
col.Label.String = 'Velocity (ms^{-1})';
caxis([min(min(W)),max(max(W))])
s1=streamline(X,Z,U,W,startx,startz);
set(s1,'color','black')
set(hTitle3,'FontSize',28)
set(gca,'FontSize',20)
%
figure %Horizontal velocity (x)
hold on
pcolor(X,Z,U)
shading interp
ylabel('Height from reference depth')
xlabel('Distance from centre of flux function (m)')
hTitle4 = title('Horizontal velocity in x-direction (u)');
colormap(darkb2r(min(min(U)),max(max(U))))
col = colorbar;
col.Limits = [min(min(U)),max(max(U))];
col.Label.String = 'Velocity (ms^{-1})';
caxis([min(min(U)),max(max(U))])
s1=streamline(X,Z,U,W,startx,startz);
set(s1,'color','black')
set(hTitle4,'FontSize',28)
set(gca,'FontSize',20)
%
figure %Horizontal velocity (y)
hold on
pcolor(X,Z,V)
shading interp
ylabel('Height from reference depth')
xlabel('Distance from centre of flux function (m)')
hTitle5 = title('Horizontal velocity in y-direction (v)');
colormap(darkb2r(min(min(V)),max(max(V))))
```

```
col = colorbar;
col.Limits = [min(min(V)),max(max(V))];
col.Label.String = 'Velocity (ms^{-1})';
caxis([min(min(V)),max(max(V))])
s1=streamline(X,Z,U,W,startx,startz);
set(s1,'color','black')
set(hTitle5,'FontSize',28)
set(gca,'FontSize',20)
```

A.2 General solution for problems with bathymetry

This is the script used for Section 2.6 Here, the seabed flux functions are added in the same way, although only one is present for this example script. The bathymetry functions are defined similarly. Setting the bathymetry function to zero, the option which is commented out in this script, will produce the same plots as the previous script. The plots for velocity fields are exactly the same, so I have not reproduced those lines of code here. But there are additions to the plots for speed/flow lines and sea surface elevation, to reflect the bathymetry in the problems.

Listing A.2: Matlab script for the analytical model with bathymetry

```
% Give values to constants
lat = 3; %latitute
rho = 1027; %density of top layer
drho = 3; %change in density
res = 8; %resolution 1/res degrees of NEMO
l = 10000; %(111000/res)*5; % radius of upward flux
L = 100000; %(111000/res)*25; %radius of downward flux
R = 1; %friction
H = 1000; %water depth where b=0,eta=0
wr = 1e-7; %maximum vertical flux velocity
grid = 71; %grid spacing for plots

%Calculations from constants
f = 2*7.292115*10^(-5)*sin(lat*2*pi/360); %Coriolis force
g1 = 9.81;
g = g1*drho/rho; %reduced gravity

% Set bounds for plot
xl = -1.2*L;
xu = 1.2*L;
lims = [xl,xu,-100,1.2*H];
xvec = linspace(xl,xu,grid-1);

% Define symbolic variables
syms x z real;

%%%%%%%%%%%%%%%%%%%%%%%%%%%%%%%%%%%%%%%%%%%%%%%%%%%%%%%%%%%%%%%%%%%

% Symbolic bathymetry functions. Choose one:

%flat
% bath = 0*x;

%General ridge (enter values for alpha and beta)
```

```
alpha = 500;
beta = 0;
cc = ((alpha-beta)/(2*sqrt(2)))+((alpha+beta)/2);
aa = cc/(L-(5*l/4))^2;
bb = 2*aa*(L-(5*l/4));
bath = (heaviside(x+L)-heaviside(x+(5*l/4)))*(aa*(x+(5*l/4))^2 + bb*(x+(5*l/4)) + cc) ...
     + (heaviside(x+(5*l/4))-heaviside(x-(5*l/4)))*(-((alpha-beta)/2)*cos((pi*x)/l)+((
         alpha+beta)/2)) ...
     + (heaviside(x-(5*l/4))-heaviside(x-L))*(aa*(x+(5*l/4)-2*L)^2 + bb*(x+(5*l/4)-2*L) +
          cc);

%%%%%%%%%%%%%%%%%%%%%%%%%%%%%%%%%%%%%%%%%%%%%%%%%%%%%%%%%%%%

% Symbolic seabed flux functions. Choose one (and corresponsing 'startx' value for
    plotting streamlines):

%Single inflow
w_bound = (heaviside(x+L)-heaviside(x+l))*(-(wr*l)/(L-l)) ...
       + (heaviside(x+l)-heaviside(x-l))*wr ...
       + (heaviside(x-l)-heaviside(x-L))*(-(wr*l)/(L-l));
startx = linspace(-l,l,20);

%%%%%%%%%%%%%%%%%%%%%%%%%%%%%%%%%%%%%%%%%%%%%%%%%%%%%%%%%%%%

% Differential of bathymetry function
dbath = diff(bath);

%Calculate h
dh2 = -2*(((f^2)+(R^2))*(int(w_bound,x,-L,x))/(R*g))-2*(H-bath)*dbath;
h = sqrt(H^2 + int(dh2,x,-L,x));

%Calculate u
u = int(w_bound,x,-L,x)/h;

%Calculate v
v = -f*u/R;

%Calculate w
w = (1 - z/h + bath/h)*w_bound - (((f^2+R^2)*u*u*(z-bath))/(R*g*h)) + (u/(h*h))*h*(bath-z
    )*dbath + u*dbath;

%Set up empty vectors in preparation for loop
U=zeros(length(xvec));
W=zeros(length(xvec));
Z=zeros(length(xvec));
V=zeros(length(xvec));

%Vectors for x,u,z,w
X=repmat(xvec,length(xvec),1);
for i=1:length(xvec)
    U(:,i) = subs(u,x,xvec(i));
    Z(:,i) = linspace(subs(h+bath,x,xvec(i)),subs(bath,x,xvec(i)),length(xvec));
    V(:,i) = subs(v,x,xvec(i));
    for j=1:length(xvec)
        W(j,i) = subs(w,[x,z],[X(j,i),Z(j,i)]);
    end
end

%Speeds, for colorbar
speed = sqrt(U.^2 + W.^2);
maxspeed = max(speed(:));

```

```
%%%%%%%%%%%%%%%%%%%%%%%%%%%%%%%%%%%%%%%%%%%%%%%%%%%%%%%%%%%%%%%%%%%%%%%%%%%%%%%%

%Create plots

figure %Flow lines and speed
myplot(h+bath,lims)
hold on
pcolor(X,Z,speed)
shading interp
ylabel('Height from seabed (m)')
xlabel('Distance from centre of flux function (m)')
col = colorbar;
col.Limits = [min(min(speed)),max(max(speed))];
col.Label.String = 'Speed (ms^{-1})';
startz = zeros(length(startx),1);
for i=1:length(startx)
    startz(i)= subs(bath,x,startx(i));
end
sl = streamline(X,Z,U,W,startx,startz);
set(sl,'color','black','linewidth',1)
xvec2 = linspace(xl,xu);
a1 = subs(bath,x,xvec2);
a2 = area(xvec2,a1);
a2.FaceColor = 'black';
hTitle = title('Steady state flow in a homogeneous ocean layer with volume flux through
    the sea bed');
set(hTitle,'FontSize',28)
set(gca,'FontSize',20)
%
figure %Free surface elevation
myplot(h+bath-H,lims)
ylabel('Free surface elevation (m)')
xlabel('Distance from centre of flux function (m)')
hTitle2 = title('Free surface of the flow');
set(hTitle2,'FontSize',28)
set(gca,'FontSize',20)
```

A.3 Problems in cylindrical coordinates

This script contains the calculations for the cylindrical solutions from Section 2.7. I have removed extra seabed flux functions and most of the figure creation, since they are the same as in previous scripts.

Listing A.3: Matlab script for the analytical model of the Ekman layer solutions

```
% Give values to constants
lat = 3; %latitute
rho = 1027; %density of top layer
drho = 3; %change in density
res = 12; %resolution 1/res degrees of NEMO
l = 10000; %(106000/res)*5; % radius of upward flux
lm = (106000/res)*25; %middle radius; from l to lm there is no flux
L = 100000; %(106000/res)*30; %radius of downward flux
R = 1; %1*10^(-9); %friction
H = 1000; %water depth where b=0,eta=0
wr = 1e-7; %10^(-6); %maximum vertical flux velocity
grid = 25; %grid spacing for plots
```

```
13
14 %Calculations from constants
15 f = 2*7.292115*10^(-5)*sin(lat*2*pi/360);
16 g1 = 9.81;
17 g = g1*drho/rho;
18
19 % Define symbolic variables
20 syms r z real
21
22 %%%%%%%%%%%%%%%%%%%%%%%%%%%%%%%%%%%%%%%%%%%%%%%%%%%%%%%%%%%%%%%%%%%%%%%
23
24 % Symbolic bathymetry functions. Choose one:
25
26 %flat
27 bath = 0*r;
28
29 %%%%%%%%%%%%%%%%%%%%%%%%%%%%%%%%%%%%%%%%%%%%%%%%%%%%%%%%%%%%%%%%%%%%%%%
30
31 % Symbolic seabed flux functions. Choose one (and corresponsing 'startx' value for
       plotting streamlines):
32
33 %Single jet
34 w_bound = (heaviside(r-l)-heaviside(r-L))*(-(wr*l^2)/(L^2-l^2)) + (heaviside(r)-heaviside
       (r-l))*wr;
35 startr = linspace(0.1,l,10);
36
37 %%%%%%%%%%%%%%%%%%%%%%%%%%%%%%%%%%%%%%%%%%%%%%%%%%%%%%%%%%%%%%%%%%%%%%%
38
39 % Differential of bathymetry function
40 dbath = diff(bath);
41
42 %Work out h
43 dh2 = -2*(((f^2)+(R^2))*(int(r*w_bound,r,-l,r))/(R*g*r));
44 h = sqrt(H^2 - int(dh2,r,0,L) + int(dh2,r,0,r) - (2*H*bath - (bath*bath)));
45
46 %Calculate u
47 u = int(r*w_bound,r,-l,r)/(r*h);
48
49 %Calculate w
50 w = w_bound + u*dbath - ((z-bath)/h)*(w_bound + (((f^2+R^2)*u*u)/(R*g)) + ((H-bath)*u*
       dbath/h));
51
52 % Set bounds for plot
53 rl = 1;
54 ru = 1.2*L;
55 lims = [0,ru,-100,1.2*H];
56 rvec = linspace(rl,ru,grid-1);
57
58 %Set up empty vectors in preparation for loop
59 zvec = zeros(length(rvec));
60 uvec = zeros(length(rvec));
61 vvec = zeros(length(rvec));
62 wvec = zeros(length(rvec));
63
64 %Arrays for r,u,v,z,w
65 rhovec = repmat(rvec,length(rvec),1);
66 for i=1:length(rvec)
67     zvec(:,i) = linspace(subs(h+bath,r,rvec(i)),subs(bath,r,rvec(i)),grid-1);
68     uvec(:,i) = subs(u,r,rvec(i));
69     vvec(:,i) = subs(-(f/R)*u,r,rvec(i));
70     for j=1:length(rvec)
71        wvec(j,i) = subs(w,[r,z],[rhovec(j,i),zvec(j,i)]);
```

```
    end
end

%Set up vectors for plotting mirror images to compare with NEMO
rhomir = -fliplr(rhovec);
zmir = fliplr(zvec);
umir = -fliplr(uvec);
vmir = -fliplr(vvec);
wmir = fliplr(wvec);

rhoful = horzcat(rhomir,rhovec);
zful = horzcat(zmir,zvec);
uful = horzcat(umir,uvec);
vful = horzcat(vmir,vvec);
wful = horzcat(wmir,wvec);

startrmir = -fliplr(startr);
startrful = horzcat(startrmir,startr);
startz = zeros(1,length(startr));
for i=1:length(startr)
    startz(i)= subs(bath,r,startr(i));
end
startzmir = fliplr(startz);
startzful = horzcat(startzmir,startz);

speed = sqrt(uful.^2 + wful.^2);
maxspeed = max(speed(:));

speed_half = sqrt(uvec.^2 + wvec.^2);
maxspeed_half = max(speed_half(:));

%Figure with r axis.
%For full cross section to compare with NEMO, use 'speed' instead of 'speed_half'
% and 'rhoful','zful','uful','vful','wful' in place of the original vectors

figure
myplot(h+bath,lims)
hold on
pcolor(rvec,zvec,speed_half)
shading interp
ylabel('Height from seabed (m)')
xlabel('Distance from centre of flux function (m)')
col = colorbar;
col.Limits = [min(min(speed_half)),max(max(speed_half))];
col.Label.String = 'Speed (ms^{-1})';
startz = zeros(length(startr),1);
for i=1:length(startr)
    startz(i)= subs(bath,r,startr(i));
end
sl = streamline(rvec,zvec,uvec,wvec,startr,startz);
set(sl,'color','black','linewidth',1)
hold on
rvec2 = linspace(rl,ru);
a1 = subs(bath,r,rvec2);
a2 = area(rvec2,a1);
a2.FaceColor = 'black';
hTitle = title('Steady state flow in a homogeneous ocean layer with volume flux through
    the sea bed');
set(hTitle,'FontSize',28)
set(gca,'FontSize',20)

figure %Surface elevation
```

```
myplot(h+bath-H,lims);
ylabel('Free surface elevation (m)')
xlabel('Distance from centre of flux function (m)')
hTitle2 = title('Free surface of the flow');
set(hTitle2,'FontSize',28)
set(gca,'FontSize',20)
%mirror image if required:
%hold on
%myplot((h_minus+bath_minus-H),-lims);
```

A.4 Ekman layer problems

This script contains the calculations for the Ekman layer solutions from Section 2.8. Once again, extra seabed flux functions and most of the figures have been removed to avoid repetition.

Listing A.4: Matlab script for the analytical model of the Ekman layer solutions

```
% Give values to constants
lat = 3; %latitute
rho = 1027; %density of top layer
drho = 1027; %change in density
nu = 1; %eddy viscosity
l = 10000; % radius of upward flux
L = 100000; %radius of downward flux
wr = 1e-7; %maximum vertical flux velocity
grid = 81; %grid spacing for plots

%Calculations from constants
f = 2*7.2921*10^(-5)*sin(lat*2*pi/360);
g1 = 9.81;
g = g1*drho/rho;
d = sqrt(2*nu/f);

height = 5*d; %height for plot
strnum = 20; %Number of horizonatal streaklines in plot

% Define symbolic variables
syms x y z real;

% Symolic background velocity functions.
ubar = 1e-6;
wbar = 0;
%vbar = 0;

%%%%%%%%%%%%%%%%%%%%%%%%%%%%%%%%%%%%%%%%%%%%%%%%%%%%%%%%%%%%%%%%

% Symbolic seabed flux functions. Choose one (and corresponsing 'startx' value for
    plotting streamlines):

%Single jet
w_bound = (heaviside(x+L)-heaviside(x+l))*(-(wr*l)/(L-l)) ...
       + (heaviside(x+l)-heaviside(x-l))*wr ...
       + (heaviside(x-l)-heaviside(x-L))*(-(wr*l)/(L-l));
startx = linspace(-l,l,20);

%%%%%%%%%%%%%%%%%%%%%%%%%%%%%%%%%%%%%%%%%%%%%%%%%%%%%%%%%%%%%%%%
```

```
39
40 %Calculate remaining interior flow direction
41 if exist('vbar','var')==0
42     dubar = diff(ubar,y);
43     dvbar = dubar + (wbar-w_bound)*2/d;
44     vbar = int(dvbar,x);
45 elseif exist('ubar','var')==0
46     dvbar = diff(vbar,x);
47     dubar = dvbar - (wbar-w_bound)*2/d;
48     ubar = int(dubar,y);
49 elseif exist('wbar','var')==0
50     dubar = diff(ubar,y);
51     dvbar = diff(vbar,x);
52     wbar = (d/2)*(dvbar-dubar) + w_bound;
53 else disp('Must prescribe two interior flow directions')
54 end
55
56 % Calculate u,v,w
57 u = symfun(ubar - exp(-z/d)*(ubar*cos(z/d)+vbar*sin(z/d)),[x z]);
58 v = symfun(vbar + exp(-z/d)*(ubar*sin(z/d)-vbar*cos(z/d)),[x z]);
59 w = symfun(wbar + exp(-z/d)*(w_bound-wbar)*(cos(z/d)+sin(z/d)),[x z]);
60
61 % Calculation of stream function
62 vint = ubar + vbar*1i; %Interior velocity, u+vi
63 phi = symfun((d/4)*(vint*(1-1i)*(1-exp(-(1+1i)*z/d)) + conj(vint)*(1+1i)*(1-exp(-(1-1i)*z
        /d))) + int(w_bound,x,-L,x),[x z]);
64 psi = matlabFunction(phi);
65
66 % Set bounds for plot
67 xl = -1.2*L;
68 xu = 1.2*L;
69 lims = [xl,xu,-100,height];
70 xvec = linspace(xl,xu,grid-1);
71
72 %Set up empty vectors in preparation for loop
73 X=zeros(length(xvec));
74 U=zeros(length(xvec));
75 V=zeros(length(xvec));
76 W=zeros(length(xvec));
77 Z=zeros(length(xvec));
78 PHI=zeros(length(xvec));
79
80 %Convert syms functions
81 u_mf = matlabFunction(u);
82 v_mf = matlabFunction(v);
83 w_mf = matlabFunction(w);
84
85 %Vectors for u,w,phi
86 for i=1:length(xvec)
87     X(:,i) = xvec(i);
88     Z(:,i) = linspace(height,subs(0,x,xvec(i)),grid-1);
89     for j=1:length(xvec)
90         U(j,i) = u_mf(X(j,i),Z(j,i));
91         V(j,i) = v_mf(X(j,i),Z(j,i));
92         W(j,i) = w_mf(X(j,i),Z(j,i));
93         PHI(j,i) = psi(X(j,i),Z(j,i));
94     end
95 end
96
97 %Speed, for colorbar
98 speed = sqrt(U.^2 + W.^2);
99 maxspeed = max(speed(:));
```

```
100
101 %Create plots
102
103 figure %speed and flow lines
104 hold on
105 pcolor(X,Z,speed)
106 shading interp
107 ylabel('Height from seabed (m)')
108 xlabel('Distance from centre of flux function (m)')
109 col = colorbar;
110 col.Limits = [min(min(speed)),max(max(speed))];
111 col.Label.String = 'Speed (ms^{-1})';
112 startz = zeros(length(startx),1);
113 for i=1:length(startx)
114     startz(i)= subs(0,x,startx(i));
115 end
116 sl = streamline(X,Z,U,W,startx,startz);
117 set(sl,'color','black','linewidth',1)
118 xvec2 = linspace(xl,xu);
119 plot([xl,xu],[d,d],'--r')
120 sidestartz = linspace(0,height,strnum);
121 if subs(ubar,x,-10)>0;
122     sidestartx = xl*ones(1,length(sidestartz));
123 elseif subs(ubar,x,-10)<0;
124     sidestartx = xu*ones(1,length(sidestartz));
125 else sidestartx = repmat([1,-1],1,length(sidestartz)/2);
126 end
127 s2=streamline(X,Z,U,W,sidestartx,sidestartz);
128 set(s2,'color','black')
129 hTitle = title('Ekman layer flow');
130 set(hTitle,'FontSize',28)
131 set(gca,'FontSize',20)
```

Appendix B

NEMO code

B.1 Definitions

The code segments presented in this appendix were written specifically for NEMO 3.4. They may not work if directly transferred to other versions of the model.

Before displaying original segments of code used in the experiments of Chapter 3, the definitions of parameters and variables used are presented below to allow these code segments to be interpreted:

Variables and arrays used in calculations

- `jpidta` or `jpi` is the number of grid cells in the x-direction.
- `jpjdta` or `jpj` is the number of grid cells in the y-direction.
- `x_cent` is the midpoint of the x-axis.
- `y_cent` is the midpoint of the y-axis.
- `qgh_trd0` is the array which contains the conductive geothermal heat trend used by the model.
- `ro0cpr` is equal to $\frac{1}{\rho c_p}$.
- `geo_bg` is a parameter which prescribes a background conductive heating across the entire domain. Here it is set to 0.
- `alp_rat` is the value of α_H.
- `geo_hy` is the geothermal heat flux, which can have different definitions. For these experiments it is equivalent to G.

- `r1`, `r2` and `r3` are radii or distances from the centre. `r1` and `r3` are equivalent to ℓ_1 and L_G, while `r2` is third distance which can be set to allow a gap between the discharge and recharge regions.
- `mig` is the i-index, the grid cell number in the x-direction.
- `mjg` is the j-index, the grid cell number in the y-direction.
- `rpi` is equal to π.
- `wbot` is the array of vertical velocities through the seabed.
- `tbot` is the array of the temperature of flows through the seabed.
- `sbot` is the array of the salinity of flows through the seabed.
- `tb_hy` is the array of temperatures in the bottom level of the model.
- `flx_hy` is the array of hydrothermal heat fluxes.
- `zemp_n` is a prescribed velocity for the inflow.
- `zemp_h` is the velocity of the inflow.
- `zemp_s` is the velocity of the outflow.
- `zsalt_n` is a prescribed salinity for the inflow.
- `ztemp_n` is a prescribed temperature for the inflow.
- `ztemp_h` is the temperature of the inflow.
- `tmask` is an array used by NEMO to ensure that calculations are not carried out on grid cells which are part of the bathymetry or walls of a model domain.
- `zsdmp` is an upper damping coefficient (surface damping).
- `zbdmp` is a lower damping coefficient (bottom damping).
- `pn_surf` is a time scale for the upper damping coefficient.
- `pn_bot` is a time scale for the lower damping coefficient.
- `rday` is the number of seconds in a day.
- `jpkm1` is the number of the deepest level.
- `gdept_0` is the array of vertical level depths.
- `rn_dep1` and `rn_dep2` are prescribed depths at which the restoring formulation changes.
- `presto` is the array of damping coefficients for the entire domain.

Namelist parameters for different cases

- `flx_tot` is a logical variable. When true, as it is in these experiments, `geo_hy` is the total average heat flux G. Otherwise `geo_hy` is the average heat flux in the discharge region, $C + H_1$.
- `alp_app` is a logical variable. When true, the flux is partitioned according to the value of `alp_rat`.
- `kflow` sets the shape of the flow function through the seabed. The uniform flux distribution is set by a value of 0, and cosine distribution functions set by a value of 3.
- `kshelf` sets the shape of the domain. When equal to 1, it is the rectangular domain used here. When 0 it is the cylindrical basin used in Section 3.3.
- `hy_var` sets whether the hydrothermal flux is calculated by prescribing temperature as in (3.3a) or prescribing velocity as in (3.3b).
- `hy_t_in` is a logical variable. When true, the prescribed temperature `ztemp_n` is taken to be the difference ΔT rather than T_1 itself.
- `rn_treq` selects the formulation of the vertical restoring.
- `horN` and `horS` are logical variables which, if true, turn on restoring down the northern and southern horizontal boundaries respectively.

B.2 Adding hydrothermal flux through the seabed in NEMO

Adding vertical velocities and associated heat to the seabed boundary conditions involves several small changes to the code, as detailed below. They make use of `key_geothermal`, which is used as a switch to activate lines of code specific to the hydrothermal flux.

In the module `istate`, the following must be inserted at the start of the subroutine `istate_gyre`. The new variables must be added to a namelist and read in from there.

```
1 #if !defined key_geothermal
2       INTEGER, PARAMETER ::   ntsinit = 0   ! (0/1) (analytical/input data files) T&S
            initialization
3       INTEGER            ::   idinit        !  logical unit of initial conditions file
4 #else
5       !Add a few more cases for ntsinit when using key_geothermal
6       INTEGER             ::   ntsinit  ! (0/4) (0: analytical; 1: input data files; 2:
            barotropic; 3: 2-layer initial conditions) T&S initialization; 4: read from
            file
7       REAL                ::   h_1  ! initial layers-1 thickness (if ntsinit = 3)
```

```
      REAL                ::   temp_1,temp_2  ! initial temperatures in layers 1 and 2 (
          if ntsinit = 3)
      REAL                ::   salt_1,salt_2  ! initial salinities in layers 1 and 2 (if
          ntsinit = 3)
      CHARACTER(len=19)   ::   flnm_init  ! name of initial temperature file (used if
          ntsinit=4)
      INTEGER             ::   idinit  ! unit number of flnm_init ((used if ntsinit=4)
      INTEGER             ::   nhdr_init  ! number of header lines in flnm_init (used if
          ntsinit=4)
      INTEGER             ::   ndta_init  ! number of temperatures and salinity depths in
           flnm_init (used if ntsinit=4)
      INTEGER             ::   kk,kflag  ! k index
      REAL, ALLOCATABLE, DIMENSION(:) :: dpth_init  ! initial depths (used if ntsinit=4)
      REAL, ALLOCATABLE, DIMENSION(:) :: theta_init  ! initial temperatures (used if
          ntsinit=4)
      REAL, ALLOCATABLE, DIMENSION(:) :: salt_init  ! initial salinities (used if ntsinit
          =4)
#endif
```

In the module `sbc_oce`, a few new variables must be defined and allocated:

```
#if defined key_geothermal
   REAL(wp), PUBLIC, ALLOCATABLE, SAVE, DIMENSION(:,:) ::   wbot              !:
       hydrothermal inflow                          [m/s]
   REAL(wp), PUBLIC, ALLOCATABLE, SAVE, DIMENSION(:,:) ::   tbot              !:
       hydrothermal temperature                     [C]
   REAL(wp), PUBLIC, ALLOCATABLE, SAVE, DIMENSION(:,:) ::   sbot              !:
       hydrothermal salinity                        [psu]
#endif
```

```
#if defined key_geothermal
      ALLOCATE( wbot (jpi,jpj) )
      ALLOCATE( tbot (jpi,jpj) )
      ALLOCATE( sbot (jpi,jpj) )
#endif
```

In the module `sshwzv`, under the heading `After Sea Surface Height`, a line must be altered:

```
#if defined key_geothermal
      ssha(:,:) = (  sshb(:,:) - z2dt * ( z1_rau0 * ( emp_b(:,:) + emp(:,:) ) - wbot(:,:)
           + zhdiv(:,:) )  ) * tmask(:,:,1)
#else
      ssha(:,:) = (  sshb(:,:) - z2dt * ( z1_rau0 * ( emp_b(:,:) + emp(:,:) ) + zhdiv
          (:,:) )  ) * tmask(:,:,1)
#endif
```

Then under the heading `Now Vertical Velocity` the code should start with:

```
#if defined key_geothermal
      !Set vertical velocities below the sea floor to wbot to perform vertical
          integration
      wn(:,:,jpk) = wbot(:,:)
#endif
```

and end with:

```
#if defined key_geothermal
      !Now restore vertical velocities below sea floor to 0
      wn(:,:,:) = wn(:,:,:) * tmask(:,:,:)
#endif
```

In the module **traadv**, near the top, a module must be added to the USE list:

```
#if defined key_geothermal
   USE sbc_oce          !wbot
#endif
```

Later on in subroutine **tra_adv**, another couple of additions are required:

```
#if defined key_geothermal
      !add indexes ji,jj,jn and tsb_bot
      INTEGER ::   ji,jj,jk,jn,ik   ! dummy loop indexes
      REAL(wp), POINTER, DIMENSION(:,:) :: tsb_bot
#endif
      REAL(wp), POINTER, DIMENSION(:,:,:) :: zun, zvn, zwn
      !!----------------------------------------------------------------------
      !
      IF( nn_timing == 1 )  CALL timing_start('tra_adv')
      !
      CALL wrk_alloc( jpi, jpj, jpk, zun, zvn, zwn )
#if defined key_geothermal
      !Allocate tsb_bot
      CALL wrk_alloc( jpi, jpj, tsb_bot )
#endif
```

Finally, at the end of the subroutine before printing the mean trends, this segment should be added:

```
#if defined key_geothermal
      !Need to ensure that properties are conserved both at the surface and at the ocean
          floor
      !Conservation at the level adjacent to the ocean floor.
      DO jn=1,jpts
         DO jj=1,jpj
            DO ji=1,jpi
              ik = mbkt(ji,jj)
              tsb_bot(ji,jj) = tsb(ji,jj,ik,jn)
            END DO
         END DO
         IF ( jn .eq. 1 ) THEN
            WHERE ( tbot .ne. 9999._wp ) tsb_bot = tbot
         ELSE
           IF ( jn .eq. 2) THEN
              WHERE ( sbot .ne. 9999._wp ) tsb_bot = sbot
           ELSE
              ! Do nothing. no other tracers are being considered so far
           ENDIF
         ENDIF
         DO jj=1,jpj
            DO ji=1,jpi
               ik = mbkt(ji,jj)
               tsa(ji,jj,ik,jn) = tsa(ji,jj,ik,jn) + wbot(ji,jj) / fse3t(ji,jj,ik) *
                   tsb_bot(ji,jj)
            END DO
         END DO
      END DO
#endif
```

B.3 Controlling the heat fluxes in NEMO

In the module `trabbc`, a new case is added to the options for the conductive geothermal heat flux of Emile-Geay and Madec (2009) which implements (3.2a) in the model analytically. The following section of code contains the implementation for both the rectangular domain used in the majority of the work, and the cylindrical basin from Section 3.3.

```
CASE ( 3 )   ! Variable geothermal heat flux : analytically defined in W/m2
             x_cent = FLOAT(jpidta)/2._wp
             y_cent = FLOAT(jpjdta)/2._wp + 0.5
             qgh_trd0(:,:) = 0._wp
             qgh_trd0(:,jpj/2-r3+1:jpj/2+r3) = ro0cpr * geo_bg * alp_rat
             IF (flx_tot .AND. alp_app .AND. kflow == 0) THEN
                geo_hy = (geo_hy*alp_rat*(jpj-2) - geo_bg*alp_rat*2*(r3-r1))/(2*r1)
             ELSEIF (flx_tot .AND. alp_app .AND. kflow == 3) THEN
                geo_hy = (geo_hy*alp_rat*(jpj-2) - geo_bg*alp_rat*2*(r3-r1))/(2*r1)
             END IF
             IF (kshelf == 1) THEN
                DO jj = 2, jpj-1
                   DO ji = 2, jpi-1
                      radius = SQRT((FLOAT(mjg(jj))-y_cent)**2)
                      IF (kflow == 0 .AND. radius .lt. r1) THEN
                         qgh_trd0(ji,jj) = qgh_trd0(ji,jj) + ro0cpr * geo_hy
                      ELSEIF (kflow == 3 .AND. radius .lt. r1) THEN
                         qgh_trd0(ji,jj) = qgh_trd0(ji,jj) + 2. * ro0cpr * geo_hy * r1 *
                             COS(rpi*radius/(2.*r1)) * SIN(rpi/(4.*r1))
                      END IF
                   END DO
                END DO
             ELSEIF (kshelf == 0) THEN
                DO jj = 2, jpj-1
                   DO ji = 2, jpi-1
                      radius = SQRT((FLOAT(mig(ji))-x_cent)**2+(FLOAT(mjg(jj))-y_cent)**2)
                      IF (radius .lt. r1) THEN
                         qgh_trd0(ji,jj) = qgh_trd0(ji,jj) + ro0cpr * geo_hy
                      END IF
                   END DO
                END DO
             END IF
```

Additionally, in the module `sbcana` which contains analytical surface boundary conditions, a new section is created to give options for hydrothermal fluxes. In the existing model structure there is no module for advective bottom boundary conditions, since their inclusion has not been attempted previously, hence them being introduced in this module. The following has been edited down to show only the parts relevant to the uniform and cosine function formulations used in Chapter 3, but several other formulations have been written into this section.

```
!Hydrothermal contribution
      wbot(:,:) = 0._wp
      tbot(:,:) = 9999._wp
      sbot(:,:) = 9999._wp
   !Applying proportionality constant alp_rat and properly defining temperature of
       discharged flow
      IF (alp_app) THEN
         tb_hy(:,:) = 0._wp
```

```
8           flx_hy(:,:) = 0._wp
9           DO jj = 2, jpj-1
10             DO ji = 2, jpi-1
11                tb_hy(ji,jj) = tsn(ji,jj,mbkt(ji,jj),jp_tem)*tmask(ji,jj,1)
12             END DO
13          END DO
14       END IF
15       IF (kshelf == 1) THEN
16          y_cent = (FLOAT(jpjdta) - FLOAT(jp_cfg))/2._wp + FLOAT(jp_cfg) + 0.5
17          IF (kflow == 0) THEN       ! Uniform central discharge
18             IF (.NOT. flx_tot) geo_hy = geo_hy*2.*r1/(alp_rat*(jpj-2))
19             IF (alp_app) THEN
20                IF (hy_var == 0) THEN ! constant prescribed velocity
21                   IF (hy_ave) THEN
22                      zemp_h = zemp_n*(jpj-2)/(4.*r1)
23                   ELSE
24                      zemp_h = zemp_n
25                   END IF
26                   ztemp_h = geo_hy*ro0cpr*(1-alp_rat)*(jpj-2)/(zemp_h*2*r1) + ( ( SUM(
                         tb_hy(2,jpj/2-r3+1:jpj/2-r2)) + SUM(tb_hy(2,jpj/2+1+r2:jpj/2+r3)) )
                         /(2*r3-2*r2) )
27                   IF (alp_rat == 1) zemp_n = 0
28                ELSEIF (hy_var == 1) THEN ! prescribed temperature
29                   IF (hy_t_in) THEN
30                      ztemp_h = ztemp_n + SUM(tb_hy(2,jpj/2-r1+1:jpj/2+r1))/(2.*r1) !
                            prescribed above seabed value
31                   ELSE
32                      ztemp_h = ztemp_n                                          !
                            constant prescribed temperature
33                   ENDIF
34                   zemp_h = (1-alp_rat)*geo_hy*(jpj-2)*ro0cpr/( 2.*r1*(ztemp_h - ( SUM(
                         tb_hy(2,jpj/2-r3+1:jpj/2-r2)) + SUM(tb_hy(2,jpj/2+1+r2:jpj/2+r3)) )
                         /(2.*(r3-r2))) )
35                END IF
36             END IF
37             zemp_s = -zemp_h * r1/( r3 - r2 )
38             DO jj = 2, jpj-1
39                DO ji = 2, jpi-1
40                   radius = SQRT((FLOAT(mjg(jj))-y_cent)**2)
41                   IF (radius .lt. r1) THEN
42                     wbot  (ji,jj) = zemp_h * tmask(ji,jj,1)
43                     tbot  (ji,jj) = ztemp_h * tmask(ji,jj,1)
44                     sbot  (ji,jj) = zsalt_n * tmask(ji,jj,1)
45                     flx_hy(ji,jj) = tbot(ji,jj) * wbot(ji,jj) * rau0 * rcp
46                   ELSEIF ( (r2 <= radius) .and. (radius < r3) ) THEN
47                     wbot  (ji,jj) = zemp_s * tmask(ji,jj,1)
48                     tbot  (ji,jj) = tbot(ji,jj) * tmask(ji,jj,1)
49                     sbot  (ji,jj) = sbot(ji,jj) * tmask(ji,jj,1)
50                     flx_hy(ji,jj) = tb_hy(ji,jj) * wbot(ji,jj) * rau0 * rcp
51                   ELSE
52                     wbot  (ji,jj) = wbot(ji,jj) * tmask(ji,jj,1)
53                     tbot  (ji,jj) = tbot(ji,jj) * tmask(ji,jj,1)
54                     sbot  (ji,jj) = sbot(ji,jj) * tmask(ji,jj,1)
55                   END IF
56                END DO
57             END DO
58          ELSEIF ( kflow == 3 ) THEN         !Cosine functions
59             IF (.NOT. flx_tot) geo_hy = geo_hy*2.*r1/(alp_rat*(jpj-2))
60             IF (hy_var == 1) THEN ! prescribed temperature
61                IF (hy_t_in) THEN    !prescribed above seabed value
62                   ztemp_h = ztemp_n + SUM(tb_hy(2,jpj/2-r1+1:jpj/2+r1))/(2.*r1)
63                ELSE      !constant prescribed temperature
```

```
64                ztemp_h = ztemp_n
65             ENDIF
66             A_in   = 0.
67             B_in   = 0.
68             C_in   = 0.
69             A_in_T = 0.
70             B_in_T = 0.
71             C_in_T = 0.
72             DO jj = 2, jpj-1
73                radius = SQRT((FLOAT(mjg(jj))-y_cent)**2)
74                IF ( radius .lt. r1 ) THEN
75                   A_in   = A_in + (4. * r1 / rpi) * COS(rpi*radius/(2.*r1)) * SIN(rpi
                        /(4.*r1))
76                   A_in_T = ztemp_h * A_in
77                ELSEIF ( (r2 <= radius) .and. (radius < r3) .and. (jj < jpj/2) ) THEN
78                   B_in   = B_in + (2.*(r3-r2) / rpi) * COS(rpi*(-radius+r2)/(r3-r2) +
                        rpi/2.) * SIN(rpi/(2.*(r3-r2)))
79                   B_in_T = B_in_T + tb_hy(2,jj) * (2.*(r3-r2) / rpi) * COS(rpi*(-
                        radius+r2)/(r3-r2) + rpi/2.) * SIN(rpi/(2.*(r3-r2)))
80                ELSEIF ( (r2 <= radius) .and. (radius < r3) .and. (jj > jpj/2) ) THEN
81                   C_in   = C_in + (2.*(r3-r2) / rpi) * COS(rpi*(radius-r2)/(r3-r2) -
                        rpi/2.) * SIN(rpi/(2.*(r3-r2)))
82                   C_in_T = C_in_T + tb_hy(2,jj) * (2.*(r3-r2) / rpi) * COS(rpi*(radius
                        -r2)/(r3-r2) - rpi/2.) * SIN(rpi/(2.*(r3-r2)))
83                END IF
84             END DO
85             A_cos = (1-alp_rat) * geo_hy * (jpj-2) * ro0cpr / ( A_in_T - 2*A_in*B_in_T
                    / (B_in + C_in*(B_in_T/C_in_T)) )
86             B_cos = - A_in * A_cos / ( B_in + C_in*(B_in_T/C_in_T) )
87             C_cos = B_cos * (B_in_T/C_in_T)
88          END IF
89          DO jj = 2, jpj-1
90             DO ji = 2, jpi-1
91                radius = SQRT((FLOAT(mjg(jj))-y_cent)**2)
92                IF (radius .lt. r1) THEN
93                  wbot  (ji,jj) = (4. * A_cos * r1 / rpi) * COS(rpi*radius/(2.*r1)) *
                        SIN(rpi/(4.*r1)) * tmask(ji,jj,1)
94                  tbot  (ji,jj) = ztemp_h * tmask(ji,jj,1)
95                  sbot  (ji,jj) = zsalt_n * tmask(ji,jj,1)
96                  flx_hy(ji,jj) = tbot(ji,jj) * wbot(ji,jj) * rau0 * rcp
97                ELSEIF ( (r2 <= radius) .and. (radius < r3) .and. (jj < jpj/2) ) THEN
98                  wbot  (ji,jj) = (2. * B_cos * (r3-r2) / rpi) * COS(rpi*(radius-r2)/(
                        r3-r2) - rpi/2.) * SIN(rpi/(2.*(r3-r2))) * tmask(ji,jj,1)
99                  tbot  (ji,jj) = tbot(ji,jj) * tmask(ji,jj,1)
100                 sbot  (ji,jj) = sbot(ji,jj) * tmask(ji,jj,1)
101                 flx_hy(ji,jj) = tb_hy(ji,jj) * wbot(ji,jj) * rau0 * rcp
102               ELSEIF ( (r2 <= radius) .and. (radius < r3) .and. (jj > jpj/2) ) THEN
103                 wbot  (ji,jj) = (2. * C_cos * (r3-r2) / rpi) * COS(rpi*(radius-r2)/(
                        r3-r2) - rpi/2.) * SIN(rpi/(2.*(r3-r2))) * tmask(ji,jj,1)
104                 tbot  (ji,jj) = tbot(ji,jj) * tmask(ji,jj,1)
105                 sbot  (ji,jj) = sbot(ji,jj) * tmask(ji,jj,1)
106                 flx_hy(ji,jj) = tb_hy(ji,jj) * wbot(ji,jj) * rau0 * rcp
107               ELSE
108                 wbot  (ji,jj) = wbot(ji,jj) * tmask(ji,jj,1)
109                 tbot  (ji,jj) = tbot(ji,jj) * tmask(ji,jj,1)
110                 sbot  (ji,jj) = sbot(ji,jj) * tmask(ji,jj,1)
111               END IF
112            END DO
113         END DO
114      END IF
115   END IF
```

B.4 Newtonian damping

The lines in the code which control the restoring used in the models of Chapter 3 were added into the module `tradmp`, which deals with the damping of active tracers. The following has been edited down to remove some irrelevant lines of code.

```
         zsdmp = 1._wp / ( pn_surf * rday )
         zbdmp = 1._wp / ( pn_bot  * rday )
         DO jk = 1, jpkm1
            IF ( gdept_0 ( jk ) .lt. rn_dep1 ) THEN
              presto(:,:,jk) = zsdmp
            ELSE
               IF ( gdept_0 ( jk ) .ge. rn_dep1 .and. gdept_0 ( jk ) .lt. rn_dep2 ) THEN
                  IF ( rn_treq == 1 ) THEN !Linear
                     presto(:,:,jk) = zsdmp * MAX ( 0. , ( rn_dep2 - gdept_0 ( jk ) ) / (
                          rn_dep2 - rn_dep1) )
                  ENDIF
               ELSE
                  presto(:,:,jk) = 0.
               ENDIF
            ENDIF
            !Adding switches for restoring at each side
            IF ( zbdmp > presto(1,1,jk) ) THEN
               IF( ln_horS ) THEN                        !lateral boundary condition on
                    the south
                  presto(:,2,jk) = zbdmp
                  presto(:,3,jk) = ( presto(:,3,jk) + 2*zbdmp ) / 3
                  presto(:,4,jk) = ( 2*presto(:,4,jk) + zbdmp ) / 3
               ENDIF
               IF( ln_horN ) THEN                        !lateral boundary condition on
                    the north
                  presto(:,jpj-1,jk) = zbdmp
                  presto(:,jpj-2,jk) = ( presto(:,jpj-2,jk) + 2*zbdmp ) / 3
                  presto(:,jpj-3,jk) = ( 2*presto(:,jpj-3,jk) + zbdmp ) / 3
               ENDIF
            ENDIF
         END DO
         ! Mask resto array and set to 0 first and last levels
         presto(:,:, : ) = presto(:,:,:) * tmask(:,:,:)
         presto(:,:,jpk) = 0._wp
```

References

Adcroft, Alistair, Jeffery R Scott, and Jochem Marotzke (2001). "Impact of geothermal heating on the global ocean circulation". In: *Geophysical Research Letters* 28.9, pp. 1735–1738.

Airy, George Biddell (1845). "Tides and waves". In: *Encyclopaedia Metropolitana*.

Alt, Jeffrey C et al. (1986). "Hydrothermal alteration of a 1 km section through the upper oceanic crust, Deep Sea Drilling Project Hole 504B: Mineralogy, chemistry and evolution of seawater-basalt interactions". In: *Journal of Geophysical Research: Solid Earth* 91.B10, pp. 10309–10335.

Amante, Christopher and Barry W Eakins (2009). *ETOPO1 1 arc-minute global relief model: procedures, data sources and analysis*. US Department of Commerce, National Oceanic et al.

Anderson, RN et al. (1982). "DSDP Hole 504B, the first reference section over 1 km through Layer 2 of the oceanic crust". In: *Nature* 300.5893, p. 589.

Anderson, Roger N and Michael A Hobart (1976). "The relation between heat flow, sediment thickness, and age in the eastern Pacific". In: *Journal of Geophysical Research* 81.17, pp. 2968–2989.

Baker, Edward T and Christopher R German (2004). "On the global distribution of hydrothermal vent fields". In: *Mid-ocean ridges*, pp. 245–266.

Balmaseda, Magdalena A, Kevin E Trenberth, and Erland Källén (2013). "Distinctive climate signals in reanalysis of global ocean heat content". In: *Geophysical Research Letters* 40.9, pp. 1754–1759.

Banyte, D et al. (2018). "Geothermal heating in the Panama Basin. Part I: hydrography of the basin." In: *Journal of Geophysical Research: Oceans*.

Barnes, Jowan M et al. (2018). "Idealised modelling of ocean circulation driven by conductive and hydrothermal fluxes at the seabed". In: *Ocean Modelling* 122, pp. 26–35.

British Oceanographic Data Centre (2015). *GEBCO_2014 Grid*. Version 20150318. URL: `http://www.gebco.net/data%5C_and%5C_products/gridded%5C_bathymetry%5C_data`.

Clarke, W Brian, MA Beg, and Harmon Craig (1969). "Excess 3He in the sea: Evidence for terrestrial primodal helium". In: *Earth and Planetary Science Letters* 6.3, pp. 213–220.

Converse, DR, HD Holland, and JM Edmond (1984). "Flow rates in the axial hot springs of the East Pacific Rise (21 N): Implications for the heat budget and the formation of massive sulfide deposits". In: *Earth and Planetary Science Letters* 69.1, pp. 159–175.

Craig, Harmon, WB Clarke, and MA Beg (1975). "Excess 3He in deep water on the East Pacific Rise". In: *Earth and Planetary Science Letters* 26.2, pp. 125–132.

Cushman-Roisin, Benoit and Jean-Marie Beckers (2011). *Introduction to Geophysical Fluid Dynamics: Physical and Numerical Aspects*. 2nd. Amsterdam: Academic Press.

Davies, J Huw and D Rhodri Davies (2010). "Earth's surface heat flux". In: *Solid Earth* 1.1, p. 5.

Detrick, R S et al. (1974). "The Galapagos Spreading Centre: Bottom-Water Temperatures and the Significance of Geothermal Heating". In: *Geophysical Journal of the Royal Astronomical Society* 38.3, pp. 627–637.

Ekman, Vagn Walfrid et al. (1905). "On the influence of the earth's rotation on ocean-currents." In:

Elderfield, H and A Schultz (1996). "Mid-ocean ridge hydrothermal fluxes and the chemical composition of the ocean". In: *Annual Review of Earth and Planetary Sciences* 24, pp. 191–224.

Emile-Geay, Julien and Gurvan Madec (2009). "Geothermal heating, diapycnal mixing and the abyssal circulation". In: *Ocean Science* 5.2, pp. 203–217.

Fisher, Andrew T and Robert N Harris (2010). "Using seafloor heat flow as a tracer to map subseafloor fluid flow in the ocean crust". In: *Geofluids* 10.1-2, pp. 142–160.

Fisher, AT et al. (2003). "Hydrothermal recharge and discharge across 50 km guided by seamounts on a young ridge flank". In: *Nature* 421.6923, pp. 618–621.

Flato, G et al. (2013). *Evaluation of Climate Models*. In: *Climate Change 2013: The Physical Science Basis. Contribution of Working Group I to the Fifth Assessment Report of the Intergovernmental Panel on Climate Change*. Ed. by TF Stocker et al. Cambridge: Cambridge University Press.

Gent, Peter R and James C McWilliams (1990). "Isopycnal mixing in ocean circulation models". In: *Journal of Physical Oceanography* 20.1, pp. 150–155.

Gill, Adrian E (1982). *Atmosphere-Ocean Dynamics*. New York: Academic Press.

Ginster, Ursula, Michael J Mottl, and Richard P Von Herzen (1994). "Heat flux from black smokers on the Endeavour and Cleft segments, Juan de Fuca Ridge". In: *Journal of Geophysical Research: Solid Earth* 99.B3, pp. 4937–4950.

Hannington, Mark et al. (2011). "The abundance of seafloor massive sulfide deposits". In: *Geology* 39.12, pp. 1155–1158.

Harris, Robert N and David S Chapman (2004). *Deep-seated oceanic heat flux, heat deficits, and hydrothermal circulation*. In: *Hydrology of the Oceanic Lithosphere, Volume 1*. Ed. by Earl E Davis and Harry Elderfield. Cambridge: Cambridge University Press, pp. 311–336.

Hessler, Robert R and Victoria A Kaharl (1995). *The Deep-Sea Hydrothermal Vent Community: An Overview*. In: *Seafloor Hydrothermal Systems: Physical, Chemical, Biological, and Geological Interactions*. Ed. by Susan E Humphris et al. Washington DC: American Geophysical Union, pp. 72–84.

Hofmann, M and Miguel Angel Morales Maqueda (2009). "Geothermal heat flux and its influence on the oceanic abyssal circulation and radiocarbon distribution". In: *Geophysical Research Letters* 36.3.

Huang, Rui Xin (1999). "Mixing and energetics of the oceanic thermohaline circulation". In: *Journal of Physical Oceanography* 29.4, pp. 727–746.

Hutnak, M et al. (2006). "Hydrothermal recharge and discharge guided by basement outcrops on 0.7–3.6 Ma seafloor east of the Juan de Fuca Ridge: Observations and numerical models". In: *Geochemistry, Geophysics, Geosystems* 7.7.

Jacobson, Michael et al. (2000). *Earth System Science: from biogeochemical cycles to global changes*. Vol. 72. Academic Press.

Jones, Helen and John Marshall (1997). "Restratification after deep convection". In: *Journal of Physical Oceanography* 27.10, pp. 2276–2287.

Joyce, Terrence M and Kevin G Speer (1987). "Modeling the large-scale influence of geothermal sources on abyssal flow". In: *Journal of Geophysical Research: Oceans* 92.C3, pp. 2843–2850.

Joyce, Terrence M, Bruce A Warren, and Lynne D Talley (1986). "The geothermal heating of the abyssal subarctic Pacific Ocean". In: *Deep Sea Research Part A. Oceanographic Research Papers* 33.8, pp. 1003–1015.

Koschinsky, Andrea et al. (2008). "Hydrothermal venting at pressure-temperature conditions above the critical point of seawater, 5°S on the Mid-Atlantic Ridge". In: *Geology* 36.8, pp. 615–618.

Laird, Norman P (1969). "Anomalous temperature of bottom water in the Panama Basin". In: *Journal of Marine Research* 27.3, p. 355.

— (1971). "Panama Basin deep water properties and circulation". In: *Journal of Marine Research* 29.3, pp. 226–234.

Lee, William H K and Seiya Uyeda (1965). *Review of heat flow data*. Wiley Online Library.

Lévy, Marina et al. (2010). "Modifications of gyre circulation by sub-mesoscale physics". In: *Ocean Modelling* 34.1-2, pp. 1–15.

Locarnini, R A et al. (2013). *World Ocean Atlas 2013, Volume 1: Temperature*. Ed. by S. Levitus. Vol. 73. NOAA Atlas NESDIS.

Locarnini, R A et al. (2018). *World Ocean Atlas 2018, Volume 1: Temperature*. Ed. by A. Mishonov. Vol. 81. NOAA Atlas NESDIS.

Lonsdale, Peter (1977). "Inflow of bottom water to the Panama Basin". In: *Deep Sea Research* 24.12, pp. 1065–1101.

Lupton, JE, RF Weiss, and H Craig (1977). "Mantle helium in hydrothermal plumes in the Galapagos Rift". In: *Nature* 267.5612, p. 603.

Lupton, John E and Harmon Craig (1981). "A major helium-3 source at 15 S on the East Pacific Rise". In: *Science* 214.4516, pp. 13–18.

Madec, Gurvan (2008). *NEMO ocean engine*. 27. Note du Pôle de modélisation, Institut Pierre-Simon Laplace (IPSL), France, ISSN No. 1288-1619.

Marshall, John and Friedrich Schott (1999). "Open-ocean convection: Observations, theory, and models". In: *Reviews of Geophysics* 37.1, pp. 1–64.

Mashayek, A et al. (2013). "The role of the geothermal heat flux in driving the abyssal ocean circulation". In: *Geophysical Research Letters* 40.12, pp. 3144–3149.

Mesinger, Fedor and Akio Arakawa (1976). "Numerical methods used in atmospheric models". In:

Müller, R Dietmar et al. (1997). "Digital isochrons of the world's ocean floor". In: *Journal of Geophysical Research: Solid Earth* 102.B2, pp. 3211–3214.

Park, Young-Gyu et al. (2013). "The effects of geothermal heating on the East/Japan Sea circulation". In: *Journal of Geophysical Research: Oceans* 118.4, pp. 1893–1905.

Piecuch, Christopher G et al. (2015). "Sensitivity of contemporary sea level trends in a global ocean state estimate to effects of geothermal fluxes". In: *Ocean Modelling* 96, pp. 214–220.

Pollack, Henry N, Suzanne J Hurter, and Jeffrey R Johnson (1993). "Heat flow from the Earth's interior: analysis of the global data set". In: *Reviews of Geophysics* 31.3, pp. 267–280.

Pollard, RT (1977). "Observations and theories or Langmuir circulations and their role in near surface mixing". In: *George Deacon 70th Anniversary Volume, 1977*, pp. 235–251.

Ramondenc, Pierre et al. (2006). "The first measurements of hydrothermal heat output at 9°50′N, East Pacific Rise". In: *Earth and Planetary Science Letters* 245.3, pp. 487–497.

Redi, Martha H (1982). "Oceanic isopycnal mixing by coordinate rotation". In: *Journal of Physical Oceanography* 12.10, pp. 1154–1158.

Saito, Mak A et al. (2013). "Slow-spreading submarine ridges in the South Atlantic as a significant oceanic iron source". In: *Nature Geoscience* 6.9, pp. 775–779.

Sarrazin, Jozee et al. (2009). "A dual sensor device to estimate fluid flow velocity at diffuse hydrothermal vents". In: *Deep Sea Research Part I: Oceanographic Research Papers* 56.11, pp. 2065–2074.

Satoh, Masaki (2013). *Atmospheric Circulation Dynamics and General Circulation Models*. 2nd. Berlin: Springer-Verlag.

Sclater, J G, C Jaupart, and D Galson (1980). "The heat flow through oceanic and continental crust and the heat loss of the Earth". In: *Reviews of Geophysics* 18.1, pp. 269–311.

Sclater, J G and K D Klitgord (1973). "A detailed heat flow, topographic, and magnetic survey across the Galapagos spreading center at 86 W". In: *Journal of Geophysical Research* 78.29, pp. 6951–6975.

Scott, Jeffery R, Jochem Marotzke, and Alistair Adcroft (2001). "Geothermal heating and its influence on the meridional overturning circulation". In: *Journal of Geophysical Research: Oceans* 106.C12, pp. 31141–31154.

Stein, Carol A and Seth Stein (1992). "A model for the global variation in oceanic depth and heat flow with lithospheric age". In: *Nature* 359.6391, pp. 123–129.

— (1994). "Constraints on hydrothermal heat flux through the oceanic lithosphere from global heat flow". In: *Journal of Geophysical Research: Solid Earth* 99.B2, pp. 3081–3095.

Stommel, Henry (1982). "Is the South Pacific helium-3 plume dynamically active?" In: *Earth and Planetary Science Letters* 61.1, pp. 63–67.

Thomson, Richard E, Earl E Davis, and Brenda J Burd (1995). "Hydrothermal venting and geothermal heating in Cascadia Basin". In: *Journal of Geophysical Research: Solid Earth (1978–2012)* 100.B4, pp. 6121–6141.

Urakawa, L Shogo and Hiroyasu Hasumi (2009). "A remote effect of geothermal heat on the global thermohaline circulation". In: *Journal of Geophysical Research: Oceans* 114.C7.

Van Dover, Cindy (2000). *The ecology of deep-sea hydrothermal vents*. Princeton University Press.

Williams, David L and Richard P Von Herzen (1974). "Heat loss from the earth: new estimate". In: *Geology* 2.7, pp. 327–328.

Zalesak, Steven T (1979). "Fully multidimensional flux-corrected transport algorithms for fluids". In: *Journal of computational physics* 31.3, pp. 335–362.

Zikanov, Oleg, Donald N Slinn, and Manhar R Dhanak (2002). "Turbulent convection driven by surface cooling in shallow water". In: *Journal of Fluid Mechanics* 464, pp. 81–111.

Zweng, M M et al. (2013). *World Ocean Atlas 2013, Volume 2: Salinity*. Ed. by S. Levitus. Vol. 74. NOAA Atlas NESDIS.

Zweng, M M et al. (2018). *World Ocean Atlas 2018, Volume 2: Salinity*. Ed. by A. Mishinov. Vol. 82. NOAA Atlas NESDIS.